Vol. 267, No. 1, September 11, 1992 ISSN 0003-2670

ANALYTICA CHIMICA ACTA

An international journal devoted to all branches of analytical chemistry

ELSEVIER

ANALYTICA CHIMICA ACTA

Scope. *Analytica Chimica Acta* publishes original papers, preliminary communications and reviews dealing with every aspect of modern analytical chemistry. Reviews are normally written by invitation of the editors, who welcome suggestions for subjects. Preliminary communications of important urgent work can be printed within four months of submission, if the authors are prepared to forego proofs.

Submission of Papers

Americas

Prof. Harry L. Pardue
Department of Chemistry
1393 BRWN Bldg, Purdue University
West Lafayette, IN 47907-1393
USA
Tel:(+1-317) 494 5320
Fax:(+1-317) 496 1200

Computer Techniques

Prof. J.T. Clerc
Universität Bern
Pharmazeutisches Institut
Baltzerstrasse 5, CH-3012 Bern
Switzerland
Tel:(+41-31) 654171
Fax:(+41-31) 654198

Other Papers

Prof. Alan Townshend
Department of Chemistry
The University
Hull HU6 7RX
Great Britain

Tel:(+44-482) 465027
Fax:(+44-482) 466410

Prof. Willem E. van der Linden
Laboratory for Chemical Analysis
Department of Chemical Technology
Twente University of Technology
P.O. Box 217, 7500 AE Enschede
The Netherlands
Tel:(+31-53) 892629
Fax:(+31-53) 356024

Prof. Paul Worsfold
Dept. of Environmental Sciences
University of Plymouth
Plymouth PL4 8AA
Great Britain

Tel:(+44-752) 233006
Fax:(+44-752) 233009

Submission of an article is understood to imply that the article is original and unpublished and is not being considered for publication elsewhere. *Anal. Chim. Acta* accepts papers in English only. There are no page charges. Manuscripts should conform in layout and style to the papers published in this issue. See inside back cover for "Information for Authors".

Publication. *Analytica Chimica Acta* appears in 14 volumes in 1993. The subscription price for 1993 (Vols. 267–280) is Dfl. 4214.00 plus Dfl. 462.00 (p.p.h.) (total approx. US$ 2555.25). *Vibrational Spectroscopy* appears in 2 volumes in 1993. The subscription price for *Vibrational Spectroscopy* (Vols. 4 and 5) is Dfl. 700.00 plus Dfl. 66.00 (p.p.h.) (total approx. US$ 418.50). The price of a combined subscription (*Anal. Chim. Acta* and *Vibr. Spectrosc.*) is Dfl. 4592.00 plus Dfl. 528.00 (p.p.h.) (total approx. US$ 2797.75). All earlier volumes (Vols. 1–253) except Vols. 23 and 28 are available at Dfl. 259.50 (US$ 141.75), plus Dfl. 18.00 (US$ 9.75) p.p.h., per volume. The Dutch guilder price is definitive. The U.S. dollar price is subject to exchange-rate fluctuations and is given only as a guide. Subscriptions are accepted on a prepaid basis only, unless different terms have been previously agreed upon.
Our p.p.h. (postage, packing and handling) charge includes surface delivery of all issues, except to subscribers in the U.S.A., Canada, Australia, New Zealand, China, India, Israel, South Africa, Malaysia, Thailand, Singapore, South Korea, Taiwan, Pakistan, Hong Kong, Brazil, Argentina and Mexico, who receive all issues by air delivery (S.A.L.–Surface Air Lifted) at no extra cost. For Japan, air delivery requires 25% additional charge of the normal postage and handling charge; for all other countries airmail and S.A.L. charges are available upon request.

Subscription orders. Subscription orders can be entered only by calendar year and should be sent to: Elsevier Science Publishers B.V., Journals Department, P.O. Box 211, 1000 AE Amsterdam, The Netherlands. Tel: (+31-20) 5803 642, Telex: 18582, Telefax: (+31-20) 5803598, to which requests for sample copies can also be sent. Claims for issues not received should be made within three months of publication of the issues. If not they cannot be honoured free of charge. Readers in the U.S.A. and Canada can contact the following address: Elsevier Science Publishing Co. Inc., Journal Information Center, 655 Avenue of the Americas, New York, NY 10010, U.S.A. Tel: (+1-212) 6333750, Telefax: (+1-212) 6333990, for further information, or a free sample copy of this or any other Elsevier Science Publishers journal.
Advertisements. Advertisement rates are available from the publisher on request.

Detailed "Instructions to Authors" for *Analytica Chimica Acta* was published in Volume 256, No. 2, pp. 373–376. Free reprints of the "Instructions to Authors" of *Analytica Chimica Acta* and *Vibrational Spectroscopy* are available from the Editors or from: Elsevier Science Publishers B.V., P.O. Box 330, 1000 AH Amsterdam, The Netherlands. Telefax: (+31-20) 5862845.

US mailing notice – Analytica Chimica Acta (ISSN 0003-2670) is published biweekly by Elsevier Science Publishers (Molenwerf 1, Postbus 211, 1000 AE Amsterdam). Annual subscription price in the USA US$ 2244.75 (subject to change), including air speed delivery. Application to mail at second class postage rate is pending at Jamaica, NY 11431. *USA Postmasters*: Send address changes to Anal. Chim. Acta, Publications Expediting, Inc., 200 Meacham Av., Elmont, NY 11003. Airfreight and mailing in the USA by Publication Expediting.

ANALYTICA CHIMICA ACTA

An international journal devoted to all branches of analytical chemistry

(Full texts are incorporated in CJELSEVIER, a file in the Chemical Journals Online database available on STN International; Abstracted, indexed in: Aluminum Abstracts; Anal. Abstr.; Biol. Abstr.; BIOSIS; Chem. Abstr.; Curr. Contents Phys. Chem. Earth Sci.; Engineered Materials Abstracts; Excerpta Medica; Index Med.; Life Sci.; Mass Spectrom. Bull.; Material Business Alerts; Metals Abstracts; Sci. Citation Index)

VOL. 267 NO. 1 CONTENTS SEPTEMBER 11, 1992

(Continued overleaf)

Contents (continued)

ANALYTICA CHIMICA ACTA
VOL. 267 (1992)

ANALYTICA CHIMICA ACTA

An international journal devoted to all branches of analytical chemistry
Revue internationale consacrée à tous les domaines de la chimie analytique
Internationale Zeitschrift für alle Gebiete der analytischen Chemie

Anal. Chim. Acta, Vol. 267 (1992)

ELSEVIER, Amsterdam–London–New York–Tokyo

0003-2670/92/$05.00

Analytica Chimica Acta, 267 (1992) 1–24
Elsevier Science Publishers B.V., Amsterdam

Review

Dispersion phenomena in flow-injection systems

R. DeLon Hull

Department of Chemistry, University of Cincinnati, Cincinnati, OH 45221-0172; and National Institute for Occupational Safety and Health, 4676 Columbia Parkway, Cincinnati, OH 45226-1998 (USA)

Robert E. Malick and John G. Dorsey

Department of Chemistry, University of Cincinnati, Cincinnati, OH 45221-0172 (USA)

(Received 4th November 1991; revised manuscript received 18th February 1992)

Abstract

Reproducible dispersion is the basis for analysis by flow-injection (FI) methods and is also utilized in several other sample handling and analysis systems (e.g., liquid chromatographic connecting tubing, injectors, detectors and post-column reactors). However, a uniformly acceptable understanding or description of dispersion is currently not available. Theoretical treatments (mathematical models) of dispersion have been developed for both non-reactive (sample does not react with carrier) and kinetic (sample and carrier react) systems. Historically, chemical engineering hydraulic models were used as predictive estimators for FI response curves. These predictive models typically describe only the dispersion in the FI manifold and do not incorporate the influence of the injection, detection or connecting components of the system. Recently, descriptive models which utilize deconvolution of the response curve to describe the dispersion produced by the analysis system have been reported. This review details the various approaches that have been utilized to describe dispersion in FI systems and includes both predictive and descriptive models.

Keywords: Flow injection; Dispersion; Review

Although reproducible dispersion is the underlying principle of flow-injection (FI) systems and the various approaches to its understanding have been chronicled in previous reviews [1–4], a uniformly acceptable description of the dispersion process has not yet surfaced. However, the utility of FI is not diminished by this limited understanding of dispersion. Methods development and applications procedures are adequately described for preparing analytical methods for numerous types of samples [5–8]. Dispersion, as it applies to FI systems, is also descriptive of processes occurring in other analytical systems, e.g., chromatographic injectors, detectors, connecting tubing and post-column reactors.

Theoretical treatments of dispersion traditionally involved the use of chemical engineering hydraulic models [9,10] wherein these equations were investigated for their accuracy in predicting FI response curves. Early investigations were performed with dye solutions (no reaction between sample and carrier) but the scope of these predictive equations was eventually broadened to include reaction between the injected sample and the carrier stream. Recent research has included the development of descriptive methods in which the response curve is used as a descriptor of the analysis system (e.g., deconvolution). Descriptive approaches have been utilized with both non-reactive and chemically reactive kinetic systems.

Correspondence to: J.G. Dorsey, Department of Chemistry, University of Cincinnati, Cincinnati, OH 45221-0172 (USA).

The purpose of this review is to compare these various approaches to understanding dispersion.

This review deals only with continuous (non-segmented) FI systems. The term "manifold" refers to the system tubing between the injector and detector. The term "reactor" is not used as it is not descriptive of an FI system in which dispersion without chemical reaction is utilized. The dispersion coefficient (D), defined by Ruzicka and Hansen [5] as the ratio of injected to detected sample concentrations, has been used by several workers and is also included.

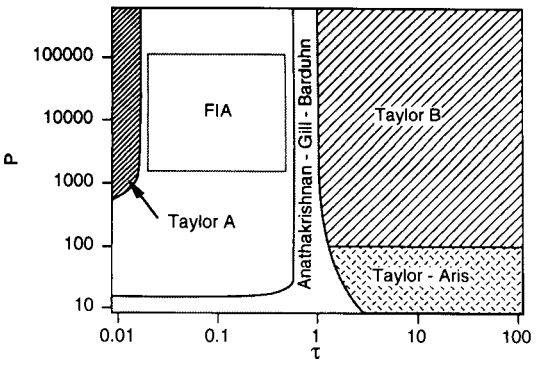

Fig. 1. Regions of validity for various solutions of the diffusion–convection equation and typical FI applications plotted as Peclet number (P) versus reduced time (τ).

PREDICTIVE NON-REACTIVE

Diffusion–convection

Solutions for the general diffusion–convection equation:

$$dC/dt + (u/L)(dC/dx') = (D_m/L^2)(d^2C/dx'^2) \quad (1)$$

where C is concentration (M), t is time (s), u is linear flow velocity (cm s^{-1}), L is manifold length (cm), x' is axial distance divided by manifold length (unitless) and D_m is the molecular diffusion coefficient (cm^2 s^{-1}), were first provided by Taylor [11,12] for two extremes. In one extreme, the transport time was assumed to be minimal so that the contribution of molecular diffusion to dispersion was neglected and therefore convection predominated. The other solution assumed that molecular diffusion predominated. Aris provided a modification to the Taylor approximation by allowing for a substantial increase in radial mixing by diffusion [13] and later, in an interesting perspective on Taylor's work, described the approach he used to remove the restriction on Taylor's solution [14]. Ananthakrishnan and co-workers [15,16] and Bate and co-workers [17,18] approximated diffusion–convection solutions in a region between laminar flow and molecular diffusion (part of the region between the two Taylor approximations). However, as shown in Fig. 1 (adapted from [1,19,20]), none of these treatments describe the diffusion–convection region typically encountered with FI systems.

Vanderslice et al. [19] developed solutions for the general diffusion–convection equation that are relevant to FI-type analyses. Their solutions are given as travel time (t_A) and baseline-to-baseline time (Δt_B):

$$t_A = (109 r^2 D_m^{0.025}/f)(L/q)^{1.025} \quad (2)$$

$$\Delta t_B = (35.4 r^2 f/D_m^{0.36})(L/q)^{0.64} \quad (3)$$

where t_A and Δt_B both have units of seconds, f is an experimentally determined accomodation factor that varies between 0.5 and 1.0 and is unitless, q is the flow-rate (ml min^{-1}) and r is the manifold radius (cm). These equations predict that for a specific manifold and analyte, t_A will vary according to $q^{-1.025}$ and Δt_B is proportional to $q^{-0.64}$ (i.e., log–log plots of t_A and Δt_B should be linear with slopes of -1.025 and -0.64). However, these equations apply only under certain restrictive conditions [21], which include the following: laminar flow (achievable in their laboratory with a syringe pump but not with a reciprocating pump); range of validity is $0.002 \leqslant 30\pi D_m L/q \leqslant 0.8$; does not account for coiling (i.e., the manifold must be linear); the bolus (curved shape of the sample front produced by laminar flow) size must be $\leqslant 20\%$ of total system volume; the injected solute must be in the same solvent as the carrier; detector sensitivity must be adjusted so that peak heights are similar even under different experimental conditions; and the

detector is assumed to be perpendicular to the direction of solution flow.

Gomez-Nieto et al. [22] demonstrated that Vanderslice et al.'s accomodation factor [19,21] is influenced by the manifold geometry (length and diameter) and flow-rate. They proposed the use of a new accomodation factor (f'), which is the ratio of the mean residence time to the statistical residence time. They also utilized preliminary experiments and multiple regression analysis to obtain expressions for t_A and Δt_B for their particular FI system and analyte. This approach eliminated the restrictive conditions of Vanderslice et al. In their system,

$$t_A = 0.465 d^{0.950} (L/q)^{0.850} \quad (4)$$

and

$$\Delta t_B = 56.7 d^{0.293} L^{0.107} q^{1.057} \quad (5)$$

where d is the manifold diameter (mm). Equations were also defined for the Ruzicka and Hansen dispersion coefficient D [5]:

$$D = 2.342 d^{0.496} L^{0.167} q^{-0.0206} \quad (6)$$

and the appearance time of the peak maximum (t_{max}):

$$t_{max} = 0.840 d^{0.683} L^{0.801} q^{-0.977} \quad (7)$$

A dispersion (peak) volume (ΔV_B) was estimated by obtaining the product of the baseline-to-baseline time (Δt_B) and the flow-rate (q). This empirical approach incorporates the influence of all components of the system (including injection and detection) on the dispersion and consequently should be relevant for most FI systems [23].

Kempster et al. [24] utilized this empirical approach with larger injection volumes (300 instead of 30 μl), spectrophotometric detection and inductively coupled plasma (ICP) emission spectrometric detection. The equations obtained for the baseline-to-baseline time for spectrophotometric detection:

$$\Delta t_B = 35.6 d^{0.444} L^{0.282} q^{-0.893} \quad (8)$$

and for ICP emission detection:

$$\Delta t_B = 22.8 d^{0.504} L^{0.367} q^{-0.888} \quad (9)$$

were similar to those of Gomez-Nieto et al. except the exponent of q was of opposite sign. Kempster et al. attributed this to a typographical error in the original published report. The exponent of q should be negative, as an inverse relationship exists between Δt_B and q (both theoretically and in the data provided by Gomez-Nieto et al. and Kempster et al.). Differences between Eqn. 5 (Gomez-Nieto et al.) and Eqn. 8 (Kempster et al.) indicate differences between the two systems employed, even though both systems utilized spectrophotometric detection (the detectors did have different cell volumes). The differences between Eqns. 8 and 9 indicate differences only in the detectors employed (spectrophotometric and ICP), as the same FI system was used with both detectors. Differences should be expected between these two detection systems as the fraction of sample detected by each system is probably different [the spectrophotometer had a 147-μl dead volume preceding a 30-μl cell whereas the ICP detector had an aspirator followed by an 11-ml cloud chamber prior to the plasma (i.e., the detectors contributed different degrees of dispersion or variance to the overall system)]. Kempster et al. reported a predictive accuracy (relative error $< 20\%$ for $> 75\%$ of experiments) similar to that found by Gomez-Nieto et al. (relative error for t_A was $< 10\%$ for $> 85\%$ of experiments and for Δt_B was $< 15\%$ for $> 85\%$ of experiments).

Golay and Atwood [25,26] investigated dispersion in straight (linear), open manifolds as a combination of diffusion and Poiseuille (viscosity-controlled) flow. Simulations performed at various flow-rates demonstrated elution profiles approaching a Gaussian distribution at conditions equivalent to 30 or more theoretical plates. They also attributed a high degree of dependence of peak shape on linearity of the manifold [25]. In an experiment investigating the additivity of variances for manifolds of different length, the variance observed for a 100-cm continuous manifold was greater than the variance (dispersion) observed when the manifold was cut into four 25-cm pieces and rejoined with unions [26]. The unions apparently disrupted laminar flow sufficiently to reduce the bolus length.

Secondary flow

In an investigation of linear and coiled open tubes, Hofmann and Halasz [27] attributed secondary flow effects to be the cause of decreased plate heights in the coiled tubes. The theoretical plate height in a 1.2 mm i.d. manifold was ca. 300 times smaller when it was coiled than when it was linear. Tijssen [28] provided a description of secondary flow patterns in coiled tubes utilizing the Dean number (De), which incorporates the Reynolds number (Re), manifold radius and coil radius. He also described a velocity profile factor (K) which is a function of the shape of the velocity profile. This term was utilized in a general van Deemter-type relationship (under simplifying conditions [29,30]) between plate height (H) and linear velocity (u):

$$H = (2D_m/u) + (2Kr^2u/D_r) \quad (10)$$

where D_r is the radial dispersion coefficient (cm^2 s^{-1}) and is comprised of molecular diffusion and secondary flow. The first term represents axial molecular diffusion and is usually negligible owing to the low molecular diffusion constant values in liquids and high flow velocities used in FI [29]. Equation 10 also applies to straight tubes where $K = K_0 = 1/48$ and $D_r = D_m$. This results in a plate height for straight manifolds (H_0) given by

$$H_0 \approx r^2u/24D_m \quad (11)$$

These equations were utilized to evaluate the efficiency (sampling rate and reagent consumption) of coiled versus straight manifolds. Analysis was determined to be more efficient with small (narrow) rather than large (wide) coil diameter or linear manifolds.

Leclerc et al. [31] predicted maxima in FI response curves by plotting theoretical plate height (divided by four times the manifold radius) against the product of the Reynolds (Re) and Schmidt (Sc) numbers. The critical Reynolds number (Re_c, which is the Reynolds number required for the onset of turbulence) was later included and dispersion was demonstrated to increase as $(Re/Re_c)^{2/3}Sc$ at low fluid velocities and to decrease as $Re_c^{1/6}/(Re/Re_c)^{4/3}Sc^{0.08}$ at higher velocities [32]. Additionally, it was experimentally determined that twisted manifolds (curved in several different directions) produced less dispersion than similar coiled manifolds [32,33]. Similarly, Katz and Scott [34] developed serpentine manifolds (wave-shaped) and experimentally demonstrated that they also produced less dispersion than similar coiled manifolds. Engelhardt and Lillig [35] and Curtis and Shahwan [36] modified the serpentine geometry by stitching stainless-steel capillary through a wire net [35] and stitching polytetrafluoroethylene capillary through an electronic breadboard [36]. In both of these Serpentine II manifolds, the direction of flow is alternately reversed in two dimensions, ultimately producing less dispersion than the original Serpentine I manifold, in which the flow was reversed in only one dimension [36].

Axially dispersed plug flow

Kolev and Pungor [37–42] published a series of papers utilizing the axially dispersed plug flow hydraulic model:

$$\partial C/\partial t = D_L\, \partial^2 C/\partial x_a^2 - u\, \partial C/\partial x_a \quad (12)$$

where C is concentration (kmol m^{-3}), t is time (s), x_a is axial position (m) and D_L is the axial dispersion coefficient (m^2 s^{-1}), to describe dispersion. Equations for predicting the mean residence time and variance of the output signal for systems consisting of three sections (fore-section, manifold and aft-section, all of different diameters) were developed for delta function (infinitely narrow spike), rectangular function and arbitrary input signals [37]. This effort was extended by investigating end effects produced by adding an additional section either before the fore-section or after the aft-section and utilizing only the delta function input [38]. The following observations were found with this system: back-mix flow exists for Peclet numbers [P, where $P = (\bar{u}L)/D_m$ and $\bar{u}$ is the average linear flow velocity] ≤ 0.01; the critical lengths (length at which the error caused by end effects does not exceed some previously stated value) for the fore- and aft-sections of a given system are equal; curve fitting for experimental data processing results in a reduced critical length compared with that obtained when

statistical moments of the curves are utilized; and the critical length becomes shorter when the flow pattern in the additional sections deviates from back-mix flow [38].

The axially dispersed plug flow model was solved in the Laplace domain to predict dispersion (as the mean and variance of the concentration curves) arising from the various system components of a single-line FI system (injector, manifold, detector and connecting components) [39]. Assumptions on which their model is made include the following: each section of the FI system is tubular (i.e., can be characterized by geometrical dimensions and dispersion properties); analyte dispersion in each system component can be described by the axially dispersed plug flow model; connecting tubes before and after the manifold are of infinite length; the time required to go from rest (before sample injection) to steady-state flow (after sample injection) was neglected; mass transfer resulting from hydrodynamic injection (between injected sample and carrier solution before and after the injector) can be neglected; uniform sample injection (with no significant disturbance in the system flow pattern) occurs with syringe injection; and the axial dispersion coefficient and the molecular diffusion coefficient of the analyte are independent of concentration (both analyte concentration and carrier solution concentration).

Model equation solutions utilizing Laplace transforms and respecting the stated assumptions were obtained for local and average concentrations for both syringe and hydrodynamic (valve) injections. The developed models were used to predict the Peclet numbers of the various system components. Experimentally determined Peclet numbers for valve injection were greater than those predicted, probably owing to the valve not acting as a linear, continuously smooth and constant-diameter manifold [39]. Investigations into determining the most appropriate method (in terms of precision and computation time) for numerical inversion of the solution model in the Laplace domain demonstrated that the use of Chebyshov polynomials of the first kind was optimum for small Peclet numbers and Fourier sine series were best for large Peclet numbers [40].

In a similar effort, the dimensionless form of the axially mixed plug flow model:

$$\partial \boldsymbol{C}/\partial \boldsymbol{\Theta} = (1/P)\left(\partial^2 \boldsymbol{C}/\partial \boldsymbol{X}^2\right) - \partial \boldsymbol{C}/\partial \boldsymbol{X} \qquad (13)$$

where $\boldsymbol{C}$, $\boldsymbol{\Theta}$ and $\boldsymbol{X}$ are dimensionless concentration, time and axial distance, respectively, and P is the Peclet number, was applied to the different sections of an analytical system and the resulting differential equations were solved in the Laplace domain [41]. The first statistical moment (mean, M_1) identifies the center of gravity of the concentration curve:

$$M_1 = -\lim(\mathrm{d}\boldsymbol{C}'/\mathrm{d}\boldsymbol{P}') \qquad (14)$$

where C' is the Laplace transform of $\boldsymbol{C}$ and $\boldsymbol{P}'$ is the Laplace complex variable [41]. The second statistical moment (variance, M_2) characterizes the curve width:

$$M_2 = \sigma^2 = \lim\left(\mathrm{d}^2\boldsymbol{C}'/\mathrm{d}\boldsymbol{P}'^2\right) - M_1^2 \quad (p \to 0) \qquad (15)$$

Mathematical treatment of these equations utilizing previously obtained experimental data resulted in regression equations for the Peclet number of linear manifolds not described by Taylor's theory (i.e., $\tau < 0.8$ where $\tau = D_m t/r^2$). Regression equations were also derived for the axial dispersion coefficient of a rotary valve injector [41]. These equations were used for simulation of an FI system and revealed the importance of considering all the system components in mathematical models [42]. Additionally, it was noted that as the Peclet number of the manifold increased, the significance of the contribution from other system components also increased. The axially dispersed plug flow model was also extended to parallel plate laminar flow (e.g., on-line dialysis component of an FI manifold [43]).

Tank(s) models

The well stirred tank (mixing chamber) model utilizes a single tank that provides complete mixing between the injector and detector. Pungor et al. [44] utilized a physical mixing chamber while Tyson and Idris [45] considered the complete FI system as a hypothetical tank in developing models for estimating responses for flame atomic absorption spectrometric (AAS) detection. The

following equations were used [45] for predicting time–concentration profiles:

$$C = C_0 - (C_0 - C_1)\ \exp(-ut/V_t)$$
$$(\text{for } t < t_m) \quad (16)$$

$$C_p = C_0 - (C_0 - C_1)\ \exp(-V_i/V_t)$$
$$(\text{for } t = t_m) \quad (17)$$

$$C = C_1 - (C_1 - C_p)\ \exp[-u(t - t_m)/V_t]$$
$$(\text{for } t > t_m) \quad (18)$$

where C is the concentration at time t, C_1 is the concentration of analyte in the carrier stream, C_0 is the analyte concentration in the injected sample, C_p is the concentration at the peak maximum, V_i is the volume injected, V_t is the volume of the hypothetical tank (i.e., the volume of the complete FI system), u is the carrier velocity and $t_m = V_i/u$. The value of V_t must be determined experimentally [45]. In typical FI applications, $C_1 = 0$ and $C_0 = C_m$ (where C_m is the measured concentration in the injected sample). However, Tyson and Idris utilized these equations with standard additions procedures in which the sample was used as the carrier into which standards were injected. The equations were used to predict system characteristics for limited ($D < 3$), medium ($3 < D < 10$) and high ($D > 10$) dispersion FI systems [45].

Stone and Tyson [46] evaluated the effects of flow-rate, manifold length, manifold diameter and injection method with two models of FI systems (well stirred tank and two tanks in series). The two tanks in series model assumes two well stirred tanks of different volume, connected in series and incorporating a step input instead of a delta function input. Experimental data collected for comparison with the models showed that the dispersion coefficient decreased with increasing flow-rate for short manifold lengths (30 cm) and became constant at flow-rates above 5 ml min^{-1}. Two maxima were observed (ca. 1.5 and ca. 6.5 ml min^{-1}) for long (360-cm) manifolds, whereas at an intermediate length (110 cm) a maximum was observed at low flow-rates (ca. 0.4 ml min^{-1}) decreasing again to a constant above a flow-rate of ca. 5 ml min^{-1}. As expected, the dispersion coefficient increased with increasing manifold length (although not linearly above ca. 100 cm) and also increased with increasing manifold diameter (at a constant manifold length). For constant manifold volumes, the dispersion coefficient generally increased with increasing diameter; however, the effects were dependent on flow-rate. Also, the peak shapes were different for different experimental configurations. Time injection (the sample valve was switched back to the fill position before the dispersed sample tail could enter the manifold) and slug injection (the sample valve was left in the injection mode so that even the rear of the sample, which began dispersing in the valve, was allowed to enter the manifold) were compared and it was concluded that differences between injection methods would be largest when the sample volume injected was a large fraction of the total system volume.

Comparison of experimental data with the well stirred tank model of Tyson and Idris [45] showed that the model was accurate for portions of the rise and fall curves (i.e., system response, concentration vs. time) but missed the inflection point of the rise curve and demonstrated a flattened peak maximum. The two tanks in series model appeared to give a closer approximation to the experimental data than the well stirred tank model. Stone and Tyson [47] extended the well stirred tank model to the two tanks in parallel model. Equations describing the two tanks in parallel model are similar to the well stirred tank model except that terms relative to the flow fraction through each tank (f_1 and f_2) were incorporated. In general, comparison of the well stirred tank and two tanks in parallel models with experimental data showed the two tanks in parallel model to be a more accurate predictor than the well stirred tank model. However, the well stirred tank model exhibited good agreement for short (< 40 cm) manifold lengths and high flow-rates and the two tanks in parallel model did not remain accurate for long (> 50 cm) manifold lengths [47].

Reijn et al. [48] investigated the contribution of injection to the overall system variance and concluded (from a systems analysis theoretical approach and confirmed by experimentation) that

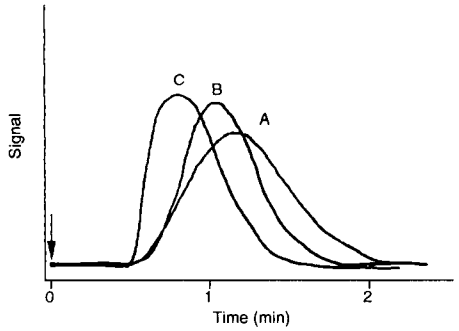

Fig. 2. Elution curves for injection of 125 μl of $KMnO_4$ (10^{-3} M) solution into water for (A) an open straight manifold, (B) an open coiled manifold and (C) a single-bead string reactor. Reproduced with permission of Elsevier from [49].

minimum variance is obtained by minimizing the sample volume. In additional efforts at minimizing dispersion, a single-bead string reactor was developed [49]. The single-bead string reactor utilizes a manifold packed with glass beads which have a diameter of up to 70% of the inner diameter of the manifold. Comparison with other manifold configurations (Fig. 2) showed that dispersion was minimum with the single-bead string reactor and greatest with a linear, open manifold, with a coiled manifold having an intermediate dispersion [49]. However, the peak height with the single-bead string reactor was nearly constant and independent of flow-rate (up to ca. 1.5 ml min^{-1}, at which the connectors began to leak due to the increased back-pressure caused by the packing) [50]. Design equations for maximum sampling frequency and minimum reagent consumption were developed utilizing liquid chromatographic concepts for straight, open manifolds, coiled manifolds and single-bead string reactor systems [51].

Estimating sample plug bolus shapes

Vanderslice et al. [52] used the reduced units of Ananthakrishnan et al. [15] to solve the diffusion convection equation for predicting laminar flow bolus shapes under typical FI conditions. The results were generally as expected, e.g., increasing the manifold diameter caused an increase in dispersion and the use of different diffusion constants gave different bolus shapes. These results were experimentally confirmed by Korenaga et al. [53], who used microscopic detection to photograph laminar flow bolus shapes. Their studies showed the axial dispersion decreased as flow-rates were decreased and that molecular diffusion decreased the axial dispersion at the interface of the sample zone. A needle-shaped bolus 500 mm long was observed for a 2 m manifold (1 mm i.d.) with a 10-μl sample injection and a 1 ml min^{-1} flow-rate. The sample zone was observed to become more pointed and longer as the distance traveled (by the sample plug) increased. As expected, the baseline-to-baseline time (dispersion) was observed to decrease with coiling of the manifold. This work also confirmed similar conclusions reached by solution of the diffusion–convection equation by a finite element method [54].

Powell and Fogg [55] built a resistance–capacitor circuit as a simulator of the well stirred tank model. The addition of a filter circuit caused the response to correspond to a two tanks in series model where the tanks are of equal volume. The simulated two tanks in series responses were more similar to actual FI response curves than the simulated well stirred tank responses.

PREDICTIVE CHEMICALLY REACTIVE

Although Ruzicka and Hansen [56] realized the significance of chemical reaction kinetics to an eventual comprehensive theory of FI, these aspects were seldom included in theoretical treatments until their relevance was noted by Pardue and Fields [57,58] and Painton and Mottola [59,60].

Variable-time kinetic model

Pardue and Fields [57,58] used a variable-time kinetic model to evaluate a FI system containing a gradient chamber. Their model is based on the following assumptions: all reactions go to completion rapidly and follow first-order kinetics; plug-flow sample introduction; instantaneous mixing; and mixing does not occur between the gradient chamber and the detector. The time required to

remove all reactant from the gradient chamber when the analyte is in excess was defined by

$$t_1 = (V_g/q)\ \ln\left[1 + z\left(C^0_{rg}/C_0\right)\right] \quad (19)$$

where V_g is the gradient chamber volume, q is the volumetric flow-rate, z is the reaction ratio, C^0_{rg} is the reactant concentration in the gradient chamber when sample first enters and C_0 is the initial sample concentration. The concentration of sample in the gradient chamber (C_{ag}) increases between t_1 and t_2 as

$$C_{ag} = C_0\left\{1 - \exp\left[-(q/V_g)(t - t_1)\right]\right\} \quad (20)$$

At t_2, the time at which all sample has entered the chamber, a maximum analyte concentration exists in the chamber ($[A]^{max}_g$) and is defined by

$$[A]^{max}_g = C_0\left\{1 - \exp\left[-(q/V_g)(t_2 - t_1)\right]\right\} \quad (21)$$

After t_2 the concentration decreases as

$$C_{ag} = [A]^{max}_g \exp\left[-(q/V_g)(t - t_2)\right] - zC^0_r\left\{1 - \exp\left[-(q/V_g)/(t - t_2)\right]\right\} \quad (22)$$

where C^0_r is the initial reactant concentration in the flow stream. Agreement between experimental and predicted data was good (5% or better for slopes and 3% or better for intercepts). Moreover, the equations predicted the influence of various experimental parameters on the system response. The kinetic model was accurate at predicting peak shapes except at the maximum, in which the experimental data exhibited more curvature [61]. This was attributed to the trailing edge of the sample plug being dispersed (instead of behaving as a "plug" according to the assumption made in developing the model). Additionally, a difference between the predicted and experimental curves, after the maximum, demonstrated the assumption that the entire process followed first-order kinetics was not entirely valid. The dilution process, from reactant continuously flowing into the chamber, corresponds to a zero-order process and the resulting experimental curve was therefore a combination of zero-order and first-order kinetic behavior [61]. These equations were later modified to account for the sensitivity observed with conventional detectors [62]. The modified equations were used to develop relationships for determining whether analyte or reagent was in excess for both single- and dual-channel systems [63]. For single-channel systems:

$$C^0_{rg} = C_0\left[\exp(V_i/V_g) - 1\right] \quad (23)$$

where V_i is the volume of sample injected, describes the condition where there is just sufficient sample to remove all reactant from the chamber. The similar situation for a dual-channel system is described by

$$C^0_r = C_0\left[1 - \exp(-V_s/V_g)\right] \quad (24)$$

Equations describing concentration profiles for the analyte and reactant in systems both with and without chemical reaction were also developed [63].

Diffusion–convection

Painton and Mottola [60] reviewed dispersion as it applies to physiological circulation research, chemical reactor engineering and chromatography and described, as a major omission in the literature at that time, that chemical reaction kinetics should be included in descriptions of dispersion since chemical reactions introduce kinetic complications in the description of dispersion. Additionally, they noted that the dispersion coefficient [5] did not provide information about the signal shape (as it does not describe a distribution of residence times) and consequently was restricted in usefulness [59,60].

Chemical reaction-induced alterations of the concentration profile within the sample plug and its boundaries were later investigated by developing a numerical model based on solution of the general diffusion–convection equation (Eqn. 1) modified by an assumed pseudo-first-order chemical reaction occurring as the sample plug disperses [20]. Initial comparison of experimental data with predicted responses showed that the rate constant was not fixed throughout the sample plug, i.e., the predicted curves were broader than the experimental curves. This was corrected by adjusting the rate coefficient of the reaction to that extrapolated from the experimental data. Additionally, Painton and Mottola observed that

under certain unconventional experimental conditions (sample volumes larger than manifold volumes and in the presence of chemical reaction) a double humped peak occurred which was not present when dispersion was only physically driven [20].

Vanderslice et al. [64] solved the diffusion–convection equation with the assumption that the concentration of the rate-limiting solute was being monitored and that it was undergoing a first-order reaction in the carrier stream. Curves obtained with and without reaction were compared for rate constant determination. Rate constants obtained in this manner [$(1.05 \pm 0.05) \times 10^{-2}$ s^{-1}] were in excellent agreement with those determined by conventional methods (1.05×10^{-2} s^{-1}).

An additional observation was that the baseline-to-baseline times were the same for reaction and no-reaction peaks, which is in contrast to the findings of Painton and Mottola [20], who found that baseline-to-baseline times decreased when reaction occurred. The difference was attributed to the two different types of FI systems used; Vanderslice et al. used a mixing tee to premix reactants whereas Painton and Mottola injected one reactant directly into the other.

Wada et al. [65] also utilized solution of the diffusion–convection equation with chemical reaction:

$$\partial C_i/\partial t = -u_{max}(1 - x_r^2/r^2)(\partial C_i/\partial x_a) + (D_i/x_r)\,\partial(x_r\,\partial C_i/\partial x_r)/\partial x_r \pm kC_AC_B \quad (25)$$

(where C_i is the concentration (mol l^{-1}) of species i when i is A, B or P (i.e., sample A + reagent B → product P), D_i is the diffusion coefficient of species i (cm^2 s^{-1}), x_r is the radial distance from the tube axis and x_a is the axial distance), to simulate response signals. The simulated curves agreed reasonably well with experimental data except that for some conditions (analyte injected directly into reactant at low flow-rates) peak appearance times were delayed for experimental results compared with simulations. When no reaction was involved, the peak appearance times for simulated and experimental curves were similar; however, the peak shapes were not identical. Differences between the predicted and experimentally determined curves were attributed to difficulties in maintaining laminar flow (i.e., secondary flow resulting from manifold non-linearity, connections and flow pulsations produced by the pump).

Axially dispersed plug flow

Van den Berg et al. [66] used the axially dispersed plug flow model to compare coiled (open) manifolds and packed-bed (inert packing) reactors which had the same mean residence time (ca. 35 s). The coiled manifold was 10 cm × 0.025 mm i.d. wound in a 2.5-cm diameter coil while the packed-bed reactor was 7 cm × 4.6 mm i.d. packed with 40-μm mean diameter glass beads. The packed-bed reactor produced narrower peaks (σ_t = 1.8 s) than the coiled manifold (σ_t = 4.1 s) and consequently had a higher sample throughput rate (500 h^{-1} compared with 220 h^{-1} for the coiled manifold). However, the pressure drop was an order of magnitude higher in the packed-bed reactor ($\Delta p = 4$ atm) than the coiled manifold ($\Delta p = 0.4$ atm). Based on maximum sample throughput, the packed-bed reactor was concluded to be an attractive alternative to coiled reactors.

The axially dispersed plug flow model was also used by Montesinos et al. [67] to predict outputs for FI sandwich techniques in which each end of the sample plug is in contact with a different reagent. The model incorporates consideration of the leading and trailing edges of the sample plug as described by Vanderslice et al. [19] and Painton and Mottola [59]:

$$dC_{ij}/dt = D_{Lij}\,d^2C_{ij}/dx_a^2 - udC_{ij}/dx_a - kC_{Aj}C_{Rj} \quad (26)$$

where C is dimensionless concentration, i is A (analyte) or R (reagent), $j = 1$ (leading section of sample plug) or 2 (trailing section of sample), D_L is the effective axial dispersion coefficient (cm^2 s^{-1}), x_a is the axial distance (cm), u is the flow velocity (cm s^{-1}) and k is the rate constant (s^{-1}). Initial and boundary conditions for the leading plug section are $C_A = 0$ and $C_R = 1$ at $x_a > 0$ (for $t = 0$); $C_A = 1$ and $C_R = 0$ at $x_a = 0$ (for $t > 0$); and $C_A = 0$ and $C_R = 1$ at $x_a = \infty$ (for $t > 0$).

Complementary conditions apply for the trailing plug section. Effective axial dispersion coefficients (for both the leading and trailing sections) were estimated by residence time distribution techniques and the rate constant (k) was determined by unidirectional search (the mean square error function was minimized). Agreement between the predicted and experimental curves was not quantified but was fairly good.

Tank(s) models

Reijn et al. [68] used a single-bead string reactor and the tanks in series model to describe dispersion calculated from the statistical moments of the experimentally determined residence time distribution function. When a sufficiently large number of tanks was used, the mean and variance of FI curves were independent of reaction rate although the peak height was dependent on reaction rate. An additional observation was that dispersion in a single-bead string reactor (when expressed as the number of tanks) was independent of flow-rate, molecular diffusion coefficient and conversion level of a reacting tracer. Van Veen et al. [69] extended the single-bead string reactor–tanks in series approach to FI systems with consecutive reactions [i.e., A + reagent(s) → B → C] and concluded that under certain conditions dispersion of the sample plug and kinetics are independent processes. These conditions, $kt_r \ll N$ and $N > 10$, where k is the rate constant, t_r is the mean residence time, N is the number of tanks in the tanks in series model and $N > 10$, are typical for a single-bead string reactor but not a conventional manifold.

An extended tanks in series model where a

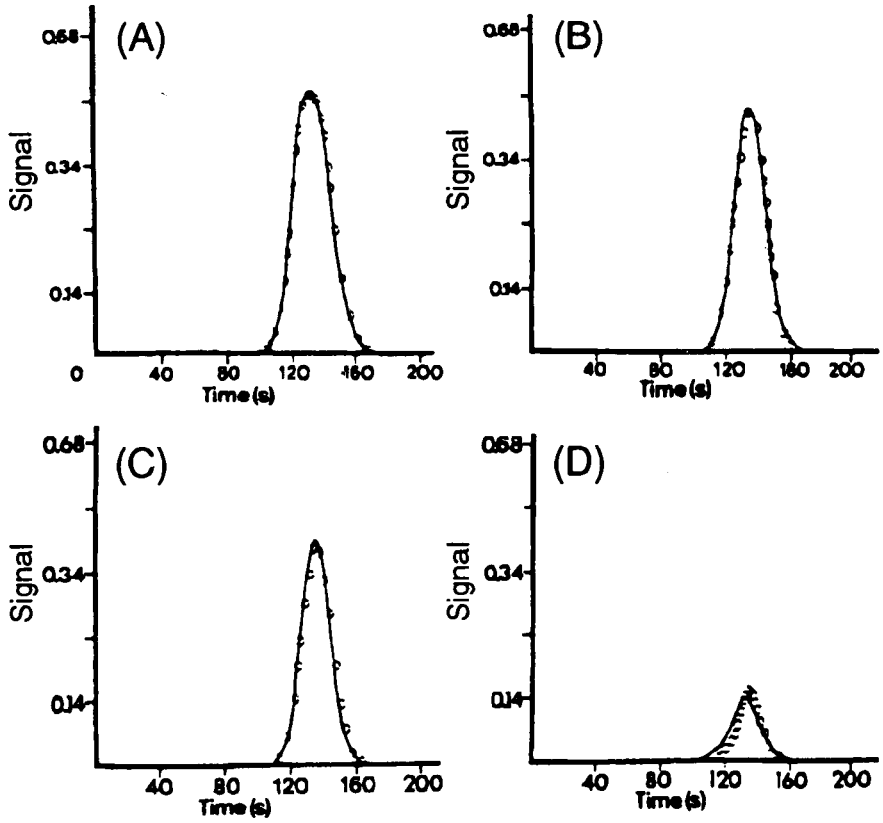

Fig. 3. Experimentally observed (solid lines) and predicted (open circles) response curves for permanganate dispersion (A) and crotonate (reagent) at three concentrations, (B) 1.01×10^{-5} M, (C) 2.02×10^{-5} M and (D) 1.01×10^{-4} M. Reproduced with permission of Elsevier from [70].

residence time model was combined with an empirical mass-transfer term was used by Hungerford and Christian [70] to explain narrow product peaks. A dimensionless product distribution curve with a response function described by $F_p(t)$ was developed:

$$F_p(t) = C_p(t)/C_0 = D_{AP}(a_{AP}, t)^{-1} \times \{1 - \exp[-k_2 t C_r D_R(a_R, t)]\}^{-1} \quad (27)$$

where $C_P(t)$ is the product response function, C_0 is the concentration of analyte injected, $D_{AP}(a_{AP}, t)$ is a function defining analyte dispersion, k_2 is the second-order rate constant (l mol^{-1} s^{-1}), C_r is the initial reagent concentration and $D_R(a_R, t)$ is a function defining reagent dispersion. The exponential term in this equation describes the chemical kinetics of the system and shows that chemical kinetics in this system are a function of dispersion kinetics. Consequently, slow kinetics in a single-line FI system are not pseudo-first order as reagent dispersion prevents a constant reagent concentration from being maintained. Agreement between the observed and predicted curves was very good (Fig. 3), particularly for the three peaks (A–C) for which chemical reactions were slow compared with the mixing process. A narrowing of the analyte distribution curve was observed as the reagent concentration increased since the sample (in the leading and trailing sections) was consumed more quickly.

Appleton and Tyson [71] used both single-tank and parallel-tanks models to investigate dispersion in FI–AAS systems. Typical measurement of dispersion coefficients (as the ratio of initial to measured sample concentrations) by using measured peak height was shown not to apply for FI–AAS systems as the nebulizer contributes its own dispersion to the overall system. Comparison of experimental data with those predicted by single-tank and parallel-tanks models (Fig. 4) demonstrated the parallel-tanks model to be the most accurate.

Tyson [72] defined a reagent dispersion coefficient (D_R) which is analogous to the sample dispersion coefficient of Ruzicka and Hansen [5]

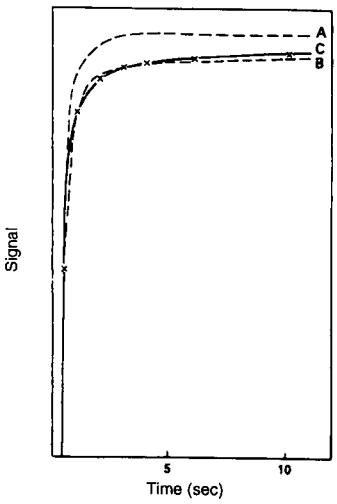

Fig. 4. Comparison of single- and parallel-tanks models of the absorbance–time function for a step concentration change from 0 to 0.5 mg l^{-1} Mg. (A) Best fit for single-tank model, (B) best fit for parallel-tanks model; and (C) experimental curve. Reproduced with permission of the Royal Society of Chemistry from [71].

except that it applies to the reagent instead of the sample. This term was used with the well stirred mixing chamber model to derive equations for relating peak width (Δt_B) to injected concentration for single-line manifolds:

$$\Delta t_B = (V_c/q) \ln[(C^0/C_w) - 1] - (V_c/q) \ln D \quad (28)$$

where V_c is the volume of the mixing chamber, q is the volumetric flow-rate, C^0 is the initial sample concentration, C_w is the concentration at which peak width is measured and D is the dispersion coefficient. It was also applied to merging stream manifolds for the case where reagent concentration is always in excess of sample concentration:

$$\Delta t_B = (V_c/q_c) \ln[(C^0/C_w) - 1/f_s] - (V_c/q_c) \ln(D - 1/f_s) \quad (29)$$

where f_s is the fraction of total flow-rate caused by the merged sample stream, defined as

$$f_s = q_c/(q_r + q_c) \quad (30)$$

where q_c and q_r are the volumetric flow-rates of the carrier and reagent streams, respectively. In

order to expand the working range of FI methods and determine stability constants, this work was extended [73,74] by defining the time interval between doublet peaks (Δt_{eq}) caused by injecting a sufficiently large sample so that the center of the sample plug does not react:

$$\Delta t_{eq} = (V_c/q)\ \ln C_0[\exp(V_i/V_c) - 1]/C_r \qquad (31)$$

where V_i is the injection volume and C_r is the initial reagent concentration. Agreement with experimental data was generally good, with differences being attributed to the fact that time injection was assumed in the mixing chamber model and the experimental data were obtained with plug (volume) injection. During plug injection, the trailing section of the sample plug undergoes greater dispersion since dispersion occurs as the sample travels through the sample loop toward the manifold. Therefore, the sample "observes" a mixing chamber volume slightly larger than the actual chamber volume.

Random walk

Betteridge et al. [75] used a random walk model to investigate the effects of several variables in FI systems. This model was chosen as it deals with individual molecules and therefore is well suited for investigating sample size, chemical kinetics and the combination of reaction rate and physical dispersion. In this approach, a sample plug of 500–3000 molecules (each with three-dimensional space coordinates) was assumed to be injected and then subjected to laminar flow for a predetermined time. A random step, the length of which was based on the diffusion coefficient, was then attributed to each molecule and a new position was calculated. Chemical reaction was included by calculating sample and reagent concentrations in defined zones and combining this with the probability of reaction (reaction rate constant and reaction stoichiometry). This model successfully predicted many observations made with real FI systems. For example, peak height decreased exponentially with time when no chemical reaction occurred in the system; a linear relationship existed between Δt_B and the distance the plug traveled; peak height increased with increasing D_m; and high flow-rates produced rapid mixing and high longitudinal dispersion. Additionally, the model allowed the visualization of the product profile undergone by injecting medium- or large-volume samples. For these samples a double peak was initially produced which became Gaussian (in the absence of flow) or skewed Gaussian (in the presence of flow) and continued to increase in height and width, resulting finally in a single, shouldered peak. The models also predicted that fast reactions should give higher maximum product concentrations and in less time than slow reactions. Hence the peak height and shape result from interaction of both physical and chemical dispersion and are therefore affected by flow-rate and rate of chemical reaction.

The random walk model was extended to the simulation of FI systems with merging zones by Crowe et al. [76]. In these systems, sample and reagent are injected into two separate carrier streams and combine, mix and react at a downstream mixing tee. Simulations were performed to determine the effects of reagent plug size, reagent plug offset, reagent concentration, reagent stream flow-rate, injection delay, reaction stoichiometry, rate constant, reagent diffusion constant, system viscosity and temperature. Comparisons with experimental data showed that the simulations quantitatively predicted the experimental behavior. Ruzicka and Marshall [77] used the random walk model to show that sequential injection of sample and reagent together with reversing the direction of pump flow (to maintain the analyte within the same section of the manifold) reduced sample and reagent consumption. This was verified with experimental data.

Distributed and lumped parameter models

Kolev [78] proposed simple relationships for reducing the solution of distributed mathematical models to their solutions for step- or delta-function inputs. Distributed models considered detailed variations in behavior from point to point throughout the system (e.g., axially dispersed plug flow model) and lumped parameter models assumed that point-to-point variations were small enough to be ignored (e.g., well stirred tank and tanks in series models). For plug injection, the assumption was made that for each subsequent

moment in time both the leading and trailing portions of the sample (represented by a step function) will have traveled the same distance. Therefore, the trailing portion can be described mathematically in terms of the leading portion. Utilizing this, the axially dispersed plug flow model for plug injection was solved at $X = 1$, where $X = x/L$, the dimensionless axial distance:

$$C(\Theta, 1) = 0.5\{\mathrm{erf}[(\Theta - 1)/2(\Theta/P)_{1/2}] + \mathrm{erf}[(1 + \alpha - \Theta)/2(\Theta/P)_{1/2}]\} \quad (32)$$

where C is dimensionless concentration, Θ is dimensionless time and α is the dimensionless length of the initial sample plug. A similar approach was used for time injection in that a term β, equal to the dimensionless duration of the time injection, was defined. Utilizing these assumptions, solution of the well stirred tank model was obtained for $0 \leqslant \Theta \leqslant \beta$:

$$C(\Theta) = 1 - \exp(-\Theta) \quad (33)$$

and for $\Theta \geqslant \beta$:

$$C(\Theta) = \exp(-\Theta)[\exp \beta - 1] \quad (34)$$

Solution of the tanks in series model for plug injection was determined for $0 \leqslant \Theta \leqslant \beta$:

$$C(\Theta) = 1 - \exp(-N\Theta) \sum_{i=0}^{N-1} (N\Theta)^i/i! \quad (35)$$

where N is the number of theoretical tanks in the model. For $\Theta \geqslant \beta$:

$$C(\Theta) = \exp(-N\Theta) \times \sum_{i=0}^{N-1} \left[\exp(N\beta)(\Theta - \beta)^i - \Theta^i\right] N^i/i! \quad (36)$$

These relationships are general in that only the response of the model for a step-function input was used, irrespective of the processes it included (e.g., physical dispersion, chemical reaction or separation). Consequently, these relationships can be applied to other models as long as their step function input solutions are available.

Confluent streams

Zagatto et al. [79] investigated the effects of a confluent (reagent) stream on sample dispersion and found that these effects could be described by

$$[A'] = [A][q_c/(q_c + q_r)] \quad (37)$$

and

$$w' = w[(q_c + q_r)/q_c] \quad (38)$$

where [A] and [A'] are the mean concentrations of A in a thin slice of fluid immediately preceding and following the confluence, respectively, q_c and q_r are the flow-rates of the carrier and reagent streams, respectively, and w and w' are the axial lengths of the fluid element associated with [A] and [A'], respectively. The site of the confluence point is consequently an important factor in the overall dispersion of the sample, as post-confluence dispersion is influenced by w', which is influenced by w. Also, w is influenced by the injection volume so that dilution can be minimized by injecting large volumes, using a low flow-rate confluent stream and having the confluence near the injection port. To maximize dilution, the opposite conditions should be used (small V_i, confluent at high flow-rate and confluence far from the injection point). Clark et al. [80] utilized different confluence point configurations and manifold configurations downstream of the confluence to optimize mixing.

A confluence (mixing tee) with a 30° angle of intersection between each confluent stream and the effluent stream was the optimum while the influence on mixing of the manifold configuration downstream of the confluence was similar to that of single-line FI systems, i.e., linear manifolds caused less mixing than coiled manifolds, which were less efficient mixers than knotted manifolds.

Liquid chromatographic applications

Post-column reaction in liquid chromatography (LC) is a specific application directly analogous to chemical reaction kinetic-based FI. A critical requirement of these reactors is that they add minimum peak broadening (dispersion) to the sample as it passes. Huber et al. [81] compared coiled open-tubular and packed-bed reactors and found

that for reactors of equivalent residence times, packed-bed reactors produced less peak broadening and pressure drop than small-diameter tubular reactors. Shih and Carr [82] investigated the flow-rate dependence and reactor length of post-column reactors for low extent of reaction systems (low reaction rates) and found that the peak height increased as the flow-rate decreased (the peak area quadrupled for every factor of two decrease in flow-rate). They also concluded that there is an optimum reactor length for any set of chemical and chromatographic conditions and that optimum results are obtained at a peak height corresponding to 71.5% of reaction completion. In a review of LC reaction detectors, Frei et al. [83] noted that the increased peak width with the reactor in place was frequently less than double the peak width without the reactor. However, detection limits were often improved by one to two orders of magnitude when reactors were utilized.

Shankar and Lenhoff [84] investigated dispersion in linear connecting tubing in LC systems, utilizing the general diffusion–convection equation (neglecting the axial diffusion term). They found that peak shapes could be adequately predicted and were different than that predicted by Taylor [11,12] and Aris [13,14] (because of the geometries of LC system components). When multiple components were connected in series, the variances were found to be additive provided that sufficient radial mixing occurred.

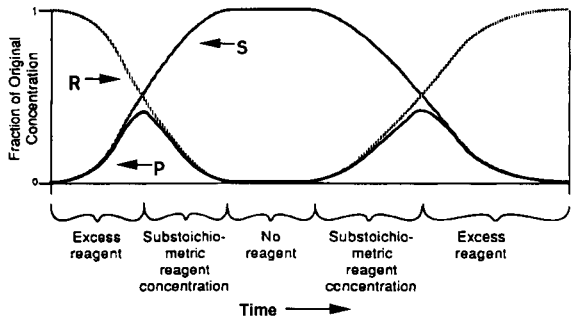

Fig. 5. Concentration effects on sample (S) and reagent (R) as the reaction product (P) is generated. Reproduced with permission of Elsevier from [89].

DESCRIPTIVE METHODS

Detector response deconvolution

Descriptive methods utilize information obtained from the response curve to define or describe the FI system. Poppe [85] applied this approach in a theoretical treatment of flow-through detection systems. An output signal function $V(t)$, which is defined as the signal value at time t, for a time-invariant detector was defined as the convolution (indicated in equations with an asterisk) of the concentration input function $[C(t)]$ with the detector system impulse response function $[h_d(t)]$:

$$V(t) = C(t) * h_d(t) = \int_0^\infty C(t-\tau)h_d(\tau)\,d\tau \tag{39}$$

where τ is a time variable. Peak broadening was defined as a volume standard deviation ($\sigma^2_{V,d}$) and is comprised of broadening occurring in the tubing and connectors ($\sigma^2_{V,t}$), finite effective detector measuring volume ($\sigma^2_{V,c}$) and the dynamic behavior of the transducer and signal amplifying and handling equipment ($\sigma^2_{V,e}$):

$$\sigma^2_{V,d} = \sigma^2_{V,t} + \sigma^2_{V,c} + \sigma^2_{V,e}$$
$$= (\pi r^4 L/24D_m)q + f_c^2 V_d^2 + C_e^2 q^2 \tag{40}$$

where f_c is a factor correlating volume standard deviation and detector cell volume, V_d is the detector cell volume and C_e is the signal produced by the detector electronic components. Additionally, a concentration detection limit (C_d) was defined:

$$C_d = n_2 s_v / S \tag{41}$$

where n_2 is a numerical factor dependent on the statistical confidence level desired, s_v is the volume standard deviation of the noise where noise refers to all signal fluctuations not containing input (concentration) information and S is the static sensitivity (ratio between signal change and concentration change). Characterization of the detection system by $\sigma_{V,d}$ and C_d allowed the estimation of the maximum sample throughput and the absolute detection limit. The volumetric fraction described by Zagatto et al. [86] "ex-

presses the relative contribution of a solution, in terms of volume, to a given fluid element at a certain time" and is similar to the volume standard deviation of Poppe [85].

Fast Fourier transforms

Van Nugteren-Osinga et al. [87] used a fast Fourier transform to deconvolute response curves resulting from FI systems with and without various components, in order to determine impulse/response functions of individual components. Once these functions had been developed for each system component, it was possible to predict responses for various system configurations by using mathematical convolution. This procedure was used to evaluate coiled and knitted manifolds and six different configurations of mixing tee-pieces. Very little difference was found in the dispersion produced by the different mixing tee-pieces and the knitted manifold produced less dispersion than coiled manifolds. The predicted response curve for two coils in series was nearly identical with experimental data.

Large-volume injections

Fogg et al. [88] investigated the shapes of normal (sample injected into reagent stream) and reverse (reagent injected into sample stream) FI signals by utilizing large-volume plug- and time-based injections. These large-volume (2 ml) injections resulted in two independent peaks due to dispersion at the front and rear boundaries of the injected material. Comparison of outputs from normal and reverse FI using time injection showed that the two peaks produced by each technique were identical, but in reverse order. For plug injection, the peaks were in reverse order and not identical, with the differences being attributed to the larger amount of dispersion undergone by the trailing section of the sample. As injection volumes were reduced (for both reverse and normal FI), the two peaks moved closer together until they merged with the smaller peak, becoming a shoulder on the larger peak. Also, for normal FI, a single peak was observed for injections of less than ca. 800 μl, whereas for reverse FI, single peaks did not occur until the injection volume was reduced to ca. 200 μl.

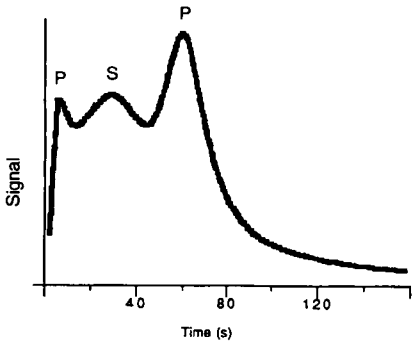

Fig. 6. Concentration profile of double peaks from product (P) and background [sample (S)]. Reproduced with permission of Elsevier from [89].

Self-modeling curve resolution

Erickson et al. [89] exploited the double peaks produced by large-volume injection by applying self-modeling curve resolution to enhance species resolution for multiple wavelength spectral detection. Self-modeling curve resolution incorporates algorithms that utilize only general assumptions about multivariate data to resolve the contribution of each species to the total overlapped curve. By using a sufficiently large injection volume (500 μl) and a short manifold (20 cm), double peaks (one each for the leading and trailing sections of the sample plug) were observed. For the system

$$S + R \rightarrow P \qquad (42)$$

where S, R and P are the sample, reagent and product, respectively, and both the sample and product give a detector response (Fig. 5), the output signal is not resolved (Fig. 6). Each spectrum was normalized by summing the absorbances over all wavelengths and dividing the absorbance at each wavelength by the total absorbance. Normalized spectra were then plotted in a two-dimensional factor loading space where each point represented a dimensional spectral vector (one-dimensional spectral vector for each wavelength). Factor analysis was used to confirm that two principal eigenvectors contained the information associated with the chemical components. Following this, spectra were normalized to unit area and their points again plotted in the loading space of the factors. Bands of possible solution of the spectra were then plotted and

compared with the actual spectra. Appropriate boundary conditions were applied and multivariate least squares was used to obtain concentration profiles (from the estimated spectra) for the product and sample. Areas of the product peaks were calculated and compared with areas produced by standards, good agreement being observed.

Evolving factor analysis is a form of self-modeling curve resolution that takes advantage of unused information in the time domain. An additional eigenvalue is used to explain the variability caused by a new component eluting in an overlapped peak; consequently, the magnitudes of eigenvalues change over time. Gemperline and Hamilton [90] used this technique in an attempt to mathematically resolve a seven-component mixture (Bi^{3+}, $BiCl^{2+}$, $BiCl_2^+$, $BiCl_3$, $BiCl_4^-$, $BiCl_5^{2-}$ and $BiCl_6^{3-}$). A covariance matrix was calculated from the raw data and eigenanalysis was performed on the submatrices of the covariance matrix. Iterative least-squares fitting was applied to the vector resulting from splicing eigenvalues with the resultant test vector being the estimated concentration profile for one component. Estimated profiles of the other components were similarly obtained. The test vectors were arranged into a matrix, adjusted for relative peak height, and the estimated spectral matrix was then calculated using an iterative least-squares fit. Evolving factor analysis was applied to each peak twice, once on the first half of the peak and once on the second half, since it responds to evolving (eluting) components and it was assumed that all of the peak components would be encountered by the mid-point of the sample plug. However, applying evolving factor analysis to the two halves of a peak in this manner placed the restriction on the peak that the mid-point of the sample plug should not contain more than two components.

The number of estimated elution profiles for the bismuth complexes for the two peak halves were six for the first half and seven for the second half. When evolving factor analysis was applied to the entire peak, six profiles were satisfactorily determined and seven were not. The reason for this was attributed to the $BiCl_5^{2-}$ concentration profile totally overlapping the $BiCl_6^{3-}$ profile and also that the two spectra are very similar (i.e., the seventh factor was not modeled with a sufficient signal-to-noise ratio to be resolved by the evolving factor analysis). The six-factor model estimated $BiCl_5^{2-}$ and $BiCl_6^{3-}$ as a single component. Spectral assignments of the remaining species compared favorably with previously predicted spectra [91].

Digital filtering

The Kalman filter is a digital filtering technique for extracting parameters from noisy data and modeling complex systems [92]. Wentzell et al. [93] used response surface modeling based on this technique to evaluate FI data and compared the results with the more traditional singular value decomposition. Evaluation of a FI system with seven different variables (reagent pH, carrier pH, flow-rate, temperature and three reagent concentrations) showed that the Kalman filter and singular value decomposition gave essentially identical results. However, the model obtained was inadequate for predictive or diagnostic uses as it was developed from an insufficient number of data points. When used with a five-variable FI system (manifold length, flow-rate, pH, reagent concentration and injection volume), the model generally predicted the appropriate response for changing variables except for high reagent concentrations. This problem resulted from attempting to fit an exponential with a quadratic model. The primary advantage of the Kalman filter was due to it being recursive. As new measurements were made, they were incorporated into the model and a new model equation was obtained, allowing ongoing modification of planned experiments. There were also some computer programming time advantages.

Response surface mapping

Wade et al. [94] used response surface mapping in devising a computer-controlled FI methods development system. This approach incorporates interactions of several parameters or variables on the system output instead of dealing with the variables in a conventional univariate manner. Mapping studies were first conducted to

develop a set of response surfaces (one variable vs. a second variable vs. detector response) for each experimental response or combination of responses. Next a comparison of simplex optimization and grid search methods was made. Although simplex optimization produced similar maximum peak heights and required significantly fewer observations (16–40 points) than the grid search method (64 points), the surface contour maps generated from simplex data did not portray the true general shape of the surface even though good coverage was observed near the maximum. The grid search method provided good overall coverage that represented the true surface shape but had the potential for missing narrow, sharp peaks.

However, as the number of variables in a system increased, it became necessary to use simplex optimization. A five-variable system typically required 35–40 experiments for simplex optimization whereas a conventional grid search approach required 8^5 (32 768) experiments. Response surfaces were also obtained for different variables as a function of the relative standard deviation of the measurements. These surfaces indicated optimum operating conditions based on precision. The overall system optimum conditions occurred where the minimum of the relative standard deviation map overlapped the maximum of the absorbance map. Both response surfaces were used to establish optimum working ranges and to visualize non-optimum conditions, chemical and flow contributions, experimental repeatability, wavelength shifts, time to peak maximum shifts and variation in peak shape as a function of flow and chemical contributions.

Error analysis

Chen and Zeng [95] applied error analysis to FI signals (in terms of both peak height and peak area) to determine the contribution of random detector noise and the precision of repetitive determinations. Their studies demonstrated that peak-area measurements were better than peak-height measurements (in terms of noise reduction), as random noise was reduced in peak-area measurements. However, the signal intensity of peak-area measurements was less than the corresponding intensity of peak-height measurements, resulting in a better precision for peak-height measurements. Least-squares filtering was used to increase the signal-to-noise ratio, which further improved the precision of peak-height measurements. Pattern recognition of first-derivative signals was used to eliminate response spikes caused by bubbles passing through the detector.

Moment calculation

Harris [96] compared three methods of peak shape analysis in evaluating methods for obtaining diffusion coefficients from dispersion peaks. The height-area method, moment calculation by direct integration and moment calculation from a non-linear least-squares fit to a truncated Edgeworth–Cramer series were used. The height–area method assumed a Gaussian distribution, the variance (σ^2) of which can be expressed as

$$\sigma^2 = A^2/2\pi h^2 \tag{43}$$

where A is the peak area and h is the peak height. The peak area (expressed as the zeroth moment of the signal, M_0) can be determined by numerical integration:

$$M_0 = \int_{-\infty}^{+\infty} V(t)\ \mathrm{d}t \tag{44}$$

where $V(t)$ is the signal value at time t. First, second and higher moments (M_1, M_2 and M_n, respectively) were calculated by direct integration:

$$M_1 = \bar{t} = 1/M_0 \int_{-\infty}^{+\infty} tV(t)\ \mathrm{d}t \tag{45}$$

$$M_2 = \sigma^2 = 1/M_0 \int_{-\infty}^{+\infty} (t-\bar{t})^2 V(t)\ \mathrm{d}t \tag{46}$$

$$M_n = 1/M_0 \int_{-\infty}^{+\infty} (t-\bar{t})^n V(t)\ \mathrm{d}t \tag{47}$$

where t is time and $\bar{t}$ is the mean flow time. Higher moments (M_3 and M_4) were used to calculate skewness (of tailing peaks) and excess (of stretched peaks), which were used as measures of experimental quality and reproducibility. The $(t-\bar{t})^n$ weighting in these calculations accentuates the points furthest from the peak center and therefore makes the choice of practical

integration limits critical. Moment calculation utilizing the Edgeworth–Cramer series provided additional information from the higher moments and included information resulting from distortion of the Gaussian peak. Diffusion coefficients obtained utilizing the height–area method were found to vary significantly from those calculated from least-squares series fit as the actual peak varies from a true Gaussian. Diffusion coefficients obtained utilizing the moments calculation by direct integration method were very dependent on the peak width chosen, whereas coefficients obtained from moment calculation utilizing the Edgeworth–Cramer series appeared to address adequately the actual peak deviation from true Gaussian and yielded results comparable to other literature data.

While evaluating the merits of FI as a precursor to laser-induced fluorescence detection, Harris [97] described typical FI response peaks as having both Gaussian and exponential components, where Gaussian predominates in the rising section (front) of the curve and exponential predominates in the falling (tail) section. Foley and Dorsey [98,99] and Jeansonne and Foley [100] reviewed the use of the exponentially modified Gaussian function and its associated statistical moments, and applied it to the calculation of chromatographic figures of merit. Reijn et al. [68] used statistical moments to calculate a measure of dispersion as the number of tanks in the tanks in series model and applied this to a single-bead string reactor. Hernandez Torres et al. [101] and Brooks et al. [102] extended the use of the exponentially modified Gaussian function (more precisely, the second moment calculated from the function) to a method of describing dispersion in FI systems. Peak height, width and asymmetry were used to confirm that peak shapes were Gaussian or exponentially modified Gaussian [103], then the second moment (peak variance) was calculated:

$$M_2 = (w_{0.1})^2/\left[1.764(b/a)^2 - 11.15(b/a) + 28\right] \quad (48)$$

where $w_{0.1}$ is the peak width at 10% of the maximum peak height and b/a is the asymmetry factor measured at the same peak height as the width. For the asymmetry factor, a is the distance between the peak front (at $w_{0.1}$) and the point (also at $w_{0.1}$) on a vertical line drawn through the peak maximum, and b is the corresponding distance (again at $w_{0.1}$) between the vertical line and the peak tail. This equation was used for $1.00 \leqslant b/a \leqslant 2.76$. For the asymmetry range $2.77 \leqslant b/a \leqslant 5.6$, second moments were calculated according to a modification [104] of the original equations:

$$M_2 = (w_{0.1})^2/\{7.35 + 22.6 \exp[-0.708(b/a)]\} \quad (49)$$

The variance of an exponentially modified Gaussian peak is the sum of variances resulting from Gaussian processes (σ_G^2) and a time constant (τ_t^2) of the exponential peak tailing function, where

$$\sigma_G = w_{0.1}/[3.27(b/a) + 1.2] \quad (50)$$

for $1.09 \leqslant b/a \leqslant 2.76$ and

$$\sigma_G = w_{0.1}/[3.38(b/a) + 0.969] \quad (51)$$

for $2.77 \leqslant (b/a) \leqslant 5.6$. τ_t can be calculated from

$$M_2 = \sigma_G^2 + \tau_t^2 \quad (52)$$

Second moments, peak areas and dispersion coefficients were determined for various flow-rates in an FI system and second moments were the only descriptor found to vary linearly with flow-rate (Fig. 7). Second moments also varied linearly with flow-rate for both straight and coiled manifolds (Fig. 8). The utility of the second mo-

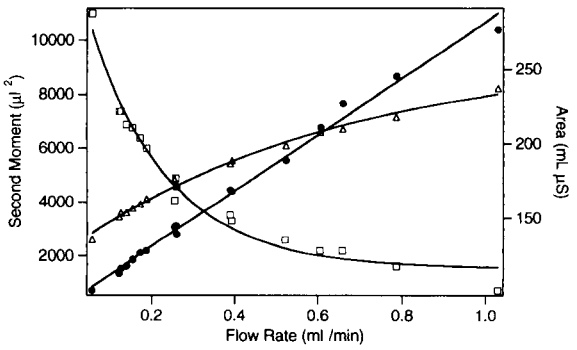

Fig. 7. Effect of flow-rate on second moment (●, left axis), area (□, right axis) and dispersion coefficient (△, left axis/10^3 μl^2), in a flow-injection system. Data taken from Table I in [102] with permission of the American Chemical Society.

ment as a descriptor of FI response curves was further evaluated with additional manifold configurations (coiled, knitted, Serpentine II and single-bead string reactor) under physical (sample and reagent did not react) dispersion [105]. Second-moment values with the Serpentine II manifold did not change as the concentration was varied over a 50-fold range and were found to be constant with injection volume for a coiled manifold over the range 5–20 μl and increased at larger injection volumes. Similar to the findings of Atwood and Golay [26] for a linear manifold, the peak variances of a coiled manifold, cut and rejoined with unions at four locations, was less than the peak variance of the uncut manifold. The mean variance for the rejoined manifold was 76% of the mean variance for the continuous manifold.

Correlation of second moments with coiled, knitted and Serpentine II manifolds is shown in Fig. 9. The variance generally was maximum for the coiled manifold and minimal for the Serpentine II manifold. The observation that the variance decreased with increasing flow-rate above some maximum (ca. 1 ml min^{-1}) for the Serpentine II manifold was in agreement with the greater peak heights observed with this manifold than the coiled manifold. A reduction in variance at increased flow-rates was also observed with the coiled manifold, but the maximum occurred at a higher flow-rate than for the Serpentine II manifold. Increasing the manifold inner diameter or adding a confluence while maintaining other parameters constant (including manifold volume) resulted in an increase in variance. Additionally, it was shown that for single-bead string reactors and Serpentine II manifolds, a decrease in reagent use (per sample) could be obtained by increasing the flow-rate and optimizing the injection spacing. This is due to the decrease in variance at higher flow-rates for these manifolds.

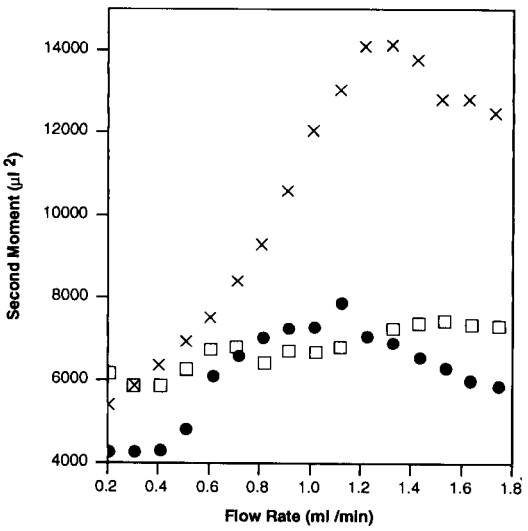

Fig. 9. Correlation of second moment (variance) with flow-rate for (●) coiled, (□) knitted and (×) Serpentine II manifolds. Reproduced with permission of Elsevier from [105].

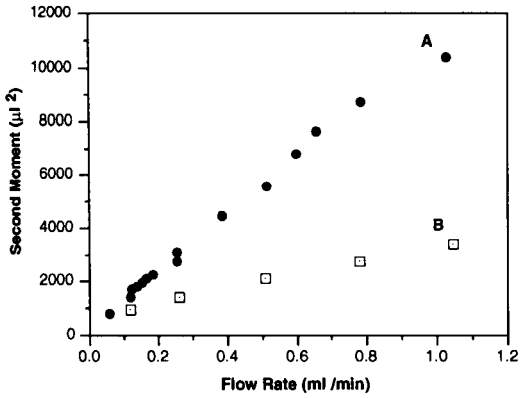

Fig. 8. Second moment versus flow-rate for a 20-μl sample of 0.10 M sodium iodide solution injected into an aqueous carrier stream through a 100-cm manifold. The symbols indicate whether the manifold is (A) straight or (B) coiled. Reproduced with permission of the American Chemical Society from [102].

Berthod [106] developed a generating function [$U(t)$] to produce the exponentially modified form of functions representing parameter change with time and applied it to square, triangle and Gaussian functions. This recursive generating function was defined as

$$U(t) = U(t - \Delta t) + [E(t) - U(t - \Delta t)]/A \quad (53)$$

where $U(0) = E(0)$, $E(t)$ is a time-dependent function representing the unconvoluted, observed signal (e.g., concentration, absorbance or electrical potential) which is measured over a finite time period T in which N data points are ob-

tained, Δt is the time interval between two measurements ($\Delta t = T/N$) and A is a dimensionless factor $\geqslant 1.0$. $U(0)$, the first convoluted point, is for the time interval $0 \leqslant t \leqslant \Delta t$; $U(\Delta t)$, the second convoluted point, corresponds to $\Delta t \leqslant t \leqslant 2\Delta t$, with additional points corresponding to appropriate time intervals. The dimensionless factor A can be calculated:

$$A = 1/[1 - \exp(-\Delta t/\tau_t)] \quad (54)$$

where τ_t is the time constant of the exponential modifier and is defined by

$$\tau_t = 1/(1 - \exp\{-\Delta t/\ln[A/(A-1)]\}) \quad (55)$$

For the square function $[S(t)]$ defined by $S(t) = 0$ at $t < 3$, the corresponding exponentially modified square function, $EMS_1(t)$, is also equal to zero. For $S(t) = 10$ at $3 \leqslant t < 10$, the corresponding $EMS_2(t)$ is

$$EMS_2(t) = 10\{1 - \exp[-(t-3)/\tau_t]\} \quad (56)$$

and for $S(t) = 0$ at $t \geqslant 10$, then

$$EMS_3(t) = EMS_2(10)\ \exp[-(t-10)/\tau_t] \quad (57)$$

The exponentially modified square function corresponds to the well stirred mixing chamber model described by Tyson [72] when τ_t is equivalent to V_f/q (volume/flow-rate) and when $\tau_t = 4$ it corresponds to the tanks in series model [5]. Dueto these correlations, further study of the exponentially modified square function is warranted.

The exponentially modified triangle function, $EMT_1(t)$, is defined for $T(t) = t$ at $0 \leqslant t \leqslant 10$ by

$$EMT_1(t) = t - \tau_t + \tau_t\ \exp(-t/\tau_t) \quad (58)$$

The triangle function $[T(t)]$ is equivalent to $-t + 20$ for the time interval $10 \leqslant t \leqslant 20$ and $EMT_2(t)$ is given by

$$EMT_2(t) = -t + 20 + \tau_t\{1 + \exp(-t/\tau_t) - 2\ \exp[-(t-10)/\tau_t]\} \quad (59)$$

For $t < 0$ and $t > 20$, $T(t) = 0$ and $EMT_3(t)$ is given by

$$EMT_3(t) = [1 + \exp(-20/\tau_t) - 2\ \exp(-10/\tau_t)]\tau_t \times \exp[-(t-20)/\tau_t] \quad (60)$$

Equation 53 was used to produce exponentially modified Gaussian profiles from a Gaussian function with $\sigma = 3$ time units, $t_{max} = 10$ time units and $A = 10$. The variance (M_2) has already been described (Eqn. 52), and the mean flow time ($\bar{t}$) was defined as M_1:

$$M_1 = t_{max} + \tau_t \quad (61)$$

Peak skew (s) and peak excess (e) were defined by M_2, M_3 and M_4:

$$s = M_3/M_2^{3/2} \quad (62)$$

$$e = M_4/M_3^2 - 3 \quad (63)$$

where

$$M_3 = 2\tau_t^3 \quad (64)$$

and

$$M_4 = 3\sigma^4 + 6\sigma^2\tau_t^2 + 9\tau_t^4 \quad (65)$$

Fractals

Coincident with early publications describing FI techniques [107], fractal surfaces and concepts were introduced [108]. Mottola [109] related the fractal dimension (which categorizes boundaries) to kinetics in fractal-like situations and discussed the potential of these concepts (incorporating random walk processes) in FI analysis.

CONCLUSION

Predictive (hydraulic) models often contain approximations which restrict the usefulness of the analytical solutions; however, these models can often be used successfully to predict the effects of changes in system parameters. Reaction kinetics add another variable to these predictive models. Likewise, increasing the sophistication of FI systems (adding confluences, multiple reagents or reactions, etc.) makes it increasingly difficult to develop accurate predictive models. Completely empirical approaches would account for imperfect unions, etc., but would be time consuming to develop and would apply only to the system for which they were determined (i.e., they would have no predictive power). Gradient techniques [110,111] and high-speed pseudo-titrations [112]

performed by FI exploit the fact that FI signals contain considerably more useful information than just the peak maximum. Descriptive methods characterize the information in the complete peak and as such should be useful with these techniques.

Although each approach to describing dispersion in FI systems (predictive non-reactive, predictive chemically reactive kinetic and descriptive) has merit and is useful in specific applications, descriptive approaches describing fundamental FI parameters allow the comparison of different systems and are likely to find increased usage.

The different models have been shown to be accurate for certain specific FI systems; however, very little correlation among the various models has been documented. Work is in progress to develop this correlation and provide practical interpretations of these models and theories. This includes evaluation of the various models (theories) using similar FI system variables for both non-reactive and chemically reactive kinetic systems. The limits of each of these models will be investigated and descriptive methods will be evaluated and applied to the response curves obtained from the various models.

SYMBOLS AND ABBREVIATIONS

A	Peak area
[A]	Concentration of analyte in a finite volume of fluid immediately preceding a confluence
[A′]	Concentration of analyte in a finite volume of fluid immediately following a confluence
$[A]_g^{max}$	Maximum analyte concentration in gradient chamber
b/a	Asymmetry factor of a peak, where a is equal to the distance, at a stated fraction of the peak height (typically 10%), between the peak front and a vertical line drawn through the peak maximum, and b is the corresponding distance to the peak tail
C	Concentration
C_{ag}	Concentration of analyte in gradient chamber
C_d	Concentration detection limit
C_e	Signal produced by detector electronic components
C_0	Initial sample concentration (concentration of sample when injection is made)
C_m	Measured concentration of injected sample
C_p	Analyte concentration at peak maximum
C_r	Reagent concentration
$C(t)$	Signal at time t
C_w	Concentration at which peak width is measured
C_{rg}^0	Initial reactant concentration in gradient chamber
$\boldsymbol{C}$	Dimensionless concentration ($\boldsymbol{C} = C/C_0$)
$\boldsymbol{C}'$	Laplace transform of $\boldsymbol{C}$
d	Manifold diameter
D	Dispersion coefficient (injected concentration/detected concentration [5])
D_r	Radial diffusion coefficient
D_L	Axial diffusion coefficient
D_m	Molecular diffusion coefficient
e	Excess (of a Gaussian distribution)
EMS	Exponentially modified square function
EMT	Exponentially modified triangle function
$E(t)$	Time-dependent function representing the unconvoluted observed signal
f	Experimentally determined accomodation factor [19]
f'	Accomodation factor [21]
f_c	Factor correlating volume standard deviation and detector cell volume (typically $0.3 \leqslant f_c \leqslant 1.0$
$f_p(t)$	Product distribution curve (response function)
f_s	Fraction of total flow-rate caused by merged sample stream
h	Peak height
$h_d(t)$	Impulse response function of the detection system
H	Theoretical plate height
H_0	Theoretical plate height for linear manifolds
k	Reaction rate constant
K	Velocity profile factor
L	Manifold length

n_2	Numerical factor dependent on statistical confidence level desired (typically 2–4)
M_0	Zeroth statistical moment (area)
M_1	First statistical moment (mean)
M_2	Second statistical moment (variance)
M_n	Higher statistical moments ($n \geqslant 3$)
N	Number of tanks in TIS model
p	Pressure
P	Peclet number $[(\bar{u}L)/D_m]$
P	Product
$\boldsymbol{P}'$	Laplace complex variable
q	Volumetric flow-rate
q_c	Volumetric flow-rate of carrier stream
q_r	Volumetric flow-rate of reagent stream
r	Manifold radius
R	Reagent
Re	Reynolds number
Re_c	Critical Reynolds number (i.e., Re required for onset of turbulence)
s	Skewness (of a Gaussian peak)
s_v	Volume standard deviation of noise where noise refers to all output (concentrations) fluctuations not containing input information
S	Static sensitivity (ratio between signal change and concentration change)
S	Sample
Sc	Schmidt number
$S(t)$	Square-wave function
t	Time
$\bar{t}$	Mean flow time
t_A	Travel time
Δt_B	Baseline-to-baseline time (peak width)
Δt_{eq}	Time interval between doublet peaks
t_m	V_i/u
t_{max}	Appearance time of peak maximum
t_r	Mean residence time
t_1	Time required to fill gradient chamber
t_2	Time at which all sample has entered gradient chamber
u	Linear flow velocity
$\bar{u}$	Average linear flow velocity
u_{max}	Maximum linear flow velocity
$U(t)$	Generating function for producing the exponentially modified form of another function
V_c	Volume of mixing chamber
V_d	Detector cell volume
V_i	Injection volume
V_t	Volume of (hypothetical) tank
$V(t)$	Signal value at time t
V_g	Gradient chamber volume
ΔV_B	Dispersion volume
w	Axial length of the fluid element associated with the analyte concentration prior to a confluence
w'	Axial length of the fluid element associated with the analyte concentration following a confluence
$w_{0.1}$	Peak width at 10% of maximum peak height
x_a	Axial distance
x_r	Radial distance from tube axis
x'	x_a/L
$\boldsymbol{X}$	Dimensionless axial distance
z	Reaction ratio (i.e., $A + zB \rightarrow P$)
$\boldsymbol{\alpha}$	Dimensionless length of initial sample plug
$\boldsymbol{\beta}$	Dimensionless duration of the time injection
$\boldsymbol{\Theta}$	Dimensionless time
τ	Reduced time $[(D_m t)/r^2]$
τ_t	Time constant of the exponential modifier

J.G.D. is grateful for support of this work by NIEHS ES-04908.

REFERENCES

1 G. Horvai and E. Pungor, CRC Crit. Rev. Anal. Chem., 17 (1987) 231.
2 C.C. Painton and H.A. Mottola, Anal. Chim. Acta, 154 (1983) 1.
3 J. Ruzicka and E.H. Hansen, Anal. Chim. Acta, 179 (1986) 1.
4 K.K. Stewart, Anal. Chem., 55 (1983) 931A.
5 J. Ruzicka and E.H. Hansen, Flow Injection Analysis, Wiley, New York, 2nd edn., 1988.
6 M. Valcarcel and M.D. Luque de Castro, Flow-Injection Analysis: Principles and Applications, Horwood, Chichester, 1987.
7 B. Karlberg and G.E. Pacey, Flow Injection Analysis: a Practical Guide, Elsevier, New York, 1989.
8 J.L. Burguero, Flow Injection Atomic Spectroscopy, Dekker, New York, 1989.

9 O. Levenspiel, Chemical Reaction Engineering, Wiley, New York, 1962.
10 T.B. Drew, J.W. Hoopes and T. Vermeulen, Advances in Chemical Engineering, Academic, New York, 1963.
11 G. Taylor, Proc. R. Soc. London, Ser. A, 219 (1953) 186.
12 G. Taylor, Proc. R. Soc. London, Ser. A, 225 (1954) 473.
13 R. Aris, Proc. R. Soc. London, Ser. A, 235 (1956) 67.
14 R. Aris, Curr. Contents: Phys. Chem. Earth Sci., 31(2) (1991) 8.
15 V. Ananthakrishnan, W.N. Gill and A.J. Barduhn, AIChE J., 11 (1965) 1063.
16 W.N. Gill and V. Ananthakrishnan, AIChE J., 13 (1967) 801.
17 H. Bate, S. Rowlands, J.A. Sirs and H.W. Thomas, Br. J. Appl. Phys., 2 (1969) 1447.
18 H. Bate, S. Rowlands and J.A. Sirs, J. Appl. Physiol., 34 (1973) 866.
19 J.T. Vanderslice, K.K. Stewart, A.G. Rosenfeld and D.J. Higgs, Talanta, 28 (1981) 11.
20 C.C. Painton and H.A. Mottola, Anal. Chim. Acta, 158 (1984) 67.
21 J.T. Vanderslice, G.R. Beecher and A.G. Rosenfeld, Anal. Chem., 56 (1984) 292.
22 M.A. Gomez-Nieto, M.D. Luque De Castro, A. Martin and M. Valcarcel, Talanta, 32 (1985) 319.
23 M. Valcarcel and M.D. Luque De Castro, Talanta, 32 (1985) 339.
24 P.L. Kempster, H.R. van Vliet and J.F. van Staden, Talanta, 36 (1989) 969.
25 M.J.E. Golay and J.G. Atwood, J. Chromatogr., 186 (1979) 353.
26 J.G. Atwood and M.J.E. Golay, J. Chromatogr., 218 (1981) 97.
27 K. Hofmann and I. Halasz, J. Chromatogr., 173 (1979) 211.
28 R. Tijssen, Anal. Chim. Acta, 114 (1980) 71.
29 R. Tijssen, Sep. Sci. Technol., 13 (1978) 681.
30 R. Tijssen and R.T. Wittebrood, Chromatographia, 5 (1972) 286.
31 D.F. Leclerc, P.A. Bloxham and E.C. Toren, Anal. Chim. Acta, 184 (1986) 173.
32 D.F. Leclerc, C.J. Smith and E.C. Toren, Anal. Chim. Acta, 194 (1987) 109.
33 H. Engelhardt and U.D. Neue, Chromatographia, 15 (1982) 403.
34 E.D. Katz and R.P.W. Scott, J. Chromatogr., 268 (1983) 169.
35 H. Engelhardt and B. Lillig, J. High Resolut. Chromatogr. Chromatogr. Commun., 8 (1985) 531.
36 M.A. Curtis and G.J. Shahwan, LC·GC, 6 (1988) 158.
37 S.D. Kolev and E. Pungor, Anal. Chim. Acta, 185 (1986) 315.
38 S.D. Kolev and E. Pungor, Talanta, 34 (1987) 1009.
39 S.D. Kolev and E. Pungor, Anal. Chem., 60 (1988) 1700.
40 S.D. Kolev and E. Pungor, Anal. Chim. Acta, 194 (1987) 61.
41 S.D. Kolev and E. Pungor, Anal. Chim. Acta, 208 (1988) 117.
42 S.D. Kolev and E. Pungor, Anal. Chim. Acta, 208 (1988) 133.
43 S.D. Kolev and W.E. Van der Linden, Anal. Chim. Acta, 247 (1991) 51.
44 E. Pungor, Z. Feher, G. Nagy, K. Toth, G. Horvai and M. Gratzl, Anal. Chim. Acta, 109 (1979) 1.
45 J.F. Tyson and A.B. Idris, Analyst, 106 (1981) 1125.
46 D.C. Stone and J.F. Tyson, Analyst, 112 (1987) 515.
47 D.C. Stone and J.F. Tyson, Analyst, 114 (1989) 1453.
48 J.M. Reijn, W.E. Van der Linden and H. Poppe, Anal. Chim. Acta, 114 (1980) 105.
49 J.M. Reijn, W.E. Van der Linden and H. Poppe, Anal. Chim. Acta, 123 (1981) 229.
50 J.M. Reijn, W.E. Van der Linden and H. Poppe, Anal. Chim. Acta, 126 (1981) 1.
51 J.M. Reijn, H. Poppe and W.E. Van der Linden, Anal. Chim. Acta, 145 (1983) 59.
52 J.T. Vanderslice, A.G. Rosenfeld and G.R. Beecher, Anal. Chim. Acta, 179 (1986) 119.
53 T. Korenaga, F. Shen, H. Yoshida, T. Takahashi and K. Stewart, Anal. Chim. Acta, 214 (1988) 97.
54 T. Korenaga, H. Yoshida, F. Shen and T. Takahashi, Trends Anal. Chem., 8 (1989) 323.
55 F.E. Powell and A.G. Fogg, Analyst, 114 (1989) 799.
56 J. Ruzicka and E.H. Hansen, Anal. Chim. Acta, 99 (1978) 37.
57 H.L. Pardue and B. Fields, Anal. Chim. Acta, 124 (1981) 39.
58 H.L. Pardue and B. Fields, Anal. Chim. Acta, 124 (1981) 65.
59 C.C. Painton and H.A. Mottola, Anal. Chem., 53 (1981) 1715.
60 C.C. Painton and H.A. Mottola, Anal. Chim. Acta, 154 (1983) 1.
61 H.L. Pardue and P. Jager, Anal. Chim. Acta, 179 (1986) 169.
62 P. Jaeger and H.L. Pardue, Anal. Chim. Acta, 187 (1986) 343.
63 H.L. Pardue and J.M. Jordan, Anal. Chim. Acta, 220 (1989) 23.
64 J.T. Vanderslice, G.R. Beecher and A.G. Rosenfield, Anal. Chem., 56 (1984) 268.
65 H. Wada, S. Hiroaka, A. Yuchi and G. Nakagawa, Anal. Chim. Acta, 179 (1986) 181.
66 J.H. van den Berg, R.S. Deelder and H.G.M. Egberink, Anal. Chim. Acta, 114 (1980) 91.
67 J.L. Montesinos, J. Bartroli, M. Poch, M. Del Valle, J.L.F.C. Lima and A.N. Araujo, Anal. Chim. Acta, 234 (1990) 67.
68 J.M. Reijn, H. Poppe and W.E. Van der Linden, Anal. Chem., 56 (1984) 943.
69 J.J.F. van Veen, M.A.J. van Opstal, J.M. Reijn, W.P. van Bennekom and A. Bult, Anal. Chim. Acta, 204 (1988) 29.
70 J.M. Hungerford and G.D. Christian, Anal. Chim. Acta, 200 (1987) 1.
71 J.M.H. Appleton and J.F. Tyson, J. Anal. At. Spectrom., 1 (1986) 63.
72 J.F. Tyson, Anal. Chim. Acta, 179 (1986) 131.

73 J.F. Tyson, Analyst, 112 (1987) 523.
74 J.F. Tyson, Analyst, 112 (1987) 527.
75 D. Betteridge, C.Z. Marczewski and A.P. Wade, Anal. Chim. Acta, 165 (1984) 227.
76 C.D. Crowe, H.W. Levin, D. Betteridge and A.P. Wade, Anal. Chim. Acta, 194 (1987) 49.
77 J. Ruzicka and G.D. Marshall, Anal. Chim. Acta, 237 (1990) 329.
78 S.D. Kolev, Anal. Chim. Acta, 229 (1990) 183.
79 E.A.G. Zagatto, B.F. Reis, M. Martinelli, F.J. Krug, H. Bergamin F°. and M.F. Gine, Anal. Chim. Acta, 198 (1987) 153.
80 G.D. Clark, J.M. Hungerford and G.D. Christian, Anal. Chem., 61 (1989) 973.
81 J.F.K. Huber, K.M. Jonker and H. Poppe, Anal. Chem., 52 (1980) 2.
82 Y.T. Shih and P.W. Carr, Anal. Chim. Acta, 167 (1985) 137.
83 R.W. Frei, H. Jansen and U.A.Th. Brinkman, Anal. Chem., 57 (1985) 1529A.
84 A. Shankar and A.M. Lenhoff, J. Chromatogr., 556 (1991) 235.
85 H. Poppe, Anal. Chim. Acta, 114 (1980) 59.
86 E.A.G. Zagatto, G.F. Reis and H. Bergamin F°., Anal. Chim. Acta, 226 (1989) 129.
87 I.C. van Nugteren-Osinga, M. Bos and W.E. Van der Linden, Anal. Chim. Acta, 214 (1988) 77.
88 A.G. Fogg, X. Wang and J.F. Tyson, Analyst, 114 (1989) 1119.
89 B.C. Erickson, J. Ruzicka and B. Kowalski, Anal. Chim. Acta, 218 (1989) 303.
90 P.J. Gemperline and J.C. Hamilton, J. Chemometr., 3 (1989).
91 J.J. Kankare, Anal. Chem., 42 (1970) 1322.
92 S.D. Brown, Anal. Chim. Acta, 181 (1986) 1.
93 P.D. Wentzell, A.P. Wade and S.R. Crouch, Anal. Chem., 60 (1988) 905.
94 A.P. Wade, P.M. Shiundu and P.D. Wentzell, Anal. Chim. Acta, 237 (1990) 361.
95 D. Chen and Y. Zeng, Anal. Chim. Acta, 235 (1990) 337.
96 K.R. Harris, J. Solut. Chem., 20 (1991) 595.
97 J.M. Harris, Anal. Chem., 54 (1982) 2337.
98 J.P. Foley and J.G. Dorsey, J. Chromatogr. Sci., 22 (1984) 40.
99 J.P. Foley and J.G. Dorsey, Anal. Chem., 55 (1983) 730.
100 M.S. Jeannsonne and J.P. Foley, J. Chromatogr. Sci., 29 (1991) 258.
101 M.A. Hernandez Torres, M.G. Khaledi and J.G. Dorsey, Anal. Chim. Acta, 201 (1987) 67.
102 S.H. Brooks, D.V. Leff, M.A. Hernandez Torres and J.G. Dorsey, Anal. Chem., 60 (1988) 2737.
103 J.P. Foley, Anal. Chem., 59 (1987) 1984.
104 D.J. Anderson and R.R. Walters, J. Chromatogr. Sci., 22 (1984) 353.
105 S.H. Brooks and J.G. Dorsey, Anal. Chim. Acta, 229 (1990) 35.
106 A. Berthod, Anal. Chem., 63 (1991) 1879.
107 J. Ruzicka and E.H. Hansen, Anal. Chim. Acta, 78 (1975) 145.
108 B. Mandelbrot, The Fractal Geometry of Nature, Freeman, New York, 1977.
109 H.A. Mottola, Trends Anal. Chem., 9 (1990) 297.
110 M. Gisin, C. Thompson and K.F. Mansfield, Anal. Chim. Acta, 179 (1986) 149.
111 E.H. Hansen, Fresenius' Z. Anal. Chem., 329 (1988) 656.
112 A.U. Ramsing, J. Ruzicka and E.H. Hansen, Anal. Chim. Acta, 129 (1981) 1.

Analytica Chimica Acta, 267 (1992) 25–30
Elsevier Science Publishers B.V., Amsterdam

Trifluoroanilide derivatization method for the gas chromatographic determination of propionic acid herbicides in water

Hideaki Ozawa and Tadashi Tsukioka

Nagano Research Institute for Health and Pollution, 1978 Komemura, Amori, Nagano-shi, Nagano 380 (Japan)

(Received 4th October 1991; revised manuscript received 21st April 1992)

Abstract

Propionic acid herbicides, tetrapion and dalapon, in aqueous solution could be extracted into an organic phase as their trifluoroanilide derivatives formed by reaction with dicyclohexylcarbodiimide and trifluoroaniline at room temperature. This direct derivatization reaction was applied to the microdetermination of these herbicides in water. The derivatives extracted were determined by gas chromatography with electron-capture detection (GC–ECD) or by gas chromatography–mass spectrometry (GC–MS) with selected ion monitoring. The detection limits of tetrapion and dalapon with a 50-ml water sample were 0.5 and 2 $\mu g\ l^{-1}$, respectively, by GC–ECD and for both 0.1 $\mu g\ l^{-1}$ by GC–MS. Their recoveries from spiked natural water were more than 70% at concentrations of 2–20 $\mu g\ l^{-1}$. The proposed method was applied to the analysis of river water.

Keywords: Gas chromatography; Gas chromatography–mass spectrometry; Sample preparation; Dalapon; Herbicides; Tetrapion; Waters

Tetrapion (sodium 2,2,3,3-tetrafluoropropionate; TFP-Na) and dalapon (2,2-dichloropropionic acid; DCPA) are herbicides used for the control of gramineous plants. They are mainly used in forestry, orchards and/or non-farming fields, the former exerting its effect for 2–3 months and the latter for 20–40 days [1]. They are halogenated derivatives of propionic acid or the salt, which have high water solubility and relatively high mobility in soil [1], and hence are likely to cause water environment pollution.

The determination of these herbicides has been based on ion-exchange chromatography [2] or ion-pair liquid chromatography [3] for DCPA products and thin-layer chromatography [4] for DCPA in waste water. Trace determinations of these compounds in environmental water or soil usually involve liquid–liquid extraction under acidic conditions and their conversion into ester derivatives, such as methyl [5,6], butyl [7], 3-phenylpropyl [8] or benzyl [9] esters, which are determined by gas chromatography with electron-capture detection (GC–ECD) or gas chromatography–mass spectrometry (GC–MS). These procedures often require many steps and are tedious. The high volatility of the free acid form of TFP-Na in the organic phase after extraction is another analytical difficulty [9].

The authors previously developed a direct derivatization method in an aqueous matrix using dicyclohexylcarbodiimide (DCC) in order to determine a small hydrophilic carboxylate, monofluoroacetate, in water, and successfully determined traces of it by GC–ECD [10]. As in the

Correspondence to: H. Ozawa, Water and Soil Environment Division, National Institute for Environmental Studies, 16–2 Onogawa, Tsukuba-shi, Ibaraki 305 (Japan).

procedure derivatization and extraction occur in one step, the time of operation could be reduced, and also the volumes of water sample and extraction solvent could be decreased without decreasing the sensitivity of analysis.

In this work, a direct derivatization reaction, that is, trifluoroanilide derivatization using trifluoroaniline (TFA) and DCC, was tried for TFP-Na and DCPA. A method was developed and evaluated for the determination of these compounds in water by the use of direct derivatization.

EXPERIMENTAL

Reagents

TFP-Na analytical standard was provided by Daikin Kogyo (Tokyo) and DCPA was obtained from Tokyo Kasei Kogyo (Tokyo). Stock solutions of TFP-Na and DCPA were prepared at a concentration of 1000 $\mu g\ l^{-1}$ in distilled water. TFA was obtained from Tokyo Kasei Kogyo and DCC from Kanto Chemical (Tokyo). TFA and DCC were dissolved in ethyl acetate prior to use. Triethanolamine was obtained from Dojin Kagaku (Kumamoto, Japan). Ethyl acetate, hexane, diethyl ether and anhydrous sodium sulphate were of pesticide residue analysis grade. Other reagents were of analytical-reagent grade.

Alumina (Aluminiumoxid 90, activity II–III, 70–230 mesh, Merck) was activated at 180°C for 3 h and by adding distilled water alumina of 5% (w/w) water content was prepared, 5 g of which was packed in a glass column (10 mm i.d.).

Apparatus

A Shimadzu Model GC-3BE gas chromatograph equipped with an electron-capture detector (^{63}Ni, 10 mCi) was used. The glass column (3 m × 3 mm i.d.) was half packed with diethylene glycol succinate (5%) + H_3PO_4 (1%) on Chromosorb W AW DMCS (60–80 mesh) and half with Apiezon L grease (5%) + H_3PO_4 (3%) on Chromosorb W AW DMCS (60–80 mesh). The former was packed in the front half and the latter in the back half. The column oven and detector temperature were 170°C and the injection port temperature was 190°C. The carrier gas was nitrogen at a flow-rate of 30 ml min^{-1}.

A JEOL Model JMS-AX505w gas chromatograph–mass spectrometer was used. A DB-17 fused-silica capillary column (15 m × 0.53 mm i.d.; film thickness 1.0 μm) (J&W Scientific) was employed. The column oven temperature was maintained at 70°C for 1 min, then increased at 20°C min^{-1} to 200°C. The injection port temperature was 220°C, the separator temperature 230°C and the ion source chamber temperature 260°C. The ionization current was 300 μA and the ionization voltage was 70 eV. The carrier gas was helium at a flow-rate of 15 ml min^{-1}.

Procedure

A 50-ml portion of sample water (after filtration over glass-fibre filter-paper when necessary) was placed in a 100-ml separating funnel. To the sample water, 1 g of sodium chloride, 0.5 ml of 10 M hydrochloric acid, 0.5 ml of 1 M TFA solution in ethyl acetate and 0.5 ml of 1 M DCC solution in ethyl acetate were added and the mixture was gently stirred. Subsequently, 15 ml of ethyl acetate extracting solvent was added and the mixture was shaken vigorously for 30 min with a reciprocating shaker. After separation of the aqueous layer with the addition of 5 g of sodium chloride, the aqueous layer was again extracted with 5 ml of ethyl acetate. The combined organic layer was washed with 5 ml of 3 M hydrochloric acid, saturated sodium hydrogencarbonate solution and saturated sodium chloride solution and dried with anhydrous sodium sulphate.

The solution was evaporated to dryness on a rotary evaporator with addition of 1 ml of triethanolamine solution in acetone (10 mg ml^{-1}). To the residue a small volume of hexane was added and the mixture was again evaporated to dryness. The residue was sonicated with 2 ml of hexane–benzene (1:1, v/v) for 1 min and dissolved. The solution was loaded onto the alumina column (water content 5%, w/w) with insoluble matter, the column was washed with 40 ml of hexane, then eluted with 40 ml of diethyl ether–hexane (1 + 1, v/v). The eluate was concentrated to 10 ml and subjected to GC analysis. The injec-

tion volume was 5 μl for GC–ECD and 2 μl for GC–MS.

The calibration graph was prepared as follows. TFP-Na in the range 0.05–4.0 μg and DCPA in the range 0.2–8.0 μg were added to 50-ml portions of distilled water and chromatograms were obtained from these standard solutions according to the analytical procedure. Peak height was measured for GC–ECD and peak area for GC–MS.

RESULTS AND DISCUSSION

Derivatization reaction and its optimization

Preliminary experiments revealed that TFP-Na and DCPA in aqueous solution could be converted at room temperature into their trifluoroanilide derivatives by the use of TFA and DCC. Accordingly, in order to develop an analytical procedure, the derivatization reaction conditions were investigated. The reaction yield with 4 μg of TFP-Na and 8 μg of DCPA in 50-ml portions of distilled water was checked by GC with variation of the amount of DCC, TFA or hydrochloric acid and of the reaction time.

Effect of DCC. The influence of the amount of DCC on the derivatization reaction is shown in Fig. 1. DCC in the range 0.06–0.1 mmol afforded almost constant and maximum yields of both the derivatives of TFP-Na and DCPA (Fig. 1a), whereas a decrease in the yield was observed for amounts of DCC greater than 0.1 mmol (Fig. 1b).

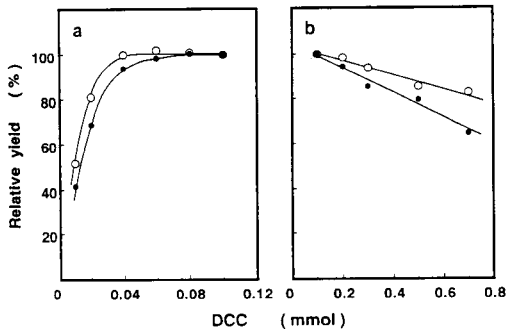

Fig. 1. Effect of the amount of DCC on the derivatization of (○) TFP-Na and (●) DCPA. Relative yield was calculated on the basis of the value obtained with 0.1 mmol of DCC.

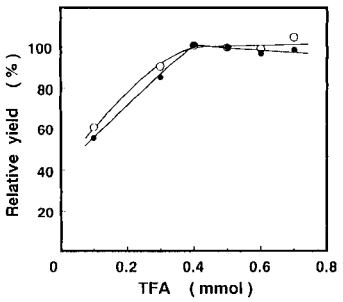

Fig. 2. Effect of the amount of TFA on the derivatization of (○) TFP-Na and (●) DCPA. Relative yield was calculated on the basis of the value obtained with 0.5 mmol of TFA.

Therefore, the amount of DCC adopted the analytical procedure was 0.1 mmol (0.5 ml of 0.2 M solution). This amount of DCC was considerably less than that used in the determination of chloroacetic acids [11].

Effect of TFA. The influence of the amount of TFA on the derivatization reaction is shown in Fig. 2. With more than 0.4 mmol of TFA, almost constant yields of both the derivatives of TFP-Na and DCPA were obtained. In the analytical procedure, 0.5 mmol of TFA (0.5 ml of 1 M solution) was used.

Effect of hydrochloric acid. The influence of the amount of hydrochloric acid with DCC and TFA concentrations as above is shown in Fig. 3. Addition of 10 M hydrochloric acid in the range 0.4–0.6 ml afforded maximum yields of the derivatives of TFP-Na and DCPA. Use of more than 0.6 ml of the acid reduced the yield of the

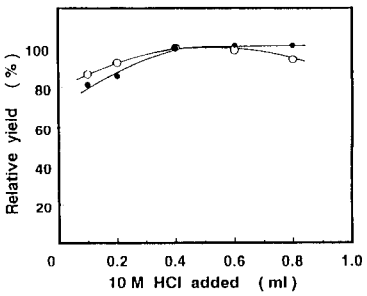

Fig. 3. Effect of the volume of hydrochloric acid added on the derivatization of (○) TFP-Na and (●) DCPA. Relative yield was calculated on the basis of the value obtained with 0.4 ml of 10 M hydrochloric acid.

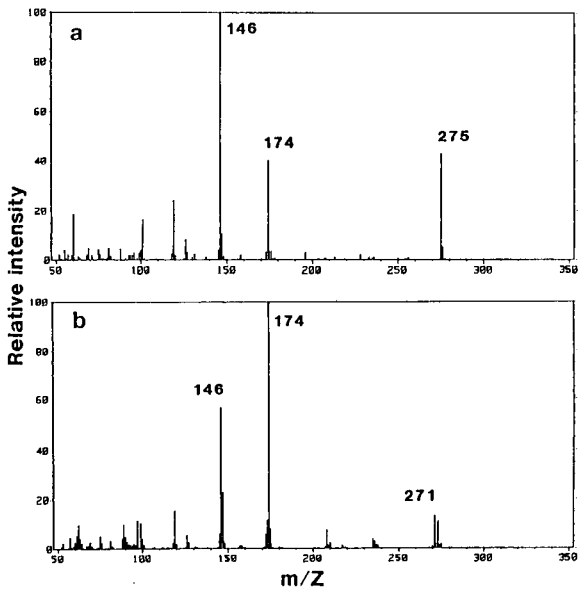

Fig. 4. EI mass spectra of the derivatives of (a) TFP-Na and (b) DCPA.

TFP-Na derivative. In the analytical procedure, 0.5 ml of 10 M hydrochloric acid was added to samples of water.

Effect of reaction time. The influence of reaction time, that is, the shaking time of the mixture of sample water, derivatizing reagents and extractant, on the derivatization was investigated in the range 5–90 min at room temperature with other conditions as above. It appeared that TFP-Na reacted more slowly than DCPA. However, the yields of the derivatives of both TFP-Na and DCPA reached a maximum in 30 min, which was constant up to 90 min. Consequently, the reaction time was fixed at 30 min in the final analytical procedure.

Confirmation of the derivative

Electron impact (EI) mass spectra of the products of the derivatization of TFP-Na and DCPA are shown in Fig. 4. The TFP-Na derivative had a molecular ion peak at m/z 275 and the DCPA derivative at m/z 271. Formation of trifluoroanilide derivatives of TFP-Na (TFP-TFA) and DCPA (DCP-TFA) by using TFA and DCC was confirmed. Peaks of fragments ions cleaved from both sides of the carbonyl carbon atom of the trifluoroanilide derivatives were observed, the base peaks being at m/z 146 for the TFP-Na derivative and at m/z 174 for the DCPA derivative.

Clean-up

Alumina column chromatography was applied to clean up the products of the derivatization reaction of TFP-Na and DCPA. The derivatives of TFP-Na and DCPA on 5 g of alumina with 5% (w/w) water content in a glass column (10 mm i.d.) were not eluted with 40 ml of hexane, but non-polar contaminants were eluted to a considerable extent. When diethyl ether–hexane (1 + 1, v/v) was subsequently passed through the column, the DCPA derivative was eluted in 10 ml of eluate and the TFP-Na derivative in the next 30 ml. Therefore, the TFP-Na and DCPA derivatives can be separated in the alumina column.

Prior to chromatography in the alumina column it is essential to remove ethyl acetate from the extract solution of the derivatization reaction mixture. Rotary evaporation of the extracted solution to dryness led not only to the removal of ethyl acetate but also to a considerable loss of the TFP-Na derivative by volatilization. Therefore, triethanolamine was added to the extracted solution before evaporation to dryness in order to suppress the loss of the TFP-Na derivative.

Determination by GC–ECD

Standard solutions were treated according to the derivatization procedure and chromatograms were obtained. A calibration graph prepared by peak-height measurements showed excellent linearity in the range of 10–100 $\mu g\ l^{-1}$ for both the TFP-Na and DCPA. The retention time of the DCPA derivative was longer than that of the TFP-Na derivative, and hence the slope of the calibration graph of DCPA was smaller than that of TFP-Na. Therefore, in the standard solution of DCPA concentration was made twice that of TFP-Na. Figure 5 shows a gas chromatogram obtained from a standard solution. Another calibration graph was constructed for the lower concentration range in the same way and good linearity was obtained at the $\mu g\ l^{-1}$ level. It was concluded that the trifluoroanilide derivatization

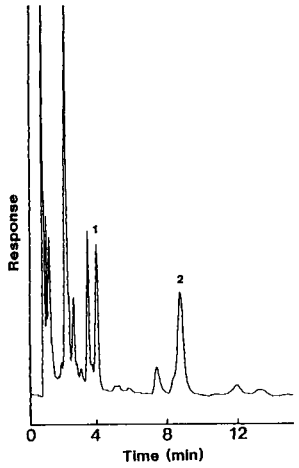

Fig. 5. Gas chromatogram obtained from a standard solution (TFP-Na, 10 $\mu g\ l^{-1}$; DCPA, 20 $\mu g\ l^{-1}$). Peaks: 1 = TFP-TFA; 2 = DCP-TFA.

procedure could be used for the determination of TFP-Na and DCPA. In this measurement the volume of the solution subjected to GC analysis should be 10 ml or more because the interferences on the chromatogram. The detection limits of TFP-Na and DCPA with simultaneous measurement were ca. 0.5 and 2 $\mu g\ l^{-1}$, respectively.

Determination of GC–MS

Detection of the TFP-Na and DCPA derivatives was investigated by selected ion monitoring (SIM). Among the molecular ion and fragment ion peaks, monitoring ions were selected; the TFP-Na derivative was monitored at m/z 275 and the DCPA derivative at m/z 174. A typical SIM profile obtained from a standard solution is shown in Fig. 6.

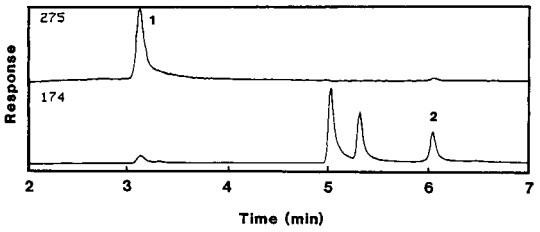

Fig. 6. SIM profile obtained from a standard solution (TFP-Na, 10 $\mu g\ l^{-1}$; DCPA, 20 $\mu g\ l^{-1}$) without clean-up. Peaks: 1 = TFP-TFA; 2 = DCP-TFA.

A calibration graph was prepared by peak-area measurements; both the TFP-Na and DCPA derivatives showed excellent linearity even at the $\mu g\ l^{-1}$ level. In GC–MS measurements the analytical solution could be concentrated to 1 ml and the detection limits of both TFP-Na and DCPA were ca. 0.1 $\mu g\ l^{-1}$. Monitoring at m/z 174 was also available for TFP-Na analysis and at m/z 271 or 146 for DCPA analysis, to confirm peak identification.

Recovery experiments and application to environmental samples

Recovery experiments were done on natural waters. River and lake waters were first analysed, and TFP-Na and DCPA could not be detected. TFP-Na and DCPA added to the river and lake waters were determined according to the analytical procedure, at high spiking levels without clean-up by alumina column chromatography. The results are shown in Table 1 and indicate the usefulness of the proposed method. The recovery of DCPA from lake water using GC–MS was relatively low with a poorer precision. Low recov-

TABLE 1

Recovery of propionic acid herbicides from spiked natural water

Sample	Herbicide	Amount added (μg)	Concentration added ($\mu g\ l^{-1}$)	Mean recovery (%) ($n = 3$)	R.S.D. (%)	Method
River water	TFP-Na	0.50	10	99	2.0	GC–ECD
	DCPA	1.0	20	110	1.9	GC–ECD
Lake water	TFP-Na	0.10	2.0	98	5.7	GC–MS
	DCPA	0.20	4.0	67	9.7	GC–MS

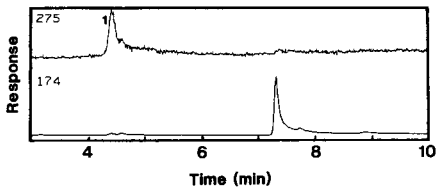

Fig. 7. SIM profile obtained from a stream water. TFP-Na was detected (peak 1). GC–MS operating conditions were as given in the text, except that the column temperature was programmed from 70°C (held for 2 min) at 10°C min^{-1} to 200°C.

eries at lower concentration levels are possibly caused by the influence of coexisting substances in water such as organic compounds.

The proposed GC–MS method was applied to real environmental waters. A stream water sample taken in a forested area where TFP-Na had been spread 1 week before was analysed and TFP-Na was detected at a concentration of 2.4 $\mu g\ l^{-1}$ (Fig. 7). Three weeks later the concentration in samples from the same location had decreased to 1.0 $\mu g\ l^{-1}$.

Conclusion

The trifluoroanilide derivatization method for the propionic acid herbicides TFP-Na and DCPA using TFA and DCC can be applied to the determination of these compounds in environmental waters at $\mu g\ l^{-1}$ levels. For water samples with small amounts of contaminants, the extracted solution of the derivatives could be directly subjected to instrumental analysis, which suggests a simpler method of determination.

REFERENCES

1 T. Takematsu, Josouzai Kenkyuu Souran, Hakuyuusha, Tokyo, 1982, p. 576.
2 T.S. Stevens and C. Wedelstaedt, J. Assoc. Off. Anal. Chem., 66 (1983) 1390.
3 T.S. Stevens and K.M. Chritz, J. Assoc. Off. Anal. Chem., 70 (1987) 47.
4 Z.I. Chalaya and T.V. Gorbonos, Zh. Anal. Khim., 35 (1980) 1352.
5 P.A. Frank and R.J. Demint, Environ. Sci. Technol., 3 (1969) 69.
6 V.D. Chmil, Zh. Anal. Khim., 33 (1978) 2232.
7 E.G. Cotterill, J. Chromatogr., 106 (1975) 409.
8 J.M. Van der Poll and R.H. De Vos, J. Chromatogr., 187 (1980) 244.
9 T. Tsukioka, S. Shimizu and T. Murakami, Analyst., 110 (1985) 39.
10 H. Ozawa and T. Tsukioka, Anal. Chem., 59 (1987) 2914.
11 H. Ozawa and T. Tsukioka, Analyst, 115 (1990) 1343.

Analytica Chimica Acta, 267 (1992) 31–37
Elsevier Science Publishers B.V., Amsterdam

Determination of copper and cadmium in sea water by preconcentration and electrothermal atomic absorption spectrometry

Zhen-Shan Liu and Shang-Da Huang

Department of Chemistry, National Tsing Hua University, Hsinchu 30043 (Taiwan)

(Received 29th January 1992; revised manuscript received 9th April 1992)

Abstract

A preconcentration procedure was developed for the determination of trace copper and cadmium in sea water. The chelating agent ammonium tetramethylenedithiocarbamate [ammonium pyrrolidinedithiocarbamate (APDC)] and a miniature column packed with 5 mg of silica gel C_{18} were used for preconcentration. Only 100–1000 μl of sample was required. The whole volume of the methanol eluate (40 μl) was injected directly into the graphite furnace of the atomic absorption spectrometer. The calibration graph method was used. This technique is simple and rapid and provides results of high accuracy and precision. The accuracy of the results was demonstrated by the analysis of various reference standard sea-water samples.

Keywords: Atomic absorption spectrometry; Sample preparation; Cadmium; Copper; Preconcentration; Sea water; Solid-phase extraction; Waters

Various techniques have been applied to the determination of trace heavy metals in sea water. Direct instrumental analysis of sea water is difficult because many complex and large matrices such as sodium chloride exist in sea water, which always affect the capability of the instrument to obtain the correct result in normal operation. In addition to the interference of matrices in the analysis, some metals have a concentration in the mg l^{-1} or μg l^{-1} range, which is near or below the limit of detection of the instrument. Preconcentration can solve the above two problems and lead to easy determination. There are many methods of preconcentration, including coprecipitation, chelating ion-exchange resins, chelation and liquid–liquid extraction and chelation and solid-phase extraction [1]. Liquid/liquid extraction could be replaced with solid-phase extraction, because the latter is efficient, reproducible and simple in sample handling and transfer [2].

Various kinds of dithiocarbamates are widely used for the determination of heavy metals [3], because they complex strongly with many metal ions. Both ammonium tetramethylenedithiocarbamate [ammonium pyrrolidine dithiocarbamate (APDC)] and sodium diethyldithiocarbamate (NaDDTC) are commonly used [4,5]. It has been shown that APDC is more stable than NaDDTC in acidic solution, whereas NaDDTC has a larger formation constant for most complexes. APDC operates in a broad pH range without decomposition [6,7].

Traditional off-line solid-phase extraction requires very large sample volumes (500–1000 ml) for preconcentration and only a small part of the

Correspondence to: S.-D. Huang, Department of Chemistry, National Tsing Hua University, Hsinchu 30043 (Taiwan).

eluate (10–100 μl) was used in graphite furnace atomic absorption spectrometry (GFAAS); most of the eluate is wasted [8–10]. The concentration factors are 50–200. The problem of sample consumption can be solved by using a flow-injection preconcentration system coupled with flame atomic absorption spectrometers, inductively coupled plasma atomic spectrometers or inductively coupled plasma mass spectrometers. Flow-injection on-line column preconcentration in atomic spectrometry has been reviewed recently by Fang [11,12].

Because GFAAS requires a non-continuous delivery of the sample, various types of flow-injection preconcentration systems to reduce the sample consumption successfully have been described [11–20]. The system used by Bäckström and Danielsson [13,14] involves a two-step extraction of metal dithiocarbamates using a set of membrane phase separators. The components of the flow-injection system for GFAAS used by Fang et al. [11,15] are almost identical with those for flame AAS, but programmable automatic valves and pump with much smaller column capacities are used.

Although the systems with microcolumns used by Fang et al. [15] and Sperling et al. [17–19] are simpler in comparison with the membrane extraction system, the total eluate volume of about 200 μl exceeds the capacity of the graphite furnace. Therefore, only a sub-sample can be introduced into the furnace. The sub-sampling of the eluate can be performed in two ways. In the first, using the "fixed-volume" technique [15], the transfer capillary between the flow-injection system and the graphite furnace has exactly the capacity of the desired volume of the sub-sample. Only the part of the eluate stored in this capillary is injected into the graphite furnace. In the second type, using the "time-based" technique [17–19], the eluate pump is activated for a clearly defined time interval, in order to transfer the corresponding eluate volume into the furnace. The "fixed-volume" technique gave results with better sensitivity and precision than the "time-based" technique, but the latter showed much greater programming flexibility and the simpler manifold design and operation [17].

Sometimes, if necessary, the eluate from solid-phase extraction must be digested with concentrated acid [8–10] in order to decrease the interference of the organic chelating agent and to match the sample solution with the matrix of the standard solution; otherwise, the analysis of the eluate was done by standard addition method [16]. Digestion of the eluate will increase the probability of contamination and is time consuming. The use of the standard addition method is also very time consuming and it may decrease the accuracy and precision of the determination.

In this work, the chelating agent APDC and a miniature column packed with a very small amount (ca. 5 mg) of silica gel C_{18} were used for the preconcentration of copper and cadmium from sea water before their determination by GFAAS. The sample volumes were 100–2000 μl. The analytes were recovered from the preconcentration column quantitatively with 40 μl of methanol eluate, and all the eluate was injected directly into the graphite furnace. A calibration graph was produced using standards that had been treated with the same microcolumn preconcentration procedure as for the sample determination. The accuracy of the results obtained with this method was demonstrated by the analysis of reference standard sea water samples.

EXPERIMENTAL

Reagents and equipment

All chemicals were of analytical-reagent grade and further purified. The chelating agent was prepared weekly by dissolving 1 g of APDC (Fluka) in 20 ml of deionized water (using an ultrasonic tank to accelerate dissolution), purified by passing it through a Sep-Pak C_{18} cartidge (Waters) and purified ammonia solution was added dropwise to adjust the pH to 9 for stabilization [21]. Ammonium acetate (5 M) was used to prepare the buffer solution; it was purified by adding the APDC solution and the passing it through a Sep-Pak C_{18} cartridge. Purified ammonia solution was prepared from beaker of deionized water which was equilibrated for 24 h at room temperature with a beaker of concentrated

ammonia solution placed together in a closed-system. The washing solution was prepared by adding 1 ml of ammonium acetate solution (5 M) to 1.25 ml of APDC solution (5%), diluted with deionized water to 25 ml and then passed through a Sep-Pak C_{18} cartridge. Methanol was purified by means of a sub-boiling still and deionized water was obtained from the Milli-Q purification system (Millipore).

Polypropylene bottles for storage of reagents were soaked in dilute nitric acid (20%) for at least 24 h and rinsed with deionized water many times. PTFE beakers (10 ml) (Cole-Parmer) were cleaned with fumes of nitric acid [22] for several hours (the PTFE beakers were hung upside down on a rack in a 1000-ml glass beaker with a laboratory-made condenser on the top of the glass beaker, and the glass beaker with nitric acid inside was heated to produce the fumes of nitric acid), then rinsed with deionized water many times.

The sample solution was sucked into the C_{18} microcolumn by an aspirator pump (Eyela) attached to a Sep-Pak cartridge rack (Waters). A Perkin-Elmer Zeeman 5100PC atomic absorption spectrometer equipped with an HGA-600 graphite furnace and an AS-60 autosampler was used throughout. The instrument was operated with Zeeman-effect background correction. Pyrolytic graphite-coated graphite tubes with a platform were used.

NASS-2 and SLEW-1 sea-water standards were obtained from the marine Analytical Chemistry Standards Program of the National Research Council of Canada.

C_{18} microcolumn

The assemblage of the preconcentration system is shown in Fig. 1. The microcolumn was obtained from a PTFE capillary tube of the AS-60 autosampler (2.5 cm × 0.94 mm i.d.) (Perkin-Elmer), packed with 5 mg (ca. 7 μl) of silica gel C_{18} (particle size 50–105 μm) (Waters) and both ends of microcolumn were packed with polyethylene frits (porosity 0.5 μm). The silica gel C_{18} and polyethylene frits were taken from a Sep-Pak C_{18} cartridge. The smaller PTFE tube (20 cm × 1.0 mm o.d.) (Perkin-Elmer) was also taken from a

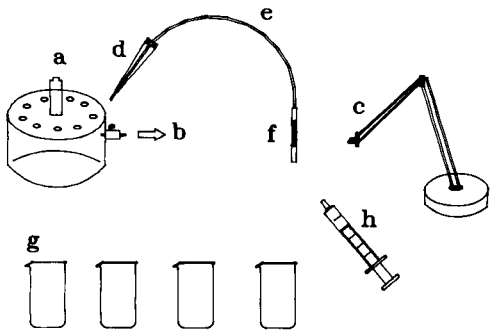

Fig. 1. Assemblage of preconcentration system. (a) Sep-Pak cartridge rack; (b) connection of vacuum regulator and aspirator; (c) flexible holder; (d) micropipette tip; (e) PTFE tube; (f) silica gel C_{18} microcolumn; (g) PTFE beaker; (h) syringe.

PTFE capillary tube of the AS-60 autosampler; one end of the tube was matched with the microcolumn and the other end was inserted into the tip of a micropipette which was convenient for the Sep-Pak rack suction and the injection of the eluate into the graphite furnace tube.

Sample and standard solution preparation

A sample aliquot (100–2000 μl) was accurately pipetted into a 10-ml PTFE beaker, followed by the addition of 10 μl of the buffer solution and 10 μl of the 5% APDC solution, then a known volume of ammonia solution was added to give the desired pH. The required volume of ammonia solution was established from a test with another sample aliquot to avoid contamination of the sample by the pH electrode. Standard aliquots (Cu 0–20 $\mu g\ l^{-1}$, 20 μl; Cd 0–1.0 $\mu g\ l^{-1}$, 20 μl) were treated in the same way as the sample aliquots.

Procedure

The C_{18} microcolumn was attached to the tip of a flexible holder, the end was connected to the tip of a micropipette with a PTFE tube and the tip of the micropipette was connected to the Sep-Pak rack for suction. The flow-rate of suction was adjusted by the vacuum regulator on the Sep-Pak rack.

First, the C_{18} microcolumn was wetted with methanol, then it was flushed with deionized water. Second, the sample solution or standard

nents were eluted with 24 μl of washing solution. Third, air was sucked through the column to dry it and the analytes were eluted with 40 μl of methanol, then sucking was stopped to keep the methanol in the PTFE tube and the C_{18} microcolumn was removed from the holder and the eluate was directly injected into the graphite furnace tube with a syringe connected to the C_{18} microcolumn.

Beakers made of PTFE were used throughout. All the preconcentration procedures were done in a class 100 laminar flow hood. The temperature programme used in GFAAS for this work is given in Table 1.

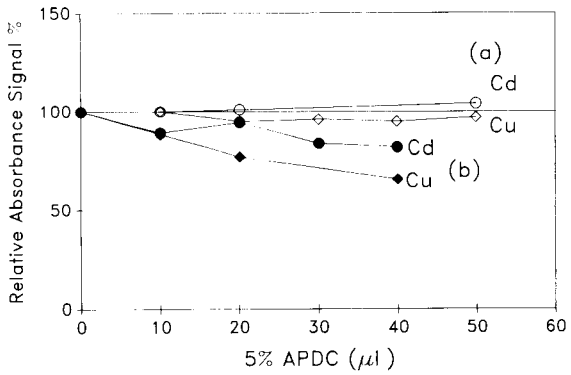

Fig. 2. Effect of APDC. Standard aliquots: (a) Cu (10 μg l^{-1}, 20 μl) and Cd (0.5 μg l^{-1}, 20 μl) with APDC added and treated according to the preconcentration procedure; (b) Cu (10 μg l^{-1}, 10 μl) and Cd (0.5 μg l^{-1}, 10 μl) with APDC added and introduced directly into the GFAAS system.

RESULTS AND DISCUSSION

Effect of APDC

Standard aliquots of 10 μl of Cu (10 μg l^{-1}) or Cd (0.5 μg l^{-1}) were spiked with 0–40 μl of APDC (5%) and injected into the furnace with the AS-60 autosampler. The results were normalized to the values using standard aliquots without APDC and are shown in Fig. 2. The results indicate that the absorbance signals of copper and cadmium decrease with increase in the dose of APDC. This is probably caused by the loss of the analyte during the graphite furnace cycle due to the volatility of metal–APDC complexes [5,23,24]. Another set of standard aliquots of 20 μl Cu (10 μg l^{-1}) or Cd (0.5 μg l^{-1}) were treated with the same procedure of preconcentration using 10–50 μl of APDC (5%) and the results are also shown in Fig. 2. Very little effect on absorbance was observed with varing APDC dosage when the preconcentration procedures were used.

Optimization of procedure

The effect of flow-rate and the extraction efficiency was evaluated by extracting the open ocean NASS-2 standard and the estuarine water SLEW-1 standard at pressure drop values varying from 5 to 25 cmHg, with the pH fixed at 6–7. Aliquots of 1000 μl of NASS-2 were used for the determination of copper and 500 μl of SLEW-1 for the determination of cadmium. The concentration factors were 50 and 25, respectively. All data were normalized to a pressure drop of 15 cmHg and are shown in Fig. 3.

No effect of flow-rate on the extraction efficiency was observed except for low flow-rates.

TABLE 1

Temperature programme of graphite furnace

Step	Cu			Cd		
	Temperature (°C)	Ramp (s)	Hold (s)	Temperature (°C)	Ramp (s)	Hold (s)
Dry	120	5	20	120	5	20
Ash	900	5	30	300	5	35
Cool	20	1	15	20	1	15
Atomize	2400	0	6	1200	0	5
Clean	2650	1	5	2600	1	5
	20	1	5			
	2650	1	5			

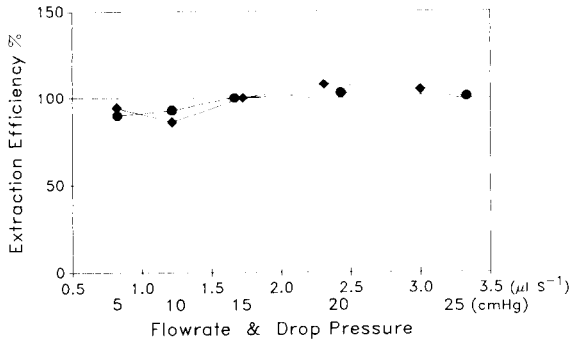

Fig. 3. Effect of flow-rate on extraction efficiency. ♦ = Cu; ● = Cd.

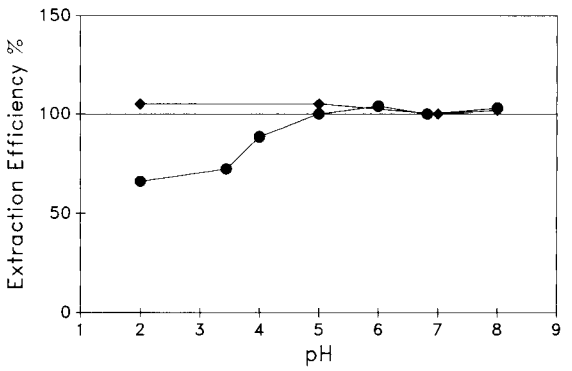

Fig. 4. Effect of pH on extraction efficiency. ♦ = Cu; ● = Cd.

This unusual trend could be explained by the fact that the C_{18} microcolumn retained more APDC at low flow-rates [2], such that more APDC was eluted and injected into the furnace. A range of pressure drops of 15–20 cmHg was chosen for the control of the flow-rate. About 8 min were needed for the preconcentration of 1000 μl of sea-water sample.

The evaluation of the optimum pH of the procedure was the same as for the flow-rate evaluation except that the pH was varied. All absorbance signals were normalized to the value at pH 7, as shown in Fig. 4. The Cu–APDC complex was stable in the pH range 2–8 but the extraction efficiency of cadmium was depressed for solutions with pH ≤ 4. When the pH was less than 4, a white precipitate was observed. The APDC could be insoluble [25] or could be decomposed in acidic aqueous [6]. When the pH was increased to 9, there was a probability of bleeding of the silica C_{18} [10], and therefore pH range 6–8 was chosen for this work.

Accuracy and precision

A sea-water sample was collected from coastal surface water of Hsinchu. The sea water was filtered through a 0.45-μm membrane filter, then passed through a Chelex-100 column [26] in order

TABLE 2

Recoveries for spiked test samples

Sample	Atomic absorbance [f]					
	Cu			Cd		
Blank						
20 μl DIW [a] + 10 μl 5% APDC + 10 μl 5 M NH_4OAc	0.004	0.005	0.005	0.005	0.006	0.005
Standard						
20 μl STD [b] + 10 μl 5% APDC + 10 μl 5 M NH_4OAc	0.072	0.070	0.071	0.097	0.097	0.099
Sample						
Sea water [c] + 10 μl 5% APDC + 10 μl 5 M NH_4OAc	0.031	0.031	0.032	0.016	0.017	0.016
Spiked sea water [c,d] + 10 μl 5% APDC + 10 ml 5 M NH_4OAc	0.096	0.096	0.097	0.106	0.105	0.108
Recovery (%) [e]	96	100	98	98	97	98

[a] DIW = deionized water. [b] STD = standard solution: Cu 10 μg l^{-1}; Cd 0.5 μg l^{-1}. [c] Sea water volume: for Cu 500 μl, for Cd 1000 μl. The concentration factors were Cu 25 and Cd 50. [d] Spiked concentrations: Cu 0.4 μg l^{-1}, Cd 0.01 μg l^{-1}. [e] Recovery = (spiked − unspiked)/(standard − blank) × 100. [f] Integrated absorbance (s).

to reduce the trace metal concentration. The pH of the sea-water sample was adjusted to 1.7 with sub-boiling nitric acid before storage. The spiked concentrations of copper and cadmium in the sea-water sample were 0.4 and 0.01 $\mu g\ l^{-1}$, respectively.

A calibration graph was constructed by injecting the methanol eluate from the C_{18} microcolumn into the furnace using aqueous standard solutions processed using the same preconcentration and determination procedure as for sea-water sample analysis. It was found that 98% of copper and cadmium were recovered, and the precision was 2% or better, as shown in Table 2. The average values of the absolute blanks for copper and cadmium are 13 and 0.54 pg, respectively. The detection limits for copper and cadmium are 2.4 and 0.178 ng l^{-1}, respectively. The absolute blank values were obtained by using the preconcentration and determination procedures with 20 μl of deionized water; the detection limit was obtained by dividing three times the standard deviation of the blank values (copper and cadmium concentration) by the concentration factor (copper, 100; Cd, 50).

The accuracy of the method was examined by the analysis of open-ocean NASS-2 and estuarine water SLEW-1 standards. The results in Table 3 show that the method provides results with high accuracy.

TABLE 3

Determination of accuracy

Metal	NASS-2		SLEW-1	
	This work ($\mu g\ l^{-1}$) [a]	Certified values ($\mu g\ l^{-1}$)	This work ($\mu g\ l^{-1}$) [a]	Certified values ($\mu g\ l^{-1}$)
Cu	0.1044 ±0.0010 (100) [b]	0.109 ±0.011	1.804 ±0.012 (10) [b]	1.76 ±0.09
Cd	0.0286 ±0.0013 (25) [b]	0.029 ±0.004	0.0186 ±0.002 (50) [b]	0.018 ±0.003

[a] Average ± standard deviations for triplicate samples. [b] Concentration factor.

Conclusion

The main differences between the technique presented here and the work of Fang et al. [15] and Sperling et al. [17] are that we use (1) a smaller amount of C_{18} material in the microcolumn (7 vs. 15 μl), (2) an APDC complex instead of NaDDTC complex and (3) methanol eluate instead of ethanol eluate. In addition to these modifications, it was found that the analytes in sea water samples can be recovered quantitatively from the microcolumn with only 40 μl of methanol, and that all the eluate can be injected directly into the graphite furnace. The disadvantages caused by the sub-sampling techniques (such as the need for a complicated and delicate design of the flow-injection system and the precision loss due to using the sub-sampling design) are avoided, and the sensitivity of the analysis is increased by a factor of two or more. Further, standard solutions are used with much higher concentrations and smaller volumes (e.g., 0.5–1.0 $\mu g\ l^{-1}$ Cd, 20 μl compared with 0.01–0.03 $\mu g\ l^{-1}$ Cd, 3 ml) to obtain the calibration graph. The risk of error caused by contamination of the standard solution is reduced using standard solutions with higher concentrations. The drawback of the technique presented here is the manual manipulation in the preconcentration procedure. However, the equipment needed in this work is simple and can be used in almost any laboratory equipped with GFAAS but without a flow-injection system. The precision and accuracy of the results using these techniques are comparable.

The authors are indebted to the National Science Council of the Republic of China for a grant (NSC 81-0208-M-007-107) in support of this work.

REFERENCES

1 A. Mizuike, Enrichment Techniques for Inorganic Trace Analysis, Springer, Berlin, Heidelberg, New York, 1983.
2 M. Zief and R. Kiser, Am. Lab., 20 (1990) 70.
3 A. Hulanicki, Talanta, 14 (1967) 1371.
4 G.A. Knauer and J.H. Martin, Anal. Chim. Acta, 105 (1979) 233.
5 S.C. Apte and A.M. Gunn, Anal. Chim. Acta, 193 (1987) 147.

6 R.J. Everson and J.E. Parker, Anal. Chem., 46 (1974) 1966.
7 M.B. Kalt and D.F. Boltz, Anal. Chem., 40 (1968) 1086.
8 H. Watanabe, K. Goto, S. Taguchi, J.W. McLaren, S.S. Berman and D.S. Russell, Anal. Chem., 53 (1981) 738.
9 R.E. Sturgeon, S.N. Willie and S.S. Berman, Anal. Chem., 57 (1985) 6.
10 R.E. Sturgeon, S.S. Berman and S.N. Willie, Talanta, 29 (1982) 167.
11 Z.-L. Fang, Spectrochim. Acta Rev., 14 (1991) 235.
12 J.F. Tyson, Spectrochim. Acta Rev., 14 (1991) 169.
13 K. Bäckström and L.-G. Danielsson, Anal. Chem., 60 (1988) 1354.
14 K. Bäckström and L.-G. Danielsson, Anal. Chim. Acta, 232 (1990) 301.
15 Z.-L. Fang, M. Sperling and B. Welz, J. Anal. At. Spectrom., 5 (1990) 639.
16 V. Porta, O. Abollino, E. Mentasti, and C. Sarzanini, J. Anal. At. Spectrom., 6 (1991) 119.
17 M. Sperling, X. Yin and B. Welz, J. Anal. At. Spectrom., 6 (1991) 295.
18 M. Sperling, X. Yin and B. Welz, J. Anal. At. Spectrom., 6 (1991) 615.
19 M. Sperling, X. Yin and B. Welz, Spectrochim. Acta, Part B, 46 (1991) 1789.
20 S. Nakashima, R.E. Sturgeon, S.N. Willie and S.S. Berman, Fresenius' Z. Anal. Chem., 330 (1988) 592.
21 R.E. Sturgeon, S.S. Berman, A. Desaulniers and D.S. Russell, Talanta, 27 (1980) 85.
22 T. Noltner, P. Maisenbacher and H. Puchelt, Spectrosc. Int., 2 (1990) 36.
23 G. Volland, G. Kolblin, P. Tschopel and G. Tolg, Fresenius' Z. Anal. Chem., 284 (1977) 1.
24 K.R. Sperling, Fresenius' Z. Anal. Chem., 310 (1982) 254.
25 J.J. Fardy, McOrist and T.M. Florence, Anal. Chim. Acta, 159 (1984) 199.
26 A.J. Paulson, Anal. Chem., 58 (1986) 183.

Analytica Chimica Acta, 267 (1992) 39–45
Elsevier Science Publishers B.V., Amsterdam

Heterogeneity as a concept in the interpretation of metal ion binding by humic substances. The binding of zinc by an aquatic fulvic acid

James H. Ephraim

Department of Water and Environmental Studies, Linköping University, S-581 83 Linköping (Sweden)

(Received 10th April 1992)

Abstract

Zinc binding by a well characterized fulvic acid was studied by the ion-exchange distribution technique and ultrafiltration method at 0.100 M $NaClO_4$ using trace amounts of zinc ($\leqslant 10^{-7}$ M) and two different fulvic acid concentrations (6.2×10^{-4} and 1.2×10^{-3} M). The results were interpreted by considering the various acidic sites envisaged from potentiometric titrations in aqueous and non-aqueous media. In addition to calculating the overall complex formation function, literature-based constants for the complexation between the metal ion and the ascribed functional group were employed to account for the observed binding patterns as a function of pH. This supported the interpretation of the functional groups assigned to the envisaged acidic sites. Results from the ultrafiltration method were in agreement with those obtained from the ion-exchange distribution technique.

Keywords: Ion exchange; Humic acids; Fulvic acids; Metal ion binding; Ultrafiltration; Waters; Zinc

That humic substances (humic and fulvic acids) are heterogeneous is accepted by all researchers involved in environmental problems. This heterogeneity shows itself in a number of properties, e.g., molecular weights and functional groups. For example, humic substances are known to have a molecular weight ranging from as low as a few hundred to as high as about 300 000 [1]. The S-shape of the acid–base potentiometric titration curve attests to their functional group heterogeneity [2]. The solution chemistry of these substances has been postulated to be perturbed by two factors, namely functional group heterogeneity and the tendency to form a separate phase in aqueous solutions (ionic strength effects) [3]. The sensitivity of measurements to ionic strength changes has been attributed to the combination of size heterogeneity [4] and the amphilic nature of these substances. The description of the interaction of metal ions with humic substances was initially made without incorporating their functional group heterogeneity, and this led to the lack of uniformity necessary for the comprehensive comparison and correlation of the influence of various environmental factors on these humic substances. Recently, the prediction of Cu(II) sequestering by a soil fulvic acid was made using a unified physico-chemical approach in which two perturbing factors were incorporated [5]. The objective of this paper is not to fit complexation curves by introducing a large number of parameters, but rather to justify the assignment of functional groups to the protolytic sites of the fulvic acid. This objective was achieved by initially estimating the overall complex formation function, β_{ov}, that characterizes the binding of zinc ion by

Correspondence to: J.H. Ephraim, Department of Water and Environmental Studies, Linköping University, S-581 83 Linköping (Sweden).

a well characterized fulvic acid. In addition, employment of literature values of the complexation constant for the interaction of zinc and the envisaged functional groups of the fulvic acid facilitated the prediction of the observed binding pattern as a function of pH.

EXPERIMENTAL

Materials and equipment

All solutions were made using water purified with a Milli-Q system (Millipore). The fulvic acid Bersbo FA, which was removed from surface water by preconcentration on dimethylaminoethyl (DEAE)-cellulose followed by purification on Amberlite XAD-8 resin [6], has been well characterized via potentiometric titrations and derivatization techniques [7,8]. Analytical-reagent grade salts obtained from Merck were used in the preparation of all solutions. Sodium hydroxide was prepared from an analytical concentrate (Merck) and standardized against potassium hydrogenphthalate prior to use. The radionuclide ^{65}Zn was purchased from Amersham Sweden. An Amicon Model 8050 ultrafiltration cell, was used in conjunction with a YM2 Diaflo membrane which has a molecular weight cut-off of 1000. The Bio-Rad cation-exchange resin AG 50W-X (50–100 mesh) in the hydrogen form was converted into the sodium form [9]. The ^{65}Zn activity was determined using an LKB (Wallac) 1282 Compugamma counter equipped with a sodium iodide crystal as detector.

Procedure

Ultrafiltration. All filtrations were performed under a nitrogen gas pressure which was maintained at 3.5 bar. After conditioning of the YM2 membrane [10], the retention coefficient of the zinc ion was determined as a function of pH (Table 1). The pH of a metal ion–fulvic acid mixture was adjusted by the addition of standard NaOH. An equilibration time of ca. 20 h was allowed, after which the pH of each mixture was determined and the samples were filtered using the YM2 Diaflo membrane in conjunction with the Amicon Model 8050 ultrafiltration cell. The first 1 ml of filtrate was discarded and about 2 ml of filtrate were collected for subsequent ^{65}Zn analysis. The pH after filtration was measured and was found to be within 0.05 of the pH before filtration. The ^{65}Zn activities in the original solution and the filtrate facilitated the determination of the metal ion bound by the fulvic acid.

TABLE 1

Retention of zinc by YM2 membrane as a function of pH [expressed as the retention coefficient, $R = \ln(C_f / C_o)/\ln(V_o / V_f)$] [a]

pH	R	pH	R
4.097	0.033	6.806	0.004
4.573	0.018	7.567	0.010
5.468	0.034	8.732	0.269

[a] C_f = concentration of filtrate; V_f = volume of filtrate; C_o = concentration of original solution; V_o = original solution volume.

Ion-exchange distribution method. Schubert's method was employed using 0.5–1.0 μCi of ^{65}Zn and 0.5–0.10 of the sodium form of the resin. A detailed description of the procedure can be found elsewhere [11,12].

MODEL FOR PREDICTING METAL ION BINDING

In a comprehensive description of ion binding by humic substances, the complicating factors have been identified as their functional group heterogeneity and the effects of ionic strength [3]. The fulvic acid has been characterized to have five predominant acidic sites with various dissociation constants and abundances [8]. The interpretation of the protonation equilibria for the aquatic fulvic acid employed in this study was based on the concept that humic substances may be considered as an ensemble of relatively small amphilic moieties which are slightly different but are composed of four or five separate acidic sites with each site characterized by a distribution of acid strengths, pK_a values, that may be averaged [13]. The steps involved in this interpretation are briefly summarized as follows: (i) a maximum of four or five "average" sites are projected and their relative abundances (Ab) are deduced from the non-aqueous titration data and titration results obtained in the presence of increasing amounts of heavy metal ions, e.g., Cu(II) and

La(III)/Eu(III); (ii) first estimates of their respective pK_a values are made taking into consideration the envisaged configuration of the sites; (iii) at each experimental pH, the degree of neutralization, α, of each of the "average" acid sites is calculated with the following expression:

$$\alpha_i = \{1 + 10^{(pK_i + \Delta pK - pH)}\}^{-1} \quad (1)$$

where ΔpK is the counter-ion concentration correction term obtained from potentiometric titrations [3], and pK_i is the dissociation constant assigned to the site and pH is the experimentally determined value; and (iv) the ultimate objective has been to obtain the following relationship:

$$\sum \alpha_i Ab_i = \alpha^{\text{computed}} = \alpha^{\text{experimental}} \quad (2)$$

This relationship is obtained in an iterative procedure which involves changing the pK_is until the residual $|\alpha^{\text{computed}} - \alpha^{\text{experimental}}|^2$ is at a minimum for the set of data points.

With the aquatic fulvic acid employed in this study, the interpretation of the protonation was extended by assigning probable functional groups to the envisaged acidic moieties. This assignment was effected by considering the non-aqueous titrations and titrations with increasing amounts of heavy metals [3,8]. The acid sites, their respective pK_a and relative abundances and their envisaged functionality for the fulvic acid employed in this study are shown in Table 2.

The modes of complexation expected between the zinc metal ion and the various acidic sites of the fulvic acid molecule are described in detail below. The first step of the approach involves the computation of the degree of neutralization for each of the acid sites at each experimental pH using Eqn. 1. In the use of this equation, ΔpK was obtained at each pH, and ionic strength by the curve-fitting equation that relates it with pH in metal-free potentiometric titrations [8]. The degree of dissociation of each acid site as a function of pH and calculated by incorporating ΔpK is represented in Fig. 1

In the proposed model, a combination of the percentages of the various acidic groups ionized at a given pH in the FA–zinc ion system and literature-based values of complex formation constants [14] for the interaction between zinc and the functionality of the assigned sites (Table 2) allowed the calculation of the ratio of bound metal (M_b) to free metal (M_f) for each site. The sum of the ratios for all the types of complexation was compared with the experimentally deter-

TABLE 2

Predominant acid sites in Bersbo FA, their envisaged complexes with Zn(II) and the literature complex formation constants employed in describing the observed binding patterns (Figs. 4a and b)

Acid site	pK_a	Abundance	Functionality	Complexes with zinc	Constants employed (l mol^{-1})
I	1.7	0.20	Unidentate –COOH	$-COOZn^+$	$\beta_1 = 10^{1.1}$
II	3.3	0.25	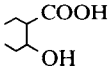	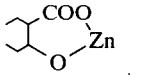	$K_{excl} = 10^{-5.2}$
				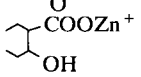	$\beta_2 = 10^{1.1}$
III	5.0	0.30	Unidentate –COOH	$-COOZn^+$	$\beta_3 = 10^{1.1}$
IV	6.5	0.20		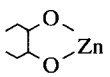	$K_{exc2} = 10^{-1.0}$
V	7.0	0.05		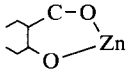	$\beta_4 = 10^{7.8}$

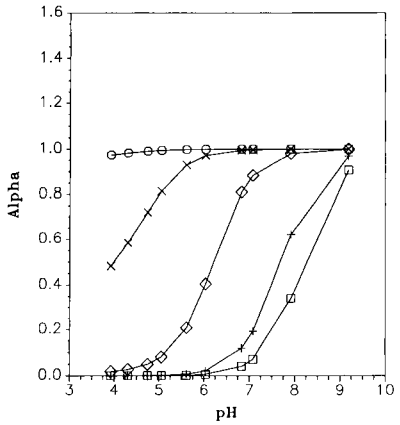

Fig. 1. Degree of neutralization for the various acidic moieties of Bersbo fulvic acid as a function of pH [8]. The values were calculated by incorporation of the counter-ion concentration correction term, ΔpK. pK: × = 3.3; + = 6.5; □ = 7.0; ○ = 1.7; ◇ = 5.0.

mined $\Sigma M_b/M_f$ for both the ion-exchange distribution and ultrafiltration methods.

Acid site I was envisaged to bind zinc in a unidentate mode involving the carboxylate ion. The complex formation constant used ($10^{1.1}$) was the literature value published for zinc–acetic acid complexation at the given ionic strength, i.e., 0.100 M $NaClO_4$ [14]. The ratio of bound metal to free metal (due to this acid site), $(M_b/M_f)_I$, was calculated at each pH using the mass action relationship by means of the following expression:

$$(M_b/M_f)_I = 10^{1.1}[RCOO^-] \cdot 10^{z\Delta pK}\gamma \qquad (3)$$

where $[RCOO^-]$ is the concentration of the ionized form of the acid site I, which is obtainable from the results of the potentiometric titrations of the fulvic acid in absence of metal ion [8], and γ is the activity coefficient of the metal ion at the defined ionic strength [15]. The counter-ion concentration correction term, ΔpK, is raised to the power z, which is the charge on the metal ion, in order to conserve electroneutrality.

Acid site II, mimicking the salicylic acid arrangement, was considered to bind zinc in two modes. The first mode involved the complexation of the ionized carboxylate by zinc in a unidentate fashion. This reaction led to the formation of the complex, $R^{**}COOZn^+OH$ and a complex formation constant of $10^{1.1}$ was employed in the calculation. The second mode of complex formation was chelation involving both the carboxylate ion and the adjacent OH with subsequent removal of a proton. The ionization of the hydroxyl moiety could only take place at high pH values ($pK_a \approx 12.0$).

The reaction leading to the formation of the complex $R^{**}COOZnO$ may be represented by the following reaction:

$$R^{**}COO^-(OH) + Zn^{2+} \rightleftharpoons R^{**}COOZnO + H^+ \qquad (4)$$

The equilibrium constant for the above reaction, K_{excl}, is obtained from the acid dissociation constant, 10^{-12}, and the complex formation constant between the ionized form of the second acid (OH) and the zinc ion ($10^{6.8}$). This leads to a value of $10^{-5.2}$, which testifies to the fact that such a pattern of binding is small.

Acid site III with a pK_a of 5.0 was considered to complex the zinc ion in a unidentate fashion and an equilibrium constant of $10^{1.1}$ was again employed because of the lack of covalency of binding as in the case of Cu(II) binding to monomeric acids [5]. An expression similar to Eqn. 3 was employed to calculate $(M_b/M_f)_{III}$ as follows:

$$(M_b/M_f)_{III} = 10^{1.1}[R^*COO^-] \cdot 10^{z\Delta pK}\gamma \qquad (5)$$

The configuration of acid site IV has been considered to mimic the catechol arrangement, i.e., a weak acid OH adjacent to a weaker acid OH. Reference to published complex formation constants reveals that the most probable fashion of complexation between this site and the zinc ion would be chelation involving the ionized oxylate and the non-ionized OH with subsequent proton removal to form the complex $R''COZnO$. Employing an acid dissociation constant of $10^{-10.9}$ and a complex formation constant of 9.9 ($\beta_{catechol-zinc}$), a K_{exc2} value of $10^{-1.0}$ was obtained for the following envisaged reaction:

$$R''CO^-(OH) + Zn^{2+} \rightleftharpoons R''COZnO + H^+ \qquad (6)$$

$(M_b/M_t)_{IV}$ is obtained from the mass relationship as follows:

$$(M_b/M_f)_{IV} = 10^{-1.0}[RCOO^-(OH)] \cdot 10^{z\Delta pK}\gamma[H^+]^{-1} \qquad (7)$$

Acid site V, envisaged as a hydroxyl (OH) adjacent to a carbonyl (C=O) as in kojic acid was considered to form a chelate with the zinc ion as follows:

$$R'O^{-}CO + Zn^{2+} \rightleftharpoons R'OZnCO^{+} \quad (8)$$

The complex formation constant of 7.8 which was employed in the calculation is compatible with constant published for the interaction of zinc with hydroxycarbonyl ligands, e.g., substituted tropolones [14]. The contribution of M_b/M_f by this site is obtained from the following expression:

$$(M_b/M_f)_V = 10^{7.8}[RO^{-}(CO)] \cdot 10^{z\Delta pK}\gamma \quad (9)$$

The ratio of bound metal to free metal at each experimental pH for each site, i, $(M_b/M_f)_{i,pH}$, was calculated from the mass action relationships as above (Eqns. 6–10) where β_i and K_{exci} can be obtained from the literature [14], γ from Kielland [15] and ΔpK from metal-free titrations, leaving only the value for the individual ionized acid site, A_i^-. This term is obtained by considering the assigned pK_a of the acid site in conjunction with the pH of the solution to obtain the degree of neutralization, α_i, of that acid site which then allows the estimation of the term A_i^- as follows:

$$A_i^- = (HA_T Ab_i \alpha_i) - M_{bi} \quad (10)$$

where HA_T is the total amount of titratable acid sites, Ab_i is the abundance of the ith site and α_i is the corresponding degree of dissociation and M_{bi} is the metal bound to the ith site. As trace amounts of metal ions are employed ($Zn \leqslant 10^{-7}$ M), the expression reduces to

$$A_i = HA_T Ab_i \alpha_i \quad (11)$$

This procedure is then repeated for the remainder of the acid sites at each pH to facilitate the calculation of each A_i^- and thus in turn to calculate M_b/M_f for each site. The sum of all $(M_b/M_f)_{i,pH}$ values was compared with the experimentally obtained $\Sigma M_b/M_f$.

RESULTS AND DISCUSSION

Retention of Zn as a function of pH

The retention of Zn by the YM2 membrane was shown to be negligible (Table 1) in the pH range 4.0–7.6, where the retention coefficient, R_{Zn-YM2}, has an average value of 0.02. The retention coefficient estimated at pH 8.73 (0.27) indicates that an appreciable proportion of the original amount of zinc is retained by the membrane. A freely permeable solute has a retention coefficient $R = 0$ whereas for a solute that is completely impermeable $R = 1$ [10]. These observations (see Fig. 2) might be explained by considering the aqueous chemistry of zinc and postulating that the formation of hydroxy species, $Zn(OH)_n^{(2-n)+}$, which is appreciable at high pH [16] ($\beta_{Zn-OH} \approx 8$), may lead to higher molecular weight species which would be retained by the membrane.

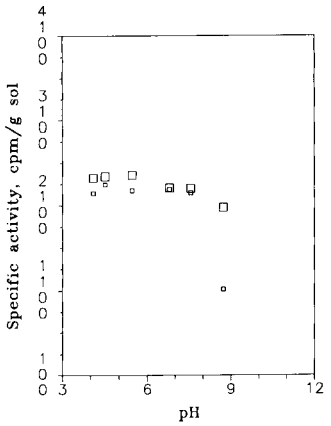

Fig. 2. Comparison of zinc activity [counts per minute (cpm)] for original solution (large squares) and filtrate (small square) as a function of pH in the absence of fulvic acid. Trace amounts of zinc were employed ($\leqslant 10^{-7}$ M) as ^{65}Zn isotope. A significant discrepancy was observed only above pH 8, where appreciable hydroxy species of zinc may form.

Comparison of ion-exchange distribution studies and ultrafiltration method

The results obtained from the two methods for identical systems were compared by resolving the overall complex formation function β_{ov}, as follows:

$$\beta_{ov} = \sum M_b / \left[(M_f \gamma \cdot 10^{z\Delta pK}) \sum A^- \right] \quad (12)$$

where ΣM_b is the sum of all forms of bound metal ion, M_f is the free metal ion which is corrected by the activity coefficient, γ, and the

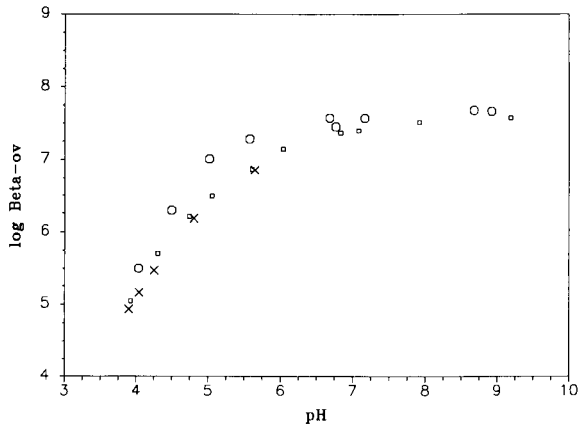

Fig. 3. Relationship between pH and logarithm of the overall complex formation function, log β_{ov}, for the zinc ion–fulvic acid system studied by the ion-exchange distribution and ultrafiltration methods. □ = Ion exchange, FA = 6.2×10^{-4} M; ○ = ion exchange, FA = 1.2×10^{-3} M; × = ultrafiltration, FA = 6.2×10^{-4} M.

counter-ion concentration correction term, ΔpK, and ΣA^- is the deprotonated form of the FA molecule which is obtainable from the potentiometric titration of the metal-free FA system. The perturbation to the potentiometric behaviour of the FA–metal ion system is considered to be negligible because of the trace amounts of metal ion employed.

The overall complex formation function, β_{ov}, which was observed to be dependent on pH (Fig. 3), showed no discrepancies between the ultrafiltration and ion-exchange distribution methods. Because of the increase in the retention of free zinc by the YM2 membrane with increase in pH (Table 1), the ultrafiltration experiments were performed in the pH range 4–6. The similarity of results in this pH range for the same FA concentration suggests that the two methods are measuring the same kind of reactions. In this pH range, the calculated β_{ov} was positively dependent on pH. The relationship between pH and log β_{ov} (as obtained by linear regression) may be expressed as follows:

$$\log \beta_{ov} = 0.90 + 1.11\text{pH} \qquad (13)$$

Above pH 7.0, a constant β_{ov} of $10^{7.5}$ was obtained. This value, which compares favourably with that in other studies of zinc–fulvate interactions [17–22], is insensitive to FA concentration changes. The usefulness of β_{ov} is limited to its provision to facilitate a quantitative estimation of the role of humic substances (fulvic acid) in the ternary system of metal ion–humic substances–geological oxide both kinetically and at equilibrium [23].

Incorporation of heterogeneous sites

In this exercise, it was the objective not only to fit experimental data (by changing the constants until a perfect fit is obtained), but also to justify

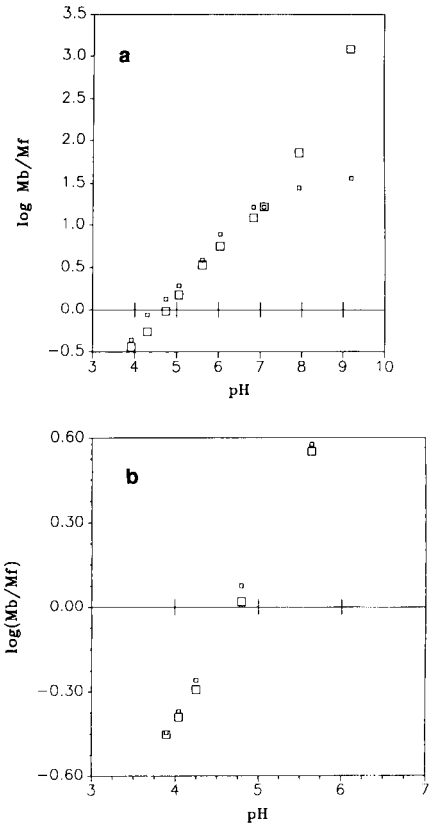

Fig. 4. (a) Comparison of model-calculated (large squares) and experimentally determined (small squares) $\Sigma M_b/M_f$ for the ion-exchange distribution studies as a function of pH. The model follows the zinc binding pattern well in the pH range 4–7. (b) Comparison of model-calculated (large squares) and experimentally determined (small squares) $\Sigma M_b/M_f$ for the ultrafiltration method. FA = 6.2×10^{-4} M, Zn $\leq 10^{-7}$ M and I = 0.100 M $NaClO_4$ in both instances.

the assignment of functionality to the predominant acid sites in the fulvic acid molecule. Typical results (Figs. 4a and b) attest to the suitability of the proposed model for predicting zinc binding by the fulvic acid. In the ion-exchange distribution method, the model calculated $\Sigma M_b/M_f$ followed the experimentally determined value in the pH range 3.8–ca. 7.0. Above pH 7.0, the model calculated value was significantly higher. The reason for this discrepancy, although not completely understood, could be attributed to a combination of the role played by the hydroxy species of zinc, the possible interference of the ion exchanger [11] and an error in the values of K_{exc2} and β_4 employed in the calculations (Table 2). In the ultrafiltration experiments, which were performed in the pH range 4–6, good agreement between model calculated and experimentally determined $\Sigma M_b/M_f$ values was obtained.

The over-estimation of $\Sigma M_b/M_f$ values calculated on the basis of the model at higher pH values might be attributed to the functionality-inspired constants employed. Notwithstanding these shortcomings, it has been shown that the combination of the assigned functional groups in the FA molecule and literature-based constants has permitted an adequate description of zinc binding by the fulvic acid molecule under acidic conditions.

Conclusions

The binding of zinc by an aquatic fulvic acid studied by two different methods yielded similar results. The overall complex formation constant, which was a function of pH, was found to be similar to results obtained by other researchers [17–22]. The description of the binding pattern by incorporating the various functionality sites reveal that the assigned functional groups of the fulvic acid are reasonable and that the zinc ion is appreciably bound to the sites where an OH is adjacent to another OH group and that site where an OH is adjacent to a C=O group. This result corroborates earlier observations [11].

Financial support from the Swedish Natural Science Research Council is gratefully acknowledged.

REFERENCES

1 F.J. Stevenson, Humus Chemistry: Genesis, Composition, Reactions, Wiley-Interscience, New York, 1982, pp. 221–243.
2 M. Schnitzer and S.V. Khan, Humic Substances in the Environment, Dekker, New York, 1972.
3 J. Ephraim, S. Alegret, A. Mathuthu, M. Bicking, R.L. Malcolm and J.A,. Marinsky, Environ. Sci. Technol., 20 (1986) 354.
4 E. Tipping, M.M. Reddy and M.A. Hurley, Environ. Sci. Technol., 24 (1990) 1700.
5 J. Ephraim and J.A. Marinsky, Environ. Sci. Technol., 20 (1986) 367.
6 C. Pettersson, I. Arsenie, J.H. Ephraim, H. Borén and B. Allard, Sci. Total Environ., 81/82 (1989) 287.
7 J.H. Ephraim, H. Borén, I. Arsenic, C. Pettersson and B. Allard, Sci. Total Environ., 81/82 (1989) 615.
8 J.H. Ephraim, H. Borén, C. Pettersson, I. Arsenie and B. Allard, Sci. Technol., 23 (1989) 356.
9 J.H. Ephraim, PhD Thesis, State University of New York at Buffalo, Buffalo, NY, 1985.
10 J.H. Ephraim and J. A. Marinsky, Anal. Chim. Acta, 232 (1990) 171.
11 J.H. Ephraim, J.A. Marinsky and S.J. Cramer, Talanta, 36 (1989) 437.
12 J. Schubert, J. Phys. Colloid Chem., 52 (1948) 340.
13 J.H. Ephraim, M.M. Reddy and J.A. Marinsky, Lec. Notes Earth Sci., 33 (1991) 263.
14 A.E. Martell and R.M. Smith, Critical Stability Constants, Vol. 3: Other Organic Ligands, Plenum, New York, 1977.
15 J. Kielland, J. Am. Chem. Soc., 59 (1937) 1675.
16 E. Högfeldt, Stability Constants of Metal-Ion Complexes. Part A: Inorganic Ligands (IUPAC Chemical Data Series, No. 21), Pergamon, Oxford, 1983.
17 K. Matsuda and S. Ito, Soil Sci. Plant Nutr. (Tokyo), 16 (1970) 1.
18 D.L. Deb, C.B.S. Kohli and O.P. Joshi, Fert. Technol., 13 (1976) 25.
19 M. Adhikari and G.C. Hazra, J. Indian Chem. Soc., 49 (1972) 947.
20 M. Schnitzer and S.I.M. Skinner, Soil Sci., 102 (1966) 361.
21 F.I. Himes and S.A. Barber, Soil Sci. Soc. Am. Proc., 21 (1957) 368.
22 J. Buffle and C. Staub, Anal. Chem., 56 (1984) 2837.
23 H. Xu, J. Ephraim, A. Ledin and B. Allard, Sci. Total Environ., 81/82 (1989) 653.

Analytica Chimica Acta, 267 (1992) 47–54
Elsevier Science Publishers B.V., Amsterdam

Solubility and fractionation of humic acid; effect of pH and ionic medium

H. Kipton J. Powell and Raewyn M. Town

Department of Chemistry, University of Canterbury, Christchurch (New Zealand)

(Received 23rd January 1992; revised manuscript received 13th April 1992)

Abstract

Gel permeation chromatography (GPC), in conjunction with equilibrium dialysis, was used to probe the fractionation of humic substances on dissolution in several media (KNO_3, $Na_4P_2O_7$, and synthetic sea water) as a function of pH and ionic strength. The solubility of humic acid (and the proportion of "large" molecules in solution) increased with increase in pH and decreased with increase in ionic strength. A pH of at least 8.0 was required to solubilize a "representative" fraction of a humic acid sample (based on GPC). Pyrophosphate (0.001 mol l^{-1}, pH 9) is proposed as a suitable solvent for the extraction of humic acid from soil.

Keywords: Gel permeation chromatography; Equilibrium dialysis; Fulvic acids; Humic acids; Waters; Soils

Humic substances are complex, heterogeneous molecules which are operationally defined on the basis of solubility: fulvic acid is completely soluble in aqueous solution whereas humic acid is "soluble" in alkali but precipitates in acid solutions. This operational division between fulvic and humic acid is not precise; for each there will be a solubility spectrum, arising from differences in molecular size and weight, and distributions of functional groups.

Extraction protocols for soil humic substances exploit their solubility characteristics; aqueous alkali (0.1–0.5 mol l^{-1} NaOH) is the most widely used extractant. However, NaOH may cause considerable alteration of the humic substances (e.g., oxidation and condensation reactions [1]); in addition, non-humic material may be extracted [1–3]. Neutral or alkaline pyrophosphate solutions have also been used as extractants for soil humic substances [4–7]. This extractant is milder and more selective than NaOH.

In an earlier paper [8] a gel permeation chromatographic (GPC) technique was described which, by use of a 0.001 mol l^{-1} spike of $Na_4P_2O_7$ in sodium tetraborate eluent, eliminated the adsorption of humic substances on Sephadex gel and achieved separations apparently based solely on molecular size differences. In this work this technique, in conjunction with equilibrium dialysis, was applied to examine the solubility and fractionation of humic acid molecules as a function of pH and ionic medium (0.10 and 0.60 mol l^{-1} KNO_3, 0.1 mol l^{-1} $Na_4P_2O_7$ and synthetic sea water). The fractional dissolution of humic substances as a function of pH has not previously been reported in detail.

A knowledge of the solubility characteristics of the molecular size fractions of humic acid is important for understanding the behaviour of, and relationship between, humic substances in soils and natural waters and for the establishment of extraction protocols.

Correspondence to: R.M. Town, Département de Chimie Analytique, Université de Genève, Sciences II, 30 Quai E.-Ansermet, CH-1211 Geneva 4 (Switzerland).

EXPERIMENTAL

Electrolyte solutions

KOH (BDH, AnalaR) solutions were prepared in carbonate-free water purified with a Milli-Q system (Millipore). Concentrated nitric acid (BDH, AnalaR) was diluted as required. Pyrophosphate solutions were prepared from $Na_4P_2O_7 \cdot 10H_2O$ (Riedel-de Haën, für Analyse). Acetate buffer (5×10^{-3} mol l^{-1}; pH 4.8) was prepared from BDH AnalaR reagents.

Synthetic sea water was prepared by dissolution of the appropriate amounts of BDH AnalaR salts in Milli-Q purified water to give the composition: chloride 0.535, sodium 0.459, magnesium 0.0523, sulphate 0.0276, calcium 0.01 and potassium 0.0097 mol l^{-1}.

Humic substances

Humic acid (HA) was the International Humic Substances Society (IHSS) reference Summit Hill humic acid. The ash content was 1.15%. Analysis by inductively coupled plasma mass spectrometry (ICP-MS) established trace impurities of Al (209 μg g^{-1}) and Fe (203 μg g^{-1}). The filtered solution (0.025 μm filter) used for dialysis was 0.2 mg ml^{-1} HA in acetate buffer.

Fulvic acid was the sample FA4, extracted from IHSS peat by the acid–pyrophosphate–XAD-7 method [5]. The ash content was 0.2%. Analysis by ICP-MS established trace impurities of Al (107 μg g^{-1}) and Fe (575 μg g^{-1}). The solution used for dialysis was 0.5 mg ml^{-1} FA in acetate buffer.

Gel permeation chromatography (GPC)

Details of the GPC apparatus have been published elsewhere [8]. The void volume of the column (V_o = 10 ml) was determined using Dextran Blue 2000; V_t was 41 ml.

Measurement of pH

The pH was measured with a combination glass–calomel electrode at 25°C in a nitrogen atmosphere. The electrode was calibrated with NBS buffers, viz., 0.05 molal potassium hydrogenphthalate (pH_{NBS} = 4.006), 0.025 molal disodium hydrogen-ortho-phosphate–0.025 molal potassium dihydrogenphosphate (pH_{NBS} = 6.863) and 0.01 molal sodium tetraborate decahydrate (pH_{NBS} = 9.180).

Solubility and fractionation of humic acid as a function of pH

HA (20 mg) was placed in a titration cell containing the pH electrode and 20 ml of electrolyte solution were added. Equilibrium was assumed when the pH remained constant for at least 30 min; the pH was then raised by addition of KOH (or lowered by addition of HNO_3). At selected pH values a small sample was removed (ca. 1 ml) and filtered (0.025 μm filter). The molecular size distribution for the dissolved fraction at each pH was determined by GPC; the area under the elution profile was taken as a measure of the amount of HA in solution.

Equilibrium dialysis

Dialysis tubing with molecular weight cut-offs (MWCOs) of 3500, 12000 and 30000 was used. It was cleaned by boiling in 2% sodium hydrogencarbonate in 10^{-2} mol l^{-1} Na_2EDTA for 10 min, followed by rinsing, then boiling in Milli-Q purified water. Clean tubing was stored in Milli-Q purified water at 6°C.

Experiments were performed in acid-washed Perspex cells covered with Parafilm. Solutions were stirred with a Teflon-coated magnetic follower. Disposable gloves were worn during manipulation of the dialysis tubing and micropipettes with disposable tips were used to remove samples.

Humic and fulvic acid solutions were placed inside the dialysis tubing, which was sealed with acid-washed Spectrum dialysis closures. The amount of material dialyzed and its molecular size distribution were monitored as a function of pH.

For fulvic acid, 2.0 ml of FA solution inside 12000 and 30000 MWCO dialysis tubing was dialyzed against 20.0 ml of acetate buffer. The solution was stirred at this pH for 39 h, then the pH was raised to 5.5 for 24 h and subsequently to 7.3 for 24 h. A 1.0-ml sample of dialyzate was removed at each pH. For humic acid the procedure was the same except that 1.5 ml of HA

solution was inside 3500, 12000 and 30000 MWCO dialysis tubing.

RESULTS

UV absorption by inorganic ion pairs

The electrolyte solutions used in this work gave absorption peaks at V_t in the gel chromatograms. It was established that these were caused by inorganic ions, e.g., NO_3^-, or ion pairs, e.g., MgCl, CaCl or CaP_2O_7. UV absorption by such species is well documented [9,10]. For clarity these peaks have not been included in the gel chromatograms reported here.

Solubility and fractionation of humic acid as a function of pH

The solubility of HA as a function of pH in 0.10 and 0.60 mol l^{-1} KNO_3 and in 0.10 mol l^{-1} $Na_4P_2O_7$ media is summarized in Fig. 1 (arbitrary units). The corresponding molecular size fractionation is given in Figs. 2, 3 and 4; in all chromatograms the elution profiles are normalized to the same absorbance scale. It was established that successive removal of samples from a saturated HA solution at low pH did not measurably alter the molecular size distribution for samples taken from more alkaline solutions.

The proportion of larger molecular size species in solution increased with increase in pH. Further, at higher ionic strength the solubility of the larger molecules in weakly acidic solution was suppressed.

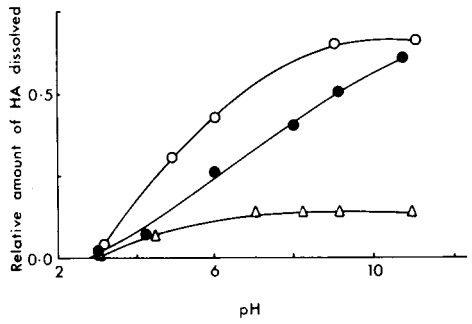

Fig. 1. Solubility of HA as a function of pH. ○ = 0.10 mol l^{-1} KNO_3; ● = 0.60 mol l^{-1} KNO_3; △ = 0.10 mol l^{-1} $Na_4P_2O_7$.

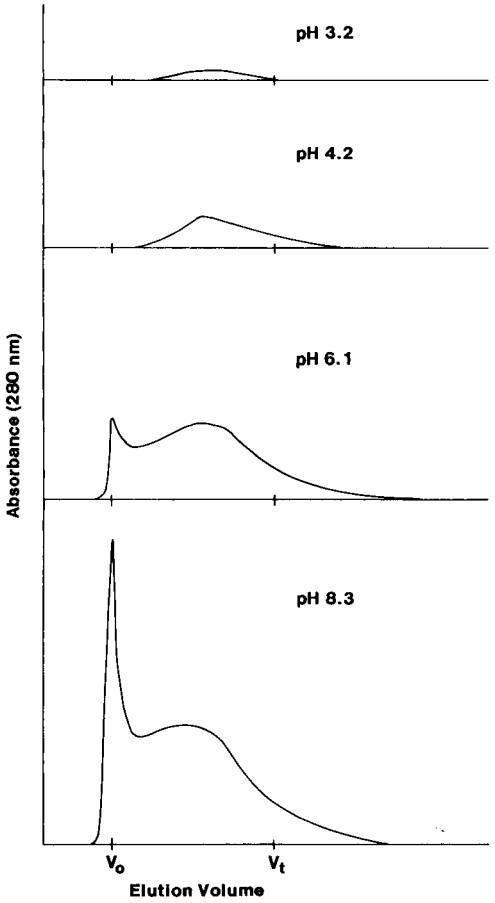

Fig. 2. Molecular size fractionation of HA in 0.10 mol l^{-1} KNO_3 at different pH values. GPC eluent: 0.01 mol l^{-1} sodium tetraborate + 0.001 mol l^{-1} $Na_4P_2O_7$; pH 9.18.

The effect of ionic strength on the solubility of HA is illustrated by the data obtained in 0.60 mol l^{-1} media (Fig. 1). The relative effect was greatest at low pH. At pH 3.0 the solubility in 0.60 mol l^{-1} KNO_3 was 60% of that in 0.10 mol l^{-1} KNO_3, and increased to 92% at pH 10.8.

The solubility of HA at pH 9.1 was also measured as a function of $Na_4P_2O_7$ concentration. The proportion of large molecules in solution increased markedly as the concentration of pyrophosphate was decreased (Fig. 5).

To test the effect of divalent ions on solubility, HA was first equilibrated in synthetic sea water (pH 8.2) that did not include Ca(II) and Mg(II); Ca(II) and Mg(II) were then added as chlorides.

The solubility of HA in this synthetic sea water (sample equilibrated for 21 h in the presence of 0.01 mol l^{-1} Ca(II) and 0.053 mol l^{-1} Mg(II)) was ca. 60% less than that in the absence of these ions. Selected molecular size distributions are shown in Fig. 6.

Equilibrium dialysis

Fulvic acid. The molecular size distribution for the dialyzate at each pH and for the final retentate was determined by GPC. In all instances a single peak was obtained. For the dialyzate at pH 4.8, the elution peak volume, V_e, was greater than that for unfractionated FA (by 4.5 and 4.0 ml for 12000 and 30000 MWCO tubing, respectively); at pH 5.5 V_e was 3.5 and 3.0 ml greater and at pH 7.3 it was 3.0 and 2.5 ml greater, respectively. V_e for the final retentates was the same as that for an unfractionated sample.

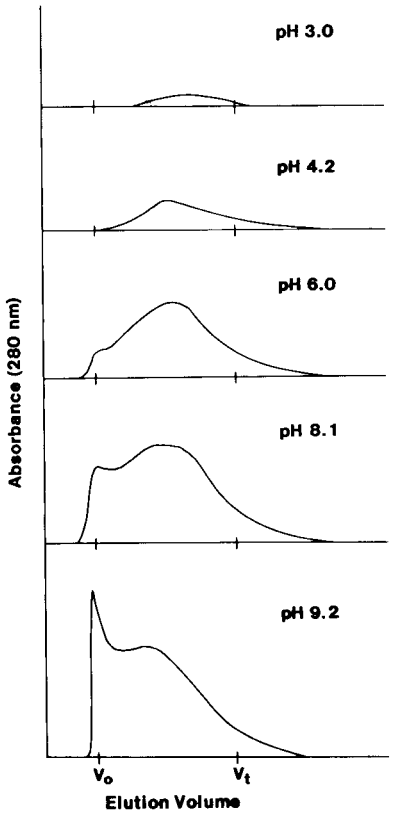

Fig. 3. Molecular size fractionation of HA in 0.60 mol l^{-1} KNO_3 at different pH values. GPC eluent: 0.01 mol l^{-1} sodium tetraborate + 0.001 mol l^{-1} $Na_4P_2O_7$; pH 9.18.

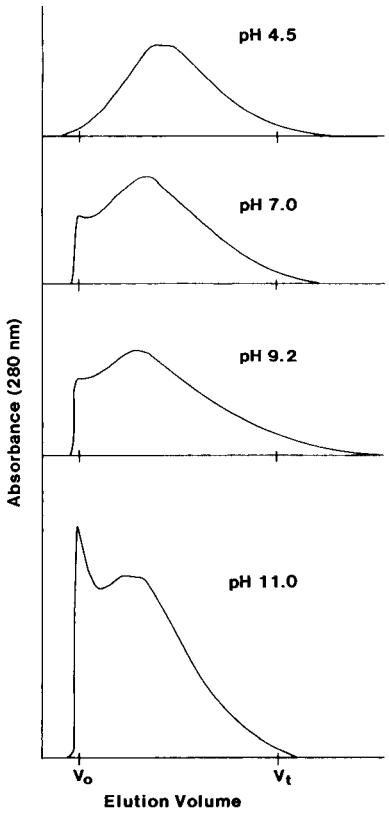

Fig. 4. Molecular size fractionation of HA in 0.10 mol l^{-1} $Na_4P_2O_7$ at different pH values. GPC eluent: 0.01 mol l^{-1} sodium tetraborate + 0.001 mol l^{-1} $Na_4P_2O_7$; pH 9.18.

To calculate the percentage of FA dialyzed, the area under the GPC elution profile was compared with that for a sample of FA after sample dilution by the external solution. For 12000 MWCO tubing the percentage of FA dialyzed at pH 4.8, 5.5 and 7.3 was 17, 22 and 34% respectively; for 30000 MWCO the values were 26, 35 and 54%, respectively.

Humic acid. At pH 4.8 no detectable amount of HA had passed through any of the dialysis membranes. At pH 5.5 no measurable amount of HA had passed through the 3500 MWCO tubing, some smaller molecules had passed through the 12000 MWCO tubing and both "large" ($V_e = V_o$) and "small" [$V_e = (V_o + V_t)/2$] molecules were detected in solution outside the 30000 MWCO

tubing. At pH 7.3 all dialysis solutions contained both large and small molecules.

The percentage of HA dialyzed at pH 5.5 and 7.3 for the 3500 MWCO tubing was 0 and 11%, for 12000 MWCO tubing 32 and 24% and for 30000 MWCO tubing 43 and 34%, respectively.

For the final retentate solutions (pH 7.3), the GPC peak which corresponded to the smaller molecules was displaced to smaller V_e relative to unfractionated HA (by 3.0, 2.0 and 0.5 ml for 30000, 12000 and 3500 MWCO tubing, respectively).

DISCUSSION

Solubility and fractionation of humic acid as a function of pH

In contrast to earlier studies, this work has examined the "soluble" humic fraction (i.e., that which is not retained by a 0.025-μm filter).

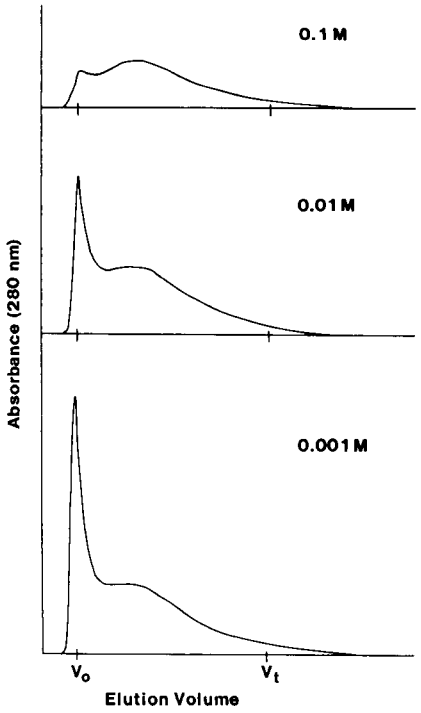

Fig. 5. Molecular size distributions for HA as a function of $Na_4P_2O_7$ concentration at pH 9.1. GPC eluent: 0.01 mol l^{-1} sodium tetraborate + 0.001 mol l^{-1} $Na_4P_2O_7$; pH 9.18.

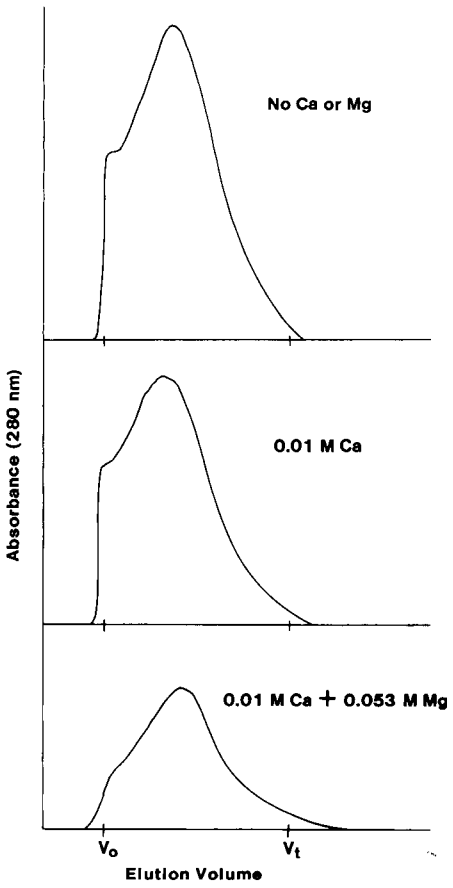

Fig. 6. Molecular size fractionation of HA in synthetic sea water; pH 8.2.

KNO_3

The solubility of HA increased with increasing pH and decreased with increased ionic strength (Fig. 1). GPC established that predominantly small molecular size humic species are soluble in weakly acidic aqueous solution. The proportion of soluble larger molecular size components increased up to pH 8.0, and decreased as the ionic strength was increased (Figs. 2 and 3). The former may indicate a greater contribution from phenolic groups to the acidity of the larger molecules.

The observed molecular size fractionation with pH is consistent with the larger HA molecules containing a lower average density of carboxyl groups than do the smaller molecules. The ratio

of "large" to "small" molecules in solution (based on peak areas) was constant above ca. pH 8.0 (not shown).

Following exposure to alkaline conditions, acidification of the HA solution indicated that re-equilibration of the molecular size fractions between the solid and aqueous "dissolved" phases was a slow process (ca. 8 h at pH 3.0).

Pyrophosphate

The solubility and molecular size fractionation of humic acid in 0.10, 0.01 and 0.001 mol l^{-1} $Na_4P_2O_7$ was studied (Figs. 4 and 5). It is noted that the humic acid sample used had been alkali extracted and purified, hence the results may not be representative of the processes that would occur on extracting soils with pyrophosphate solutions.

HA was less soluble in 0.10 mol l^{-1} $Na_4P_2O_7$ (ionic strength 1.0 mol l^{-1}) than in 0.6 mol l^{-1} KNO_3. This could arise from ionic strength effects alone; owing to their polyelectrolytic character, the solubility of humic acids is strongly influenced by electrolyte concentration. It was observed that the HA solubility increased in more dilute $Na_4P_2O_7$ solution (Fig. 5); further, the proportion of large molecular size moieties in solution increased significantly. Spiking a filtered (0.025-μm) HA solution to 0.001 mol l^{-1} $Na_4P_2O_7$ caused no apparent change in the molecular size distribution of the sample. This suggests that pyrophosphate does not promote aggregation (or disaggregation) of dissolved species.

Pyrophosphate has an affinity for Al(III) and Fe(III); hence these results may indicate that these metal ions are preferentially associated with the larger humic molecules. This is consistent with ion selective electrode potentiometric studies on the binding of Cu(II) to different molecular size fractions of humic acid [11].

Synthetic sea water

Although the natural concentration of humic substances in sea water is very low (ca. 1 mg l^{-1}), they may play an important role in buffering metal ion concentrations [12].

The solubility of HA in sea water [excluding Ca(II) and Mg(II)] was ca. 30% less than that in 0.60 mol l^{-1} KNO_3. This difference was unexpected because these solutions are of similar ionic strength. The cause of this phenomenon is not known.

In the presence of Ca(II) and Mg(II) the solubility of HA was decreased by 60%. This could be due to the increased ionic strength of the solution and/or the formation of insoluble Ca(II) and Mg(II)–humate complexes [13].

Equilibrium dialysis of humic substances

This technique was used to provide additional information on the solubility and possible dynamics of humic acid aggregation.

Fulvic acid. At pH 7.3 only 54% of FA was dialyzed through a 30000 MWCO membrane. This was surprising given that recent estimates for the molecular weight of fulvic acid are typically 1000–2000 dalton [14–17]. This highlights the fact that dialysis (like GPC) provides an estimate of the hydrodynamic size of molecules and not their weight.

The percentage of FA dialyzed decreased with decreasing pH. By definition, fulvic acid is completely soluble in aqueous solution at any pH. Therefore, this observation suggests that the hydrodynamic size of the fulvic moieties must be increasing.

Other studies on the effect of pH on the molecular size of fulvic acid molecules have reported contradictory results. Chen and Schnitzer [18,19] reported observations consistent with the present work (by use of electron microscopy, UV spectrophotometry and viscometry). In contrast, other workers [20,21] observed a decrease in the molecular weight and size of both aquatic and soil-derived fulvic acid with decreasing pH (by use of dialysis, Sephadex gel filtration, ultrafiltration and UV spectroscopy).

It is probable that many factors have an impact on the aggregation behaviour of a particular humic sample, e.g., metal content, ionic strength, sample concentration, extraction method and source of the humic material. The distribution of functional groups on individual humic molecules is probably an important determinant of solubility and aggregation behaviour. For example, deprotonation of carboxyl groups can lead to an in-

crease in hydrogen bonding interactions with unionized weak acid groups such as phenols; this may result in an increase in apparent molecular size [22,23]. On the other hand, the increase in negative charge due to deprotonation reactions disrupts hydrophobic interactions through electrostatic repulsion, causing the apparent molecular size to decrease [23].

Humic acid. At pH 7.3 only 43% of HA was dialyzed through a 30000 MWCO membrane. In contrast to fulvic acid, the percentage dialyzed decreased with increasing pH; thus the effective molecular size of the humic acid molecules increased with increased pH.

No measurable amount of HA was dialyzed at pH 4.8, indicating that the effective molecular size of dissolved humic acid molecules at this pH was greater than the pore size of the 30000 MWCO dialysis membrane. On dialysis of HA at pH 7.3, some very large molecules (which eluted at V_0 in the GPC) were observed in the dialyzate (these did not arise from leakage.) This was contrary to expectations. It is possible that humic acid exists as dynamic aggregates which are "labile", that is, the aggregates can dissociate, pass through the dialysis membrane and then reform. Such structures have been proposed to occur in fulvic acid solutions at concentrations of 0.1–1.0 mg ml^{-1} [24]. Humic acids are much more polydisperse than are fulvic acids [14,16,25,26] and it is possible that a dynamic equilibrium exists between at least a small proportion of the diverse molecules.

Alternatively, the presence of large molecules in the dialyzate may be caused by metal contamination. Despite exhaustive cleaning procedures it is very difficult to remove traces of metals from dialysis membranes [11,27]. One of these contaminants, Cu(II), is prone to forming complexes which bridge two humic molecules; this would increase the apparent molecular size [28,29].

Conclusions

Our results provide information that is useful for the development of extraction protocols for humic substances from soils. They indicate that a pH of at least 8.0 is necessary to obtain a "representative" sample of humic acid in solution. Further, an extractant of low ionic strength should favour solubilization of humic acid. Pyrophosphate (0.001 mol l^{-1}, pH 9) is potentially a suitable solvent for extracting a "representative" sample of humic acid from soil. This chemical extractant is milder than NaOH, yet has a similar extraction efficiency [6,30,31]. The oxygen uptake by humic substances in $Na_4P_2O_7$ solutions (pH 9) is only 5% of those in 0.5 mol l^{-1} NaOH [32], hence the propensity for degradative processes to occur is minimized.

The solubility of humic substances (and the molecular size distribution of the soluble components) is dependent on pH, ionic strength and the nature of the electrolyte ions. The pH-dependent molecular size fractionation of HA has implications for studies on the chemical and physical properties of humic acids [11]. In soils and natural waters it is probable that a different humic molecular size fraction dominates solution complexation of metal ions at each pH and ionic strength.

REFERENCES

1 J. Tinsley and A. Salam, Soils Fert., 14 (1961) 81.
2 G.F. Vance, S.A. Boyd and D.L. Mokma, Soil Sci., 140 (1985) 412.
3 M. Schnitzer and P. Schuppli, Soil. Sci. Soc. Am. J., 53 (1989) 1418.
4 A.U. Ramunni and F. Palmieri, Org. Geochem., 8 (1985) 241.
5 J.E. Gregor and H.K.J. Powell, J. Soil. Sci., 37 (1986) 577.
6 M. Schnitzer and P. Schuppli, Can. J. Soil Sci., 69 (1989) 253.
7 A. Piccolo, L. Campanella and B.M. Petronio, Soil Sci. Soc. Am. J., 54 (1990) 750.
8 R.M. Town and H.K.J. Powell, Anal. Chim. Acta, 256 (1992) 81.
9 P.R. Haddad and A.L. Huckenberg, Chem. Aust., 50 (1983) 275.
10 P.R. Haddad and A.L. Huckenberg, J. Chromatogr., 300 (1984) 357.
11 R.M. Town, Ph.D. Thesis, University of Canterbury, New Zealand, 1991.
12 T.M. Florence, Analyst, 111 (1986) 489.
13 E. Tipping and M. Ohnstad, Chem. Geol., 44 (1984) 349.
14 E.M. Thurman, R.L. Wershaw, R.L. Malcolm and D.J. Pinckney, Org. Geochem., 4 (1982) 27.
15 G.R. Aiken and R.L. Malcolm, Geochim. Cosmochim. Acta, 51 (1987) 2177.

16 R. Beckett, Z. Jue and J.C. Giddings, Environ. Sci. Technol., 21 (1987) 289.
17 J.A. Marinsky and M.M. Reddy, Anal. Chim. Acta, 232 (1990) 123.
18 Y. Chen and M. Schnitzer, Soil Sci. Soc. Am. J., 40 (1976) 682.
19 Y. Chen and M. Schnitzer, Soil Sci. Soc. Am. J., 40 (1976) 866.
20 H. De Haan, G. Werlemark and T. De Boer, Plant Soil, 75 (1983) 63.
21 M.T.S.D. Vasconcelos, A.P.L.M.G. Santos and A.A.S.C. Machado, Sci. Total Environ., 81/82 (1989) 489.
22 R.L. Wershaw and D.J. Pinckney, J. Res. U.S. Geol. Surv., 5 (1977) 571.
23 J.A. Leenheer, P.A. Brown and T.I. Noyes, in I.H. Suffet and P. MacCarthy (Eds.), Aquatic Humic Substances, Influence on Fate and Treatment of Pollutants, American Chemical Society, Washington, DC, 1989, p. 25.
24 G.G. Leppard, J. Buffle and R. Baudat, Water Res., 20 (1986) 185.
25 D.S. Orlov, Y.M. Ammosova, G.I. Glebova, Y.I. Gorshkova, N.P. Il'in and M.P. Kolesnikov, Sov. Soil Sci., 3 (1971) 673.
26 D.S. Orlov, Y.M. Ammosova and G.I. Glebova, Geoderma, 13 (1975) 211.
27 S.C. Apte, M.J. Gardner and D.T.E. Hunt, Environ. Technol. Lett., 10 (1989) 201.
28 L. Maggi, R. Stella and G. Ciceri, Ann. Chim. (Rome), 74 (1984) 257.
29 D.S. Orlov, O.I. Min'ko, V.V. Demin, V.G. Sal'nikov, N.B. Izmaylova and Y.Y. Milanovskiy, Sov. Soil Sci., 22 (1990) 70.
30 L.N. Aleksandrova, Sov. Soil Sci., 2 (1960) 190.
31 R.S. Beckwith and V.K. Nayyar, Commun. Soil Sci. Plant Anal., 15 (1984) 295.
32 J.M. Bremmer, J. Soil Sci., 1 (1950) 198.

Analytica Chimica Acta, 267 (1992) 55–62
Elsevier Science Publishers B.V., Amsterdam

Development of a nonisotopic acetylcholine receptor assay for the investigation of cholinergic ligands

Lu Chen, Toshifumi Takeuchi [1] and Garry A. Rechnitz

Hawaii Biosensor Laboratory, Department of Chemistry, University of Hawaii, Honolulu, HI 96822, (USA)

(Received 2nd January 1992; revised manuscript received 8th April 1992)

Abstract

A nonisotopic receptor based assay is developed which is centered upon the α-toxin-binding nicotinic acetylcholine receptor and fluorescein labeled α-bungarotoxin. The assay method is based on sequential saturation of the receptor by unlabeled and fluorophore labeled ligands, followed by separation of the free from the bound label by centrifugation. Subsequently, the free concentration is determined by use of a flow injection system. Unlabeled ligands investigated include both the agonist and antagonist types that bind to the receptor α-subunits, i.e., α-bungarotoxin, carbamylcholine, decamethonium, gallamine, *d*-tubocurarine, pancuronium, and hexamethonium. The effectiveness of the proposed method is illustrated by Scatchard analysis, Hill plot of the labeled ligand, and displacement curves for unlabeled ligands.

Keywords: Acetylcholine receptor; Cholinergic ligands

Utilization of isolated receptors in the characterization and screening of pharmacologically active substances has become an important tool in biomedical research. Radio-isotope receptor based binding assay is currently one of the most commonly used methods and has become a routine technique in drug discovery and development. Nonisotopic assay development has recently attracted great attention due to the health hazard and special disposal requirements of radio-labeled compounds [1–4]. Because of the fact that receptors exist in extremely low concentration in tissues (pmol to nmol/g protein), the labels must have good detection sensitivity, as well as high affinity and specificity for the receptor. Based on these considerations, fluorophores and enzymes have been widely accepted as nonisotopic labels for replacement of radioligands.

The α-toxin-binding nicotinic acetylcholine receptor (nAChR) is the most studied neurotransmitter receptor. It can be envisioned as an aggregation of five subunits ($\alpha_2\beta\gamma\delta$) [5]. When the two α-subunits on the receptor bind with the neurotransmitter agonist acetylcholine, or its analogs nicotine and carbamylcholine, an open channel is formed through the membrane. This results in an influx of positive charges (Na^+, K^+, and some Ca^{2+}) through the cell membrane, which causes a depolarization of the nerve fiber. Depolarization beyond a critical threshold results in an action potential. Another group of compounds binds to the same site on the receptor but blocks acetylcholine's physiological activity. Generally such compounds can be classified into two main types: depolarizing blocking drugs (agonists), e.g., decamethonium; and non-depolarizing drugs (an-

Correspondence to: G.A. Rechnitz, Hawaii Biosensor Laboratory, Department of Chemistry, Honolulu, HI 96822 (USA).
[1] Present address: Research Center for Advanced Sciences and Technology, University of Tokyo, Meguro-ku, Tokyo 153, Japan.

tagonists) such as gallamine, *d*-tubocurarine, pancuronium, and hexamethonium [6]. An important antagonist, α-bungarotoxin (α-Bgt), which binds to the acetylcholine site with a high affinity (association constant 10^8–10^{12} M), has been extensively utilized in the study of the nAChR, although it does not have any clinical use. Because of the large affinity difference compared to other ligands, sequential saturation binding assays are more suitable than equilibrium binding assays for obtaining a satisfactory dose-dependent behavior [7–9].

Generally speaking, the nAChR is convenient to prepare, and the density of binding sites is relatively high compared to other crude receptor preparations. Several techniques have been employed towards developing acetylcholine receptor based assays [2,10] and biosensors [9,11]. In this paper, we propose a fluorophore labeled receptor binding assay for the investigation of cholinergic drugs, mostly muscle relaxants, which bind to the α-subunits of the nAChR. Labeled ligand, i.e., α-bungarotoxin fluorescein isothiocyanate conjugate (α-Bgt-FITC), binds competitively with unlabeled analyte using a sequential saturation procedure. After a separation step, the free label concentration is determined via flow-injection analysis (FIA). Once corrected for nonspecific binding, the signal difference between the "total" and "free" peaks is considered to be the amount of ligand which is specifically bound by the receptor.

EXPERIMENTAL

Materials and instruments

α-Bgt, α-Bgt-FITC (1 mol FITC/mol), fluorescein, carbamylcholine, decamethonium, *d*-tubocurarine, pancuronium, and hexamethonium were purchased from Sigma. Gallamine was ordered from Aldrich. Triton X-100 was purchased from Pierce. Electric organ of *Torpedo California* was obtained from Pacific Bio-Marine Laboratory and stored at -70°C.

The homogenizer employed was a Brinkmann PTA 20 S. Centrifugations were carried out in 1.5 ml microcentrifuge tubes (Fisher Scientific) with an IET-HT centrifuge. The Shaker Bath was a GCA/Precision Scientific Co. Model 25. The FIA system consisted of a solvent pump (Solvent Delivery Module, LC-9A, Shimadzu), a pulse damper (SSI, Model LP-21), an injection valve (Rheodyne, Model 7010) equipped with a 20 μl sample loop, a fluorescence detector (Jasco, Model 821-FP), and a chromato-integrator (Hitachi, Model D-2500).

Preparation of the nAChR

All the nAChR preparation steps were performed at 4°C, following the procedure of Hallowell and Rechnitz [2], with some modifications. First, 30 g of *Torpedo* electric organ was chopped with a knife into small pieces at 4°C and put into 45 ml of *Torpedo* buffer (154 mM NaCl, 50 mM Tris, 5 mM Na_2HPO_4, and 1 mM EDTA, pH 7.4). The mixture was homogenized 4×15 s at speed "2" setting, allowed to stand for 1 min in between each interval. The homogenate was then centrifuged at 7000 rpm (5900 *g*) for 10 min and filtered through four layers of cheese cloth. Saving the supernatant at 4°C, the remaining pellet was again homogenized, centrifuged and filtered as described above. The combined supernatant was finally centrifuged at 15000 rpm (27000 *g*) for 90 min. Pellets were suspended at a ratio of 0.5 g/ml *Torpedo* buffer, resulting in an average protein concentration of 8 mg/ml. The protein assay was based on the Bradford dye-binding procedure using the Bio-Rad Protein Assay Dye Reagent Concentrate. From Scatchard analysis, the calculated α-binding site concentration of this preparation method was approximately 40 nmol/g protein (see Results and Discussion section). The nAChR preparation was distributed into several small vials and stored at -70°C, with the receptor α-binding sites remaining active for at least one month.

Fluorescence detection

Fluorescence intensities were detected through an FIA system, which is similar to the instrumentation of another fluorophore labeled ligand receptor-based assay reported from our lab. [4]. The excitation wavelength for the detection of fluorescent signal was 490 nm, and emission wavelength was 525 nm. Signals were detected at

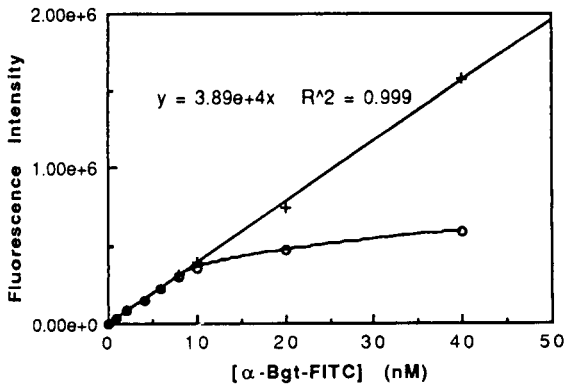

Fig. 1. Self-quenching of α-Bgt-FITC buffer solution (50 mM phosphate plus 0.1% Triton X-100, pH 7.0). (○) direct injection of α-Bgt-FITC solution; (+) α-Bgt-FITC was first diluted 10 fold before injection at concentrations above 5 nM. This is also the calibration curve for fluorescence intensity versus [α-Bgt-FITC].

emission wavelength. The eluant employed was 50 mM phosphate buffer (pH 7.0).

The plot of fluorescence intensity versus [α-Bgt-FITC] showed a serious negative departure from linearity at high concentrations (Fig. 1). This nonlinearity may arise from three factors: the inner filter effect, self-absorption, and self-quenching. Assuming that the path length of the fluorometer used is 1 mm, the molar extinction of FITC is 80000 cm^{-1} M^{-1}, and the concentration of α-Bgt-FITC is 40 nM, thus $A = \epsilon bc < 0.01$, which excludes the possibility of the inner filter effect. Self-absorption should not be significant because of the small overlaps between the emission and excitation spectrum. Therefore, self-quenching must be responsible for the observed nonlinearity. The strategy for overcoming this problem, when the concentration of α-Bgt-FITC above 10 nM, was to dilute the sample 10 fold before injection. The true fluorescence intensity of the sample was then calculated by multiplying the signal obtained by 10. Of course it is desirable to avoid α-Bgt-FITC concentrations higher than 10 nM in order to keep the procedure as simple as possible. All fluorophore peaks in the other studies were converted to their corresponding fluorophore label concentrations utilizing the calibration curve shown in Figure 1.

Assay procedures

The nAChR was resuspended and diluted 40 times with phosphate buffer (PB, 50 mM, pH 7.0) each time immediately before use. Commercial α-Bgt-FITC solid was dissolved in PB to make a 1×10^{-4} M stock solution. 0.1% Triton X-100 was added to prevent α-Bgt-FITC adsorption onto the walls of the vessel. The same buffer (with 0.1% Triton X-100) was also used in the preparation of all the subsequent assay samples.

Due to the presence of a significant amount of nonspecific ligand binding with the crude preparation of nAChR, two parallel sets of samples were run to generate a saturation curve. The first set of the samples was run to determine the nonspecific binding. These samples were prepared by first incubating 50 μl of the nAChR preparation with 50 μl of carbamylcholine (final concentration 0.1 M) for 30 min, then incubating with the appropriate concentration of α-Bgt-FITC (0.5–20 nM) for 2 h, PB (with 0.1% Triton X-100) was added to make the total volume 500 μl. All incubations were conducted in 1.5 ml microcentrifuge tubes with constant shaking at 4°C. After centrifugation, the supernatant was injected to determine the fluorescent signal. This signal we defined as the "total" signal for each respective sample, and is dependent upon both the α-Bgt-FITC and the receptor concentration. Carbamylcholine was chosen as a specific displacer occupying all the α-binding sites during the two incubation steps [12]. Thus the added α-Bgt-FITC could only bind nonspecifically to the crude membrane preparation.

The second set of the samples was run to determine the specific binding. It was performed by incubating the nAChR preparation with appropriate concentration of α-Bgt-FITC alone for the same period of time (2 h). Fluorescence was determined as described above after centrifugation. In this case, α-Bgt-FITC binds both specifically and nonspecifically with the receptor preparation, and signals yielded were defined as "free". The difference between "total" and "free" was defined as specifically "bound" signal.

For displacement studies, the drugs analyzed were incubated with the nAChR for 2 h, followed by the addition of α-Bgt-FITC and incubation for

1 h with constant shaking. In the first incubation step, the drug concentrations were significantly lower than the carbamylcholine concentration used to generate the saturation curve, thus, longer incubation time, 2 h, was needed to reach equilibrium. The second incubation step was set at 1 h which meant that the system did not reach equilibrium. A short incubation time (less that needed for equilibrium) was used to minimize the dissociation of the unlabeled ligand–receptor complex [13].

Centrifugation has the advantage that the ligand remains bound during the separation step [12]. This is in contrast to the filtration method which is more suitable for K_d values less than 10^{-8} M, owing to the risk of bound ligand dissociating during the separation step. Since most of the unlabeled cholinergic ligands we studied have K_d values greater than 10^{-7} M, centrifugation is a more suitable technique. High centrifuge speeds are desirable due to better separation and less entrapment of free ligand by the pellet. We centrifuged the samples at 15000 rpm (27000 g), which was determined not establishing a concentration gradient of α-Bgt-FITC in the centrifuge tube.

RESULTS AND DISCUSSION

Characterization of reagent concentrations

It is well known that many biological substances are fluorescent. Because the nAChR has not been completely purified, the receptor preparation contains numerous such components. The centrifugation following the assay incubation step removed nearly all of the nAChR from the sample solution; however, the lower density components of the biological matrix were found to remain in the supernatant. These components yielded an unacceptable background signal when the nAChR concentration was above 2 nM (background signal/bound signal > 15%) (Fig. 2). Furthermore, nonspecific binding increased linearly with the amount of nAChR, while specific binding also increased but at a lower rate which supposedly exhibited a saturable behavior. Thus, after subtracting the blank signals of the biological matrix, the "total" and "free" fluorescent intensities both decreased but at significantly different rates. The combination of all these factors produced a nAChR binding curve that appears unusual in that a maximum occurs in the bound signal. A receptor concentration of 0.8 nM (1.6 nM α-binding sites), which gives the maximum bound signal, was chosen for all studies.

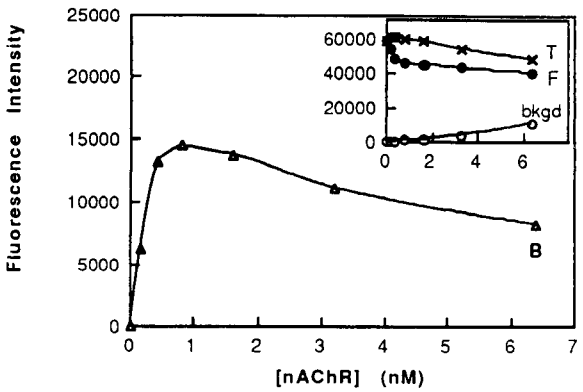

Fig. 2. Optimization of the nAChR concentration. [α-Bgt-FITC] = 2 nM. (×) total signal, T (background corrected); (●) free signal, F (background corrected); (○) background signal, bkgd (from biological matrix); (△) bound fluorescence intensity, B (obtained by subtracting "free" from corresponding "total").

Figure 3 illustrates a study to quantify the amount of nonspecific binding, utilizing the experimental procedure of displacement studies at

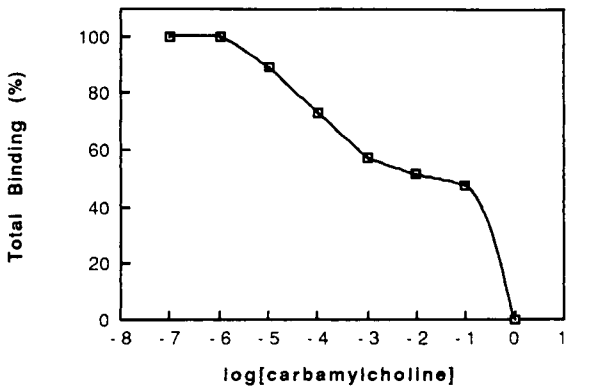

Fig. 3. Study of the amount of nonspecific binding. Total binding (%) = [(specific + nonspecific) binding]/[maximum binding (specific + nonspecific)]. [nAChR] = 0.8 nM, [α-Bgt-FITC] = 2 nM.

a receptor concentration of 0.8 nM. The displacement curve shows three different regions. Between the concentration of 10^{-6} M to 10^{-3} M, carbamylcholine displaced the specific binding sites. At carbamylcholine concentrations between 10^{-3} M to 0.1 M, there is a plateau where no significant additional α-Bgt-FITC is displaced from the receptor preparation. However, at concentrations greater than 0.1 M, α-Bgt-FITC is displaced from the nonspecific sites. Therefore, the amount of nonspecific binding of α-Bgt-FITC can be considered as the bound at a carbamylcholine concentration of 0.1 M, which is 45% of the overall binding (specific plus nonspecific). In addition, 0.1 M carbamylcholine proved to be an appropriate concentration for determining the "total" signal, because this is the concentration at which all the specific binding sites are occupied by carbamylcholine.

Saturation curve and Scatchard analysis

The Scatchard plot, which is one of the diagnostic relationships for a binding assay system, has the form

$$[L^*R]/[L^*] = -[L^*R]/K_d^* + [L^*R]_{max}/[K_d^*]$$

where R stands for receptor, $[L^*]$ = free labeled ligand concentration, $[L^*R]$ = receptor bound labeled ligand concentration, $[L^*R]_{max}$ = maximum receptor binding sites for labeled ligand = B_{max}, and K_d^* = dissociation constant of the labeled ligand for receptor [14]. Figure 4 shows a typical saturation curve for α-Bgt-FITC and the corresponding Scatchard plot. The slope of the Scatchard plot yields a value of 4 nM for the dissociation constant of α-Bgt-FITC, and the *X*-intercept along with the slope give a maximum number of binding sites under the given experimental conditions, which is 80 nmol/g protein or 1.6 nmol/l of the assay solution (the protein concentration was determined to be 8 mg/ml). Assuming each nAChR has two α-Bgt-FITC binding sites (one binding site per α-subunit), the concentration of the nAChR is calculated to be 40 nmol/g protein or 0.8 nM. Since the average molecular weight of the nAChR is 256000 g/mol, 1% (w/w) of protein is active receptor.

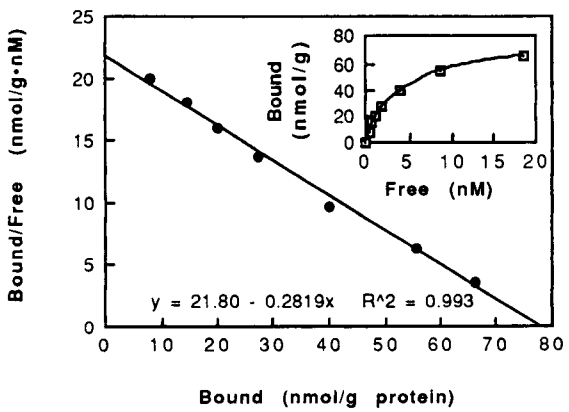

Fig. 4. Scatchard analysis for binding of α-Bgt-FITC to the nAChR. [nAChR] = 0.8 nM. Small (inset), saturation curve, obtained by varying the amount of α-Bgt-FITC in the assay samples; large, Scatchard plot.

In order to get a reliable Scatchard transformation of saturation data, ideally the assay should cover the range of 10–90% saturation of the receptor binding sites [12]. This range of saturation is most easily obtained when the receptor binding site concentration is equal to K_d^*, and the labeled ligand concentration ranges from about 0.1 to 10 times K_d^*. Yet a concentration of 0.8 nM nAChR was chosen for our assay instead of the suggested 4 nM (K_d^*) for the reasons discussed previously. The α-Bgt-FITC concentration covered the range of 1 nM to 40 nM, which was 0.25–10 times K_d^*, and as a result, the bound labeled ligand ranged from 10% to 86% of B_{max}. Therefore, since almost the whole saturation range is covered, the Scatchard transformation is not comprised.

In order to quantitate the homogeneity of binding sites, the Hill plot

$$\log [\text{Bound}\%/(1 - \text{Bound}\%)] = \text{Hill coefficient} \times \log[L^*] + C$$

is often employed [14]. In this equation, Bound% = specifically bound/B_{max}. Figure 5 shows that the Hill coefficient = slope = 1.02. A Hill coefficient that approximately equals one, along with the good linearity of Scatchard plot, indicate homogeneous binding of α-Bgt-FITC to the receptor preparation. As to this point, there has been

some controversy about the binding of α-Bgt to the nAChR, which was reported to be either monophasic [8,15] or multiphasic [16]. More recently, Conti-Tronconi et al. [17] observed that α-Bgt binds to the two sites with very different affinities when the receptor is associated with its native membrane. But if the assay is carried out with detergent-solubilized nAChR or with nAChR-rich membranes isolated by using protocols in which proteases were not inhibited, the two α-Bgt sites will have very similar binding properties. The latter observation explains why the Hill coefficient is unity in our work.

Kinetic study of temperature effects

A kinetic study was conducted at 4°C and it was found that the assay samples took about 1 h to achieve 90% of B_{max} and 2 h to reach maximum binding (Fig. 6). Therefore, for Scatchard analysis and characterization of the reagent concentrations, 2 h was chosen as the incubation time in order to reach equilibrium. An incubation time of 1 h was employed in the displacement analysis because this minimizes the amount of dissociation of receptor bound analytes and yet allows for 90% of the available receptor sites to bind α-Bgt-FITC.

Hoping that increased temperature might speed up the assay time, samples were incubated at higher temperatures. At 25°C and 37°C, less incubation time (1 h) is required to reach equilibrium; nevertheless, temperature does not show a dramatic influence on the binding rates. It can also be concluded that careful control of temperature is not critical for obtaining good results with this assay. All other assay sample incubations were fixed at 4°C.

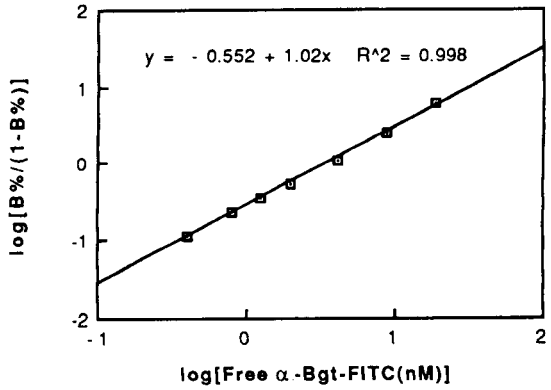

Fig. 5. Hill plot for the study of homogeneity of α-Bgt-FITC binding with the nAChR. Same conditions as Fig. 4. *B%* = specifically bound/maximum specifically bound.

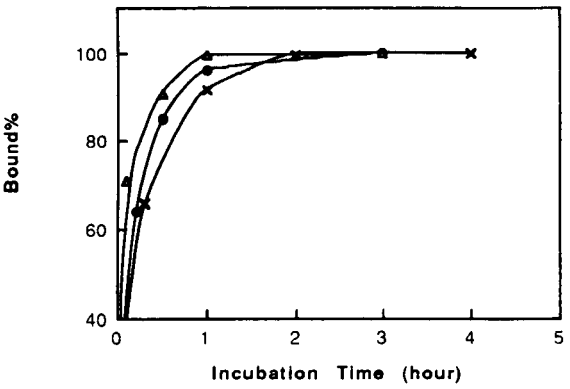

Fig. 6. Kinetic study of temperature effects for α-Bgt-FITC and receptor binding. [nAChR] = 0.8 nM. [α-Bgt-FITC] = 5 nM. Bound% = bound/maximum bound under given conditions. Assay samples were incubated at indicated temperatures. (×) 4°C; (●) 25°C; (△) 37°C.

Dose response curves of agonists and antagonists

The specific binding of α-Bgt-FITC to the nAChR was inhibited by agonists and antagonists (Fig. 7). The concentration of labeled ligand and receptor (binding sites) were chosen at 2 nM and 1.6 nM, respectively, giving a ratio of [L*]/[R] = 1.3. Table 1 lists the apparent dissociation constants K_d of analytes which are calculated from the equation

$$K_d = IC_{50}/[1 + (L^*/K_d^*)]$$

where IC_{50} = concentration of unlabeled ligand that inhibits 50% of the specific binding of labeled ligand, L* = free labeled ligand concentration (2 nM), and K_d^* = dissociation constant of α-Bgt-FITC (4 nM) [14]. Reproducibility with the same batch of the nAChR preparation proved to be quite good, showing no more than 9% error for the 95% confidence interval (Fig. 8).

The apparent dissociation constant values obtained from this method are comparable to most

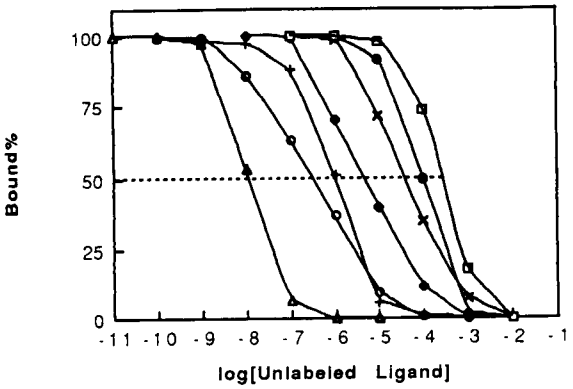

Fig. 7. Dose response curves for some agonists and antagonists to the α-subunits of the nAChR. 4°C, [nAChR] = 0.8 nM, [α-Bgt-FITC] = 2 nM. Bound% (specific binding) = bound/maximum bound (obtained from the assay samples when no displacers were introduced). (△) α-Bgt; (○) pancuronium; (+) *d*-tubocurarine; (◆) gallamine; (×) carbamylcholine; (●) decamethonium; (□) hexamethonium.

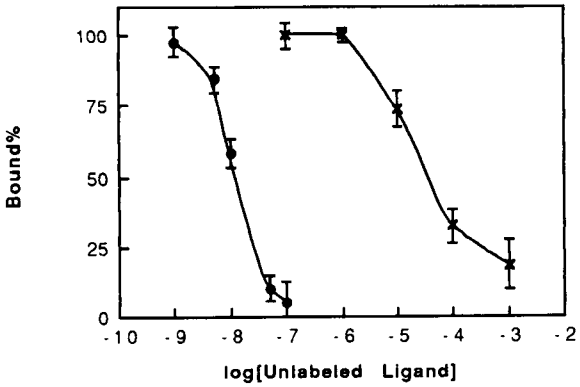

Fig. 8. Reproducibility of two representative dose response curves. Error bars (95% confidence interval) were obtained from injections of 5 trials. Same conditions as Fig. 7. "Bound" refers to specific binding. (×) carbamylcholine; (●) α-Bgt.

literature data using radio labeled α-Bgt [8,18], but generally up to one order of magnitude higher. Likely sources for the discrepancy is that the assay did not measure equilibrium binding of reversible ligands. Because of the large affinity difference between the labeled and unlabeled ligand, the true equilibrium binding parameters are usually determined by quantifying the initial rate of α-Bgt-FITC binding which is inhibited by a cholinergic ligand, thus the initial rate will be directly proportional to unoccupied sites. However, the necessity of centrifugation makes our assay design inappropriate for monitoring binding kinetics. Therefore, due to the dissociation of analytes during the incubation, the binding constants we obtained are only apparent constants, not true equilibrium constants. Moreover, the presence of 0.1% Triton X-100 may slightly solubilize the membrane in the incubation, possibly modifying the receptor binding behavior. In actuality, the mechanism of nAChR binding is much more complicated than the simple picture we describe here. Yet from an analytical point of view, this deviation from a true equilibrium measurement does not hamper the development of our assays as long as the system is calibrated by standards.

TABLE 1

Apparent dissociation constants (M) of some agonists and antagonists to the α-subunits of the nAChR, utilizing α-Bgt-FITC as the labeled ligand

Analyte	Fluorophore labeled nAChR-based assay	RRA (from literature)	
		Ref. 8	Ref. 18
α-Bgt	9×10^{-9}		
Carbamylcholine	3×10^{-5}	1.2×10^{-7}	4.8×10^{-7}
d-Tubocurarine	8×10^{-6}	2.0×10^{-7}	3.8×10^{-7}
Pancuronium	3×10^{-7}		2.3×10^{-8}
Gallamine	4×10^{-6}		1.1×10^{-6}
Decamethonium	8×10^{-5}	1.8×10^{-7}	8.3×10^{-7}
Hexamethonium	2×10^{-4}	1.2×10^{-4}	

An interesting feature of the displacement curves is their "steepness". It is concluded that the steepness (sensitivity) and IC_{50} (potency) of the displacement curves are functions of two factors: one is $K_a \cdot [L^*]$ and $K_a \cdot [R]$, and the other is K_a^*/K_a (K_a = association constant of the analyte, K_a^* = association constant of the labeled ligand) [19]. Different $K_a \cdot [L^*]$ and $K_a \cdot [R]$ relationships provide the basis for different types of techniques that are generally employed in binding assays [20]. Once $K_a \cdot [L^*]$ and $K_a \cdot [R]$ have been fixed, the lower the K_a^*/K_a ratio is, the lower the $(K_a) \cdot (IC_{50})$ will be, while a maximum "steepness" prevails at a certain K_a^*/K_a value [19]. Cholinergic ligands have different association constants and consequently each tends to show different "steepness" for its displacement

curve, which can partially explain the phenomena. Nevertheless, it is believed that there exists another factor which has significant impact on the shape of the curves. A shallow competition curve is usually evidence for different affinity sites of the unlabeled displacer. Although the labeled ligand may have similar affinities for the multiple sites, structurally dissimilar unlabeled ligands are most likely to display different affinities for these binding sites [14]. As a matter of fact, it has been demonstrated that cholinergic antagonists can bind to as many as four sites [21] or as few as one site on the nAChR molecule [22]. Evidence from cholinergic agonists binding to nAChR also suggests that multiple sites, possibly up to four, exist on the receptor molecule. As a result, activation and desensitization could be independent, parallel processes, triggered by different agonists binding to different sites or subunits [23]. All of these observations suggest that a network of interacting binding sites may exist on the nAChR molecule, characterized by different binding properties for the different agonists and antagonists.

In conclusion, fluorescein labeled α-bungarotoxin can be utilized as a nonisotopic probe in a screening assay for agonists and antagonists which bind to the α-subunits of the acetylcholine receptor. The technical procedure is uncomplicated and can be easily conducted in any analytical laboratory because of the simple instrumentation requirements. This technique's simplicity offers an improvement over existing radio-labeled receptor assays. Purified nAChR could be employed to increase the concentration of the receptor, which would be beneficial by reducing the blank signals thereby improving the sensitivity of the assay. However it must be remembered that further purification of the receptor would increase the effort required to perform the assay and complicate the technique. With the proposed assay method, if another separation technique, such as size exclusion chromatography, can be incorporated into the FIA system to remove the fluorescent biological matrix that is of lower molecular weight than α-Bgt-FITC, achievement of better sensitivity and a lower detection limit can be excepted.

We thank Dr. Alan K. Hauser and Glenn B. Martin for their very helpful suggestions and discussions. The support of NIH grant GM-25308 is gratefully acknowledged.

REFEENCES

1 W. Hanna and B.G. Mobbs, Am. J. Clin. Pathol., 91 (1989) 182.
2 S.F. Hallowell and G.A. Rechnitz, J. Clin. Lab. Anal., 4 (1990) 64.
3 I.C. King and J.J. Catino, Anal. Biochem., 188 (1990) 97.
4 T. Takeuchi and G.A. Rechnitz, Anal. Biochem., 194 (1991) 250.
5 R.M. Stroud, M.P. McCarthy and M. Shuster, Biochemistry, 29 (1990) 11009.
6 P.B. Bradley, Introduction to Neuropharmacology, Wright, London, 1989, p. 43.
7 M. Weber, T. David-Pfeuty and J. Changeux, Proc. Natl. Acad. Sci. USA, 72 (1975) 3443.
8 S.G. Blanchard, U. Quast, K. Reed, T. Lee, M.I. Schimerlik, R. Vandlen, T. Claudio, C.D. Strader, H.H. Moore and M. Raftery, Biochemistry, 18, (1979) 1875.
9 K.R. Rogers, J.J. Valdes and M.E. Eldefrawi, Anal. Biochem., 182 (1989) 353.
10 J. Bode, T. Moody, M. Schimerlik and M. Raftery, Biochemistry, 18 (1979) 1855.
11 R.F. Taylor, I.G. Marenchic and E.J. Cook, Anal. Chim. Acta., 213 (1988) 131.
12 G.G. Lunt, in A.J. Turner and H.S. Bachelard (Eds.), Neurochemistry — A Practical Approach, IRL Press, Oxford, 1987, p. 149.
13 A. Zettner, Clin. Chem., 20 (1974) 5.
14 M. Titeler, in M. Williams, R.A. Glennon and P.B.M.W.M. Timmermans (Eds.), Receptor Pharmacology and Function, Marcel Dekker, New York, 1989, p. 21.
15 R.J. Lukas, H. Morimoto, M.R. Hanley and E.L. Bennett, Biochemistry, 20 (1981) 7373.
16 P. Leprince, R. Noble and G.P. Hesse, Biochemistry, 20 (1981) 5565.
17 B.M. Conti-Tronconi, F. Tang, S. Walgrave and W. Gallagher, Biochemistry, 29 (1990) 1046.
18 P. Taylor, R.D. Brown and D.A. Johnson, Current Topics in Membranes and Transport, 18 (1983) 407.
19 L.G. Bachas, C.D. Tsalta and M.E. Meyerhoff, Bio Tech., 4 (1986) 42.
20 A. Zettner, Clin. Chem., 19 (1973) 699.
21 B.M. Conti-Tronconi and M.A. Raftery, Proc. Natl. Acad. Sci. U.S.A., 83 (1986) 6646.
22 P. Culver, W. Fenical and P. Taylor, J. Biol. Chem., 259 (1984) 3763.
23 S.M.J. Dunn, B.M. Conti-Tronconi and M.A.Raftery, Biochemistry, 22 (1983) 2512.

Analytica Chimica Acta, 267 (1992) 63–71
Elsevier Science Publishers B.V., Amsterdam

A comparison of the heuristic evolving latent projections and evolving factor analysis methods for peak purity control in liquid chromatography with photodiode array detection

H.R. Keller and D.L. Massart

Pharmaceutical Institute, Vrije Universiteit Brussel, Laarbeeklaan 103, B-1090 Brussels (Belgium)

Y.Z. Liang and O.M. Kvalheim

Department of Chemistry, University of Bergen N-5007 Bergen (Norway)

(Received 28th January 1992; revised manuscript received 25th March 1992)

Abstract

The performance of the heuristic evolving latent projections (HELP) method is investigated for peak purity control in liquid chromatography with photodiode array detection. HELP and evolving factor analysis performed equally well; both techniques could detect less than 1% of a spectrally similar impurity even for small chromatographic separations. In certain cases, the two techniques may be limited by instrumental and experimental difficulties.

Keywords: Liquid chromatography; Heuristic evolving latent projections; Peak purity control; Evolving factor analysis

Hyphenated techniques such as liquid chromatography with photodiode array detection (LC-DAD) are becoming increasingly important for the analysis of multicomponent systems. In principle, a single analysis provides enough data to determine the number of species present in a mixture and, by means of self-modelling curve resolution [1–5], to resolve the data into the spectra and chromatograms of the pure constituents. Assessment of peak purity in LC-DAD by such methods should therefore be possible. In practice, however, the determination of the number of chemical species is not that simple. Assessment of the rank of the bilinear data by a statistical test tends to overestimate the number of underlying species as shown by Gerritsen et al. [6]. Instrumental and experimental difficulties may lead to artefacts when applying latent variable methods on LC-DAD data. Evolving factor analysis (EFA) for peak purity control in LC-DAD [4,7–8] can be limited by artefacts due to nonzero baselines, the DAD's scan time, a nonlinear calibration curve and heteroscedasticity [9,10]. Although these sources of errors may lead to serious problems, using the fixed size window EFA (FSW) in combination with appropriate data pretreatment less than 1% of a spectrally similar isomer could be detected under a chromatographic peak [11].

This paper studies the performance of the recently developed heuristic evolving latent projections (HELP) method [12,13] to detect a small

Correspondence to: D.L. Massart, Pharmaceutical Institute, Vrije Universiteit Brussel, Laarbeeklaan 103, B-1090 Brussels (Belgium).

amount of a spectrally similar impurity under a main chromatographic peak and investigates the effects of the known sources of artefacts on this technique. The results will be compared with the ones obtained with FSW.

THEORY

LC-DAD generates a data table **X**, where the rows correspond to spectra measured at different times. The columns of **X**, are chromatograms taken at a different wavelength each. The aim of all techniques for curve resolution is to decompose this bilinear data matrix **X** into chromatograms **C** and spectra **A** of the individual species

$$\mathbf{X} = \mathbf{CA} \quad (1)$$

X can be decomposed by principal component analysis (PCA) [14] into a matrix of scores **S** and a matrix of loadings **L** according to

$$\mathbf{X} = \mathbf{SL} \quad (2)$$

Whereas classical overall factor analysis (FA) decomposes the whole data matrix **X** and works therefore on all n spectra, EFA successively works on the first $i = 1 \cdots n$ spectra (Fig. 1). FSW on the other hand, decomposes a fixed number of successive spectra. Initially, PCA is performed on the first 7 spectra; spectra 2–8 are decomposed next and so on. HELP however, is most flexible in that it works on both all n and a limited number

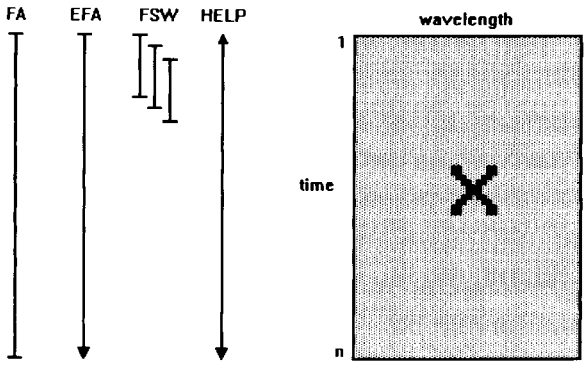

Fig. 1. Schematic representation of overall FA, EFA, FSW and HELP for analysis of a data matrix **X**. For details see text.

of successively recorded spectra. To better explain the method a simple bivariate example is given first.

Suppose a pure peak were measured at two wavelengths only and the signals measured at these wavelengths, A_1 and A_2, were plotted against each other. Provided Beer's law holds, a straight line passing close to the origin would result. If a sample consisting of two compounds with different spectra were measured, a plot of A_1 vs. A_2 would result in Fig. 2. As one measurement is made after the other, the data are intrinsically ordered and lines can be drawn to connect the points representing these measurements. One observes two straight lines passing through the origin of the coordinate system. The first line consists of the points representing the spectra 13 to 20 and maps the region where only the first compound elutes. Both compounds overlap from time 21 to 29 and the second straight line corresponds to pure compound 2 (30–37). In other words such a graph visualizes directly the pure compound regions of each substance. Instead of plotting the signals on the original variables one could equally well represent the data by their scores on the first two principal components (PCs) as illustrated in Fig. 2c. In this simple bivariate case, projection of the data on latent variables corresponds to a rotation of the coordinate system and the two straight lines still map the regions where only one compound elutes.

Generally, however, one measures the signals at more than two wavelengths and the problem to solve is not a bivariate but a multivariate one. The first step of the HELP method works as explained above for the didactical example. As the data cannot be visualized on the original variables, i.e. on all the wavelengths, the spectra are represented by their scores on the first two PCs. Fig. 3 illustrates such a scores plot for a two compound mixture. One notices a remarkable similarity with the bivariate example and the same conclusions can be made. The two straight lines in direction of the origin of the coordinate system map the regions where only one compound elutes. The spectra of the substances can easily be obtained in the corresponding time windows. To obtain the spectrum of compound 1 for instance,

one could take a spectrum of the original data matrix **X** in the range 13 to 20. Referring back to Fig. 1, the first step of HELP decomposes the

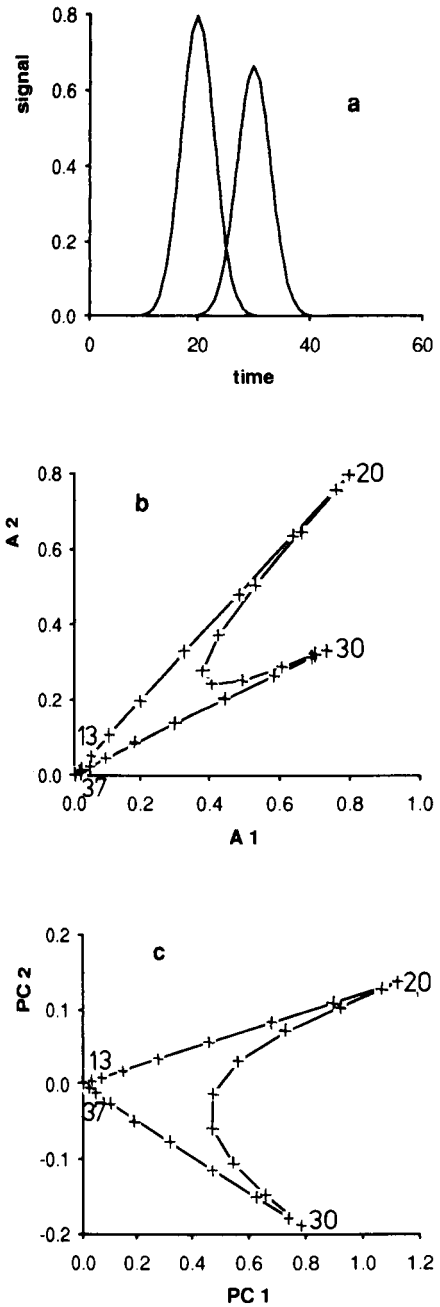

Fig. 2. Simulated chromatogram of two substances with some noise added (a), signals measured at two wavelengths, A_1 and A_2, plotted against each other (b) and corresponding scores plot (c).

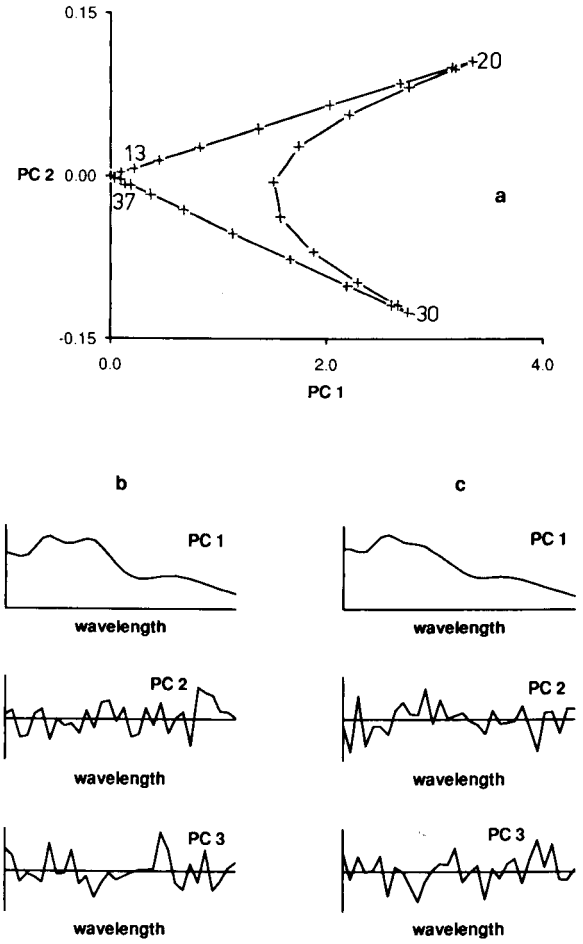

Fig. 3. Scores plot for simulated multivariate data (a), loadings on the first 3 PCs obtained from spectra 13–20 (b) and spectra 30–37 (c).

whole data matrix; as all spectra are analyzed, this procedure is similar to FA.

The HELP method is based on latent variable projections of ordered data such as the scores plot discussed above. To improve the resolution of the technique and to confirm the information obtained by the scores plot, the second step focuses on smaller parts of the data. This is termed local rank analysis and aims at revealing the local data structure (datascope). HELP is therefore an inductive and evolving method based on latent variable projections.

To confirm the information found by the initial scores plot, i.e. to verify that the straight lines

TABLE 1

Eigenvalues obtained from $\mathbf{X}_{13-20}$

PC number	Eigenvalue
1	35.4
2	1.80×10^{-6}
3	1.51×10^{-6}
4	1.30×10^{-6}

correspond to a single species, the user must select local regions of the chromatogram, which he wants to inspect in more detail. For the given example one may determine the PCs of the first straight line. The loadings obtained from spectra 13 to 20, i.e. the relative importance of the variables for the submatrix $\mathbf{X}_{13-20}$, are given in Fig. 3b. One notices that PC1 corresponds to the spectrum of compound 1. The other PCs are of higher frequencies and represent noise only. From this one would conclude that in the interval 13 to 20 there is only one pure substance eluting. This can be confirmed by the eigenvalues (EVs) obtained from the same submatrix. Table 1 shows that the first EV is much larger than the other ones, which are all of approximately the same size and represent noise.

$\mathbf{X}_{30-37}$ is then analysed in the same way and the spectrum of compound 2, which is slightly different from the first, can be obtained. In fact, the spectra of the two species can be taken from either the loadings plots or the original data matrix $\mathbf{X}$ in the corresponding pure compound regions. Once the spectra of all species $\mathbf{A}$ have been determined, the unknown chromatograms $\mathbf{C}$ can be calculated using

$$\mathbf{C} = \mathbf{X}\mathbf{A}'(\mathbf{A}\mathbf{A}')^{-1} \quad (3)$$

HELP is not restricted to two-compound mixtures but it can also be applied to samples with more compounds, as shown by Kvalheim and Liang [12]. This work aims at studying this technique with respect to the detection of a small amount of a spectrally similar impurity under a chromatographic peak and at investigating its limitations caused by instrumental and experimental problems.

EXPERIMENTAL

The sample consisted of two isomers of a drug, used as available in the laboratory and dissolved directly in the mobile phase. The liquid chromatograph was a Kontron pump 420 with a Rheodyne injection valve and a 20-μl sample loop (Valco). A 100×4.6 mm i.d. RP-18 column (Brownlee Spheri-5, 5 μm) was used at ambient temperature. The mobile phase was a degassed and filtered mixture of acetonitrile (Lichrosolv, Merck) and 0.1 M diammonium hydrogenphosphate (analytical-reagent grade, Merck) in water at pH 2.5 (adjusted with 85% phosphoric acid, analytical-reagent grade, Merck). The flow-rate was 2 ml min^{-1}. Spectra were recorded on a Perkin Elmer LC235 DAD in the range of 210 to 365 nm (32 diodes). Data transfer to an IBM compatible personal computer with math coprocessor and conversion to ASCII files were performed with the Perkin Elmer LC View software. All programs for simulation and data analysis were written and compiled in this laboratory using Microsoft BASIC 7.0.

RESULTS AND DISCUSSION

Peak purity control

An illustrative example of HELP is given in Fig. 4, where the amount of the second isomer is 10%. As the relative concentration of the impurity is relatively high, two more or less straight lines can easily be seen in the scores plot, indicating regions of the chromatogram where only one analyte elutes. The resulting loadings plots are very similar to those in Fig. 3 and confirm that the two lines correspond to two different underlying substances.

To be able to detect small amounts of an impurity, on the other hand, the scores plot needs to be read with some caution because the straight line representing this minor compound will only be short. This is illustrated in Fig. 5 where 0.7% of a spectrally similar isomer is present under another one with $R_s = 0.5$. From the scores plot, where all spectra are represented (Fig. 5a),

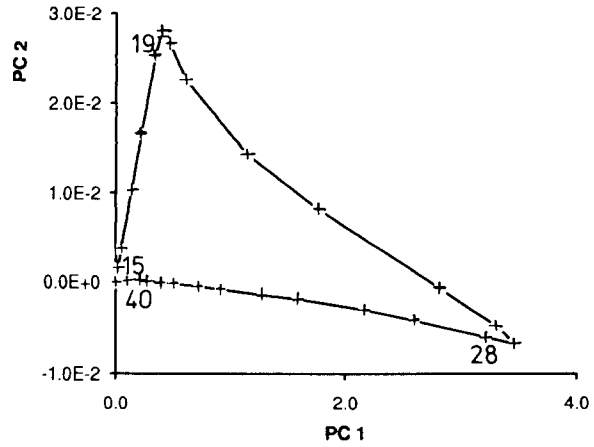

Fig. 4. Scores plot of experimental data with 10% impurity and $R_s = 0.5$.

straight lines in direction of the centre of the PC coordinate system cannot be found immediately. Careful inspection will reveal the impurity, however. Enlarging the scores plot close to the origin of the coordinate system, shows two more or less straight lines. The first line is being described by spectra 15 to 19 and corresponds to the region

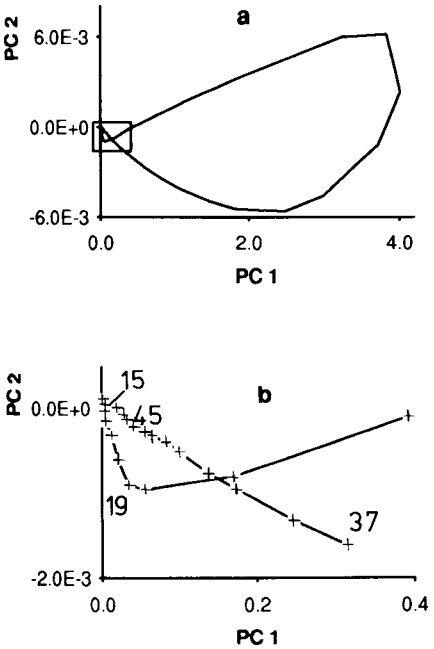

Fig. 5. Full (a) and enlarged (b) scores plot of experimental data with 0.7% impurity and $R_s = 0.5$.

TABLE 2

Eigenvalues obtained from $\mathbf{X}_{15-19}$ and $\mathbf{X}_{37-45}$

PC number	$\mathbf{X}_{15-19}$	$\mathbf{X}_{37-45}$
1	1.88×10^{-3}	0.235
2	5.14×10^{-8}	1.01×10^{-7}
3	2.48×10^{-8}	5.02×10^{-8}
4	1.72×10^{-8}	2.24×10^{-8}
5	5.19×10^{-9}	1.25×10^{-8}

where only one isomer elutes. The second isomer elutes as pure analyte for instance in the region 37 to 45, since the points representing spectra 37 to 45 fall approximately on a straight line, which goes towards the centre of the coordinate system. The loadings obtained from the submatrices $\mathbf{X}_{15-19}$ and $\mathbf{X}_{37-45}$ are almost the same as the ones shown in Fig. 3b and c; assuring that in each of the two selected regions there is only one substance present. The EVs listed in Table 2 confirm this; the first EV is significantly larger than the other ones, which are all of comparable size.

A different situation occurs in cases where one peak is completely overlapped by another as shown in Fig. 6. In such a case, there is only one line in direction of the origin of the coordinate system representing the region where only the major analyte elutes; the region where the analytes overlap, maps as a loop. Therefore only the spectrum of one substance can readily be extracted, as discussed in more detail in Ref. [12].

A systematic evaluation of the limits of detection for an impurity based on HELP was performed by varying chromatographic separation systematically from $R_s = 1.0$ to 0.1 in steps of 0.1 while the relative concentration of one isomer in the other was 10%, 2% and 0.7% respectively. The results obtained are summarized in Fig. 7, where the line indicates the limits of detection for the tested impurity in function of R_s and relative concentration. In the area above and to the right of this line the second isomer will be detected. One notices that the HELP method permits detection of a small amount of a spectrally similar impurity even for small separations. It is interesting to note that exactly the same results have been obtained with FSW [11]. The

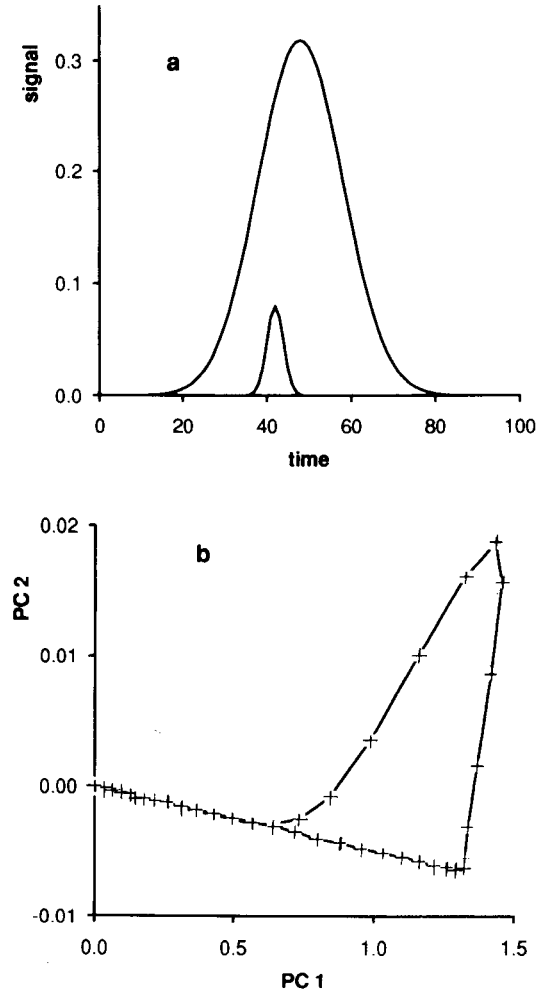

Fig. 6. Simulated chromatogram (a) and scores plot (b) for completely overlapping peaks.

performance of HELP and FSW in detecting a small amount of a spectrally similar impurity in LC-DAD is therefore identical.

Artefacts

It has been shown that instrumental and experimental difficulties may lead to artefacts when applying latent variable methods on LC-DAD data [9–11]. Therefore, the effects of the known sources of these problems on the HELP method were also studied. Supposing a pure peak was measured at two wavelengths and A_1 and A_2 were plotted against each other. A straight line

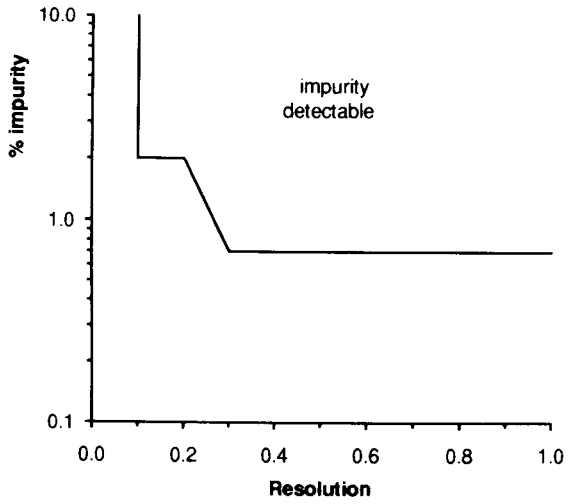

Fig. 7. Limits of detection for an impurity in function of the relative amount and of the chromatographic separation.

passing close to the origin should normally result and a single PC should describe such a situation. In the presence of instrumental or experimental problems, however, deviations from straight lines may be observed as illustrated in Fig. 8. To describe such cases completely, a second PC has to

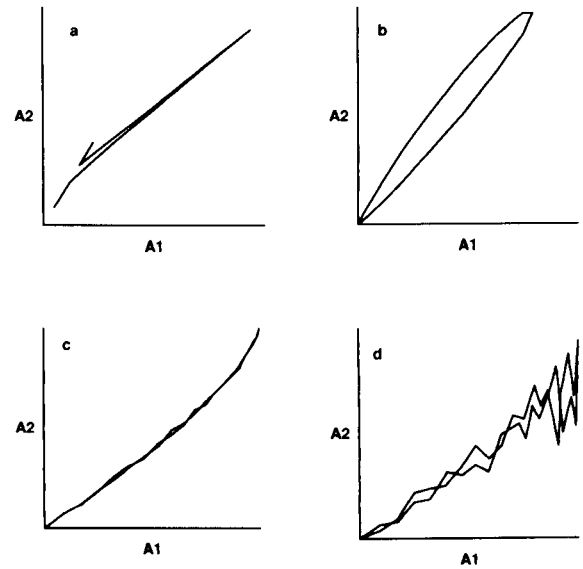

Fig. 8. Signals measured at two wavelengths obtained for a pure peak with nonzero baseline (a), a DAD with significant scan time (b), a nonlinear calibration curve (c) and heteroscedasticity (d). Adapted from Ref. [10].

be included as discussed in detail elsewhere [9,10]. Generally, two PCs would indicate that there are two underlying chemical species, which is in this case incorrect. The second PC is therefore an artefact, which is due to instrumental or experimental difficulties.

Nonzero baselines, a relatively long scan time of the DAD, nonlinear calibration curves and heteroscedasticity all lead to artefacts in EFA. Simulated LC-DAD data where these problems occur, were therefore also analyzed with HELP. The results obtained from such multivariate data, plotted on the first two PCs (Fig. 9), are similar to the ones obtained from the corresponding bivariate cases, plotted on the two original variables (Fig. 8). The patterns of the points representing the spectra are essentially the same in the two cases. PC1 accounts for most of the variation in the data, i.e. the variation caused by the analyte and PC2 represents either one of the artefacts or noise. It is important to note that the PC2 is scale expanded.

As HELP originally works on raw data, nonzero baselines will induce a second PC. In Fig. 9a two lines directed towards the origin, denoted as AB and CD, can be observed. From this scores plot one might conclude that these lines are due to one or more analytes, which is not correct. However, the second part of HELP, where the loadings of AB and CD are determined, makes the right diagnosis. The loadings on all PCs are of high frequency, since the lines are entirely due to the nonzero baseline. From this it follows that AB and CD are not due to analytes and that there is a baseline problem. To eliminate such irregularities from the scores plots, one may apply row centering on **X** [10]. This will remove all artefacts due to nonzero baselines and make interpretation easier in such situations.

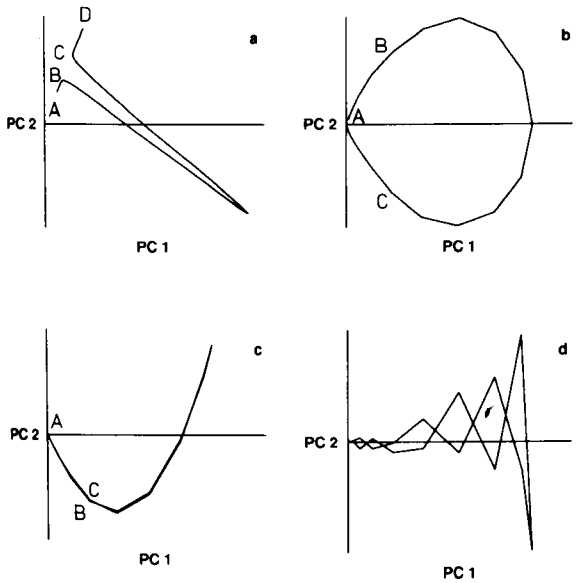

Fig. 9. Scores plot on the first two PCs obtained for a simulated pure peak with nonzero baseline (a), a DAD with significant scan time (b), a nonlinear calibration curve (c) and heteroscedasticity (d). Expanded scale on PC 2.

A DAD does not measure the whole spectrum at once, usually about 10 to 50 ms are required to scan a spectrum from the lowest to the highest wavelength. For situations where this scan time is relatively large, the concentration of the analyte changes significantly during the measurement of a spectrum. In the upslope of a chromatographic peak, the concentration of the analyte measured at the last diode will be higher than the one measured at the first diode. In the downslope on the other hand, the concentration measured at the first diode will be larger than the one measured at the last diode. As a result of this two more or less straight lines (AB and AC), which may again be mistaken as being due to different substances, can be observed in Fig. 9b. The loadings on PC1 obtained in such a case from the upslope and downslope of a peak are shown in Fig. 10. As the signals observed at high wavelengths in the upslope spectra are overestimated and analogously the ones measured for the downslope spectra are underestimated, one notices at higher wavelengths a small, systematic difference between the two spectra. Provided the scan time of the instrument is known, the observed data can be corrected by estimation of the true signals in each spectrum as proposed elsewhere [9, 10], and the artefacts due to the scan time can be removed.

In case of a nonlinear calibration curve, more than one PC is required to describe a pure compound system (Fig. 9c). Whereas the highest deviations from linearity usually occur at high signals, i.e. next to the peak maximum, the calibration

curve is almost linear at low signals. As a consequence, regions AB and AC, representing the beginning and the end of the chromatographic peak, map almost as straight lines. The loadings on PC1 obtained from these parts of the chromatogram are the same while the loadings on the other PCs represent noise; AB and AC correspond therefore to the same single analyte.

While heteroscedasticity seems to be one of the most serious problems for EFA based methods, HELP is much less affected because PCA is initially performed on all spectra. Inspecting Fig. 9d one notices that there is no straight line passing through the origin, as required in the discussion above for a pure peak. Still, one can diagnose heteroscedasticity because high signals are characterized by high values on PC2, i.e. high noise. A pure peak with homoscedastic noise would result in Fig. 11. Here, the noise, i.e. the values on PC2, is independent of the signal and this noise–signal relationship is known as homoscedasticity. Although for both homo- and heteroscedastic data, there is no straight line passing through the origin, one can still show that the analyzed peaks are pure. The loadings on the first three PCs obtained from $\mathbf{X}_{12-28}$ of the homoscedastic example are given in Fig. 11c. One observes that only the first PC is of low frequency and the right diagnosis can therefore be made. In contrast to FSW, heteroscedasticity does not lead to any problems when analyzing a two compound sample. A scores plot obtained from a two compound sample with heteroscedastic noise is virtually the same as one obtained from homoscedastic data (e.g. Fig. 3a), and two straight lines now represent the pure compound regions of the analytes.

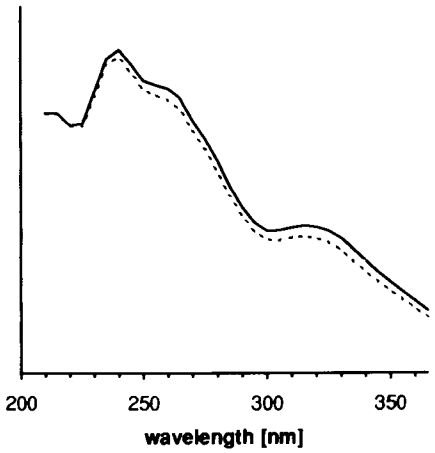

Fig. 10. Standardized loadings obtained from regions AB (———) and AC (– – –) of Fig. 9b.

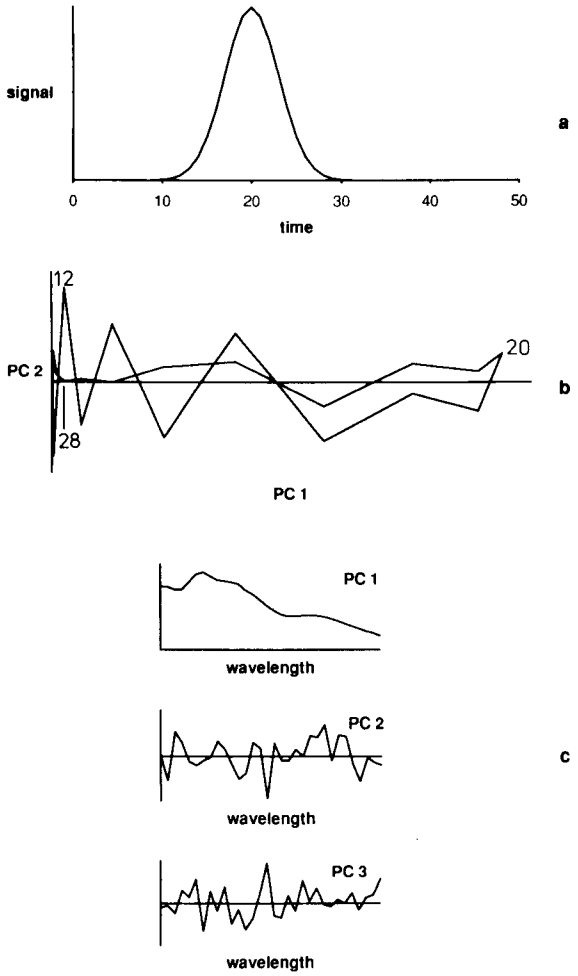

Fig. 11. Chromatogram of a simulated pure peak with homoscedastic noise (a), scores plot on the first two PCs (b) and loadings of spectra 12–28 (c).

Comparison of HELP and FSW

Both HELP and FSW rely on intrinsically ordered data, such as obtained from LC-DAD

where one spectrum is measured after the other. The two techniques are based on latent variables and do not make any assumption about the peak shape or the spectra. Both methods are subject to artefacts caused by instrumental and experimental problems. HELP and FSW performed equally well in detecting a small amount of a spectrally similar impurity under a chromatographic peak. However, the two methods differ in several ways. FSW works on a fixed number of spectra and determines the importance of the underlying latent variables. It can therefore only indicate whether the analyzed data set consists of one or more substances; the pure compound regions and the spectra cannot easily be obtained using the method as published earlier, although it would be possible to include this option relatively easily. An advantage of FSW is that it can be automated, since no user interaction is required. HELP on the other hand, involves two different steps and demands user interaction. First, the whole data set is analyzed and the spectra are represented on the first two PCs. After selection of a number of consecutively recorded spectra HELP focuses on the relative importance of the variables. Since this method processes the data in two different ways, it can extract more information than FSW. Both, the regions where only one substance elutes and the corresponding spectra can readily be obtained. HELP is therefore somewhat more powerful and more flexible than FSW. While both techniques are subject to artefacts due to instrumental and experimental problems, only HELP can make an albeit limited diagnosis. On the other hand, HELP requires user interaction and several trials are usually needed for a good selection of the submatrices.

The authors thank P. Kiechle and F. Erni for their collaboration and Sandoz Pharma Ltd. and Shell Research Laboratories for financial assistance. Y.-Z. Liang thanks the Royal Norwegian Council for Scientific and Industrial Research (NTNF).

REFERENCES

1 W.H. Lawton and E.A. Sylvestre, Technometrics, 13 (1971) 617–633.
2 B.G.M. Vandeginste, W. Derks and G. Kateman, Anal. Chim. Acta, 173 (1985) 253–264.
3 R.F. Lacey, Anal. Chem., 58 (1986) 1404–1410.
4 M. Maeder, Anal. Chem., 59 (1987) 527–530.
5 J.C. Hamilton and P.J. Gemperline, J. Chemom., 4 (1990) 1–13.
6 M.J.P. Gerritsen, N.M. Faber, M. van Rijn, B.G.M Vandeginste and G. Kateman, Chemom. Intell. Lab. Syst., 12 (1992) 257–270.
7 H.R. Keller and D.L. Massart, Chemom. Intell. Lab. Syst., 12 (1992) 209–224.
8 H.R. Keller and D.L. Massart, Anal. Chim. Acta, 246 (1991) 379–390.
9 H.R. Keller, D.L. Massart, P. Kiechle and F. Erni, Anal. Chim. Acta, 256 (1992) 125–131.
10 H.R. Keller and D.L. Massart, Anal. Chim. Acta, 263 (1992) 21–28.
11 H.R. Keller, D.L. Massart, Y.Z. Liang and O.M. Kvalheim, Anal. Chim. Acta, 263 (1992) 29–36.
12 O.M. Kvalheim and Y.Z. Liang, Anal. Chem., 64 (1992) 936–946.
13 Y.Z. Liang, O.M. Kvalheim, H.R. Keller, D.L. Massart, P. Kiechle and F. Erni, Anal. Chem., 64 (1992) 946–953.
14 S. Wold, K. Esbensen and P. Geladi, Chemom. Intell. Lab. Syst., 2 (1987) 37–52.

Analytica Chimica Acta, 267 (1992) 73–80
Elsevier Science Publishers B.V., Amsterdam

Wavelet transform for the evaluation of peak intensities in flow-injection analysis

M. Bos and E. Hoogendam

Department of Chemical Technology, University of Twente, P.O. Box 217, 7500 AE Enschede (Netherlands)

(Received 18th September 1991; revised manuscript received 13th April 1992)

Abstract

The application of the wavelet transform in the determination of peak intensities in flow-injection analysis was studied with regard to its properties of minimizing the effects of noise and baseline drift. The results indicate that for white noise and a favourable peak shape a signal-to-noise ratio of 2 can be tolerated at the 5% error level, which means that a significant reduction in the detection limit can be obtained in comparison with the classical signal-processing methods. With regard to the influence of a changing baseline it was found that its d.c. level has a negligible effect, but a linear or exponentially rising baseline introduces an error that depends on the chosen frequency of the wavelet that is used to determine the peak intensity. The optimum choice of this frequency, in turn, depends on the shape of the peak that is studied. In this respect significant differences were observed for pure Gaussian and exponentially modified Gaussian peaks.

Keywords: Flow injection; Signal processing methods; Peak intensities; Wavelet transform

The main limitations in the determination of peak intensities in flow-injection analysis (FIA) are noise and a drifting baseline. Peak overlap generally is not a problem because it can easily be avoided by adjusting the sample rate. Several methods have been described [1–4] that address the automatic evaluation of the peak-shaped FIA signals. In general, the procedure can be fairly straightforward if sufficient attention is paid to the design of the FIA system in order to obtain a baseline free from drift and a well formed peak. The aforementioned problems only come into play when a FIA system is operated near its detection limits. Here automatic signal processing encounters practical difficulties in locating the peak and finding the right baseline correction method.

Correspondence to: M. Bos, Department of Chemical Technology, University of Twente, P.O. Box 217, 7500 AE Enschede, Netherlands.

The detection of weak signals embedded in stochastic noise is a more general problem for which correlation of the observed signal with a replica of the desired signal is in use. Correlation is most effective if the shape and the time of occurrence of the relevant signal is known. Instead of correlation a matched filter can be used. Also in this case the shape of the signal or at least the band width should be known.

This paper shows the advantages of the use of a signal-processing technique called wavelet transformation to tackle these problems. The main characteristic of this technique is that it transforms the information contained in the signal into a two-dimensional time–frequency form. In this transform time and frequency information of the signal is retained. This permits the choice of a coefficient in this two-dimensional representation that reflects the peak intensity optimally filtered from noise. This choice can be automated by searching for the maximum coefficient in the

transform of a well defined peak obtained for a sample with a relatively high concentration. The position of this maximum on the horizontal time axis of the transform conveys the positional information of the peak whereas its position on the vertical frequency axis determines the noise-filtering characteristic that can be obtained.

Automatic full compensation of baseline d.c. level drift and, to a lesser extent, of a sloping baseline of various mathematical forms can be realised by proper choice of the form of the analysing wavelet.

THEORY

The purpose of the wavelet transform procedure is to decompose a signal into localized contributions that are characterized by a so-called scale parameter. The mathematical techniques to perform this decomposition have been described in a number of papers [5–9]. Here only a short review of the main equations is given.

Just like other types of transforms, e.g., the Fourier transform, the wavelet transform realizes a correspondence between physical space t and spectral space ω, by convoluting the signal $s(t)$ to be analysed with a given analysing function $\psi(t)$ defined in the two-dimensional space $[\omega,t]$. Figure 1 shows four examples of analysing functions $\psi(t)$. It shows how the time-scale methods windowed Fourier transform and wavelet transform achieve an optimum compromise between time resolution Δt and frequency resolution $\Delta\omega$: $\Delta t \Delta\omega$ = constant. Owing to their ability to encompass time variations of spectral properties,

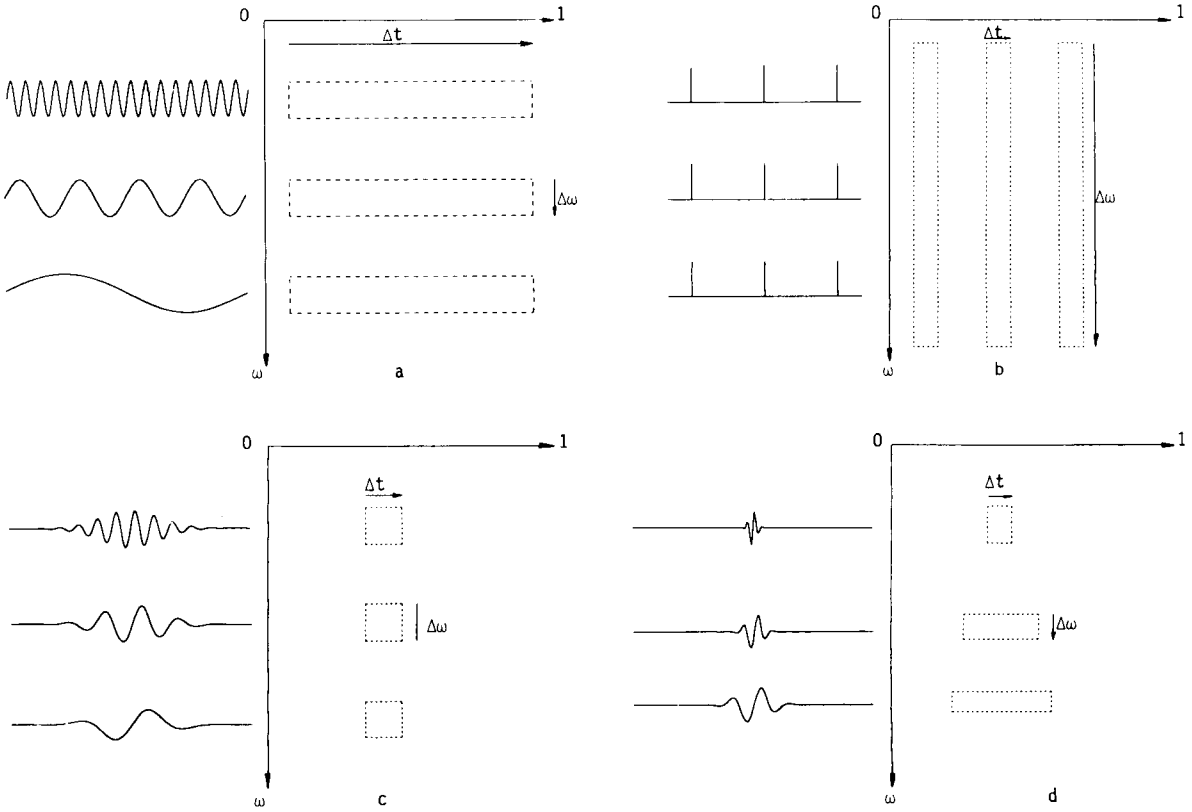

Fig. 1. Four examples of analysing functions: (a) Fourier transform, (b), sampling, (c) windowed Fourier transform and (d) wavelet transform.

time-scale representations are particularly adapted to the analysis of non-periodic, non-stationary signals.

Analysing wavelets

If the analysing wavelet is denoted as the function $g(t)$ and its Fourier transform by $\hat{g}(\omega)$, a number of "self-similar" elementary wavelets $g_{a,b}(t)$ concentrated in time and frequency can be obtained from some basic wavelength $q_{\text{basic}}(t)$ by shifts in the time variable and by dilations which act both on the time and the frequency variable:

$$g_{a,b}(t) = \frac{1}{\sqrt{a}} \cdot g_{\text{basic}}\left(\frac{t-b}{a}\right) \tag{1}$$

where $1/\sqrt{a}$ is a normalizing constant that ensures that all analysing functions have "unit energy".

The analysing wavelet function has to fulfil a number of conditions:

$$\int |g(t)|^2 \, dt < \infty \tag{2}$$

which ensures finite energy and

$$\int |\hat{g}(\omega)|^2 \frac{d\omega}{|\omega|} < \infty \tag{3}$$

which gives a restriction on the behaviour of $\hat{g}(\omega)$ around the zero frequency. It ensures a short-wave like behaviour and generally implies that $g_{\text{basic}}(t)$ does not have a d.c. component.

A third restriction imposed on the function representing the analysing wavelet is

$$\hat{g}_{\text{basic}}(\omega) = 0 \text{ for } \omega < 0 \tag{4}$$

The wavelet transform is now defined as the function $S(b,a)$ on the open (b,a) half-plane (b arbitrary, $a > 0$):

$$S(b,a) = \int_{-\infty}^{\infty} [g_{b,a}(t)]^* s(t) \, dt \tag{5}$$

where the asterisk denotes that the function g is complex. This equation can be rewritten as

$$S(b,a) = \frac{1}{\sqrt{a}} \int_{-\infty}^{\infty} g^*_{\text{basic}}\left(\frac{t-b}{a}\right) s(t) \, dt \tag{6}$$

The conditions imposed on the wavelet function imply that $\hat{g}(\omega)$ is negligible above a certain frequency $\omega_{\max}$, making $S(b,a)$ insensitive to the higher Fourier components of the signal $\hat{s}(\omega)$. This eliminates the influence of small-scale features. Further, these conditions make g negligible outside an interval $[t_{\min}, t_{\max}]$ on the t-axis, causing $S(b,a)$ to be insensitive to the values of $s(t)$ such that $t - b$ lies outside of $[t_{\min}, t_{\max}]$. The latter is the origin of the desired localization in time.

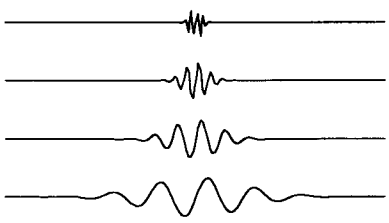

Fig. 2. Morlet analysing wavelets with different values for scaling parameter a.

A commonly used analysing wavelet that fulfils these conditions is the Morlet wavelet:

$$g^*_{\text{basic,Morlet}}(t) = e^{i\omega_0 t} e^{-t^2/2} + \text{small corrections} \tag{7}$$

These small corrections are numerically negligible when $\omega_0 > 5$ but have to be added since $\exp[-(\omega - \omega_0]^2]$ does not vanish for $\omega < 0$.

Figure 2 shows a number of these wavelets with different values for the scale parameter a.

Discretization of the wavelet transform

In practice, the signals to be analysed will be acquired by computer at discrete time intervals. This necessitates the use of a discrete form of Eqn. 6:

$$S(iT_s, a) = T_s \frac{1}{\sqrt{a}} \sum_n g^* \left[\frac{(n-i)T_s}{a}\right] s(nT_s) \tag{8}$$

where $1/T_s$ is the sampling frequency. Let $g^*_a(iT_s) = g^*(iT_s/a)$. Then, for each value of a, the analysing wavelet is sampled, yielding the sequence $g^*(iT_s)$. The convolution product between $s(nT_s)$ and $g^*_a(iT_s)$ is then computed. As $g(t)$ has finite support, the number of sampling points of $g^*_a(t)$ is finite and grows linearly with a. In this work the wavelet of Eqn. 7 is used with $\omega_0 = 5$.

All $g_a^*(t)$ wavelets are derived from $g^*_{\text{basic}}(t)$ through the dilation operator by sampling with a narrower interval.

More details and a more efficient algorithm that is suitable for larger applications can be found in [10].

EXPERIMENTAL

Chemicals

Imidazole samples were prepared from a stock solution of 0.00563 M imidazole (Merck, analytical-reagent grade) by dispensing from a piston burette and diluting with carbon dioxide-free deionized water that had been passed through a Millipore Q2 filter. With these samples a reagent stream of 0.1992 M acetic acid diluted from pure acetic acid (Merck, analytical-reagent grade) was used. This was standardized titrimetrically.

18-Crown-6 (Merck, zur Synthese) samples were prepared by dissolving the required amount of substance in deionized water obtained from a Millipore Q2 installation. The reagent stream was 0.2 M barium chloride (Merck, analytical-reagent grade, standardized titrimetrically).

Equipment for FIA with enthalpimetric detection

A schematic diagram of the FIA equipment is given in Fig. 3. The sampler and the injection valve (Skalar Model 1000 and 1550, respectively) are computer controlled (Apple IIe). The pump is a Gilson Minipuls 2. The reagent and carrier streams are immersed in a 5-l stirred water-bath that is thermally isolated from its surroundings by 1 cm of Styrofoam. The temperature of this water-bath is controlled to 0.01°C by a Tamson thermostat via a glass heat exchanger. The length of the PTFE coil (tubing i.d. 0.5 mm o.d. 1.5 mm) to equilibrate the reagent thermally is 1 m. For the sample a 20-cm stainless-steel coil (tubing i.d. 0.5 mm o.d. 1.5 mm) is used for this purpose. The enthalpimetric detector consists of a measuring and a reference thermistor (Philips, NTC626-12223) connected in a Wheatstone bridge circuit with fixed resistors of 21.5 kΩ. The supply voltage for this circuit is 5 V. The bridge signal is measured every 200 ms with a Hewlett-Packard

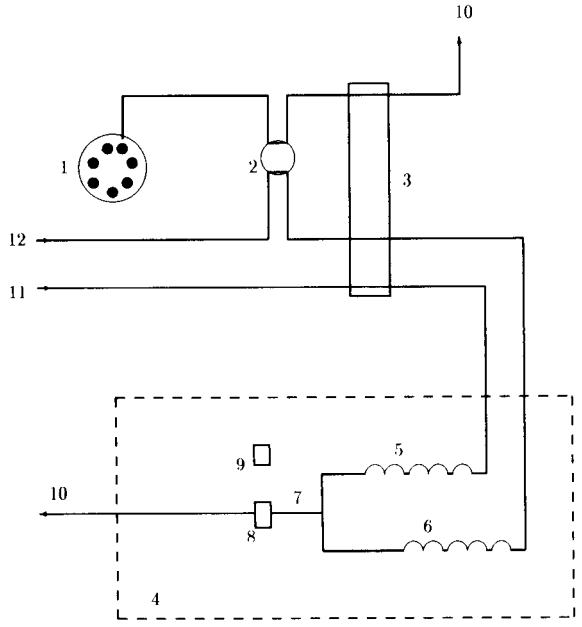

Fig. 3. Measurement set-up. 1 = sampler; 2 = injection valve; 3 = pump; 4 = water-bath; 5 = reagent thermostat coil; 6 = sample thermostat coil; 7 = mixing single-bead string reactor; 8 = measuring thermistor; 9 = reference thermistor; 10 = waste; 11 = acetic acid; 12 = carrier (water).

Model 3478A multimeter connected to the computer by its HP-IB interface. The sample loop in the injection valve has a volume of 0.200 ml. The flow-rate of the carrier and the reagent streams is 2.5 ml min^{-1}.

RESULTS AND DISCUSSION

The suitability of the wavelet transform for the evaluation of FIA peaks and its optimum parameter settings were studied on synthetic and real signals. With the use of simulated FIA signals a systematic survey of the influence of noise and various forms of baseline drift could be obtained whereas the experiments in which an enthalpimetric detector was used show what can be gained with this technique in practice for noisy signals on a drifting baseline.

Results for simulated signals

FIA peaks can have a Gaussian shape, but more generally one finds a so-called exponen-

tially modified Gaussian peak (EMG) [11–14]. The simulations were carried out with both signal types. For the Gaussian peak the following equation was used in the computer program:

$$s(i) = \frac{A}{\sqrt{2\pi}} \exp\left[-\frac{(p-i)^2}{\sigma^2} \right] \quad (9)$$

where A = peak height, σ determines the width of the peak and p is its position on the discretized t-axis.

The EGM peaks were constructed using the equations given by Foley [11]:

$$s(t) = \frac{A}{\tau} \cdot \exp\left(\frac{\sigma_g^2}{2\tau} - \frac{t - t_g}{\tau} \right) \cdot \int_{-\infty}^{Z\sqrt{2}} \frac{1}{\sqrt{\pi}} \exp\left(\frac{-x^2}{2} \right) dx \quad (10)$$

with

$$Z = \frac{t - t_g}{\sigma_g} - \frac{\sigma_g}{\tau}, \text{ time } t = 0.1j \text{ and } j = 1 \ldots 201$$

where A is the area of the peak, τ is the time constant of the exponential decay, t_g determines the position of the peak on the time axis and the ratio τ/σ_g is a measure of its asymmetry.

Random white noise of uniform distribution was generated with the use of a pseudo-random number generator provided in the CSL software library [15].

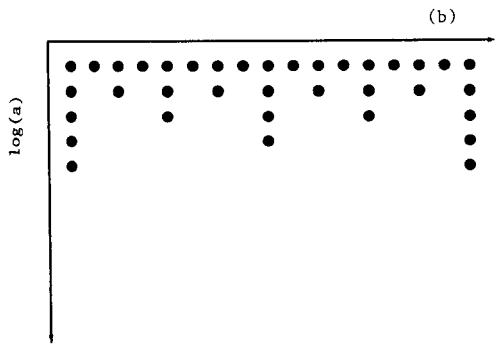

Fig. 4. Schematic representation of a grid on the plane (a,b) allowing arbitrary precise reconstruction of signals.

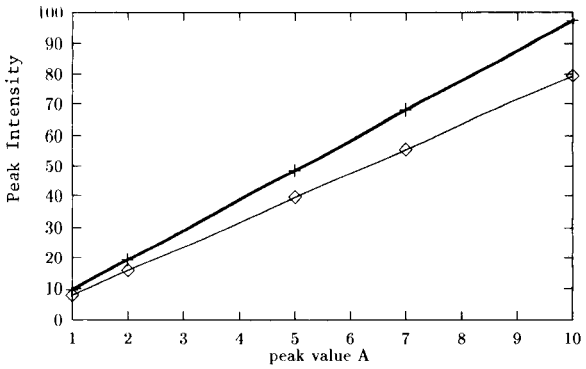

Fig. 5. Calibration graphs for peak intensities determined by the wavelet transform for (◇) EMG and (+) Gaussian peaks.

The transforms are carried out with a grid of a and b values that is depicted qualitatively in Fig. 4 and mathematically described by

$$a_i = 2^{-\alpha i},\ b_{i,j} = j\beta a_i;\ i,j \in N \quad (11)$$

where α and β are sampling constants. In the calculations the values used were $\alpha = 0.25$ and $\beta = 0.1$. Using these values, the maximum wavelet transform coefficients were found at $a = 0.35$, $b = 0.28$ (Gaussian peak) and $a = 0.500$, $b = 0.25$ (EMG).

Linearity and independence of baseline d.c. level. Figure 5 shows the perfect linear relationship between peak height and the maximum coefficient of the wavelet transform of the signal. Table 1 shows that the d.c. level has a negligible influence on the value of the transform.

Baseline drift. The error produced by a linear drifting baseline:

$$\text{baseline}[i] = \text{slope}(i - \text{offset}) \quad (12)$$

is shown in Fig. 6.

TABLE 1

Influence of d.c. level of baseline on peak intensities

Baseline value	Intensity	
	EMG peak	Gaussian peak
0.0	55.5737	68.2057
1.0	55.5745	68.2067
5.0	55.5795	68.2109
10.0	55.5856	68.2161
100.0	55.6961	68.3095

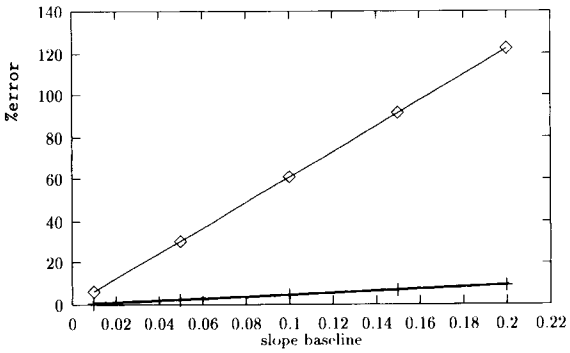

Fig. 6. Error produced by linear sloping baseline for (◇) EMG and (+) Gaussian signal peak.

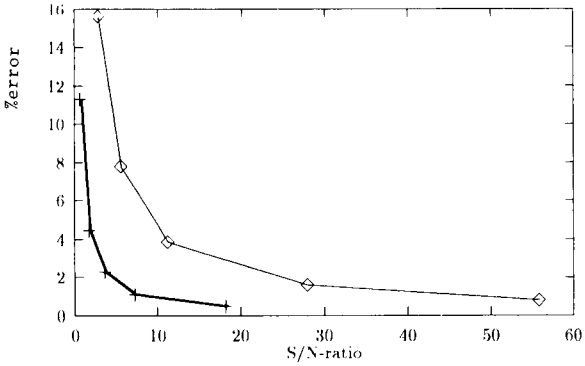

Fig. 8. Error in peak intensity versus signal-to-noise ratio for (+) EMG and (◇) Gaussian peaks.

Figure 7 shows the errors produced by an exponential rise of the baseline. The equation used to simulate the exponentially rising baseline was

$$\text{baseline}[i] = \exp[(i - 1500) \times \text{factor}] \qquad (13)$$

Noise. The influence of noise was tested by superimposing uniformly distributed random signals on the signals generated by Eqns. 9 and 10 using various amplitudes for the noise. The summary of the results given in Fig. 8 shows that this influence is less than 5% for a signal-to-noise ratio of less than 2 for the EMG peak and less than 10 for the Gaussian peak.

Experimental results

Table 2 shows the peak intensities found by the wavelet transform procedure for different samples of imidazole. The reagent used in this determination was 0.1992 M acetic acid. The linearity with concentration is within 5% down to the lowest concentration measured, i.e., 5.63×10^{-4} M. Figure 9 shows the measured signal for this concentration and clearly demonstrates the robustness of the wavelet transform technique against noise and baseline fluctuations. Table 3 shows similar results for the reaction between 0.2

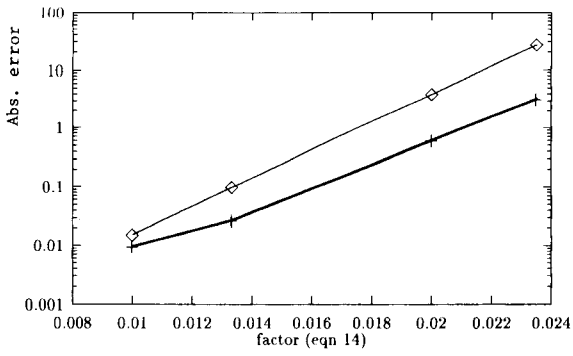

Fig. 7. Absolute error in peak intensity caused by an exponentially rising baseline for (+) Gaussian and (◇) EMG peaks.

TABLE 2

Peak intensities versus concentration for imidazole samples and acetic acid reagent

Concentration (10^{-3} M)	Calculated intensity	Intensity/ concentration	Deviation from mean (%)
5.63	4.241	0.753	1.2
5.63	4.256	0.755	1.4
5.06	3.720	0.735	−1.2
5.06	3.710	0.733	−1.4
4.53	3.481	0.768	3.2
4.53	3.459	0.763	2.5
3.94	2.826	0.717	−3.6
3.94	2.886	0.732	−1.6
3.38	2.541	0.751	0.09
3.38	2.431	0.719	−3.3
2.81	2.067	0.735	−1.2
2.81	1.917	0.682	−8.3
2.25	1.468	0.652	−11.3
2.25	1.552	0.689	−7.3
1.69	1.315	0.778	4.5
1.69	1.344	0.795	6.8
1.13	0.863	0.763	2.5
1.13	0.928	0.821	10.3
0.56	0.428	0.761	2.2
0.56	0.440	0.782	5.1

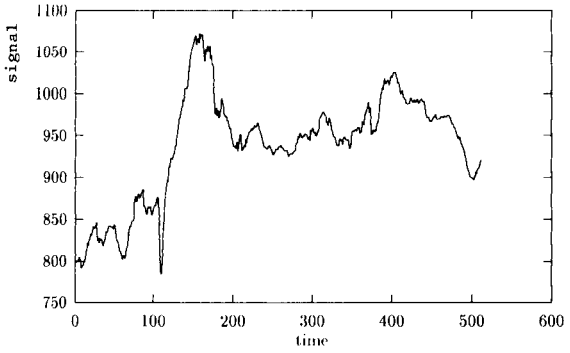

Fig. 9. Enthalpimetric FIA signal for 5.63×10^{-4} M imidazole sample.

M barium chloride and samples of 18-crown-6 of various concentrations.

During the experiments it was found that the position of the maximum wavelet transform coefficient is stable within a 1-week period. This means that in practice one does not have to perform the complete wavelet transform of the FIA signal. A convolution of the signal with a Morlet wavelet with the right parameters *a* and *b* is then sufficient.

Comparison with classical signal-processing procedures. To show the merits of the wavelet signal-processing method, the experimental data were also subjected to classical signal evaluation procedures in which the peak heights and peak areas are determined. The calibration data for wavelet intensity, peak height and peak area versus concentration were used in the procedure given by Funk et al. [16] to determine the detection limits of the various calibrations. The performance of the peak-area determination method was such that higher concentration ranges had to be used to fulfil the requirement that the lowest concentration used in the calibration series should be twice the test value x_p given by Funk et al.'s procedure.

TABLE 3

Peak intensities versus concentration for 18-crown-6 samples and barium chloride reagent

Concentration (10^{-3} M)	Calculated intensity	Intensity/ concentration	Deviation from mean (%)
4.50	3.293	0.731	0.1
4.50	3.208	0.712	−2.4
4.05	2.823	0.697	−4.5
4.05	2.809	0.693	−5.0
3.60	2.583	0.717	−1.7
3.60	2.515	0.698	−4.3
3.15	2.279	0.723	−0.9
3.15	2.136	0.678	−7.1
2.70	1.916	0.709	−2.8
2.70	2.028	0.751	2.8
2.25	1.615	0.717	−1.8
2.25	1.727	0.767	5.0
1.80	1.468	0.815	11.6
1.80	1.326	0.737	0.9
1.35	0.965	0.714	−2.1
1.35	1.102	0.816	11.7

TABLE 4

Detection limits (M) for different signal-processing techniques

Compound	Wavelet	Peak height	Peak area
Imidazole	3.8×10^{-4}	5.0×10^{-4}	3.2×10^{-3}
18-Crown-6	4.0×10^{-4}	8.5×10^{-4}	6.3×10^{-3}

The detection limits obtained are given in Table 4, which shows that the performance of the calibration with peak area is much poorer than that with peak height, whereas the improvement due to the application of the wavelet transform is more pronounced for the 18-crown-6-determination than for imidazole. This can be explained by the fact that the imidazole peaks are "narrower" and is in agreement with the simulation results where higher noise levels could be tolerated for EMG than for Gaussian peaks.

The authors express their thanks to H.F. Bulthuis for sharing his experience in wavelet theory with them.

REFERENCES

1 H. Poppe, Anal. Chim. Acta, 114 (1980) 59.
2 M. Valcarcel and M.D. Luque de Castro, Flow-Injection Analysis: Principles and Applications, Horwood, Chichester, 1987.
3 J. Ruczicka and E.H. Hansen, Flow-Injection Analyis, Wiley, New York, 2nd edn., 1988.
4 R. Tijssen, Anal. Chim. Acta, 114 (1980) 71.
5 A. Grossman and J. Morlet, J. Math. Phys., 26 (1985) 2473.

6 I. Daubechies and A. Grossmann, J. Math. Phys., 27 (1986) 1271.
7 A. Grossman and J. Morlet, SIAM J. Math. Anal., 15 (1984) 723.
8 R. Kronland-Martinet, J. Morlet and A. Grossman, Int. J. Pattern Recogn., 1 (1987) 273.
9 Y. Meyer, S. Jaffard and O. Rioul, Pour la Science, 119, September (1987) 28.
10 P. Dutilleux, in J.M. Combes, A. Grossmann and Ph. Tchamitchian (Eds), Wavelets Time–Frequency Methods and Phase Space, Springer, Berlin, 1990, p. 298.
11 J.P. Foley, Anal. Chem., 59 (1987) 1984.
12 J.P. Foley and J.G. Dorsey, J. Chromatogr. Sci., 22 (1984) 40.
13 J.J. Kirkland, W.W. Yan, H.J. Stoklosa and C.H. Dilks, Jr., J. Chromatogr. Sci., 15 (1977) 303.
14 S.H. Brooks, D.V. Leff, M.A. Hernandez Torres and J.G. Dorsey, Anal. Chem., 60 (1988) 2727.
15 K.L. Remmler, in C Scientific Library, Eigenware Technologies, Saratoga, CA, 1990, pp. 7–71.
16 W. Funk, V. Dammann and G. Donnevert, Qualitätsicherung in der Analytischen Chemie, VCH, Weinheim, 1992, pp. 21–30.

Analytica Chimica Acta, 267 (1992) 81–93
Elsevier Science Publishers B.V., Amsterdam

Comparison and evaluation of hierarchical cluster techniques applied to automated electron probe x-ray microanalysis data

Paul C. Bernard and René E. Van Grieken

Department of Chemistry, University of Antwerp (UIA) B-2610 Antwerp-Wilrijk (Belgium)

(Received 12th February 1992)

Abstract

For the processing of the large amount of data generated by automated electron probe x-ray microanalysis (EPXMA) of particulate samples, hierarchical cluster analysis are invoked. To evaluate the performance of seven hierarchical cluster techniques, cluster analyses were performed on a number of known mineral mixtures and the degree of correct classification was measured quantitatively by kappa statistics. In addition to the evaluation of the different cluster techniques, the influence on the cluster result of a number of experimental parameters was determined. In practice, ten mineral combinations were studied as a function of the mineral mixture ratio, using both normalized and unnormalized variables. For this purpose a total of 7000 cluster and kappa analyses were performed. In general, it seemed that Ward's method was most successful in finding the correct classification. For one mineral mixture, 2100 results were studied to elucidate the effect of the mixture size, of working with correlated/uncorrelated variables (principal component space) and of the quantification of the EPXMA data (different deconvolution techniques applied to quantitative data obtained by the Armstrong–Buseck ZAF corrections).

Keywords: Electron probe methods; X-ray fluorescence spectrometry; Cluster analysis; Hierarchical cluster techniques; Kappa statistics; Minerals

Owing to the ready availability of cluster algorithms in statistical computer packages an increase in cluster analysis in multivariate situations has occurred in many applications [1]. However, one of the hitherto unresolved problems in cluster analysis is the selection of a "best" method in some sense [2]. To solve this problem there have been two approaches. One of a theoretical nature was used by Jardine and Sibson [3] and Fisher and Van Ness [4]. In these cases the cluster techniques were compared with each other according to a set of theoretical criteria. On the other hand, there has been a tendency to use a mixing model to describe data sets [5]. The effectiveness of the cluster methods are compared across a variety of constructed data sets. These constructed sets are extremely useful for executing validation studies as the criterion, the true data structure, is known and the performance of the clustering algorithms can be objectively evaluated. The reports by Blashfield]6], Gross [7], Kuiper and Fisher [8], Cunningham and Ogilvie [9] and Rand [10] are some of these studies. These workers constructed artificial data sets with two or more multivariate normal distributions. Some of them perturbed their distributions to approximate natural data (measurements). However, none of them used real data. Nevertheless,

Correspondence to: R.E. Van Grieken, Department of Chemistry, University Antwerp (UIA), B-2610 Antwerp-Wilrijk (Belgium).

they all warn future users to be sceptical while considering the results of their specific application, or they suggest that any use of a cluster algorithm should be accompanied by other validation information.

Owing to the computer control of electron probe x-ray microanalysis (EPXMA) instruments, it became possible to localize, size and perform an x-ray analysis of a particle on a sequential base. This approach allows the analysis of a large number of features in a relatively short time. Applications are found in studies of atmospheric aerosols, asbestos fibres, mineral inclusions in coal and marine suspended particular matter. Because such an automated analysis rapidly yields a large data matrix, a straightforward interpretation is possible only when the individual particles are classified into particle types. For this purpose hierarchical cluster analyses can be applied. A large number of agglomerative hierarchical cluster procedures exist. These method start from m objects that are to be classified and at each step the two most similar objects or clusters are merged into a single cluster. Every object or cluster is a subgroup of a larger group. After $m-1$ steps all objects and clusters belong to one large cluster, namely the whole sample. The different hierarchical methods differ in the decision criteria of which objects and/or clusters are merged and in the calculation of the similarity of the newly obtained cluster and the remaining objects and/or clusters. In this study, the similarity between two objects or clusters is derived from the Euclidean distance coefficient. The Euclidean distance coefficient is defined as

$$d_{ij} = \left[\frac{\sum_{k=1}^{n} (x_{ik} - x_{jk})^2}{n} \right]^{1/2}$$

where d_{ij} = Euclidean distance coefficient between objects i and j;

x_{ik} = value of the ith object of the kth variable;

x_{jk} = value of the jth object of the kth variable;

n = number of variables;

for an n-dimensional orthogonal space. The Euclidean distance coefficient is calculated for every pair of objects, e.g., with m = the number of objects, $m(m-1)/2$ coefficients have to be calculated. A similarity matrix is then obtained. The standardization of the original variables can be accomplished by a z-transform:

$$z_{ij} = (x_{ij} - \bar{x}_{ij})/s_j$$

where $\bar{x}_{ij} = (1/m)\sum_{i=1}^{m}(x_{ij})$ with m objects and $s_j^2 = [1/(m-1)]\sum_{i=1}^{m}(x_{ij} - \bar{x}_{ij})^2$. All the newly formed z variables have a mean of zero and a variance 1. The overall effect of standardization is that all variables have equal weight.

Lance and Williams [11] showed that for some hierarchical methods the distances between the newly formed cluster (r) and the remaining objects and/or clusters (k) can be calculated from the existing elements of the similarity matrix and the parameters d_{ik}, d_{jk}, d_{ij}, m_i and m_j, where i and j are the clusters, with respectively m_i and m_j objects, at the smallest distance d_{ij} of the similarity matrix. The distance of the new cluster (r) and the remaining objects and/or clusters (k) is then calculated by

$$d_{rk} = \alpha_i d_{ik} + \alpha_j d_{jk} + \beta d_{ij} + \gamma | d_{ik} - d_{jk} |$$

where d_{xy} is the distance between clusters x and y. The different cluster algorithms are characterized by the values of α_i, α_j, β and γ. The values are summarized in Table 1

TABLE 1

Characterization of the hierarchical cluster methods by the coefficient values of the Lance and Williams equation [11]

Method	α_i	α_j	β	γ
Furthest neighbour	1/2	1/2	0	1/2
Nearest neighbour	1/2	1/2	0	−1/2
Group average	m_i/m_r	m_j/m_r	0	0
Simple average	1/2	1/2	0	0
Centroid	m_i/m_r	m_j/m_r	$-m_i m_j/m_r^2$	0
Median	1/2	1/2	−1/4	0
Ward's	$(m_i+m_k)/(m_r+m_k)$	$(m_j+m_k)/(m_r+m_k)$	$-m_k/(m_r+m_k)$	0

Previously we compared the hierarchical cluster techniques, used for the classification of estuarine and marine particulate EPXMA data, with respect to their applicability in the context of the geochemical studies [12]. This evaluation was rather intuitive and based on the experience gained: a satisfactory compromise was pursued between, on the one hand, describing the large data set using a minimum number of groups and, on the other, maintaining a maximum of geochemically relevant information avoiding the fusion of geochemically important groups. From this study it appeared that Ward's classification method served the purpose best. Somewhat less preferable seemed to be the furthest neighbour method, closely followed by the simple average and the group average methods. The nearest neighbour method was clearly the least satisfactory.

In this work, a more rigorous approach was used and mineral standards were analysed to serve as populations (particle types). The minerals were pulverized and measured with the automated electron microprobe. After investigation of the data structure and the removal of outliers, the data were used to construct artificial data sets, which allow the performance of the different cluster techniques to be evaluated. The hierarchical strategies used in this study were the furthest neighbour (complete linkage), nearest neighbour (single linkage), group average (unweighted average linkage), simple average (weighted average linkage), centroid sorting (unweighted centroid method), median method (weighted centroid method) and Ward's method (error sum of squares method). These were evaluated in relation to various parameters: the mixing ratio of the different minerals, the size (number of particles) of the mixtures, the use of unnormalized and normalized data and the use of a principal component space. Further, to predict the effect of the measurement errors, the influence of different x-ray spectral deconvolution techniques and the effect of the degree of accuracy and quantification in EPXMA (e.g., difference between the relative intensities data and the quantitative elemental weight composition data) were investigated.

The accuracy of the cluster solution with respect to the actual classification was measured by the statistic kappa [13]. The different cluster procedures were then compared on the basis of their kappa values. In order to provide some identification of the difficulty of the mixture for the cluster analysis, linear discriminant analysis (LDA) was conducted on each constructed data set. For some specific cases the data structure was studied by principal component analysis (PCA).

EXPERIMENTAL

Evaluation of the accuracy of the cluster solution

To measure the agreement of the obtained cluster solution with the true classification, the statistic kappa [13] was used. This statistic was introduced to provide a coefficient of agreement between two raters of nominal scales, but is also used to describe the agreement among multiple observers [14]. As the true classification is known, determined by the procedure for the generation of the mixture, kappa is a good measure of how good the cluster solution resembles the true classification. Kappa is defined as

$$\kappa = (p_o - p_c)/(1 - p_c)$$

where p_o is the observed proportion of agreements and p_c is the proportion of agreements expected by chance. The variation of kappa was calculated with an equation given by Fleiss et al. [15].

A difficulty in the determination of a kappa value for a cluster analysis is the fact that n kappa values can be calculated for a single cluster solution, where n is the number of populations (clusters). This is because, for each generated cluster, a population from the mixture has to be determined. If it is supposed that the user of the cluster techniques is able to select the appropriate population for each generated cluster, the maximum for kappa is obtained. Therefore, the largest kappa value is used for the comparison of the cluster techniques. When, however, the user makes a wrong decision about which population matches a cluster, the listed kappa values are

overestimated. On the other hand, randomly matching clusters and populations would lead to severe underestimates of the accuracy of the cluster solutions [6].

EPXMA measurements on standard minerals

The clay minerals used were dickite, montmorillonite, nontronite, illite and pyrophyllite from the American Petroleum Institute (API standards). The major elemental composition of the standards is given in Table 2. The grained mineral standards were suspended in water purified with a Milli-Q system (Millipore). Aliquots of these suspensions were filtered through a 25-mm diameter, 0.4-μm pore size Nucleopore membrane. Care was taken to obtain a sufficient loading for analysis while maintaining a low percentage (less than 5%) of overlapping particles [16]. After air drying in a laminar flow box, the filters were vacuum coated with carbon.

The automated EPXMA measurements were performed at an electron beam energy of 20 keV and a beam current of 1 nA. The magnification was 1000 × allowing particles larger than 0.28 μm in diameter to be analysed. The fast filter algorithm (FFA) [17] was used on-line and the results were stored on a floppy disk. The collected energy-dispersive x-ray spectra were stored on magnetic tape. This allowed off-line peak deconvolution of the spectra with regions of interest (ROI) and with the analytical x-ray analysis by iterative least-squares (AXIL) procedure [18,19]. The different deconvolution techniques gave the relative x-ray intensities for Na, Mg, Al, Si, K, Ca, Ti, Mn and Fe. These variables were used in the multivariate analysis. A difficulty arises in the removal of outliers at a 3σ level per variable as sometimes different outliers are generated by the different deconvolution techniques. Therefore, only real (robust) outliers are removed. These are defined as those particles which are outliers for the three techniques. In this way, homogeneous data sets are generated, which are used to create the mixtures.

Design of mixtures

In a first series of experiments, combinations of pairs of the five standard minerals were made to build up the mixtures. This resulted in ten different mineral combinations. For this purpose only the homogeneous AXIL-derived data of the minerals were used. For all these combinations the different cluster techniques were evaluated as a function of the mixing ratio of the two minerals. The mixing ratio, expressed as

$$\frac{\text{number of particles of mineral type } i}{\text{total number of particles in the mixture } i \text{ and } j} \times 100$$

was divided into five ranges, namely 1–10%, 10–30%, 30–70%, 70–90% and 90–99%. For each of these ranges ten random relative proportions were calculated and out of the pure (homogeneous) mineral data sets, objects (particles) were randomly chosen to build up the cluster structures while fulfilling the relative proportion criteria. The size of these newly formed mixtures was 100 objects (particles), which made the mixing ratio equal to the number of particles of mineral type i. Cluster analyses were performed with unstandardized and standardized (normalized) variables for each generated mixture, and the difficulty

TABLE 2

Bulk composition of the standard clay minerals, water excluded and the total iron content converted to Fe_2O_3

Mineral	Concentration (%, w/w)								
	Na_2O	MgO	Al_2O_3	SiO_2	K_2O	CaO	TiO_2	MnO_2	Fe_2O_3 [b]
Dickite	0.14		46.8	52.5	0.18	0.60	0.02	– [a]	0.01
Montmorillonite	0.22	6.06	21.6	66.4	0.61	2.95	0.42	0.01	2.11
Nontronite	0.18	0.08	6.55	51.2	0.30	2.42	–	–	40.0
Illite	0.47	2.27	20.3	62.4	5.59	1.74	0.88	–	5.76
Pyrophyllite	0.23	0.05	17.1	80.2	1.31	0.42	0.19	–	0.49

[a] –, Trace content. [b] Total metal content converted to Fe_2O_3.

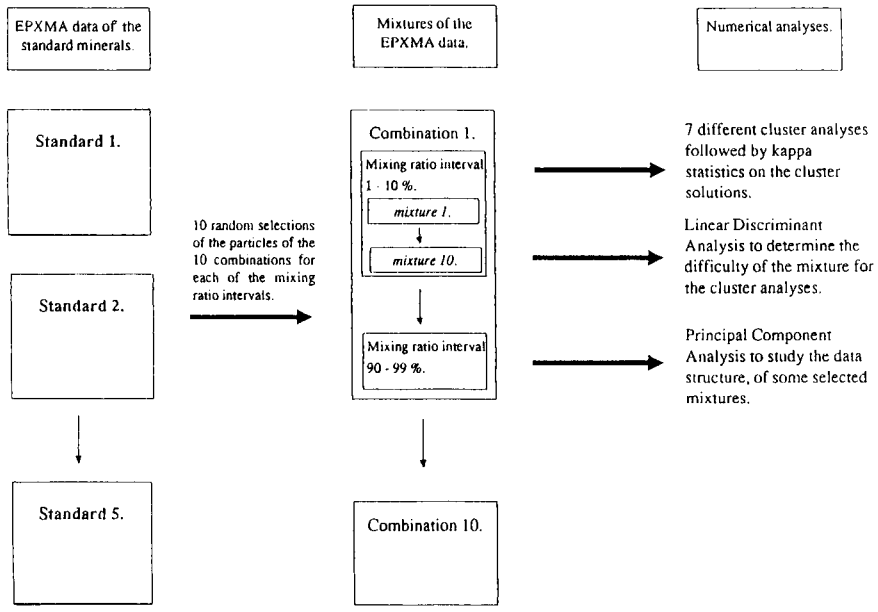

Fig. 1. Scheme of the creation of the mineral mixtures and of the analyses performed on the mixtures.

with the cluster analysis for the created mixture was checked by conducting linear discriminant analysis. The data structure of some selected mixtures was elaborated by the use of PCA. Figure 1 illustrates the scheme for the creation of the different mixtures of each mixing ratio range for every combination and of the analyses performed on the mixtures. These experiments allowed the study of the performance of the different cluster techniques for the ten different mineral combinations, the influence of the mixing ratio and the use of normalized variables.

In a second series of experiments, mixtures were constructed to study the influence of the total number of particles of the mixture, the use of uncorrelated variables (e.g., the use of a principal component space), the effect of the different deconvolution techniques and the effect of the degree of quantification. To build up these different kinds of mixtures, the homogeneous dickite and montmorillonite data sets were selected. Table 3 summarizes these experiments and lists the experimental parameters.

For the construction of all the mixtures two

TABLE 3

Experimental parameters and mixture types used for the second series of experiments

To study the influence of	Data normalization [a]	Mixture size (No. of particles)	Deconvolution technique (see text)
Mixture size	Unst.–stand.	200	FFA
Different deconvolution techniques	Unst.–stand.	100	ROI
	Unst.–stand.	100	FFA
	Unst.–stand.	100	AXIL
Clustering in the PC space	Unst.–stand.	100	FFA
Quantification of the data	Unst.–stand.	100	ZAF-corrected AXIL

[a] Unst. = unstandardized variables; stand. = standardized variables.

mineral types were used. Therefore, the multivariate analyses were performed in such a way that two clusters were obtained.

Data handling and the multivariate analysis were performed with a VAX 11/780 computer. Data presentation, the PCA and the hierarchical cluster analysis were done using the Data Processing Program (DPP) software package, developed by Van Espen [20]. A statistical program by Hebrant [21] was used for the linear discriminant analysis. Programs for the creation of the mixtures and for the calculation of the statistic kappa were written in FORTRAN 77.

RESULTS AND DISCUSSION

For the first series of experiments, the homogeneous data sets, obtained by the AXIL deconvolution technique for the standard minerals, were used. As an illustration, Table 4 shows the complete results of one such analysis, namely for the dickite–nontronite combination, for the mixing range 30–70%, using unstandardized variables. Similar tables were produced and studied for all other mineral combinations, mixing ratio intervals and standardized/unstandard variables.

For the dickite–nontronite mixing ratio range 30–70% the linear discriminant analysis (LDA) found for all the mixtures the correct classification, whereas the different cluster techniques gave a cluster solution that matched the true classification in only about 50% of the cases. The mean kappa value of the cluster solutions seems to approximate the probability for a good classification. Indeed, in most instances the kappa value is either near to one or zero, in which case binomial statistics apply. This means that either the correct classification or a totally wrong one was found.

TABLE 4

Results of the ten cluster (with unstandardized variables) and kappa analyses for the 30–70% mixing ratio interval of the dickite–nontronite combination

Mixture No.	Mixing ratio (%)	Kappa value (standard deviation)						
		Ward's	Furthest neighbour	Nearest neighbour	Group average	Simple average	Centroid	Median
1	65	1	1	1	1	1	1	1
		(0)	(0)	(0)	(0)	(0)	(0)	(0)
2	31	0.954	0.0274	0.0274	0.0274	0.0274	0.0274	0.0274
		(0.001)	(0.0003)	(0.0003)	(0.0003)	(0.0003)	(0.0003)	(0.0003)
3	38	1	0.0123	0.0123	0.0123	0.0123	0.0123	0.0123
		(0)	(0.0002)	(0.0002	(0.0002)	(0.0002)	(0.0002)	(0.0002)
4	68	1	0.929	0.083	1	0.083	1	0.083
		(0)	(0.002)	(0.003)	(0)	(0.003)	(0)	(0.003)
5	53	0.940	0.879	0.067	0.940	0.0225	0.940	0.879
		(0.001)	(0.002)	(0.001)	(0.001)	(0.0005)	(0.001)	(0.002)
6	36	0.854	0.0113	0.0113	0.0113	0.0113	0.0113	0.0113
		(0.003)	(0.0001)	(0.0001)	(0.0001)	(0.0001)	(0.0001)	(0.0001)
7	66	1	0.955	0.038	0.955	0.038	0.955	0.038
		(0)	(0.001)	(0.001)	(0.001)	(0.001)	(0.001)	(0.001)
8	65	0.9779	0.109	0.037	0.9779	0.956	0.109	0.956
		(0.0005)	(0.003)	(0.001)	(0.0005)	(0.001)	(0.003)	(0.001)
9	37	1	0.0237	0.0478	1	0.875	1	0.875
		(0)	(0.0003)	(0.0006)	(0)	(0.002)	(0)	(0.002)
10	30	0.931	0.844	0.00862	0.0351	0.00862	0.0351	0.00862
		(0.001)	(0.003)	(0.00008)	(0.0003)	(0.00008)	(0.0003)	(0.00008)
< >	49	0.97	0.48	0.13	0.60	0.30	0.51	0.39
σ	(16)	(0.05)	(0.47)	(0.31)	(0.49)	(0.44)	(0.50)	(0.47)
σ_m	(5)	(0.02)	(0.15)	(0.10)	(0.16)	(0.14)	(0.16)	(0.15)

This is also the reason for the relatively high standard deviations. To investigate the differences in performance of the different cluster techniques, two mixtures will be discussed in detail, namely mixtures 1 and 3 consisting of 65% dickite–35% nontronite and 31% dickite–69% nontronite particles, respectively. The correct cluster solution was found if the cluster techniques were applied to mixture 1. For mixture 3 the correct cluster solution was obtained only by Ward's method. PCA was used to study the data structures of these mixtures. When the scores of the first two principal components were plotted, a clear distinction was seen between the two mineral types, confirming the LDA results, which showed that no particle overlap occurred between the two groups. However, the variance for the nontronite mineral particles is higher than that for the dickite particles. When the dendrograms of Ward's and the furthest neighbour methods were compared, the main difference between the cluster solutions is that using the latter method the dickite group was joined with the nontronite group before this last group was complete. A single particle group, containing a nontronite particle and a group of 99 particles was obtained, containing dickite and nontronite particles. In practice, a specialist would probably find the correct, or nearly correct, classification by studying the dendrogram and the properties of the particles in the clusters. In this case our kappa values are underestimates.

It is seen that, on average, the cluster solutions of Ward's method have the highest probability of correct classification (0.97 ± 0.02, Table 4). For five mixtures (2, 5, 6, 8 and 10), kappa values < 1 were obtained. The only mixture for which all the cluster techniques gave the correct classification is mixture 1. It was also the only mixture for which the nearest neighbour method was successful. For all other mixtures, the nearest neighbour method gave kappa values near zero. For the other mixtures it is seen that the group average, centroid, furthest neighbour, median and simple

TABLE 5

Results of the cluster (with unstandardized variables) and kappa analyses for the 1–10% mixing ratio range of the ten combinations for the different cluster techniques

Mixture	Mean kappa value (standard deviation)						
	Ward's	Furthest neighbour	Nearest neighbour	Group average	Simple average	Centroid	Median
Dickite–montmorrinolite	1	0.98	1	1	0.98	1	1
	(0)	(0.01)	(0)	(0)	(0.01)	(0)	(0)
Dickite–nontronite	0.53	0.12	0.0028	0.20	0.11	0.20	0.12
	(0.10)	(0.07)	(0.0006)	(013)	(0.07)	(0.13)	(0.07)
Dickite–illite	0.015	0.005	0.0022	0.004	0.004	0.04	0.006
	(0.004)	(0.002)	(0.0008)	(0.002)	(0.002)	(0.002)	(0.002)
Dickite–pyrophyllite	0.027	0.028	0.005	0.027	0.031	0.027	0.04
	(0.005)	(0.005)	(0.004)	(0.005)	(0.009)	(0.005)	(0.001)
Montmorrinolite–nontronite	0.38	0.11	0.0026	0.004	0.06	0.004	0.11
	(0.10)	(0.07)	(0.0006)	(0.001)	(0.05)	(0.001)	(0.07)
Montmorrinolite–illite	0.010	0.005	0.0022	0.004	0.0024	0.004	0.0024
	(0.003)	(0.002)	(0.0008)	(0.001)	(0.0006)	(0.002)	(0.0006)
Montmorrinolite–pyrophyllite	0.027	0.027	0.005	0.027	0.021	0.027	0.031
	(0.005)	(0.005)	(0.004)	(0.005)	(0.005)	(0.005)	(0.008)
Nontronite–illite	0.017	0.11	0.10	0.004	0.005	0.004	0.006
	(0.004)	(0.07)	(0.10)	(0.002)	(0.002)	(0.002)	(0.002)
Nontronite–pyrophyllite	0.024	0.024	0.47	0.024	0.44	0.024	0.27
	(0.005)	(0.005)	(0.16)	(0.005)	(0.14)	(0.005)	(0.13)
Illite–pyrophyllite	0.021	0.06	0.08	0.07	0.06	0.07	0.06
	(0.008)	(0.05)	(0.05)	(0.05)	(0.05)	(0.05)	(0.05)

average methods do find the correct classification in some instances.

The summarized results of the first series of experiments for the cluster analysis performed with unstandardized variables are given in Tables 5–9. Each of these tables represents the results for each mixing ratio interval, for the ten combinations, and hence the result of 700 cluster and kappa analyses. Each value represents the mean of ten analyses. The standard deviations on the means are given in parentheses.

When the mixtures of the first series of experiments were studied by the use of LDA, it was seen that the dickite–montmorillonite, dickite–nontronite and dickite–illite mixtures were clearly distinguished. All other mixtures have particle overlap, the dickite–pyrophyllite, montmorillonite–nontronite and montmorillonite–illite to a lesser extent than the remaining, last four, mixtures. The difficulty with the cluster techniques for the mixtures is directly reflected in the cluster solutions and the kappa results. Relatively good results are obtained for the mixtures with no, or little, particle overlap.

In general, for all the mixtures, it seems that Ward's method was the most successful in finding the correct classification, except for the nontronite–pyrophyllite mixture where the nearest neighbour and simple average methods give significantly higher mean kappa values. This is probably due to their ability to form chained clusters. In this way the complete elongated pyrophyllite cluster is formed before the nontronite particles are jointed. In the other cluster methods, the nontronite particles are joined with part of the pyrophyllite group at an earlier stage, leading to a wrong cluster solution. For mixtures with a low difficulty for the cluster techniques, e.g., the dickite–montmorillonite mixtures, the mean kappa values of all the cluster techniques approach each other near the upper limit of one. For the more difficult mixtures. Ward's method has in most instances a significantly better mean kappa value. The furthest neighbour, group average and cen-

TABLE 6

Results of the cluster (with unstandardized variables) and kappa analyses for the 10–30% mixing ratio range of the ten combinations for the different cluster techniques

Mixture	Mean kappa value (standard deviation)						
	Ward's	Furthest neighbour	Nearest neighbour	Group average	Simple average	Centroid	Median
Dickite–montmorillonite	1	0.995	1	1	1	1	1
	(0)	(0.005)	(0)	(0)	(0)	(0)	(0)
Dickite–nontronite	0.94	0.10	0.008	0.20	0.010	0.20	0.010
	(0.03)	(0.09)	(0.001)	(0.13)	(0.001)	(0.13)	(0.001)
Dickite–illite	0.15	0.03	0.02	0.03	0.03	0.03	0.03
	(0.10)	(0.01)	(0.01)	(0.01)	(0.01)	(0.01)	(0.01)
Dickite–pyrophyllite	0.13	0.12	0.01	0.10	0.17	0.10	0.12
	(0.03)	(0.02)	(0.01)	(0.01)	(0.05)	(0.01)	(0.02)
Montmorillonite–nontronite	0.72	0.18	0.008	0.010	0.010	0.010	0.010
	(0.09)	(0.12)	(0.001)	(0.001)	(0.001)	(0.001)	(0.001)
Montmorillonite–illite	0.04	0.03	0.008	0.03	0.03	0.03	0.03
	(0.01)	(0.01)	(0.001)	(0.01)	(0.01)	(0.01)	(0.01)
Montmorillonite–pyrophyllite	0.12	0.10	0.02	0.09	0.09	0.09	0.09
	(0.02)	(0.01)	(0.01)	(0.01)	(0.02)	(0.01)	(0.01)
Nontronite–illite	0.30	0.12	0.04	0.04	0.04	0.04	0.04
	(0.13)	(0.10)	(0.02)	(0.02)	(0.02)	(0.02)	(0.02)
Nontronite–pyrophyllite	0.32	0.25	0.22	0.07	0.27	0.07	0.25
	(0.13)	(0.12)	(0.11)	(0.01)	(0.11)	(0.01)	(0.11)
Illite–pyrophyllite	0.06	0.04	0.06	0.06	0.04	0.06	0.04
	(0.02)	(0.02)	(0.02)	(0.02)	(0.02)	(0.01)	(0.01)

troid methods seem to be slightly better than the simple average, median and nearest neighbour methods. However, the differences are not always significant, and the rule is not generally applicable.

The influence of the mixing ratio can be studied by comparing Tables 5–9. The differences between the mean kappa values for the different mixing ratio ranges are sometimes significant. These differences can be understood via the data structure of the mixtures. For instance, all the dickite mixtures show high mean kappa values when a large amount of the more compact dickite group is present. Maximum kappa values are encountered for the 90–99% relative mixing ratio range. This also applies to the montmorillonite mixtures, for which in the case of the mixtures with nontronite, illite and pyrophyllite the montmorillonite group is not only more compact but also the particle overlap is reduced for the higher mixing ratio ranges. The nontronite–illite and nontronite–pyrophillite mixtures seem to have a maximum mean kappa value for the 30–70% mixing ratio range. For the illite–pyrophyllite mixture, very low kappa values were determined for all the mixing ratio ranges.

To assess the influence of variable normalization, by a z-transform, all the cluster analyses on the mixtures were also performed with standardized variables. It was seen that for mixtures having low abundance variables, or variables with low variations, which have a discriminatory power for the distinction of the minerals, the cluster solutions (in most instances only those of Ward's method) are improved when standardized variables are used. This is the case for the mixtures nontronite–pyrophyllite, dickite–illite, montmorillonite–illite, nontronite–illite and montmorillonite–pyrophyllite for some of the mixing ratio ranges. Normalization makes the low abundance variables and/or low variation more important in the calculation of the similarity matrix. For some

TABLE 7

Results of the cluster (with unstandardized variables) and kappa analyses for the 30–70% mixing ratio range of the ten combinations for the different cluster techniques

Mixture	Mean kappa value (standard deviation)						
	Ward's	Furthest neighbour	Nearest neighbour	Group average	Simple average	Centroid	Median
Dickite–montmorillonite	0.995 (0.002)	1 (0)	0.89 (0.10)	1 (0)	1 (0)	1 (0)	1 (0)
Dickite–nontronite	0.97 (0.02)	0.48 (0.15)	0.13 (0.10)	0.60 (0.16)	0.30 (0.14)	0.51 (0.16)	0.39 (0.15)
Dickite–illite	0.56 (0.15)	0.040 (0.009)	0.026 (0.004)	0.040 (0.009)	0.040 (0.009)	0.040 (0.009)	0.036 (0.008)
Dickite–pyrophyllite	0.34 (0.08)	0.19 (0.03)	0.19 (0.05)	0.19 (0.03)	0.22 (0.04)	0.19 (0.03)	0.19 (0.03)
Montmorillonite–nontronite	0.91 (0.02)	0.26 (0.13)	0.036 (0.008)	0.15 (0.10)	0.26 (0.13)	0.15 (0.10)	0.14 (0.10)
Montmorillonite–illite	0.27 (0.12)	0.04 (0.01)	0.026 (0.004)	0.040 (0.009)	0.040 (0.009)	0.040 (0.009)	0.040 (0.009)
Montmorillonite–pyrophyllite	0.21 (0.03)	0.21 (0.03)	0.19 (0.04)	0.21 (0.03)	0.24 (0.03)	0.17 (0.03)	0.21 (0.03)
Nontronite–illite	0.70 (0.11)	0.12 (0.09)	0.030 (0.004)	0.025 (0.005)	0.12 (0.09)	0.027 (0.005)	0.12 (0.09)
Nontronite–pyrophyllite	0.89 (0.02)	0.36 (0.13)	0.14 (0.08)	0.10 (0.03)	0.32 (0.12)	0.10 (0.03)	0.32 (0.12)
Illite–pyrophyllite	0.15 (0.06)	0.05 (0.01)	0.03 (0.01)	0.04 (0.01)	0.028 (0.007)	0.032 (0.009)	0.028 (0.007)

TABLE 8

Results of the cluster (with unstandardized variables) and kappa analyses for the 70–90% mixing range of the ten combinations for the different cluster techniques

Mixture	Mean kappa value (standard deviation)						
	Ward's	Furthest neighbour	Nearest neighbour	Group average	Simple average	Centroid	Median
Dickite–montmorillonite	0.996	1	0.50	1	0.75	1	0.75
	(0.004)	(0)	(0.17)	(0)	(0.14)	(0)	(0.14)
Dickite–nontronite	0.99	0.64	0.20	0.64	0.48	0.64	0.48
	(0.01)	(0.14)	(0.09)	(0.14)	(0.14)	(0.14)	(0.14)
Dickite–illite	0.86	0.17	0.15	0.17	0.17	0.17	0.17
	(0.10)	(0.04)	(0.04)	(0.04)	(0.04)	(0.04)	(0.04)
Dickite–pyrophillite	0.68	0.40	0.15	0.28	0.34	0.28	0.34
	(0.08)	(0.09)	(0.05)	(0.04)	(0.08)	(0.04)	(0.07)
Montmorillonite–nontronite	0.95	0.51	0.37	0.37	0.41	0.37	0.41
	(0.02)	(0.14)	(0.13)	(0.13)	(0.13)	(0.13)	(0.13)
Montmorillonite–illite	0.49	0.16	0.11	0.11	0.16	0.12	0.16
	(0.13)	(0.04)	(0.02)	(0.02)	(0.04)	(0.02)	(0.04)
Montmorillonite–pyrophyllite	0.40	0.34	0.24	0.29	0.34	0.29	0.34
	(0.03)	(0.03)	(0.01)	(0.03)	(0.02)	(0.03)	(0.02)
Nontronite–illite	0.71	0.03	0.04	0.03	0.03	0.03	0.03
	(0.08)	(0.01)	(0.01)	(0.01)	(0.01)	(0.01)	(0.01)
Nontronite–pyrophyllite	0.82	0.08	0.009	0.010	0.08	0.010	0.08
	(0.02)	(0.07)	(0.003)	(0.003)	(0.07)	(0.003)	(0.07)
Illite–pyrophyllite	0.15	0.02	0.008	0.02	0.010	0.02	0.02
	(0.04)	(0.01)	(0.001)	(0.01)	(0.002)	(0.01)	(0.01)

TABLE 9

Results of the cluster (with unstandardized variables) and kappa analyses for the 90–99% mixing ratio range of the ten combinations for the different cluster techniques

Mixture	Mean kappa value (standard deviation)						
	Ward's	Furthest neighbour	Nearest neighbour	Group average	Simple average	Centroid	Median
Dickite–montmorillonite	1	1	0.60	0.90	0.70	0.90	0.70
	(0)	(0)	(0.16)	(0.10)	(0.15)	(0.10)	(0.15)
Dickite–nontronite	0.993	0.84	0.75	0.76	0.76	0.76	0.76
	(0.007)	(0.10)	(0.12)	(0.12)	(0.12)	(0.12)	(0.12)
Dickite–illite	0.81	0.61	0.32	0.47	0.52	0.37	0.52
	(0.08)	(0.10)	(0.07)	(0.08)	(0.09)	(0.07)	(0.09)
Dickite–pyrophyllite	0.68	0.56	0.27	0.47	0.41	0.45	0.40
	(0.08)	(0.07)	(0.06)	(0.07)	(0.08)	(0.06)	(0.08)
Montmorillonite–nontronite	0.983	0.76	0.65	0.65	0.76	0.65	0.76
	(0.009)	(0.12)	(0.13)	(0.13)	(0.12)	(0.13)	(0.12)
Montmorillonite–illite	0.61	0.51	0.35	0.35	0.40	0.35	0.40
	(0.08)	(0.09)	(0.05)	(0.05)	(0.06)	(0.05)	(0.06)
Montmorillonite–pyrophyllite	0.60	0.42	0.36	0.39	0.42	0.41	0.41
	(0.05)	(0.07)	(0.06)	(0.06)	(0.07)	(0.06)	(0.06)
Nontronite–illite	0.48	0.02	0.05	0.09	0.02	0.06	0.02
	(0.07)	(0.02)	(0.02)	(0.05)	(0.02)	(0.04)	(0.02)
Nontronite–pyrophyllite	0.60	0.07	0.007	0.03	0.07	0.03	0.07
	(0.07)	(0.06)	(0.005)	(0.02)	(0.07)	(0.02)	(0.07)
Illite–pyrophyllite	0.07	0.0033	0.0031	0.0033	0.0033	0.0033	0.0033
	(0.01)	(0.0006)	(0.0006)	(0.0006)	(0.0006)	(0.0006)	(0.0006)

mixtures under study, these were the K, Al, Ca and Fe variables. On the other hand, the possibility exists that owing to variables with no relevant variation and/or data subject to a high experimental error, the normalization of the data leads to a data matrix in which these "insignificant" variables become relatively more important. Cluster analysis on such a matrix will result in worse cluster results.

The results of the second series of experiments (Table 3) for the cluster analysis, performed on the dickite–montmorillonite mixtures, with unstandardized variables for the 30–70% mixing ratio range are given in Table 10. This table presents the result of 420 cluster and kappa analyses, while each value is the mean of ten kappa analyses. Standard deviations on the means are given in parentheses. Similar tables were produced for all other mixing ratio ranges.

The highest kappa values are obtained for the Ward's cluster solutions, which means that these resemble the correct classification most closely. The other cluster techniques seem to perform as good as Ward's method or worse, but their results are not significantly different from each other for the mixing ratio ranges 1–10%. 10–30% and 30–70%, except for the cluster results in the PC space. For the mixing ratio ranges 70–90% and 90–99% the furthest neighbour, group average and in some instances the centroid methods seem to perform better than the other methods, as was already shown in the first series of experiments.

Influence of mixing ratio

Significant differences were encountered for the mixing ratio ranges 70–90% and 90–99%, whereas the lowest kappa values were obtained for the 0–10% and 10–30% ranges. Relatively good results were obtained for the other mixing ratio ranges. The reason for this must probably be sought in the data structures of the mixtures. However, none of the mixtures gave any problem with the linear discriminant analysis for finding the correct classification. It is assumed, however, that owing to the data structure in the ranges 1–10% and 10–30% the cluster analysis gives a solution with a single particle (montmorillonite) cluster.

Influence of mixture size

By comparing the cluster solutions of the 200 and 100 particle size mixtures (FFA derived), it is seen that in most instances no significant variations were encountered. Only the nearest neighbour method seems to perform worse with the 200 particle mixtures for higher mixing ratios.

TABLE 10

Results of the cluster (with standardized variables) and kappa analyses for the 30–70% mixing ratio range the dickite–montmorillinote mixtures (second series of experiments)

Mixture types (see Table 2)	Mean kappa value (standard deviation)						
	Ward's	Furthest neighbour	Nearest neighbour	Group average	Simple average	Centroid	Median
Mixture size	1	0.999	0.41	1	0.90	1	1
200 particles	(0)	(0.001)	(0.16)	(0)	(0.10)	(0)	(0)
Different deconvolution techniques:							
ROI	0.995	0.99	0.995	0.995	0.995	0.995	0.995
	(0.003)	(0.01)	(0.003)	(0.003)	(0.003)	(0.003)	(0.003)
FFA	1	0.89	0.89	0.89	0.89	0.89	0.89
	(0)	(0.10)	(0.10)	(0.10)	(0.10)	(0.10)	(0.10)
AXIL	0.998	1	0.89	1	1	1	1
	(0.002)	(0)	(0.10)	(0)	(0)	(0)	(0)
Clustering in the	0.84	0.13	0.020	0.03	0.04	0.019	0.019
PC space	(0.10)	(0.07)	(0.004)	(0.01)	(0.03)	(0.004)	(0.004)
Quantification of	0.998	0.998	1	1	0.998	1	0.998
the data	(0.002)	(0.002)	(0)	(0)	(0.002)	(0)	(0.002)

This phenomenon was also reported by Blashfield [6].

In general, this leads to the conclusion that for this kind of mixture, the results obtained for a limited data set can be extrapolated to larger data sets.

Influence of deconvolution technique

Among the different deconvolution techniques, no significant performance differences were observed when Ward's method was used for any of the relative mixing ratio ranges. For the other cluster techniques, it was seen that in most instances the ROI and AXIL techniques gave comparable results. Using the FFA, the probability of a good classification is reduced, in most instances, especially when cluster techniques other than Ward's method were used. This example shows that the choice of the deconvolution technique, for instance, influences not only the number of detected peaks and the accuracy of the peak intensities, but also the results of the hierarchical cluster analysis.

Influence of working in the principal component space

Applying a PCA to the data before a clustering is performed was introduced in order to eliminate redundant information by obtaining a small number of variables, i.e., removing noise by working only with the most important principal components, and to eliminate the errors introduced, when the Euclidean distance is calculated with correlated variables, by using the uncorrelated principal components for the calculation of the similarity matrix.

To elucidate the influence of working in a principal component space, a PCA was performed on the generated mixtures (mixture size = 100, deconvolution technique = FFA). The component scores of the principal components were used to determine the similarity matrix. The mean kappa values for the clustering in the principal component space are significantly smaller than for the original variable space. It seems that, while the total variance is preserved by the PCA, the use of uncorrelated variables reduces the mean kappa values. For this particular mixture it is preferable to work with the original variables.

Influence of the method of quantification of the data

The effect of the analytical error on the classification process has seldom been studied. Therefore, it was difficult to predict the influence on the cluster solution of applying the cluster analysis to the relative peak intensities rather than to the results corrected by the Armstrong–Buseck ZAF correction. The Armstrong–Buseck ZAF correction method [22,23] is applied to the net x-ray intensites to obtain an accurate chemical composition of particles of a particular shape. With respect to the required computer time it is sometimes preferred to apply the ZAF correction to the average composition of the groups obtained by the cluster analysis. To elucidate the effect of the clustering on semi-quantitative results, Armstrong–Buseck ZAF corrections were applied to the net peak intensities obtained by the AXIL technique for the standard minerals. On comparing the cluster solutions of all the cluster techniques for the AXIL semi-quantitative and quantitative EPXMA data sets, no significant differences were obtained. This will depend, of course, on the elements which have discriminatory power between the samples. For the studied dickite–montmorillonite mixtures there is no influence of the quantification of the dickite and montmorillonite particles detected on the obtained cluster solutions.

Generally, for the EPXMA analysis of mineral particles followed by the classification of the individual particulate data, the following procedure is proposed: use of the ROI or the AXIL deconvolution technique and use of Ward's method with unstandardized original variables.

This work was partially supported by the Belgian Ministry of Science Policy (under contract No. EV7/08).

REFERENCES

1 D.L. Massart and L. Kaufman, The Interpretation of Analytical Data by the Use of Cluster Analysis, Wiley, New York, 1983, Chap. 7.
2 B.S. Everitt, Biometrics, 35 (1979) 169.

3 N. Jardine and R. Sibson, Comput. J., 11 (1968) 177.
4 L. Fisher and J.W. Van Ness, Biometrika, 58 (1971) 91.
5 J.H. Wolfe, Multivar. Behav. Res., 5 (1970) 329.
6 R.K. Blashfield, Psychol. Bull., 83 (1976) 377.
7 A.J. Gross, Multivar. Behav. Res., 7 (1972) 379.
8 F.K. Kuiper and L. Fisher, Biometrics, 31 (1975) 777.
9 K.M. Cunningham and J.C. Ogilvie, Comput. Mode, 15 (1971) 209.
10 W.M. Rand, J. Am. Statist. Assoc., 66 (1971) 846.
11 G.N. Lance and W.T. Williams, Aust. Comput. J., 1 (1967) 15.
12 P.C. Bernard, R.E. Van Grieken and D. Eisma, Environ. Sci. Technol., 20 (1986) 467.
13 J. Cohen, Educ. Psychol. Meas., 20 (1960) 37.
14 J. Landis and G.G. Koch, Biometrics, 33 (1977) 363.
15 L. Fleiss, J. Cohen and B.S. Everitt, Psychol. Bull., 72 (1969) 323.
16 J.F. Kelly, R.J. Lee and S. Lentz, Scanning Electron Microsc., 1 (1980) 311.
17 J.P. Op de Beek, At. Energy Rev., 13 (1975) 743.
18 H. Nullens, P. Van Espen and F. Adams, X-Ray Spectrom., 8 (1979) 104.
19 P. Van Espen, H. Nullens and F. Adams, Nucl. Instrum. Methods, 142 (1977) 243.
20 P. Van Espen, Anal. Chim. Acta, 165 (1984) 31.
21 F. Hebrant, Biom. Praxim., 14 (1974) 15.
22 J. Armstrong and P.R. Buseck, Anal. Chem., 47 (1975) 2178.
23 H.M. Storms, K. Janssens, Sz.B. Török and R.E. Van Grieken, X-Ray Spectrom., 18 (1989) 45.

Analytica Chimica Acta, 267 (1992) 95–102
Elsevier Science Publishers B.V., Amsterdam

Application of multi-component analysis to the simultaneous resolution of phenol compounds in mixtures

Part I. Development of the calculation methods and experimental methodology

Andreu Cladera, Enrique Gómez, José Manuel Estela and Víctor Cerdà

Department of Chemistry, University of the Balearic Islands, E-07071 Palma de Mallorca (Spain)

(Received 22nd October 1991; revised manuscript received 16th March 1992)

Abstract

The computer program MULTI3, which includes new calibration methods for the resolution of mixtures of analytes by multiple linear regression from data provided by a diode-array spectrophotometer, was developed. The different calibration methods available, which include those of the single standard, multiple standards and multiple addition of standard, are described. The program was applied to the resolution of mixtures of up to nine phenol compounds by using the different calibration alternatives on the normal and first- and second-derivative absorption spectra. The sets of results thus obtained are critically compared.

Keywords: UV–Visible spectrophotometry; Phenols

The earliest attempts at developing simultaneous spectrophotometric determinations of two or more components in a chemical system were reported in the early 1970s. They were aimed at avoiding the laborious operational procedures involved whenever the mixture components had similar chemical features and thus interfered with the determination of one another.

These early attempts included a study by Sternberg et al. [1] on the kinetic determination of ergosterol and its UV photochemical isomerization products. They accomplished the simultaneous resolution of the five components of a mixture by using a least-squares matrix calculus procedure. However, the great complexity of the calculations involved in processing spectral data and the incipient stage of development of microcomputers prevented further advances in this field for some time.

The great breakthroughs in microelectronics and computer science in the last few years have fostered the gradual spread of compatible personal computers in chemical laboratories. This, among other factors, has revived interest and research on simultaneous analyses of multi-component systems that can now be performed much more affordably and with a higher success rate than in the past.

Simultaneous resolutions of mixtures of components with markedly overlapped spectra rely on the use of a number of algorithms that have been developed as part of highly specialized software. Such algorithms include those of least-squares fitting [2], the simplex iteration method [3], the Kalman filter [4] and various other programs supplied by spectrophotometer manufacturers as

Correspondence to: V. Cerdà, Department of Chemistry, University of the Balearic Islands, E-07071 Palma de Mallorca (Spain).

bundled software (e.g., the multi-component analysis algorithm from Hewlett-Packard [5]).

More recently, Sala et al. [6] compared the results obtained by using three computer programs based on different algorithms, namely multi-component analysis, simplex and MULTIC. MULTIC is a multi-linear regression program that involves fitting the calculated mixed spectrum to its experimental counterpart through the standard deviation, correlation coefficient and an independent term corresponding to the intercept on the absorbance axis. The authors applied the three algorithms to the resolution of a mixture of pharmaceuticals and found MULTIC to provide the best results.

The different algorithms applied so far to mixture resolution allow a maximum of five components to be resolved.

In continuation of previous work on this topic [7–9] a new calculation method has been developed that takes advantage of the potential of diode-array spectrophotometers for the simultaneous determination of up to nine phenol compounds. These substances, which have been thoroughly studied in the last few years on account of their relevance to environmental analysis, have been the subject of several studies aimed at developing simultaneous determinations for mixtures of up to three of them [10,11].

The resolution of the mixtures was carried out by using the program MULTI3 developed by the authors. This program, like MULTIC [6], achieved the resolution of several components by using a least-squares multiple linear regression. The chief asset of this work lies in the development of new calibration methods which allow, as shown below, a better performance in relation to earlier alternatives.

MATHEMATICAL BACKGROUND

For a mixture of N absorbing components in the absence of matrix effects and chemical interaction, Beer's law can be written as

$$A_j = \sum_{i=1}^{N} \epsilon_{ij} b c_i; \quad \forall_j = 1 \ldots M \qquad (1)$$

where A_j is the absorbance of the mixture at wavelength j, ϵ_{ij} is the molar absorptivity of component i at wavelength j, b is the optical path length and c_i is the concentration of component i in the mixture. If a number M of wavelengths greater than that of components is used, then Eqn. 1 can be converted into an overdimensioned equation system which, once all ϵ_{ij} values are known, can be solved by least-squares multiple linear regression in order to obtain the concentration of each component in the mixture minimizing the sum of the squares of the residues $(A_{\text{exp}} - A_{\text{calc}})$. In the resolution, an independent term (a) can be introduced which allows, in part, compensation for the matrix effects and chemical interactions which may cause significant deviations from a zero intercept.

The ϵ_{ij} values can be determined by various procedures. Most frequently, they are calculated by using a standard of known concentration for each component (the single standard procedure). In order to avoid the drawbacks involved in using a single standard, some workers employ averaged standards that can be obtained either by repeating the use of a given standard n times or, alternatively, standards of different concentrations within the linear range, the spectra of which are standardized to unit concentration.

One other alternative unused to date lies in calculating the ϵ_{ij} values by regression from standards of different concentrations of each component or mixtures of known composition (multiple standards). In this way, one equation system per wavelength used of the form

$$A_{jk} = z_j + \sum_{i=1}^{N} \epsilon_{ij} b c_{ik}; \quad \forall k = 1 \ldots K \qquad (2)$$

is solved. In this equation, A_{jk} denotes the absorbance of standard k at wavelength j, z_j is the independent term of the fitting and c_{ik} is the concentration of component i in standard k. This equation system can be solved by multiple linear regression provided that the number of standards used, K, is greater than that of mixture components to be resolved. The solutions obtained will include the values of ϵ_{ij} and z_j, as well as the

fitting deviation, D_j, at each wavelength, which is given by

$$D_j = \left[\frac{\sum_{k=1}^{K} (A_{jk,\mathrm{exp}} - A_{jk,\mathrm{calc}})^2}{K - N} \right]^{\frac{1}{2}} \quad (3)$$

The D_j values thus obtained can be used to resolve the unknown mixture by performing a weighted fitting of Eqn. 1 in such a way that the wavelengths yielding the greatest deviations have smaller weights than the others. In this way, the system of equations to be solved is expressed as

$$\frac{A_j}{D_j} = a' + \sum_{i=1}^{N} \frac{\epsilon_{ij}}{D_j} \cdot bc_i; \quad \forall_j = 1 \ldots M \quad (4)$$

where $a' = a/D_j$.

On the other hand, Eqn. 2 can be applied to a set of data obtained by known additions of the components to be determined to an unknown sample (multiple addition). In this case, the c_{ik} values will coincide with the added concentrations of the components in each standard. The regressions performed at each wavelength will thus provide the ϵ_{ij} and z_j values corresponding to the estimated molar absorptivities of the components and the sample absorbance, respectively. Finally, application of Eqn. 1 to the z_j values will allow the concentration of each component in the unknown sample to be determined.

EXPERIMENTAL

Apparatus

Spectrophotometric measurements were made on a Hewlett-Packard HP 8452A diode-array spectrophotometer furnished with a quartz cell of 1-cm light path and interfaced to a PC-compatible computer for acquisition and processing of the spectral data.

Reagents

Standard 1×10^{-3} M solutions of the different phenol compounds assayed were prepared from commercially available analytical-reagent or liquid chromatographic grade chemicals that were dissolved without further purification in distilled water. Working solutions were prepared as required by dilution with analytical-reagent grade 0.1 M NaOH solution.

Software [a]

Experimental data were acquired with the aid of the software bundled with the instrument and subsequently they were treated with the program MULTI3. The latter was developed in QuickBasic by the authors for the resolution of mixtures of different components on the basis of the mathematical background described above and can manage the data files generated by the detector software.

MULTI3 allows for three types of calibration: single-standard, multiple-standard and multiple standard addition. In the first case, the program requires the spectrum of one standard per component, whether standardized or not. In the second case (multiple standard), the user can employ standards of both pure compounds and known mixtures under the sole constraint that the set of standards must include all components in different proportions. Likewise, the multiple standard addition method requires the user to provide the spectra obtained by adding known amounts of one or several of the mixture components to the sample in such a way that all of them are included in the assays. In the multiple-standard and multiple standard addition procedures, once the calibration has been performed, the program allows the mixture to be resolved by a weighted or unweighted regression. In any case, the calibration can be done by using normal spectra or one of their successive derivatives.

Procedure

Once the absorption spectra of the standards to be used for calibration and that of the sample (all in 0.1 M NaOH medium) over the wavelength range 244–600 nm have been recorded, referred

[a] The software used can be obtained on request from SCIWARE, Banco de Programas, Departamento de Química, Universitat des les Illes Balears, E-07071 Palma de Mallorca, Spain.

to a blank of 0.1 M NaOH, they are input into MULTI3 for processing. The multiple standard addition method also requires inputting the spectra of the successive additions. Both the standards and the samples must contain concentrations of each component within the linear determination range (1–100 μM).

RESULTS AND DISCUSSION

The proposed method was applied to nine phenol compounds including the parent compound (phenol) plus some halogenated [2-chlorophenol(2CLP) and 4-bromophenol (4BRP)], nitro[2-nitrophenol(2NP). 3-nitrophenol(3NP), 4-nitrophenol (4NP) and 2,4-dinitrophenol (24DNP)], methyl [2,3,5-trimethylphenol (235TMP)] and methoxy [3,5-dimethoxyphenol (35DMTP)] derivatives.

First the influence of the pH of the medium was investigated. For this purpose the absorption spectra of the different phenol compounds were recorded, which were found to shift to the visible region and diminish in spectral overlap with increase in pH. As an example, Fig. 1 shows the spectra obtained for four phenol compounds (phenol, 2CLP, 2NP and 4NP) in a neutral and basic medium where this behaviour can be seen. In an acidic medium (0.1 M HCl) the spectra were virtually identical with those obtained in a neutral medium. Therefore, a 0.1 M NaOH medium was chosen in which the spectra obtained remained virtually constant. Figure 2 shows the remainder of the spectra recorded in the medium selected. As can be seen, the absorption bands of most of the compounds overlap below 300 nm.

The linear determination range for the different phenols was then calculated by measuring the absorbance at the maximum of each compound by using standards of concentrations between 1 and 100 μM. The curves obtained were linear throughout the concentration range studied.

Finally the most suitable wavelength range for the resolution of the mixtures by multi-component analysis was determined. The aim was to preserve as much spectral information as possible while avoiding the far-UV region as far as possible in order to preclude significant background noise due to the strong NaOH absorption below 240 nm. Preliminary assays showed the optimum wavelength range for the resolution of the mixtures to be 244–600 nm.

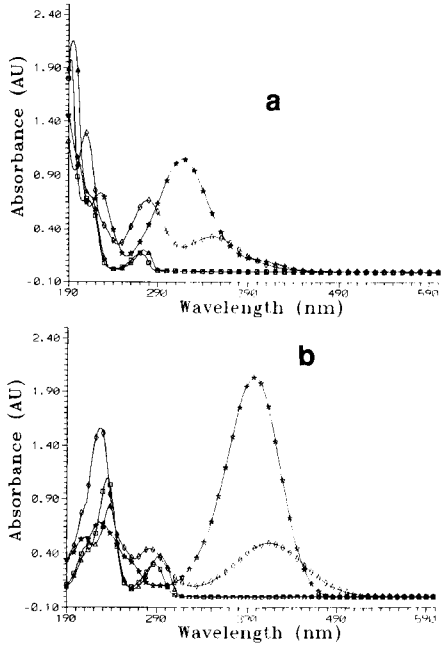

Fig. 1. Absorption spectra of four phenol compounds measured in (a) neutral and (b) basic medium. Concentration = 100 μM. □ = Phenol; △ = 2-chlorophenol; ◇ = 2-nitrophenol; ☆ = 4-nitrophenol.

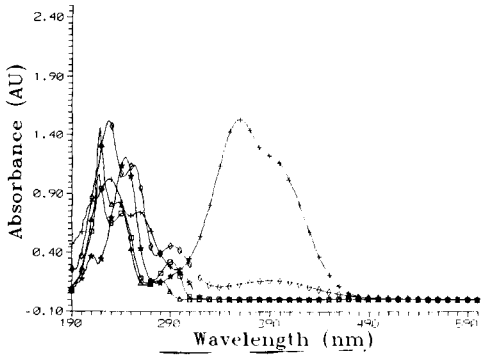

Fig. 2. Absorption spectra of the other five phenol compounds measured in a basic medium. Concentration = 100 μM. □ = 2,3,5-Trimethylphenol; △ = 3,5-dimethoxyphenol; ◇ = 3-nitrophenol; ☆ = 4-bromophenol; + = 2,4-dinitrophenol.

TABLE 1

Concentrations (μM) of the phenol compounds in the different mixtures used to obtain Tables 2 and 3

Compound	M_1	M_2	M_3	M_4	M_5
Phenol	10	10	10	10	10
2-Chlorophenol (2CLP)	10	10	10	10	10
4-Bromophenol (4BRP)	–	–	10	–	–
2-Nitrophenol (2NP)	4	4	10	10	10
3-Nitrophenol (3NP)	–	10	10	10	10
4-Nitrophenol (4NP)	10	10	4	4	4
2,4-Dinitrophenol (24DNP)	4	4	4	4	4
2,3,5-Trimethylphenol (235TMP)	–	–	–	10	10
3,5-Dimethoxyphenol (35DMTP)	–	–	–	–	10

Once the optimum working conditions had been established, the proposed method was applied to different mixtures of the above-mentioned phenol compounds by using the three calibration methods available. Tables 2 and 3 list the results obtained in the resolution of mixtures of increasing complexity, the compositions of which are given in Table 1, by using the single-standard method with a single standard per compound (Table 2) or, alternatively, one standard per compound that was standardized and averaged from those obtained for several standards of different concentrations (Table 3). Normal and derivative spectra were used in both instances and the results were found to be better with the derivative spectra. On the other hand, the single-standard and standardized single-standard procedures provided similar results with the exception of the most complex mixture (eight components), which was better resolved by the second choice overall.

In view of the results obtained, the multiple-standard and multiple standard addition methods were chosen for the resolution of the most complex samples (nine components). Tables 4 and 5 give the concentrations corresponding to the different mixtures assayed and the absorbance ratios between each component and that which gave a smaller absorbance in the mixture. In order to summarize the results obtained by processing these mixtures in a readily comprehensible way, they are expressed as mean errors calculated from the following equation:

$$\epsilon = \left[\frac{\sum_{i=1}^{N} (C_{j,\text{real}} - C_{i,\text{calc}})^2}{\sum_{i=1}^{N} C_{i,\text{real}}^2} \right]^{\frac{1}{2}} \quad (5)$$

Table 6 gives the results obtained in the resolution of twelve different mixtures by applying the standardized single-standard, multiple-standard and weighted multiple-standard procedures to normal spectra and their first two derivatives. As can be seen, the normal spectra yield much

TABLE 2

Recoveries % obtained in the resolution in various mixtures of phenol compounds by applying the program MULTI3 to the normal absorption spectra (N) and their first derivative (D_1) using the single-standard calibration method [a]

Compound	M_1		M_2		M_3		M_4		M_5	
	N	D_1	N	D_1	N	D_1	N	D_1	N	D_1
Phenol	106	108	104	109	148	118	104	100	106	100
2CLP	97	95	94	96	60	86	106	122	118	116
4BRP	–	–	–	–	72	84	–	–	–	–
2NP	127	94	128	100	103	96	103	104	115	111
3NP	–	–	107	102	144	114	106	107	121	111
4NP	98	103	98	102	93	101	103	101	90	96
24DNP	106	99	103	98	100	102	96	102	106	101
235TMP	–	–	–	–	–	–	82	70	59	69
35DMTP	–	–	–	–	–	–	–	–	97	101

[a] The compositions of mixtures M_1–M_5 are given in Table 1. Calibration with standards of 100 μM for each component.

TABLE 3

Recoveries (%) obtained in the resolution of various mixtures of phenol compounds by applying the program MULTI3 to the normal absorption spectra (N) and their first derivative (D_1) using the standardized single-standard calibration method [a]

Compound	M_1		M_2		M_3		M_4		M_5	
	N	D_1	N	D_1	N	D_1	N	D_1	N	D_1
Phenol	123	113	120	112	155	122	102	102	90	95
2CLP	91	102	93	103	58	86	95	117	119	117
4BRP	–	–	–	–	86	93	–	–	–	–
2NP	88	80	99	92	99	98	95	104	109	114
3NP	–	–	99	97	123	102	88	97	100	101
4NP	101	101	100	100	98	100	111	100	98	95
24DNP	98	100	98	100	95	103	89	102	99	103
235TMP	–	–	–	–	–	–	115	88	82	83
35DMTP	–	–	–	–	–	–	–	–	112	106

[a] The compositions of mixtures M_1–M_5 are given in Table 1. Calibration with standards of 100, 50, 10 and 1 μM for each component, standardized at a 10 μM concentration.

TABLE 4

Concentrations (μM) of each of the components in the mixtures listed in Table 6

Compound	M_6	M_7	M_8	M_9	M_{10}	M_{11}	M_{12}	M_{13}	M_{14}	M_{15}	M_{16}	M_{17}
Phenol	14	18	22	26	10	10	10	10	10	10	10	10
2CLP	10	14	18	22	26	10	10	10	10	10	10	10
4BRP	10	10	14	18	22	26	10	10	10	10	10	10
2NP	4	4	4	8	12	16	20	4	4	4	4	4
3NP	4	4	4	4	8	12	16	20	4	4	4	4
4NP	2	2	2	2	2	6	10	14	18	2	2	2
24DNP	2	2	2	2	2	2	6	10	14	18	2	2
235TMP	10	10	10	10	10	10	10	14	18	22	26	10
35DMTP	10	10	10	10	10	10	10	10	14	18	22	26

TABLE 5

Absorbance ratios of each mixture component to that with the smallest absorbance [a]

Compound	M_6	M_7	M_8	M_9	M_{10}	M_{11}	M_{12}	M_{13}	M_{14}	M_{15}	M_{16}	M_{17}
Phenol	2.4	3.0	3.6	3.6	1.5	1.5	1.5	1.7	1.7	1.7	1.7	1.7
2CLP	2.0	2.8	3.6	3.8	4.5	1.8	1.8	2.0	2.0	2.0	2.0	2.0
4BRP	1.4	1.4	1.8	2.0	2.4	2.9	1.2	1.4	1.4	1.4	1.4	1.4
2NP	1.0	1.0	1.0	1.7	2.6	3.5	4.4	1.0	1.0	1.0	1.0	1.0
3NP	1.4	1.4	1.4	1.2	2.0	2.9	3.7	5.2	1.4	1.4	1.6	1.6
4NP	2.7	2.7	2.7	2.3	2.3	6.0	9.8	15.6	19.9	2.7	2.7	2.7
24DNP	1.8	1.8	1.8	1.5	1.5	1.5	4.3	8.3	11.5	14.7	1.8	1.8
235TMP	1.8	1.8	1.8	1.6	1.6	1.6	1.6	2.5	3.2	3.9	4.6	1.8
35DMTP	1.1	1.1	1.1	1.0	1.0	1.0	1.0	1.1	1.5	1.8	2.1	2.5

[a] All absorbances were measured at the absorption maximum of each phenol compound.

TABLE 6

Mean errors [a] (%) made in the resolution of various mixtures of nine phenols by application of different calibration methods to the normal absorption (N) and first- and second-derivative spectra (D_1 and D_2, respectively) [b]

Mixture [c]	SS			UMS			WMS		
	N	D_1	D_2	N	D_1	D_2	N	D_1	D_2
M_6	20.4	10.7	22.9	9.5	11.7	16.8	8.9	7.8	10.1
M_7	22.9	9.6	23.1	8.5	10.8	16.5	7.5	7.3	9.2
M_8	18.3	10.3	23.5	11.8	11.7	16.2	10.5	7.7	8.7
M_9	21.0	9.3	19.8	9.8	10.5	11.5	8.2	7.1	7.6
M_{10}	20.3	9.7	17.8	10.2	10.1	9.9	9.9	8.3	9.1
M_{11}	18.2	8.0	13.0	10.9	6.7	7.6	11.3	6.4	7.3
M_{12}	33.7	8.8	15.3	6.1	7.2	7.6	5.9	6.1	6.7
M_{13}	29.3	21.1	60.2	10.0	23.6	57.3	11.2	5.0	10.2
M_{14}	22.3	7.5	13.3	14.8	8.3	8.7	14.6	7.0	7.5
M_{15}	21.5	7.4	71.6	10.4	7.7	8.0	10.3	6.9	7.8
M_{16}	12.2	8.4	10.2	17.7	9.4	8.3	17.6	10.3	7.9
M_{17}	10.7	10.2	13.8	19.6	11.3	10.5	18.7	9.2	9.7

[a] Mean errors calculated from Eqn. (5) [b] SS, UMS, WMS = single-standard, unweighted multiple-standard and weighted multiple-standard calibration method, respectively. Standards of 100, 10 and 1 μM in each component were used throughout (standardized to 10 μM for the SS method). [c] For mixture compositions, see Table 4.

smaller errors with the two multiple-standard procedures. With the first derivative, however, the single-standard and multiple-standard procedures provide virtually identical results and slightly worse than those of the weighted multiple-standard procedure. With the second derivative, the deviations obtained by using the single-standard and multiple-standard procedures are clearly increased, while the deviations of the weighted multiple-standard procedure are similar to those of the first derivative. This can be attributed to the fact that background noise increases with the derivative order and results in poorer regressions. Nevertheless, this effect can

TABLE 7

Relative errors (%) made in the resolution of a mixture of nine phenol compounds by applying the multiple standard addition and multiple-standard methods [a]

Compound	Concentration (μM)	MSA			WMSA			MS			WMS		
		N	D_1	D_2	N	D_1	D_2	N	D_1	D_2	N	D_1	D_2
Phenol	10	−17.9	−10.9	8.9	27.1	−4.8	−4.4	−27.4	−20.2	−27.5	−26.1	−13.9	−16.7
2CLP	10	16.5	6.4	2.0	5.8	6.7	3.6	7.8	−0.7	−0.6	8.1	−1.6	−3.2
4BRP	10	−1.0	5.6	19.2	14.3	6.3	4.6	−4.9	−0.8	−4.8	−4.7	1.7	1.3
2NP	4	5.8	6.0	−11.8	3.0	−0.7	−3.4	−2.3	15.8	24.0	−2.3	−3.8	4.5
3NP	4	−5.8	−16.3	−15.0	−7.4	−14.2	7.1	−3.8	−8.0	−10.0	−2.3	−5.8	−7.0
4NP	2	−1.5	1.0	0.0	1.0	3.4	4.4	3.0	−2.0	3.0	3.0	4.5	3.5
24DNP	2	0.5	−5.5	4.0	0.7	−1.4	9.8	0.0	1.5	0.0	0.0	−2.5	−3.0
235TMP	10	7.9	10.2	−4.5	−18.9	5.4	5.3	14.3	13.4	19.4	11.9	10.9	13.6
35DMTP	10	4.5	−1.0	−2.2	−14.1	4.1	14.7	19.8	14.3	19.3	19.6	11.0	13.0
ϵ [b]		11.3	8.0	10.0	16.9	5.9	7.6	16.3	12.5	16.8	15.5	9.1	11.0

[a] MSA, WMSA, MS, WMS = multiple standard addition, weighted multiple standard addition, multiple-standard and weighted multiple-standard methods, respectively. [b] Mean errors calculated from Eqn. 5.

be partially reduced if a weighted method is used to give less weight to those wavelengths with a high background noise. Thus, by using different derivatives one can distinguish the spectra more readily provided the background noise is minimized by using weighting procedures.

It can also be seen in Tables 5 and 6 that the mixtures with higher deviations (M_{12}–M_{15}) were those which contained some phenol compound that differed greatly in their absorbances with regard to the other mixture components. This is a common characteristic in the multi-component regression methods described in the literature. Nevertheless, this effect is more significant in the single-standard calibration method than in the unweighted multiple-standard and, especially, in the weighted multiple-standard calibration methods by using their first two derivatives.

Table 7 gives the relative errors for each component and the average error for each calculation procedure obtained in the resolution of a mixture of nine components by the multiple standard addition and the multiple-standard procedures in their weighted and unweighted variants. As shown in Table 6, the results were obtained both from normal spectra and from their first two derivatives. Overall, the multiple standard addition method provides smaller deviations than the multiple-standard method. Also, the weighted procedure and first derivative yield better results. However, the advantages in terms of accuracy occasionally do not offset the greater laboriousness of the multiple standard addition procedure.

Conclusions

The proposed methodology allows the satisfactory resolution of mixtures of up to nine phenol compounds by using a least-squares multiple linear regression procedure. The new calibration procedures thus developed allow larger numbers of components than usual to be determined in mixtures. As a rule, the best results can be obtained by using the multiple standard addition method combined with the use of the first-derivative spectra and weighted resolution. In general, first-derivative spectra yield smaller deviations, as do the weighted variants of the procedures, particularly with derivative spectra, as a result of decreasing the contribution of the wavelengths with greater background noise to the overall spectra.

The authors express their gratitude to DGICyT (Spanish Council for Research in Science and Technology) for financial support granted for the realization of Project PB 90-0359.

REFERENCES

1 J.C. Sternberg, H.S. Stillo and R.C. Schwendeman, Anal. Chem., 32 (1960) 84.
2 P. Jochum and E.L. Schrott, Anal. Chim. Acta, 157 (1984) 211.
3 D.J. Leggett, Anal. Chem. 49 (1977) 276.
4 A. Van Loosbroeck, H.J.G. Debets and P.M.J. Coenegrarcht, Anal. Lett., 17 (1984) 779.
5 M. Blanco, J. Gené, H. Iturriaga and S. Maspoch, Analyst, 112 (1987) 619.
6 G. Sala, S. Maspoch, H. Iturriaga, M. Blanco and V. Cerdá, J. Pharm. Biomed. Anal., 6 (1988) 765.
7 E. Gómez, J.M. Estela and V. Cerdà, Anal. Chim. Acta, 249 (1991) 513.
8 A. Cladera, E. Gómez, J.M. Estela and V. Cerdà, Int. J. Environ. Anal. Chem., 45 (1991) 143.
9 E. Gómez, J.M. Estela and V. Cerdà, Fresenius' J. Anal. Chem., 342 (1992) 318.
10 B. Bermúdez, F. Lázaro, M.D. Luque de Castro and M. Valcárcel, Analyst, 112 (1987) 535.
11 F. Cañete, A. Ríos, M.D. Luque de Castro and M. Valcárcel, Anal. Chim. Acta, 214 (1988) 375.

Analytica Chimica Acta, 267 (1992) 103–109
Elsevier Science Publishers B.V., Amsterdam

Application of multi-component analysis to the simultaneous resolution of phenol compounds in mixtures

Part II. Development of a closed-circuit extraction, enrichment and back-extraction system

Andreu Cladera, Enrique Gómez, José Manuel Estela and Víctor Cerdà

Department of Chemistry, University of the Balearic Islands, E-07071 Palma de Mallorca (Spain)

(Received 22nd October 1991; revised manuscript received 16th March 1992)

Abstract

A general system for the extraction and concentration of organic compounds based on a closed-circuit extraction/back-extraction procedure and real-time spectrophotometric monitoring by use of a diode-array detector is reported. Application of multi-component analysis techniques allows the changes in each mixture component to be distinguished and the components to be determined. The proposed system was used to analyse various mixtures of phenol compounds.

Keywords: Extraction; Phenols; Waters; UV–Visible spectrophotometry; Sample preparation

Liquid–liquid extraction has traditionally been used for the isolation and preconcentration of organic compounds [1]. However, because of some major shortcomings (e.g., toxicity, hazards, the need for large extractant volumes, analyte losses by manipulation), it has been gradually superseded by others using solid sorbents such as ion-exchange resins [2,3], C_{18} cartridges [4] and graphitized carbon black cartridges [5] and other types of chemically bonded phases, both for on-line and for off-line extractions [6–11]. The use of solid phases, however, has other shortcomings such as limited applicability (low sample volumes) and modest throughputs imposed by the need to avoid analyte losses. All these factors make liquid–liquid extraction still a valid alternative for solving some problems of a practical nature.

In order to extend the scope of this technique, some workers have developed continuous-flow liquid–liquid extraction systems, both for segmented flow analysis (SFA) [12] and for flow-injection analysis (FIA) [13]. These novel systems allow the extraction process to be automated, thereby avoiding the problems arising from the manipulation of organic compounds and increasing the sample throughputs typically achieved. However, inasmuch as no sample concentration is effected, nothing is gained in terms if sensitivity.

On the other hand, the advent of diode-array spectrophotometers and the use of multi-component mixture resolution procedures in closed liquid–liquid extraction systems have opened up new prospects for this technique.

The aim of this work was to assess the potential of a continuous liquid–liquid extraction/

Correspondence to: V. Cerdà, Department of Chemistry, University of the Balearic Islands, E-07071 Palma de Mallorca (Spain).

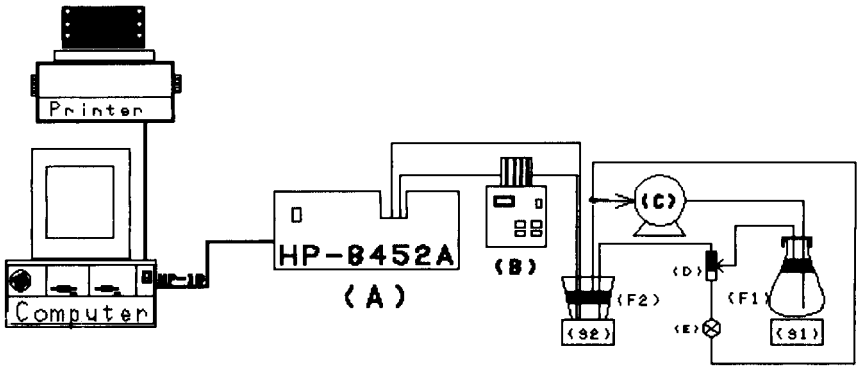

Fig. 1. Instrumental set-up used for the continuous extraction and back-extraction by the proposed method. A = Diode-array spectrophotometer; B = peristaltic pump; C = pressure pump; D = phase separator; E = flow regulator; F_1 = air-tight vessel; F_2 = collecting vessel; S_1 and S_2 = magnetic stirrers.

back-extraction system developed for the resolution of mixtures of organic compounds in general and phenol compounds in particular by real-time spectrophotometric monitoring of the back-extraction process. Mixture resolution is accomplished by using a multi-component program based on a least-squares linear multivariate regression of the absorbance data provided by the diode-array spectrophotometer. This should improve on the performance of this technique in terms of both the extractant volume to be used and the sample concentration factor achieved. Likewise, by continuously monitoring the extraction process, its time evolution can be investigated in greater depth.

EXPERIMENTAL

Apparatus

Figure 1 shows the instrumental set-up used for continuous extraction/back-extraction. It consists of a Milton Roy VS pressure minipump, a Gilson Minipuls peristaltic pump, Hewlett-Packard HP 8452A diode-array spectrophotometer furnished with a cell of 1-cm light path and 18-μl void volume, a PC-compatible computer, a customized extraction funnel, an Omnifit 1101 unidirectional stop-cock valve and two vessels furnished with magnetic stirrers (that holding the sample is air-tight).

Figure 2 depicts the phase separator used, which was constructed from methacrylate in order to withstand the attack of the organic solvents to be used.

All tubing used was PTFE of 0.5 mm i.d.

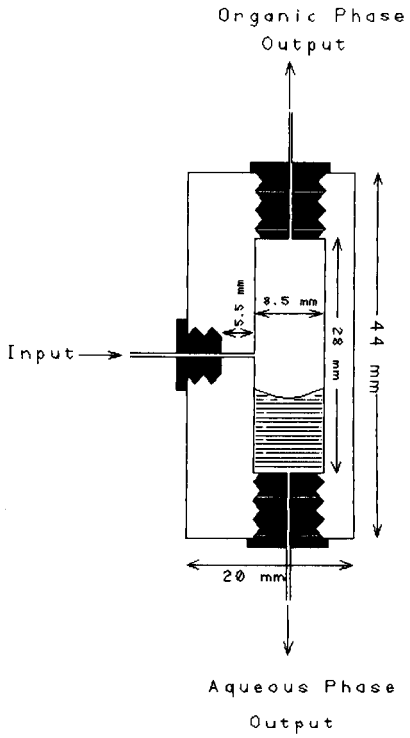

Fig. 2. Schematic diagram of the phase separator used.

Reagents

Standard solutions of the different phenol products to be assayed were prepared from the corresponding commercially available chemicals [analytical-reagent or liquid chromatographic (LC) grade] with no further purification, using distilled water as solvent. Other reagents used, with the exception of *n*-hexane (LC grade), were of analytical reagent grade.

Software [a]

Two computer programs written in QuickBasic for PC-compatible computers were used. One of them, DARRAY [14], allows the acquisition and processing of the experimental data provided the diode-array spectrophotometer; the other, MULTI3, performs multi-component resolution from the files generated by the previous program and was described in detail in Part 1.

Procedure

The first step in the process involves recording the absorption spectra of pure standards of the mixture components at different concentrations throughout the calibration range in 1 M NaOH solution. These spectra are used later for calibration with the aid of MULTI3 by applying the multiple-standard method described in Part I. Then, a given sample volume is placed in the air-tight vessel and acidified to pH 2 with dilute HCl and the vessel is capped. In the second vessel are placed 25 ml of 1 M NaOH and 20 ml of *n*-hexane. Both vessels are then stirred and the extractant circulation system is switched on simultaneously with the start of spectrum acquisition as a function of time (acquisition rate = 0.5 min^{-1}) over the wavelength range 244–600 nm. The absorbance measured at a preset wavelength (260 nm) are displayed on the computer screen in order to supervise the development of the extraction process and determine its end from the corresponding saturation curve.

[a] The software used can be obtained on request from SCI-WARE, Banco de Programas, Departamento de Química, Universitat de les Illes Balears, E-07071 Palma de Mallorca, Spain.

Once the extraction process is finished, the acquired spectrophotometric data are processed by MULTI3, which provides the concentrations of compounds extracted at different times.

RESULTS AND DISCUSSION

The proposed system relies on the extraction of organic compounds present in a sample held in an air-tight vessel (F_1) by using an appropriate solvent that is propelled by the overpressure within the aforementioned vessel to the collector vessel (F_2), in which the extracted compounds are released into a new phase. Once free from the organic compounds, the extracting solvent is re-circulated through the pressure pump to F_1, where the cycle is re-started. The system is appropriate for extractants lighter than the aqueous phase, so the extractant is injected into the bottom of the vessel and aspirated at the top. However, it could also be redesigned for extractants heavier than water.

The performance of this extraction/back-extraction system was assessed by using mixtures of phenols in water and determining the influence of the different variables affecting the process. The chemical model and working wavelength range used for this purpose (244–600 nm) were selected according to the authors' experience and the results obtained in Part I.

Preliminary experiments showed the extraction rate to be substantially higher if the vessel containing the sample was kept under vigorous stirring. This led to the design of a phase separator (Fig. 2) that was inserted between F_1 and F_2 in order to prevent the aqueous phase from passing from one vessel to the other. On emergence from the separator, the organic phase was driven to F_2 while the aqueous phase was returned to F_1, the flow of which was controlled by means of a stopcock (E). However, F_2 must not be stirred too vigorously in order to prevent the organic phase from reaching the detector. Nevertheless, because of the small volume of aqueous phase held in F_2, stirring was not too influential. On the other hand, placing the extractant in F_2 only was

TABLE 1

Recoveries obtained after 120 min (three assays on average) and standard deviations (%) (in parentheses) for each of the phenol compounds assayed by the proposed procedure in standards of known concentrations [a]

Compound	Concentration (μM)	Recovery (%)
2,4-Dinitrophenol (24DNP)	2.0	80 (3.0)
Phenol	10.0	21 (13.3)
3,5-Dimethoxyphenol (35DMTP)	10.0	5 (12.7)
4-Nitrophenol (4NP)	2.0	< 1
3-Nitrophenol (3NP)	4.0	7 (9.5)
2-Chlorophenol (2CLP)	10.0	93 (1.4)
2-Nitrophenol (2NP)	4.0	97 (1.2)
4-Bromophenol (4BRP)	10.0	58 (11.6)
2,3,5-Trimethylphenol (235TMP)	8.0	100 (0.2)

[a] Sample/extract concentration factor = 10. Extraction time = 120 min.

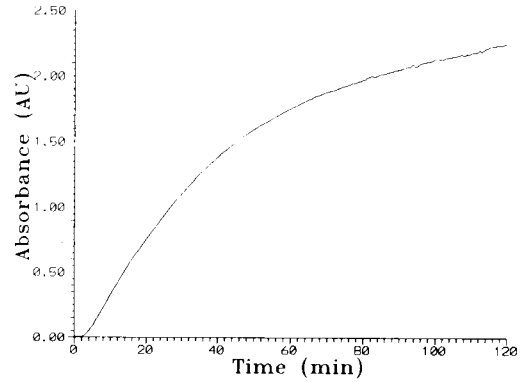

Fig. 3. Extraction curve obtained by spectrophotometric monitoring at 260 nm of a mixture of 2 μM 2,4-dinitrophenol, 10 μM phenol, 10 μM 2-chlorophenol, 4 μM 2-nitrophenol, 10 μM 4-bromophenol and 8 μM 2,3,5-trimethylphenol. Concentration factor (sample/extract) = 10.

found to result in a shorter dead time than that obtained by using it in both vessels.

On analysing the polarity changes of the phenol compound with the pH of the medium, it was found that the proposed system performed satisfactorily in terms of extraction below pH 5. An HCl medium of pH 2 was chosen for the extraction. On the other hand, the most suitable back-extraction medium was basic (1 M NaOH).

Under these conditions, different common extractants were tried and *n*-hexane was found to provide the best results. In fact, other solvents such as diethyl ether and isobutyl methyl ketone were too soluble in water to allow for proper spectrophotometric monitoring.

Under the optimum working conditions used, the recoveries of the different phenol compounds listed in Table 1 were obtained (t = 120 min). As can be seen, the proposed system allows the determination of six of the phenol compounds, but not of 3-nitrophenol, 4-nitrophenol or 3,5-dimethoxyphenol.

Figure 3 shows the extraction curve for a mixture containing the six phenols to which the method can be applied, which was obtained by spectrophotometric monitoring at 260 nm. Figure 4 gives the extraction curves for the six phenols after application of the multi-component resolution procedure. The results obtained were checked by LC according to the procedure reported by Alarcón and Bustos [15]. As can be seen from Fig. 4, the curves for three of the phenols (2-nitrophenol, 2-chlorophenol and 2,3,5-trimethylphenol) reach saturation before 120 min of extraction. However, the other three phenols continue to be extracted after that time.

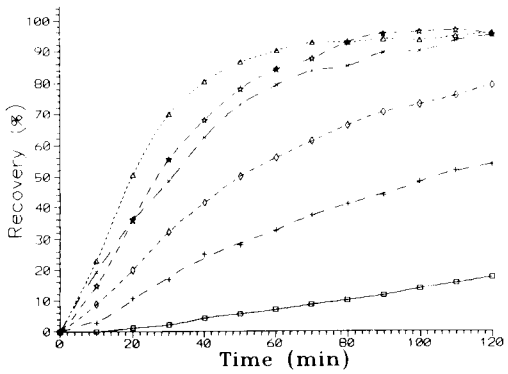

Fig. 4. Individual extraction curve for each phenol compound obtained by multi-component resolution from the data given in Fig. 3. Wavelength range = 244–600 nm. Calibration performed with standards of 2,4-dinitrophenol (80, 40 and 20 μM), phenol (200, 100 and 40 μM), 2-chlorophenol (200, 100 and 40 μM), 2-nitrophenol (80, 40 and 20 μM), 4-bromophenol (200, 100 and 40 μM) and 2,3,5-trimethylphenol (160, 80 and 40 μM). □ = Phenol; △ = 2-nitrophenol; ◇ = 2,4-dinitrophenol; ☆ = 2-chlorophenol; + = 4-bromophenol; × = 2,3,5-trimethylphenol.

TABLE 2

Recoveries (%) obtained in the resolution of four synthetic samples of the phenol compounds by the proposed procedure [a]

Compound	Mixture 1	Mixture 2	Mixture 3	Mixture 4
24DNP	90	87	–	80
Phenol	–	19	23	17
35DMTP	–	–	5	–
4NP	–	< 1	–	–
2NP	–	6	–	–
2CLP	100	–	–	95
2NP	–	98	–	96
4BRP	–	–	63	54
235TMP	100	–	88	95

[a] Working conditions, concentrations and compound abbreviations as in Table 1. Calibration performed with standards of 2,4-dinitrophenol (80, 40 and 20 μM), phenol (200, 100 and 40 μM), 3,5-dimethoxyphenol (200, 100 and 40 μM), 4-nitrophenol (40, 20 and 10 μM), 3-nitrophenol (80, 40 and 20 μM), 2-chlorophenol (200, 100 and 40 μM), 2-nitrophenol (80, 40 and 20 μM), 4-bromophenol (200, 100 and 40 μM) and 2,3,5-trimethylphenol (160, 80 and 40 μM).

Consequently, the reproducibility will predictably be higher for the first three compounds.

Table 2 gives the results obtained in the analysis of various mixtures of phenol compounds. As can be seen, the results are consistent with reference values.

The use of reagents in order to increase the recoveries of extraction procedures warrants some comments. The phenols featuring the poorer recoveries were converted into their acetyl derivatives by using acetic anhydride in a hydrogencarbonate medium [16]. The derivatives thus obtained were extracted into *n*-hexane, deacetylated and back-extracted into 1 M NaOH. Although this method provided good results in terms of recoveries and resolution when performed in a manual fashion (Table 3), the excess of acetic anhydride present in the sample built up in the collecting vessel in the continuous procedure because of its basis. This in turn gave rise to a spectral interference from the accumulated acetic anhydride that rendered correct resolution of the different components impossible.

APPLICATIONS

The proposed method and continuous extraction/back-extraction system were applied to the determination of phenol compounds in tap water and waste water samples which were spiked with the compounds as they were found not to contain them initially. Table 4 gives the results obtained by the proposed method and by LC (applied to aliquots of the final extracts).

Whereas the results obtained by applying the multi-component procedure to the tap water were satisfactory, the LC technique gave a higher than expected recovery for 2,4-dinitrophenol because of the overlap of its peak and that of injection.

The results given by both the proposed method and the LC technique for the waste water were

TABLE 3

Recoveries (average of three assays) and standard deviations (%) (in parentheses) obtained for the different acetylated phenol compounds by manual extraction of standards of the stated concentrations [a]

Compound	Concentration (μM)	Recovery (%)
24DNP	10.0	22 (2.7)
Phenol	50.0	81 (1.2)
35DMTP	100.0	76 (0.9)
4NP	10.0	83 (3.1)
3NP	50.0	89 (1.1)
2CLP	50.0	49 (1.5)
2NP	50.0	97 (2.1)
4BRP	50.0	43 (2.3)
235TMP	40.0	45 (4.8)

[a] Compound abbreviations as in Table 1. [Acetic anhydride] = 0.4%; [HCO_3Na] = 0.01 g ml^{-1}. Sample/extract concentration factor = 2.

TABLE 4

Recoveries obtained for water samples spiked with the phenol compounds [a]

Compound	Tap water			Waste water		
	Added (μM)	Recovery (%)		Added (μM)	Recovery (%)	
		Proposed method	LC		Proposed method	LC
24DNP	2.0	88	145	2.0	88	92
2CLP	10.0	100	106	10.0	97	94
2NP	–	–	–	4.0	155	152
4BRP	–	–	–	10.0	71	178
235TMP	8.0	99	88	8.0	69	40

[a] Compound abbreviations as in Table 1. Sample/extract concentration factor = 10. Extraction time = 120 min. Calibration performed with the standards given in Table 2.

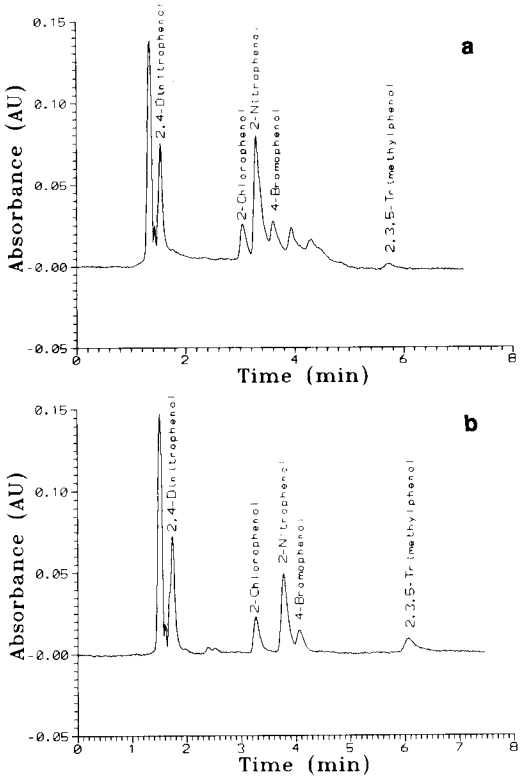

Fig. 5. Chromatograms corresponding to (a) an extract from a waste water spiked with 2 μM 2,4-dinitrophenol, 10 μM 2-chlorophenol, 4 μM 2-nitrophenol, 10 μM 4-bromophenol and 8 μM 2,3,5-trimethylphenol, with sample/extract concentration factor = 10; (b) a synthetic mixture containing the same phenol compounds at concentrations ten times higher.

divergent from expectation in some instances. The differences can be attributed to the presence of interfering compounds in the sample matrix. Figure 5 shows the chromatograms obtained for the waste water sample and a synthetic sample of the phenols used to spike it. As can be clearly seen in Fig. 5a, there are small peaks corresponding to unidentified compounds that result in a positive interference in the determination of 2-nitrophenol and 4-bromophenol by LC. The changes in the retention times for the peaks observed between Fig. 5a and 5b must be attributed to the different medium used for the real sample (an extract) and the standard mixture. Nevertheless, identification was easily achieved by spectral monitoring of the chromatographic peaks of interest.

The interferences encountered in applying the proposed method to the waste water sample can be attributed to two potential causes. On the one hand, there are spectral interferences that affect the multi-component resolution, particularly that of 2-nitrophenol. On the other, the extraction of 2,3,5-trimethylphenol also suffers interference. Thus, the multi-component and the LC results are consistent with one another and divergent from those obtained in the absence of the matrix.

Conclusions

The use of continuous liquid–liquid extraction/back-extraction plus a concentration system and multivariate analysis as applied to diode-array spectrophotometric data opens up new prospects for traditional liquid–liquid extraction as it solves some of its major shortcomings.

Thus, the proposed method allows the simultaneous resolution of mixtures of organic compounds. Moreover, the sample concentration process does not require direct handling of organic solvents. It is also a useful approach for the monitoring of individual extraction processes for mixtures of several components in uncomplicated matrices. However, the unknown matrix should be investigated preliminarily in order to determine which components are present and their spectral features and to establish the most suitable extractant and back-extractant for the purpose.

The authors express their gratitude to the DGICyT (Spanish Council for Research in Science and Technology) for financial support granted for the realization of Project PB 90-0359.

REFERENCES

1 M. Valcárcel and M. Silva, Teoría y Práctica de la Extracción Líquido–Líquido, Alhambra, Madrid, 1984.
2 R.A. Moore and F.W. Karasek, Int. J. Environ. Anal. Chem., 17 (1984) 187.
3 M.W.F. Nielen, J. De Jong, R.W. Frei and U.A.Th. Brinkman, Int. J. Environ. Anal. Chem., 25 (1986) 37.

4 J. Oszmianski, T. Ramos and M. Bourzeix, Am. J. Enol. Vitic., 39 (1988) 259.
5 C. Borra, A. Di Corcia, M. Marchetti and R. Samperi, Anal. Chem., 58 (1986) 2048.
6 B. Rossner and G. Schwedt, Fresenius' Z. Anal. Chem. 315 (1983) 610.
7 W.A. Saner, J.R. Adamec and R.W. Sager, Anal. Chem., 51 (1979) 2180.
8 R.E. Shoup and G.S. Mayer, Anal. Chem., 54 (1982) 1164.
9 C.E. Werkhoven-Goewie, U.A.Th. Brinkman and R.W. Frei, Anal. Chem., 53 (1981) 2072.
10 C.E. Rostad, W.E. Pereira and S.M. Ratcliff, Anal. Chem., 56 (1984) 2856.
11 C.E. Werkhoven-Goewie, W.M. Boon, A.J.J. Praat, R.W. Frei, U.A.Th. Brinkman and C. Little. Chromatographia, 16 (1982) 53.
12 W.B. Furman, Continuous Flow Analysis. Theory and Practice, Dekker, New York, 1976.
13 B. Kalberg and S. Thelander, Anal. Chim. Acta, 98 (1978) 1.
14 A. Cladera, E. Gómez, J.M. Estela and V. Cerdà, Analyst, 116 (1991) 913.
15 P. Alarcón and A. Bustos, Chromatographia, 24 (1987) 613.
16 T.S. Kul'bich and V.S. Kozlova, Zh. Anal. Khim., 45 (1990) 367.

Analytica Chimica Acta, 267 (1992) 111–120
Elsevier Science Publishers B.V., Amsterdam

Chemometric analysis of Al–Si–Cu metallization process for very large scale integrated circuits

Ming-Kaan Liang and Yong-Chien Ling

Department of Chemistry, National Tsing Hua University, Hsinchu, 30043 (Taiwan)

(Received 5th March 1992)

Abstract

Al–Si–Cu films deposited on substrates of Si, borophosphate silicate glass and TiW with improved electrical properties (lower sheet resistance) and reliability (higher Al[111] diffraction intensity) obtained by the proposed metallization process are described. A chemometric approach of unifying the experimental design, analysis of variance and regression analysis is shown to be an effective and efficient means of fine tuning this metallization process. Statistical results from the analysis of variance and regression analysis are helpful in validating each other. The optimum deposition conditions are dependent on both the film quality and substrate identity. The variations are attributed to the different interfacial properties.

Keywords: Experimental design, Optimization methods, Process analysis/on-line analysis; Aluminium–silica–copper films, Analysis of variance, Integrated circuits, Metallization, Regression analysis

Aluminium is the most widely used metal for interconnections and contacts on integrated circuits (IC) because of its process compatibility, cost effectiveness and low sheet resistance. With the progressive reduction in device size, reliability problems of electromigration [1] and stress migration failure [2] become more series, i.e., with very large scale integrated (VLSI) circuits. To meet these challenges, a variety of process improvements have been investigated. First, Si was added to the Al to prevent the spiking of the shallow junctions [3]. The replacement of pure Al with an Al–Si film ameliorated the electromigration problems [4] through the reduction of hillock formation [5]. Subsequent addition of Cu to the Al–Si to form an Al–Si–Cu alloy film allows better control of the size and orientation of the grains to avoid electromigration. Consequently, the lifetime of the device is increased. These improvements are attributed to a lowering of the sheet resistance, an increase in the grain size and an increased number of high-density Al(111) planes in the Al–Si–Cu film [6,7].

From the above findings, it is conceivable that further improvements to the film properties are possible by fine tuning the metallization process. With increasing demand for higher quality devices, the need for enhancing their performance under tight budgets and with limited turn-around times becomes apparent. The conventional approach of on-line process analysis is applicable to processes that can be subjected to a certain degree of perturbations. However, the uniqueness of large-batch quantity production, complicated multi-step processes and strict materials and processing environment requirements for very large-scale integrated (VLSI) circuit fabrication entail an alternative approach, namely, off-line characterization of the metallization process.

The objective of this work was to provide the basic principles for evaluating the Al–Si–Cu metallization process for VLSI. Studies were made

Correspondence to: Yong-Chien Ling, Department of Chemistry, National Tsing Hua University, Hsinchu 30043 (Taiwan).

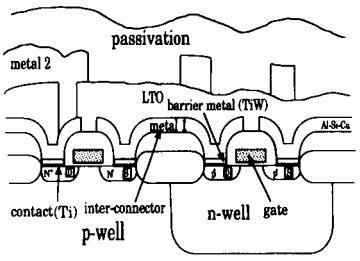

Fig. 1. Cross-sectional view of CMOS (complementary metal oxide semiconductor).

not only to produce a method of quantitatively measuring the process performance under various operating conditions but also to establish procedures for the description of the process characteristics to generate quality films. This study was done by using a total of 27 samples that were prepared by depositing the Al–Si–Cu films on substrates of Si, BPSG (borophosphate silicate glass) and TiW because of their popularity as constituents of interconnections and contacts (Fig. 1). Various deposition conditions were employed to fabricate these samples by using an L_{27} orthogonal array method of experimental design [8] to change the process parameters of sputtering temperature, sputtering bias and annealing temperature. The decision to use these three process parameters to achieve the desired electrical properties of the films was determined by the physical configuration of the depositing instruments used in this study and also literature reports [9]. The effects of these process parameters, individual or synergistic, on the properties of the film were elucidated using the statistical method of analysis of variance (ANOVA) [10].

Another multivariate statistical method, namely regression analysis [11,12], was subsequently applied to establish the correlations between the quality of the film and the process parameters. This chemometric approach of unifying the experimental design, ANOVA and regression analysis incorporates the important factors for the Al–Si–Cu metallization process and is offered to fulfil the need for an objective and cost-effective off-line analysis of the Al–Si–Cu metallization process for VLSI. This application contributes to the many examples of the important role of chemometrics [13–15].

EXPERIMENTAL

Si(100) wafers were obtained from Wacker (Berlin) and was precleaned with water–hydrofluoric acid (50 + 1) before use. The BPSG substrate was grown by depositing a 0.6-μm layer of BPSG with 4% B and 4% P inclusions on the Si(100) substrate using a low-pressure chemical vapour deposition (LPCVD) system (ASM, Netherlands). A 0.1-μm TiW substrate was grown by magnetron sputtering a single alloy target of 10% Ti–90% W on a 0.05-μm layer of Ti on top of the Si(100) substrate using a Varian (Palo Alto, CA) Model 3190 d.c. magnetron sputtering system. Film thickness measurements were made using a Rutherford backscatter spectrometer. Details of this system have been described elsewhere [16]. These Si, BPSG and TiW substrates were then subjected to a presputtering process before the Al–Si–Cu films were deposited. The same magnetron sputtering system was used to grow a 1.0-μm layer of Al–Si–Cu film on the pretreated Si and BPSG substrates and a 0.5-μm layer on the pretreated TiW. These Al–Si–Cu films were grown by magnetron sputtering an alloy target of Al–1% Si–0.5% Cu at the rate of ca. 15 Å s^{-1} using the sputtering argon gas under a pressure of 7.5×10^{-3} Torr. For convenience, these samples will be abbreviated to Al–Si–Cu/Si, Al–Si–Cu/BPSG and Al–Si–Cu/TiW. The system was pumped down to a base pressure of 5×10^{-7} Torr prior to backfilling the chamber with additional argon gas. Subsequent annealing was performed in a quartz furnace at atmospheric pressure under an ambient gas mixture of nitrogen–hydrogen (90 + 10) for 30 min.

The values for the three levels of each process parameter (or factor) are listed in Table 1. These values were selected based on past experience that they could provide films of low sheet resistance. Table 2 lists the deposition conditions for each sample using the L_{27} experimental design. Sheet resistances were measured using a four-point probe (Omni Map RS30, Prometrics, Santa

TABLE 1

Levels of process parameters (factors)

Factor	Factorial level		
	Low	Middle	High
Sputtering temperature (°C)	20	160	300
Sputtering bias (V)	0	−100	−200
Annealing temperature (°C)	370	410	450

Clara, CA). The desired orientation of the Al–Si–Cu film was determined from the diffraction intensity of the Al[111] peak using an x-ray diffractometer (PAD 5, Scintag, Santa Clara, CA).

TABLE 2

Deposition conditions for each sample using the L_{27} experimental design

Sample No.	Sputtering temperature (°C)	Sputtering bias (V)	Annealing temperature (°C)
1	L [a]	L	L
2	L	L	M
3	L	L	H
4	L	M	L
5	L	M	M
6	L	M	H
7	L	H	L
8	L	H	M
9	L	H	H
10	M [b]	L	L
11	M	L	M
12	M	L	H
13	M	M	L
14	M	M	M
15	M	M	H
16	M	H	L
17	M	H	M
18	M	H	H
19	H [c]	L	L
20	H	L	M
21	H	L	H
22	H	M	L
23	H	M	M
24	H	M	H
25	H	H	L
26	H	H	M
27	H	H	H

[a] L = low level. [b] M = middle level. [c] H = high level.

The same diffractometer was also used to measure the grain size, which was determined from the full-width at half-maximum (FWHM) of the Al[111] peak using Scherrer's method [17].

A transmission electron microscope (TEM) (Model CM20, Philips, Eindhoven) was used to observe the cross-section grain size of few Al–Si–Cu/TiW samples. Subsequent ANOVA and regression analysis were performed using the SYSTAT statistical analysis package (SYSTAT, Evanston, IL).

RESULTS AND DISCUSSION

Sheet resistance

The sheet resistance of the Al–Si–Cu films on the Si, BPSG and TiW substrates prepared under various conditions are given in Table 3 and the corresponding ANOVA results in Table 4. In the analysis, all three- and higher factor interactions are pooled into the error term. The calculated values of F for the sputtering bias factor are 113.15 for Al–Si–Cu/Si and 82.17 for Al–Si–Cu/BPSG. Both values are much higher than the critical value of F ($P = 0.05$) of 3.37, indicating that sputtering bias is the dominant effect on the measured sheet resistance at the 5% confidence level. For Al–Si–Cu/BPSG, the sputtering temperature with the calculated F value of 3.97 is also significant at the 5% confidence level. The effects from other terms, including the interaction terms, are relatively small.

For Al–Si–Cu/TiW, the results are different. First, the resistivity (which is defined as the sheet resistance times thickness and is usually used to compare the conducting performances of films of different thickness) of Al–Si–Cu/Si and Al–Si–Cu/BPSG is about 1 $\mu\Omega$ cm less than that of Al–Si–Cu/TiW. This difference might be attributed to the fact that at high temperature the TiW layer under the Al–Si–Cu film is prone to be oxidized to TiO_2 and WO_3 [18]. The other difference is that for Al–Si–Cu/TiW each individual factor is significant enough to affect strongly the measured sheet resistance at the 5% confidence level. The effects from other terms, however, are still relatively small. Therefore, sub-

TABLE 3

Sheet resistance (mΩ per square) of Al–Si–Cu films on Si, BPSG and TiW substrates

Sample No.	Substrate		
	Si	BPSG	TiW
1	35.00	35.43	57.26
2	34.78	35.73	58.58
3	34.93	35.19	63.58
4	34.71	34.81	56.70
5	34.10	34.66	57.84
6	34.57	35.22	64.35
7	40.75	40.23	62.58
8	40.17	38.88	62.94
9	37.45	38.68	80.70
10	34.33	34.82	64.81
11	34.74	34.77	65.90
12	34.96	34.94	76.98
13	34.33	34.54	62.78
14	34.12	34.41	66.10
15	34.25	34.70	70.24
16	41.41	38.83	67.87
17	39.83	38.96	64.86
18	38.96	37.64	85.13
19	34.71	34.39	71.20
20	34.70	34.89	72.54
21	35.03	35.38	90.88
22	34.46	34.13	71.06
23	34.57	34.70	70.99
24	34.36	34.88	89.11
25	40.41	37.25	76.18
26	39.40	38.04	76.25
27	39.00	37.16	102.90

sequent multiple regression analysis [11,12] is performed using a first-order linear equation as the model.

Table 5 lists the coefficients of the best-fitted equations obtained using the raw data in Table 3. These fittings are considered to be adequate as for each best-fitted equation; the squared multiple correlation coefficients are all greater than 0.60 [12]. The regression analysis results are consistent with those from ANOVA. This is inferred from the observation that the ratios between these coefficients are similar to the ratios between the corresponding calculated F values in Table 4.

To appreciate the usefulness of these model equations, Figs. 2–4 show the three-dimensional plots of the predicted sheet resistance vs. the two major factors for the Al–Si–Cu films on Si, BPSG and TiW substrates. The third factor is set to a constant value so that the pertinent measured sheet resistance is minimal. Figure 2 shows that for Al–Si–Cu/Si the higher is the sputtering bias the lower is the sheet resistance. This might be explained by the fact that under lower sputtering bias the substrate has enough energy to disorder the Al atoms in the Al–Si–Cu film so the sheet resistance increases. Similar conclusions can also be drawn from Fig. 3 for Al–Si–Cu/BPSG. The situation is different for Al–Si–Cu/TiW, as Fig. 4 shows. Both the sputtering temperature and

TABLE 4

ANOVA results of sheet resistance

Source of variation	f [e]	Al–Si–Cu/Si			Al–Si–Cu/BPSG			Al–Si–Cu/TiW			Critical value of F ($P = 0.05$)
		SS [f]	V [g]	F [h]	SS	V	F	SS	V	F	
A [a]	2	1.24	0.62	0.01	367.38	183.69	3.97	1386.47	693.23	33.95	3.37
B [b]	2	15788.04	7894.02	113.15	7593.70	3796.85	82.17	311.79	155.89	7.63	3.37
C [c]	2	243.18	121.59	1.74	8.68	4.27	0.09	1266.12	633.06	31.00	3.37
$A \times B$	4	46.72	11.68	0.16	128.10	32.02	0.69	11.78	2.94	0.14	2.74
$A \times C$	4	35.61	8.90	0.12	34.99	8.74	0.18	74.33	18.58	0.91	2.74
$B \times C$	4	284.06	71.01	1.01	72.82	17.95	0.38	71.48	17.87	0.87	2.74
E [d]	8	558.08	69.76	–	369.62	46.20	–	163.32	20.41	–	–
Total	26	16956.97	–	–	8574.32	–	–	3285.29	–	–	–

[a] A = sputtering temperature. [b] B = sputtering bias. [c] C = annealing temperature. [d] E = pooled error. [e] f = degrees of freedom. [f] SS = sum of squares. [g] V = mean square. [h] Calculated value of F.

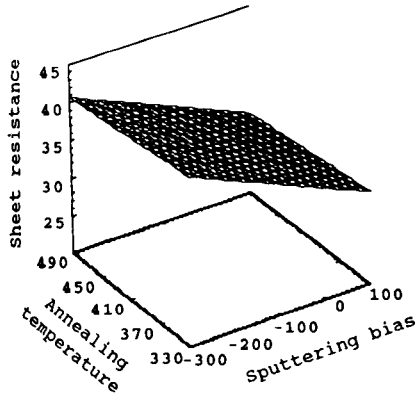

Fig. 2. Three-dimensional plot for Al–Si–Cu/Si of sheet resistance vs. sputtering bias and annealing temperature.

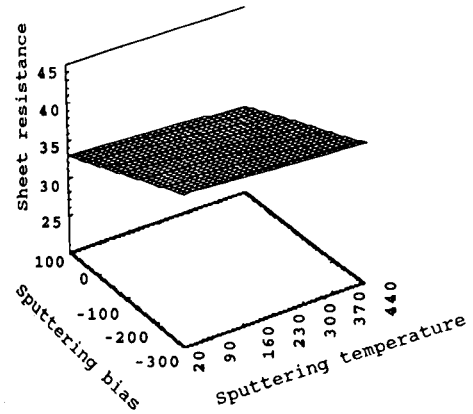

Fig. 3. Three-dimensional plot for Al–Si–Cu/BPSG of sheet resistance vs. sputtering bias and sputtering temperature.

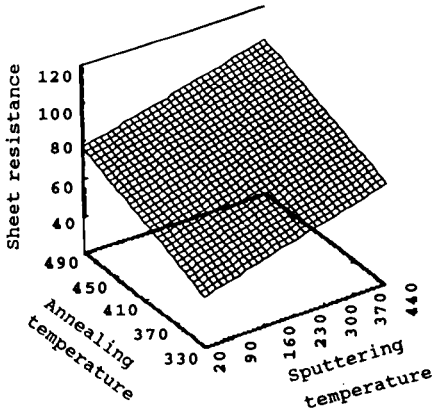

Fig. 4. Three-dimensional plot for Al–Si–Cu/TiW of sheet resistance vs. sputtering temperature and annealing temperature.

annealing temperature appear to have similar effects on the sheet resistance. Lowering either factor will decrease the sheet resistance. This is similar to a report [19] that at higher sputtering temperatures a magnetron-sputtered Al–Si film on a TiW substrate showed increasing sheet resistance.

This visual information of how the sheet resistance varies with the experimental factors is very useful for inferring the optimum deposition conditions. From Figs. 2–4, the optimum deposition conditions that will produce films of minimum sheet resistance are a high sputtering bias and a high annealing temperature for Al–Si–Cu/Si, a high sputtering bias and a high sputtering tem-

TABLE 5

Coefficients of best fitted equations [a] for sheet resistance data

Equation	Sheet resistance	Constant	Coefficient of parameter			Multiple correlation coefficient squared
			A [b]	B [c]	C [d]	
1	S_{Si} [e]	37.589	–	−0.025	−0.009	0.652
2	S_{BPSG} [f]	34.246	−0.003	−0.017	−0.001	0.630
3	S_{TiW} [g]	−18.375	0.062	−0.032	0.185	0.772

[a] The equation is of the following form: sheet resistance R_s = constant + A × sputtering temperature + B × sputtering bias + C × annealing temperature. [b] A = sputtering temperature. [c] B = sputtering bias. [d] C = annealing temperature. [e] S_{Si} = sheet resistance of Al–Si–Cu/Si. [f] S_{BPSG} = sheet resistance of Al–Si–Cu/BPSG. [g] S_{TiW} = sheet resistance of Al–Si–Cu/TiW.

TABLE 6

Optimum conditions of Al–Si–Cu films on Si, BPSG and TiW substrates to obtain minimum sheet resistance

Factor	Substrate		
	Si	BPSG	TiW
Sputtering temperature (°C)	20	300	20
Sputtering bias (V)	−100	−100	−100
Annealing temperature (°C)	450	450	370

perature for Al–Si–Cu/BPSG and a low sputtering temperature and a low annealing temperature for Al–Si–Cu/TiW. However, for practical applications other considerations must also be taken into account. These are the disadvantages of low throughput, increasing surface roughness and that a reduced resistance to electromigration accompanies the use of a low sputtering bias [20]. Hence the sputtering bias must be increased in order to overcome the above disadvantages. The final conditions thus obtained can then be regarded as the optimum conditions, and are listed in Table 6. Incidently, the fact that the resistivity of the Al–Si–Cu/Si prepared in this study is about 0.6 $\mu\Omega$ cm lower than those reported in the literature suggests the strength of this chemometric approach [21].

Diffraction intensity of Al[111] peak

Figure 5 shows the x-ray diffraction spectrum of Al–Si–Cu/Si. The diffraction intensities of the Al[111] peak of the Al–Si–Cu films on the Si, BPSG and TiW substrates prepared under various conditions are given in Table 7. The Al(111) plane is the densest plane in Al and suffers the least electromigration problems. The density of the Al(200) plane is the second densest Al(111) plane. Hence the ideal Al–Si–Cu films (or Al–Si films) on Si, BSPG and TiW substrates usually have more Al(111) or Al(200) planes [19,22,23].

The corresponding ANOVA results are given in Table 8. In the analysis, all three- and higher factor interactions are pooled into the error term. For Al–Si–Cu/Si, the calculated value of F is 8.91 for sputtering temperature and 4.48 for sputtering bias. Both values are greater than the critical value of F ($P = 0.05$) of 3.37, indicating that the sputtering temperature and sputtering

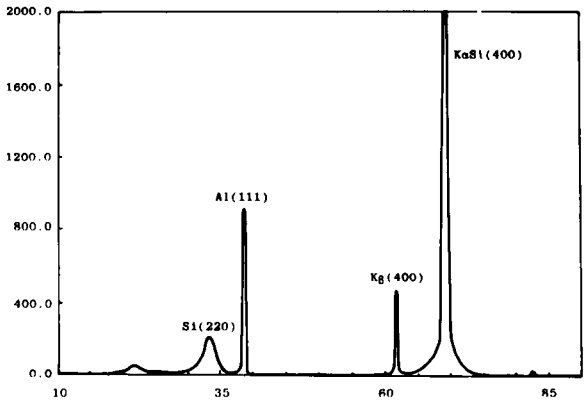

Fig. 5. X-ray diffraction spectrum of Al–Si–Cu/Si.

TABLE 7

Al[111] peak diffraction intensities (counts) of Al–Si–Cu films on Si, BPSG and TiW substrates

Sample No.	Substrate		
	Si	BPSG	TiW
1	6435	1340	2588
2	3298	1270	2427
3	2322	1377	2280
4	6378	1293	2201
5	4074	1228	1774
6	4290	1793	1862
7	3406	1525	1873
8	4645	1488	2162
9	2583	1651	2112
10	445	716	701
11	1270	993	1053
12	2823	922	935
13	1919	963	935
14	2070	1377	1072
15	2261	1370	1056
16	612	578	935
17	463	451	1129
18	479	354	1003
19	3688	1252	935
20	2415	1274	911
21	2561	1783	951
22	4153	1446	768
23	2923	1132	805
24	3574	1406	895
25	636	352	967
26	451	274	895
27	588	374	870

TABLE 8

ANOVA results of Al[111] peak diffraction intensity

Source of variation	f [e]	Al–Si–Cu/Si			Al–Si–Cu/BPSG			Al–Si–Cu/TiW			Critical value of F ($P = 0.05$)
		SS [f]	V [g]	F [h]	SS	V	F	SS	V	F	
S [a]	2	2576.76	1288.38	8.91	19223.70	9611.85	4.95	878.99	439.50	80.33	3.37
B [b]	2	1295.96	647.98	4.48	8671.76	4335.88	2.23	11.22	5.61	1.03	3.37
C [c]	2	662.57	331.28	2.29	3289.38	1644.69	0.84	0.66	0.33	0.06	3.37
$A \times B$	4	32.78	8.19	0.05	7994.84	1998.71	1.03	13.74	3.43	0.63	2.74
$A \times C$	4	206.65	51.66	0.35	49.23	12.30	0.00	2.48	0.62	0.11	2.74
$B \times C$	4	389.20	97.30	0.67	805.95	201.48	0.10	3.24	0.81	0.15	2.74
E [d]	8	1156.39	144.54	–	15517.24	1939.65	–	43.76	5.47	–	–
Total	26	6320.334	–	–	61226.640	–	–	954.09	–	–	–

[a–h] See Table 4.

bias are both significant at the 5% confidence level. For Al–Si–Cu/BPSG, the sputtering temperature with a calculated F value of 4.95 is the only factor that is significant at the 5% confidence level. For Al–Si–Cu/TiW, the sputtering temperature with a calculated F value of 80.33, which is much greater than the critical value of F ($P = 0.05$) of 3.37, is the only factor that is significant at the 5% confidence level.

From Table 7, the average diffraction intensity of all Al[111] peaks from Al–Si–Cu/Si (or from Al–Si–Cu/TiW) is larger than that from Al–Si–Cu/BPSG. This is because it is difficult to grow crystalline films with dominant Al(111) planes on an amorphous substrate such as BPSG. It is also noted that for both Al–Si–Cu/Si and Al–Si–Cu/TiW, with higher sputtering temperature the Al[111] peak intensity decreases. This is attributed to the decrease in the Al–Si–Cu film thickness resulting from the increasing interdiffusion at the film–substrate interface. This observation is consistent with other reports [24,25]. For Al–Si–Cu/BPSG, this phenomenon was not observed as the interdiffusion at the film–substrate interface was blocked by the BPSG.

Table 9 gives the coefficients of the best fitted equations obtained by fitting the raw data for Al[111] peak intensity to the three factors. The fittings are considered to be adequate, as for each best fitted equation the squared multiple correlation coefficients are greater than 0.60 [12]. The regression analysis results, however, are not totally consistent with those from the ANOVA. This might arise because the number of factors

TABLE 9

Coefficients of best fitted equations [a] for Al[111] peak diffraction intensity data

Equation	Al[111] orientation intensity	Constant	Coefficient of parameter			Multiple correlation coefficient squared
			A [b]	B [c]	C [d]	
4	O_{Si} [e]	10475.302	−6.525	8.556	−14.163	0.852
5	O_{BPSG} [f]	667.962	−1.457	2.156	2.174	0.898
6	O_{TiW} [g]	2064.777	−4.477	0.464	0.085	0.954

[a] The equation is of the following form: Al[111] diffraction intensity = constant + $A \times$ sputtering temperature + $B \times$ sputtering bias + $C \times$ annealing temperature. [b] A = Sputtering temperature. [c] B = Sputtering bias. [d] C = Annealing temperature. [e] O_{Si} = Al[111] peak diffraction intensity of Al–Si–Cu/Si. [f] O_{BPSG} = Al[111] peak diffraction intensity of Al–Si–Cu/BPSG. [g] O_{TiW} = Al[111] peak diffraction intensity of Al–Si–Cu/TiW.

TABLE 10

Optimum conditions of Al–Si–Cu films on Si, BPSG and TiW substrates to obtain maximum Al[111] diffraction intensity

Factor	Substrate		
	Si	BPSG	TiW
Sputtering temperature (°C)	20	20	20
Sputtering bias (V)	−100	0	0
Annealing temperature (°C)	370	450	410

that are significant at the 5% confidence level are sample dependent. From Table 8, the numbers are two for Al–Si–Cu/Si and one for Al–Si–Cu/BPSG and Al–Si–Cu/TiW. Nevertheless, optimum conditions such as those listed in Table 10 are still obtainable by directly analysing the raw data from Table 7. Similarly to the sheet resistance case, the improvement gained by using this chemometric approach is evident, as Fig. 5 shows. There is only one dominant peak, namely the Al[111] peak, in the Al–Si–Cu film indicating that there is little electromigration problem in this film.

Grain size

Scherrer's method [17] uses the following equation to estimate the grain size:

$$T = 0.9\ \lambda / B \cos\theta$$

where T diameter of the grain size, λ wavelength of the x-ray source, θ angle of incidence and B intensity at half of the peak maximum. From this equation, it is clear that the higher the full width

TABLE 11

FWHM of Al[111] peak diffraction intensities of Al–Si–Cu films on Si, BPSG and TiW substrates

Sample No.	Substrate		
	Si	BPSG	TiW
1	0.210	0.144	0.223
2	0.199	0.193	0.229
3	0.198	0.183	0.212
4	0.203	0.147	0.237
5	0.203	0.182	0.235
6	0.173	0.154	0.206
7	0.188	0.174	0.231
8	0.187	0.156	0.230
9	0.178	0.193	0.235
10	0.227	0.194	0.316
11	0.192	0.195	0.276
12	0.204	0.197	0.287
13	0.193	0.193	0.320
14	0.199	0.197	0.246
15	0.197	0.163	0.248
16	0.196	0.174	0.220
17	0.174	0.144	0.261
18	0.205	0.204	0.274
19	0.149	0.198	0.292
20	0.172	0.151	0.252
21	0.192	0.191	0.231
22	0.197	0.203	0.338
23	0.209	0.201	0.316
24	0.191	0.155	0.248
25	0.194	0.198	0.297
26	0.231	0.203	0.230
27	0.163	0.220	0.241

TABLE 12

ANOVA results of FWHM of Al[111] peak diffraction intensity

Source of variation	f [c]	Al–Si–Cu/Si			Al–Si–Cu/BPSG			Al–Si–Cu/TiW			Critical value of F ($P = 0.05$)
		SS [f]	V [g]	F [h]	SS	V	F	SS	V	F	
A [a]	2	451.63	225.81	0.44	21.97	10.98	1.35	123.61	61.80	3.66	3.37
B [b]	2	136.51	68.25	0.13	2.97	1.48	0.18	17.11	8.55	0.50	3.37
C [c]	2	250.29	125.14	0.25	0.99	0.49	0.06	49.45	24.72	1.46	3.37
$A \times B$	4	1179.62	294.90	0.58	5.04	1.26	0.16	1.07	0.27	0.01	2.74
$A \times C$	4	1378.74	344.68	0.68	4.47	1.12	0.14	5.05	1.26	0.07	2.74
$B \times C$	4	376.07	94.01	0.18	25.90	6.47	0.80	14.25	3.56	0.21	2.74
E [d]	8	4080.52	510.06	–	65.06	8.13	–	135.01	16.87	–	–
Total		7853.40	–	–	126.44	–	–	345.57	–	–	–

[a–h] See Table 4.

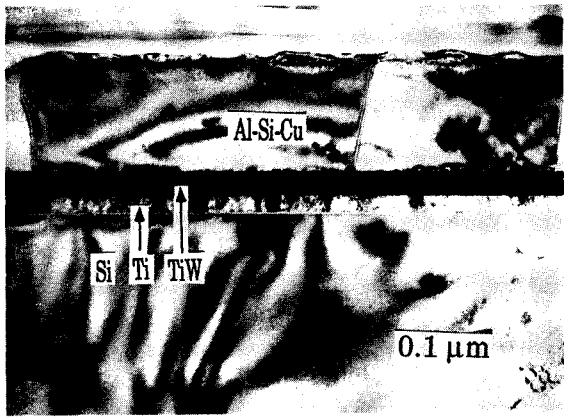

Fig. 6. TEM of Al–Si–Cu/TiW/Ti/Si.

at half-maximum (FWHM), the smaller is the grain size. The FWHM of Al[111] peak from the Al–Si–Cu films on the Si, BPSG and TiW substrates prepared under various conditions are given in Table 11 and the corresponding ANOVA results in Table 12. The calculated values of F for all three factors from all samples are smaller than the critical value of F ($P = 0.05$) of 3.37 (except for the sputtering temperature factor for the Al–Si–Cu/TiW sample). They are not significant at the 5% confidence level. There are two possible explanations. First, there is an inherent uncertainty of 30% with the x-ray measurements using Scherrer's method. Second, Scherrer's method uses the average thickness of small subgrains contained in the cross-sectional view grains to estimate the grain size. The grain size thus obtained (about 0.5 μm thickness) is different from the cross-sectional view grain size observed by the TEM (about 1–3 μm), as Fig. 6 shows. Therefore, unless a more accurate and convenient means of directly measuring the grain size is used, it is meaningless to pursue the pertinent optimum deposition condition using the grain size as the evaluation criterion.

Conclusion

The effects of sputtering temperature, sputtering bias and annealing temperature during the Al–Si–Cu metallization process on Si, BPSG and TiW substrates were investigated. The Al–Si–Cu films were deposited by magnetron sputtering in the sputtering temperature range 20–300°C, sputtering bias range 0 to −200 V and annealing temperature range 370–450°C. The sheet resistance, the intensity of the Al[111] diffraction peak and the grain size were used as the criteria to evaluate the quality of these films. The chemometric approach of unifying experimental design, analysis of variance and regression analysis used in this study has been shown to be an effective and efficient means for characterizing this metallization process. The results indicate that there is no single process that can yield films on every substrate with both the desired electrical properties (minimum sheet resistance) and reliability (maximum Al[111] peak intensity). Rather, the optimum deposition conditions are dependent on both the film quality and substrate identity. The variations are attributed to the differential interfacial properties. More detailed interfacial study is in progress. For practical applications, the economic factor of throughput must also be taken into considerations.

Financial support by the National Science Council of the Republic of China under grant NSC-80-0208-M007-80 is gratefully acknowledged. Acknowledgement is also made to the Electronics Research and Service Organization of Industrial Technology and Research Institute for preparing the samples and on-the-job training support to M.-K.L.

REFERENCES

1 S. Vaidya, D.B. Fraser and W.S. Lindenberger, J. Appl. Phys., 51 (1980) 4475.
2 S.B. Hershbein, P.A. Zulpa and J.M. Curry, in Proceedings of the 22nd Symposium on Reliability Physics, Las Vegas, NV, April 3–5, 1984, Institute of Electrical and Electronics Engineers, New York, 1984, p. 134.
3 M. Liehr and J.P. Delrue, J. Vac. Sci. Technol., A2 (1984) 288.
4 R.S. Nowicki and J.M. Harris, Thin Solid Films, 53 (1978) 195.
5 T. Turner and K. Wendel, in Proceedings of the 23rd Symposium on Reliability Physics, Orlando, FL, March 26–28, 1985. Institute of Electrical and Electronics Engineers, New York, 1985, p. 142.

6 P.H. Chang and H.Y. Liu, J. Appl. Phys., 62 (1987) 2485.
7 M.J. Attardo, R. Rutledge and R.C. Jack, J. Appl. Phys., 42 (1971) 4343.
8 G. Taguchi, System of Experimental Design, America Supplier Institute, New York, 1988.
9 R.J. Scully, J. Electrochem. Soc., 137 (1990) 1365.
10 L.R. Parker, S.L. Morgan, and S.N. Deming, Appl. Spectrosc., 29 (1975) 429.
11 J.L. Hwang, S.M. Chen and I.R. Chen, MRL Bull. Res. Dev., 3 (1989) 9.
12 P.C. Jurs, Computer Software Applications in Chemistry, Wiley, New York, 1986.
13 D.L. Massart, B.G.M. Vandeginste, S.N. Deming, Y. Michotte and L. Kaufman, Chemometrics: a Text Book, Elsevier, Amsterdam, 1988.
14 M.A. Sharaf, D.L. Illman and B.R. Kowalski, Chemometrics, Wiley, New York, 1986.
15 G. Kateman, Analyst, 115 (1990) 73.
16 C.P. Lee and T.H. Lin, J. Electron. Mater., 18 (1989) 623.
17 B.D. Cullity, Elements of X-Ray Diffraction, Addison-Wesley, Menlo Park, CA, 1978.
18 G.H. Tompkins and S. Lytle, J. Appl. Phys., 64 (1988) 3269.
19 T. Hara and N. Ohtsuka, IEEE Trans. Electron Devices, 34 (1987) 593.
20 D. Pramanik and N. Arjun, Solid State Technol., March (1990) 73.
21 D. Gardner and T. Michalka, IEEE Trans. Electron Devices, 32 (1985) 174.
22 S. Vaidya, in Proceedings of the 18th Symposium on Reliability Physics, Las, Nevada, April 8–10, 1980, Institute of Electrical and Electronics Engineers, New York, 1980, 165.
23 P. Chang and H. Liu, J. Appl. Phys., 62 (1987) 15.
24 H. Hoang, J. Hoang and M. McDavid, Solid State Technol., October (1987) 121.
25 K. Hinode and Y. Homma, in Proceedings of the 28th Symposium on Reliability Physics, New Orleans, LA, March 27–29, 1990, Institute of Electrical and Electronics Engineers, New York, 1990, p. 25.

Analytica Chimica Acta, 267 (1992) 121–129
Elsevier Science Publishers B.V., Amsterdam

Implementation of liquid secondary ion mass spectrometry on quadrupole mass spectrometers

Strategy, optimization, and evaluation

Richard B. Cole, Stephen Boue and A. Kamel Harrata

Department of Chemistry, University of New Orleans, New Orleans, LA 70148 (USA)

(Received 10th February 1992; revised manuscript received 20th April 1992)

Abstract

A detailed strategy for adding liquid secondary ion mass spectrometry (L-SIMS, similar to fast atom bombardment (FAB)) capability to a quadrupole mass spectrometer equipped with only electron ionization (EI) and chemical ionization (CI) sources is delineated. The complexity of modifications is held to a level whereby any moderately equipped machine shop could complete the work. The manufacturing of specific items to enable the reversible conversion of a Hewlett-Packard HP5985A EI/CI gas chromatography-mass spectrometry instrument to perform L-SIMS was kept to a minimum. The essential fabricated items consist of a source block, a lens assembly, and a sample probe. The rationale behind the construction, and the optimization of the size and placement of each part are described in detail. The new capabilities for L-SIMS experiments are demonstrated for selected biomolecules. Sensitivity evaluations demonstrate that protonated molecules of N^6-methyladenosine can be readily detected from as little as two picomoles of analyte.

Keywords: Mass spectrometry; Fast atom bombardment; Quadrupole mass spectrometry; Secondary ion mass spectrometry

Liquid secondary ion mass spectrometry (L-SIMS) and fast atom bombardment (FAB) [1] were introduced as ionization methods for mass spectrometry in the early 1980s. The two techniques are essentially similar, except that charged primary particles are used in the former, whereas neutral primary particles are used in the latter. The important common feature of L-SIMS and FAB which distinguishes them from previous particle-induced desorption techniques is that each uses a liquid matrix to dissolve or suspend analyte molecules. The viscous mixture is subsequently subjected to particle bombardment. It was the liquid nature of the target, rather than the charge state of the primary beam, which was the essential advance which dramatically broadened the possibilities for analyses of biomolecules by mass spectrometry. In this article, we use the term L-SIMS to encompass the particle-induced desorption techniques which employ a liquid matrix.

Success in electron ionization (EI) and chemical ionization (CI) mass spectrometry experiments often hinges upon the ability to vaporize intact sample molecules in high yield. This requirement generally restricts EI and CI mass spectrometry analyses to volatile or semi-volatile compounds. The exclusion of nonvolatile compounds from early mass spectrometry work spurred the development of alternative ionization methods such as field desorption [2], laser desorption [3], plasma desorption [4], and secondary

Correspondence to: R.B. Cole, Department of Chemistry, University of New Orleans, New Orleans, LA 70148 (USA).

ion mass spectrometry [5]. Although a certain level of success in ionizing small polar organic molecules was achieved prior to the start of the 1980s, it was not until the advent of L-SIMS that direct molecular weight analysis of thermally-labile biomolecules became routine. L-SIMS permits the analysis of nonvolatile compounds ranging in molecular weight from 100–24000 daltons [6,7]. Several important reviews have appeared, describing the utility [8], mechanisms [9], and chemical aspects [10] of L-SIMS.

Although many modern mass spectrometers have provisions for adapting an optional L-SIMS source, most older mass spectrometers designed prior to the popularization of L-SIMS in the early and mid-1980s were equipped exclusively with EI and CI sources. These older instruments must be retrofitted with new sources, lenses, probes, and even flange ports to accommodate an L-SIMS primary ion gun. When considering the choice of primary particles to be used, cesium ion guns have some significant advantages over primary beam sources which employ inert gases such as argon or xenon. For example, it is easier to focus Cs^+ particles emanating from a heated pellet than it is to focus a stream of gas which contains many uncharged gas atoms exiting from a capillary nozzle. Focusing ability allows one to increase the primary beam density at the target without significantly raising the overall pressure in the mass spectrometer. High source pressure is a drawback inherent to most primary beam sources which employ the noble gases as primary particles.

This paper describes a stepwise strategy for taking quadrupole mass spectrometers equipped exclusively with EI/CI sources and transforming them into L-SIMS instruments. The modifications have been kept to a minimum and they are reversible, so that no modes of operation are lost. In total, three essential parts were manufactured in-house at the University of New Orleans to enable the transformation: a new source block, an extraction lens assembly, and a sample probe. The specific instrument that has been modified is a gas chromatography–mass spectrometry instrument, first marketed in 1977, and equipped exclusively for EI/CI operation. Although the dimensions and placement of the constructed extraction lens and probe have been optimized for L-SIMS experiments on this particular instrument, the outlined approach to adapting an instrument may be applied to other mass spectrometers which also lack L-SIMS capability. The performance of the newly transformed instrument has been evaluated for selected biomolecules.

EXPERIMENTAL

The modified mass spectrometer is an HP5985A (Hewlett-Packard, Palo Alto, CA), equipped with a quadrupole mass analyzer (upper mass limit = m/z 1000), and an entrance port for a gas chromatograph. The data system which accompanies this mass spectrometer is a Hewlett-Packard "SIDS" system. The primary ion gun is a focusing cesium ion gun [11–13], Antek model CS-160-250B, which was purchased commercially (Antek, Palo Alto, CA). A primary ion current density of approximately 10^{12} ions cm^{-2} sec^{-1} was used in all experiments. This current density has been shown [14] to offer the optimal balance between sample renewal (via liquid matrix transport mechanisms) and sample consumption (from primary beam sputtering). A 1/2″ i.d. direct inlet port with 1/4″ i.d. insert was purchased from Phrasor Scientific (Duarte, CA) to allow electrical isolation of the 1/4″ sample probe used in all experiments. This 1/2″ i.d. inlet port replaced the standard 1/4″ i.d. direct introduction port of the HP5985A. Use of the latter creates an undesirable electrical contact between the probe and the source housing, thus preventing the application of an adjustable potential to the probe tip. A Phrasor HED conversion dynode detector, also purchased from Phrasor Scientific, was used to replace the conventional electron multiplier detector in order to improve sensitivity, especially toward the high mass limit of the quadrupole analyzer. This new detector was installed after the source and probe tip optimization studies had already been completed, but it was used during the acquisition of all displayed spectra. All of the compounds used to evaluate the L-SIMS capability of the modified instrument

were purchased commercially from Sigma (St. Louis, MO).

RESULTS AND DISCUSSION

The approach taken here to adapt an instrument for L-SIMS is to keep the modifications relatively simple, such that any moderately equipped machine shop could make the changes. In choosing the best way to situate L-SIMS components, if possible, it is advantageous to have the sample probe axis in line with either the mass analyzer axis or the primary ion axis. This type of arrangement implies that alignment is free from direction adjustment, thus simplifying subsequent distance adjustments. It is usually convenient to use a direct probe inlet port to introduce the L-SIMS sample probe into the vacuum chamber. For the HP5985A, the direct probe inlet is coplanar and at a 90° angle to the quadrupole axis; the gas chromatograph (GC) entrance port is positioned colinearly and directly on the opposite side of the ion source relative to the direct probe inlet. To minimize downtime during source transformations, the primary ion gun should not occupy the space of the GC inlet, otherwise the GC must be removed each time the L-SIMS source is mounted. Instead, as no other ports were available, an additional flange was added to the top of the source housing. Later models of the Hewlett-Packard 5985 GC-MS series, in fact, are built with a flange already located in this position. Use of this configuration implied that the primary ion axis would be at 90° to both the sample probe and the mass spectrometer axis.

Addition of the vacuum flange to the top of the source-housing involved first removing the handle on top of the manifold. A hole was drilled whose diameter corresponded to the outer diameter of the vacuum flange to be added (see Fig. 1). The base of the flange was cut such that when the cesium ion gun was in place, there was a clearance of 1/8″ between the final lens of the cesium gun (at ground potential) and the magnet yoke of the EI/CI source. The EI/CI source could thus be mounted for conventional use without disturbing the position of the cesium gun.

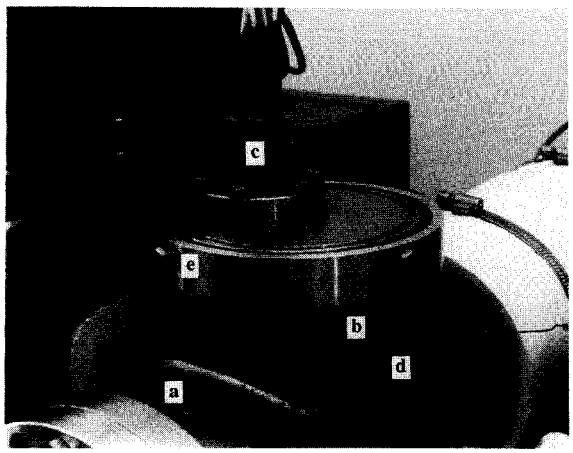

Fig. 1. Photograph of the source-housing manifold (a) showing the added vacuum flange (b) and an external view of the cesium ion gun mounting (c). The vacuum flange was secured by a 'tig' weld (d). Screw mounts containing centering bolts (e) to position the ion gun are visible along the periphery of the receiver flange.

The edges of the flange were rounded to match the curvature of the source housing, and the flange was then welded into place using a tungsten-inert gas (tig) weld. The cesium ion gun mounting holds an "O-ring" which protrudes slightly from the metal casing. This "O-ring" was greased lightly and placed on the receiver flange where it could be manually displaced up to 3/16″ in any direction from center. Four evenly spaced centering bolts are used to secure the gun in a chosen fixed position. When correctly centered, there is a space of about 1 and 7/8″ between the gun's exit aperture and the quadrupole axis. At this distance, the focusing cesium ion gun has an ultimate spot size of approximately 2 mm in diameter [15].

The next step was to design a probe to be used for sample introduction. A commercially available (Phrasor Scientific, Duarte, CA) 1/2″ i.d. vacuum inlet was mounted in place of the standard 1/4″ i.d. direct introduction probe inlet. The accompanying stainless steel sleeve has an inner diameter of 1/4″. A 1/4″ stainless steel sample probe was fabricated (Fig. 2) to fit into this sleeve where PTFE ferrules placed at each end of the sleeve served the dual functions of providing a

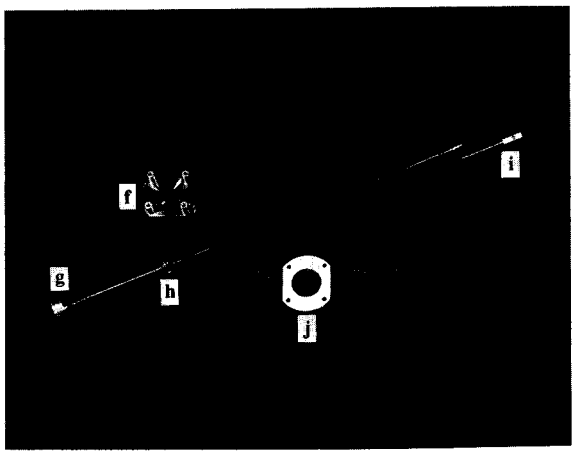

Fig. 2. Photograph of the manufactured L-SIMS source parts: aluminum open-construction source block (f), 1/4″ diameter stainless steel sample probe (center) with metallic holder (g), collar (h), and detachable probe tip (i). The extraction lens assembly (j) is shown with connecting wire, and lenses of varying aperture diameter used to optimize secondary ion collection (see Fig. 4).

vacuum seal, and electrical isolation of the sample probe. The back end of the sample probe was fitted with a metallic disk which served as a handle for probe tip angle adjustment. A metallic "alligator clip" can also be attached to this handle, thereby providing electrical contact to a power supply used to float the probe at an adjustable potential. If a magnetic sector instrument with a high voltage (e.g., 6 kV) source is being modified, extra steps must be taken to insure that the high voltage probe tip is properly shielded from the user. The front end of the sample probe was tapered and ended with a screw receptacle into which different probe tips with protruding screws can be mounted (Fig. 2). Since the quadrupole axis intersected the probe axis at the center of the probe tip, all constructed probe tips were cut flat along the diameter of the initially round tip, i.e., the end view reveals a "half moon". Perpendicular to this flat surface was drilled a round, centered reservoir hole which, when filled with sample and liquid matrix, has a top layer exactly at the center of the probe tip axis.

Although, in principle, the standard manufacturer's EI/CI source block could be employed as is, or modified [16], for L-SIMS analysis, its use has at least four major disadvantages:

(1) Cesium primary ions must pass through a small slit which normally serves as the entrance to the electron trap. Since this slit is rather narrow (1/16″) compared to the diameter of the primary ion beam, many primary ions cannot reach the target.

(2) The metallic guide which directs the sample probe into the ion source is actually part of the ion source (held at ground potential). It comes into direct electrical contact with the sample probe, thus preventing one from floating the sample probe at a potential other than ground.

(3) The source is relatively closed, thus, intolerably high pressures (due principally to matrix evaporation) may develop within the source because of inadequate immediate pumping.

(4) Sample and matrix accumulate rapidly on the inner walls of the ion source during L-SIMS experiments. They degrade performance, and necessitate source cleaning at frequent intervals.

Widening the apertures of the standard source block via machine shop intervention can help to alleviate problems 1 and 3, but this approach might prove to be deleterious to subsequent CI applications which usually require a relatively closed ion source.

For these reasons, the fabrication of an alternative "open-construction" L-SIMS source and lens assembly was undertaken. The intent was not to redesign the entire lens stack assembly, but rather to adapt the existing one for L-SIMS use. To this end, the decision was made to remove the standard source block which was responsible for the above listed problems, and replace it with an open-construction source and additional accompanying extraction lens to direct secondary ions efficiently towards the existing lens stack assembly. The new source block and extraction lens would occupy exactly the same space as the removed standard source block.

The aluminum, open-construction source block shown in Fig. 2 was thus manufactured. Bolt holes to secure the new source block to the rest of the source assembly are positioned exactly as those on the EI/CI source block. Two PTFE lens holders of varying thickness were also con-

structed (one is shown in Fig. 2). When the four posts of the manufactured source block and the four ceramics of the existing lens stack are inserted in the receiver holes of either PTFE holder, the lens stack has exactly the same height as when the EI/CI source block is in place. The different thicknesses of the two PTFE holders, and the varying depths of the receiver holes on each side, permitted the placement of lenses at four discrete distances from the probe tip. The added extraction lens was electrically connected to the source feedthrough normally used to control the potential of the "Drawout Lens" of the HP5985A. This permitted the application of a variable potential between 0 and −127.5 V (relative to ground potential) to the new extraction lens. The former so-called "Drawout Lens" of the existing lens stack which we now refer to as the "Transfer Lens" was connected to the feedthrough normally used to control the potential of the EI filament which can be varied from −10 to −255 V. Use of dual extraction lens systems entailing placement of one lens on each side of the PTFE holder was also possible. The second fabricated lens was electrically connected to an independent power supply. In addition, a 2-Ω resistor was placed across the feedthroughs normally used for the electron filament. Completing the filament circuit was necessary to permit normal functioning of the computer data system. The assembled lens stack containing the constructed source block and added (single) extraction lens is shown in Fig. 3.

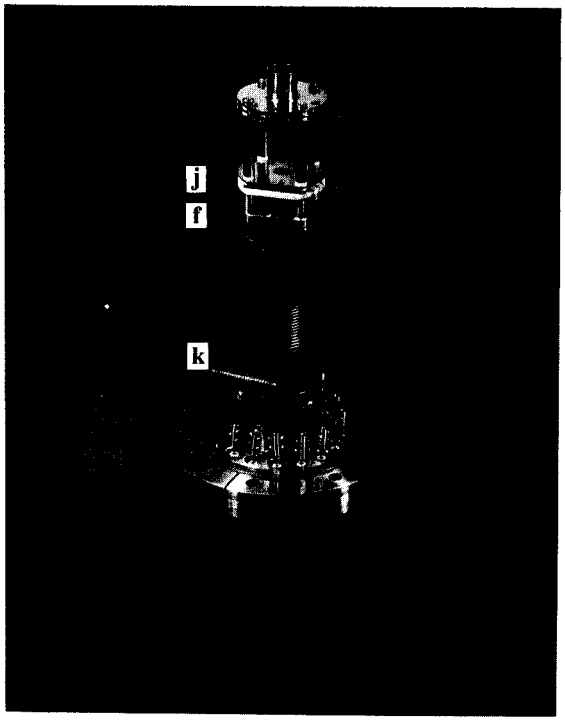

Fig. 3. Photograph of the assembled L-SIMS source containing extraction lens assembly (j), open-construction aluminum source block (f), and 2-Ω resistor (k) placed across the feedthroughs normally serving the EI filament.

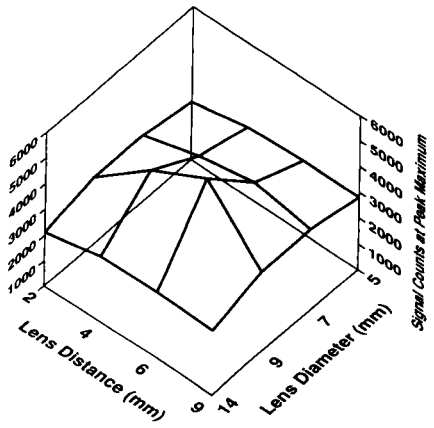

Fig. 4. Three-dimensional plot of maximum signal counts for m/z 277 from pure, dry glycerol (arbitrary units) vs. lens distance from sample reservoir (mm) vs. lens diameter (mm).

Alignment of probe tip and primary ion gun

The general procedure for positioning the probe tip and aligning the cesium ion gun relative to a fixed mass analyzer axis will now be described. This procedure should be followed each time an alignment problem is suspected. With the source completely removed and open, a ruler is fastened to the (centered) receiver flange of the source-housing manifold. The point on the ruler denoting the center of the receiver flange must be clearly marked. The sample probe and firmly attached probe tip are then introduced into the source via the direct probe inlet. The probe is positioned at the point where the sample reservoir on the probe tip is centered and colinear with both the mass spectrometer axis and the

mark on the ruler corresponding to the center of the receiver flange. Once this has been achieved, a collar (see Fig. 2) is fastened via set screws to the probe tip at the vacuum lock. This collar reproducibly stops the sample reservoir at the proper position in the source each time the probe tip enters the vacuum lock. The sample probe and ruler are then withdrawn, and the L-SIMS source is mounted and mass spectrometer pumping is actuated in a manner completely analogous to the mounting of the EI/CI source.

Once a suitable vacuum has been achieved, insulating tape is used to completely cover the probe tip *except* for a small hole pierced in the tape corresponding exactly to the diameter of the sample reservoir. The sample probe is then introduced into the source via the vacuum lock of the direct probe inlet such that the plane of the sample reservoir is parallel to that of the ion gun receiver flange. An ammeter set to measure positive ion current is connected to the handle of the isolated sample probe. The ion gun is then turned on and, in an alternating fashion, the position of the gun in the receiver flange is manually adjusted, and the focusing lenses of the gun are manipulated so as to obtain a maximum positive ion current reading on the ammeter. It is absolutely essential to iteratively adjust the gun position and the lens values, seeking maximum current at each step, in order to achieve a truly aligned primary ion gun.

Optimization of added extraction lens assembly

All of the fixed lenses in the lens stack used for the conventional EI/CI source were also used for the L-SIMS source. As these lenses have uniform apertures, it was decided to take the simplest, empirical approach to constructing an additional extraction lens close to the sample reservoir where secondary ions are formed. Without this lens, the transmission of secondary ions was clearly too low to offer acceptable sensitivities. The idea was to place circular lens plates of varying size (but close to the diameter of existing lenses) at varying distances from (but concentric to) the sample reservoir. Lens diameters of 5, 7, 9, and 14 mm were each tried at distances of 2, 4, 6, and 9 mm from the sample reservoir, a total of

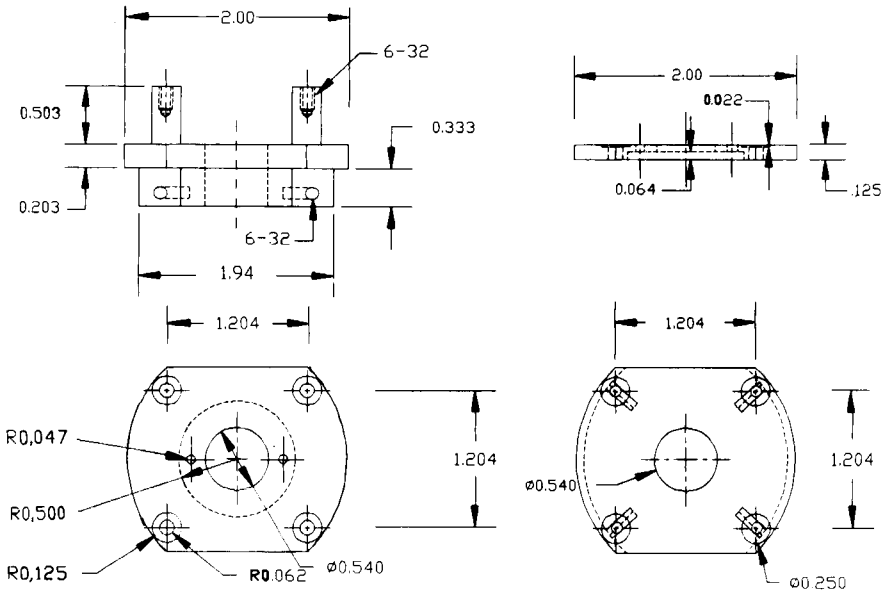

Fig. 5. Mechanical drawing showing dimensions of the aluminum source block (upper and lower left) and the PTFE extraction lens holder (upper and lower right). All dimensions are in inches. Radii measurements are preceded by the letter R, diameter measurements are preceded by the symbol ∅.

16 points in all. At each point, thorough, systematic optimization of all primary ion gun parameters, source lenses, and sample probe voltages was conducted to achieve the most intense peak for a cluster of three glycerol molecules solvating a proton (m/z 277) arising from a pure glycerol sample. The 3-dimensional plot of maximum signal counts (arbitrary units) for m/z 277 vs. lens distance from sample reservoir vs. lens diameter is shown in Fig. 4. As is evident from the figure, a 9 mm diameter lens placed at 6 mm from the target was shown to yield the greatest secondary ion signal.

An alternative approach to lens optimization would be to use an ion trajectory simulation program to size and situate the added extraction lens. Such computer programs can offer an idea of appropriate dimensions before any lenses are constructed. Precise information concerning initial kinetic energies and divergence angles of secondary ions, however, is required for these programs. In L-SIMS, a distribution of kinetic energies [17] is present for secondary ions originating from a target of several millimeters. Lens systems designed with low aberration coefficients can best accomodate a wide range of secondary ion energies and points of origin [18]. At very low kinetic energies (e.g., < 10 eV used in this study), actual ion trajectories can differ significantly from calculated trajectories [19]. Perturbations due to time-dependent fringe fields at the entrance (and exit) of quadrupole filters can inflict significant uncertainties on calculated ion trajectories. These

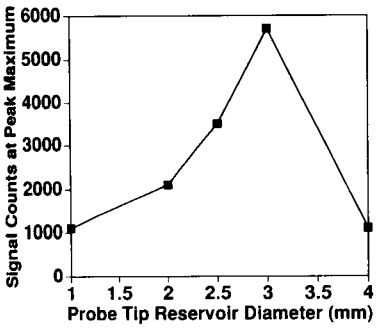

Fig. 6. Plot of maximum signal counts for m/z 277 from pure, dry glycerol (arbitrary units) vs. probe tip reservoir diameter (mm).

complications associated with theoretically optimized lens designs may eventually necessitate empirical refinements or the use of corrector units.

Contrary to expectations, several attempts to utilize a dual extraction lens system (with capability for independent optimization of voltages for each lens) failed to give secondary ion signals comparable to those observed from a single constructed extraction lens. Schematic diagrams defining the dimensions used to manufacture the final optimized PTFE lens holder and aluminum source block appear in Fig. 5.

Optimization of probe tip reservoir diameter

Adopting the 9 mm diameter lens placed at 6 mm from the target as the standard lens arrangement, a study was undertaken to determine the optimum diameter of the probe tip sample reservoir. Because individual probe tips are screwed into the sample probe (Fig. 2), it is relatively easy to fabricate tips having different reservoir diameters. In total, five probe tip reservoir diameters were tried, i.e., having diameters of 1, 2, 2.5, 3, and 4 mm. The protonated glycerol cluster at m/z 277 from pure glycerol was again chosen to evaluate the maximum secondary ion signal after thorough optimization of all primary ion gun parameters, source lenses, and sample probe voltages. As shown in Fig. 6, a probe tip reservoir diameter of 3 mm offered the optimum secondary ion signal. At reservoir diameters below 2 mm (the approximate minimum spot size of the primary ion beam), many primary ions never strike the sample, leading to a decrease in secondary ion signal. At a reservoir diameter of 4 mm, the concave surface curvature of the liquid matrix drop appears to have a deleterious effect on the secondary ion signal. Moreover, at this diameter, it is likely that collection efficiency is significantly poorer for ions formed at the outer edges of the reservoir. At 3 mm reservoir diameters and below, the drop curvature is less obvious.

Performance

To demonstrate the efficacy of the optimized L-SIMS instrument for its intended use in biochemical analysis, mass spectra of various

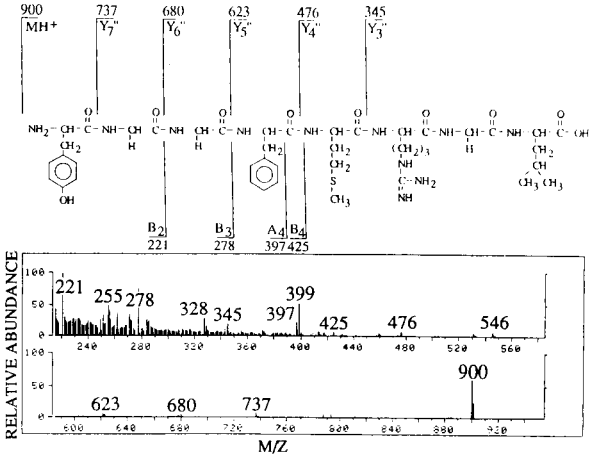

Fig. 7. L-SIMS spectrum of the peptide proenkephalin in a 1:1 glycerol–thioglycerol matrix. Oxalic acid was added as a protonating agent. The structure of the intact molecule and postulated fragment assignments are shown in the upper portion of the figure.

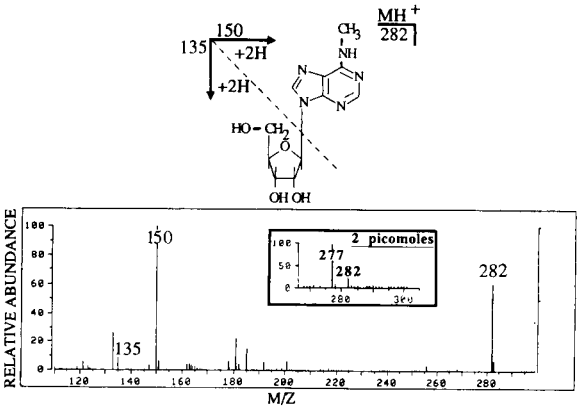

Fig. 8. L-SIMS spectrum of the nucleoside N^6-methyladenosine in a 1:1 glycerol–thioglycerol matrix. Oxalic acid was added as a protonating agent. The structure of the intact molecule and proposed fragments are shown at the top. The insert in the lower half of the figure shows the mass spectrum in the region of the protonated molecule with only 2 picomoles of compound present on the probe tip.

biomolecules have been acquired. These include peptides, nucleosides, steroid glucuronides, and acyl carnitines. Displayed in Fig. 7 is the L-SIMS spectrum of the peptide proenkephalin in a 1:1 glycerol–thioglycerol matrix with oxalic acid added as a protonating agent. The enkephalins are known to produce high yields of intact protonated molecules (MH^+) in L-SIMS [20,21]. The protonated molecule of proenkephalin appears at m/z 900 (mass axis calibrated to give nominal mass values). Many fragment ions are also formed, and the structure of the intact molecule and proposed fragment assignments (using the nomenclature of Roepstorff and Fohlman [22]) are included in Fig. 7. A second example appearing in Fig. 8 is that of the nucleoside N^6-methyladenosine, also in a matrix of 1:1 glycerol–thioglycerol with oxalic acid; the protonated molecule appears at m/z 282. Displayed in this figure are the structure of the intact molecule along with postulated fragment ion assignments. The N^6-methyladenosine compound was further used to evaluate the sensitivity of the instrument. The insert in the center portion of the displayed spectrum (Fig. 8) shows the mass spectrum in the vicinity of MH^+ obtained using only two picomoles of analyte in a glycerol matrix on the sample probe. Even at this low concentration, the peak corresponding to MH^+ stands out clearly above the background. The nearby peak at m/z 277 corresponds to the protonated cluster of three glycerol molecules. Typical ion source operating parameters for L-SIMS experiments appear in Table 1.

Conclusion

Mass spectrometers originally equipped with only EI and CI sources can be readily modified to

TABLE 1

Typical parameter settings used during operation of the L-SIMS source

L-SIMS Source component	Feedthrough connection (SIDS data system nomenclature)	Voltage (V) [a] (relative to ground)
New extraction lens	"Drawout" (D)	−22
Transfer lens	"Electron Energy" (Y)	−190
Focusing lens	"Ion Focus" (F)	−48
Entrance lens	"Ent Lens (L)	−240 mV/dalton
Sample probe	(independent power supply)	+5
Source block	none	0

[a] Unless otherwise stated.

perform L-SIMS. The HP5985A was transformed by the addition of a vacuum flange (fitted for a cesium ion gun) to the source-housing manifold. Three essential parts were manufactured: (1) an open-construction metal (e.g. aluminum) source block, (2) a lens assembly consisting of a non-conducting lens holder (e.g. PTFE) and circular metal lens, and (3) a metal sample probe with removable probe tips. Empirical optimization of the placement of the added lens revealed that optimal detection of secondary ions occurred for a 9 mm diameter lens placed at 6 mm from the probe tip's sample reservoir. The probe tip that produced the maximum signal for the above lens configuration had a reservoir diameter of 3 mm. L-SIMS spectra of selected biomolecules demonstrate the efficacy of the transformed instrument. Sensitivity evaluations show that the MH^+ ion of N^6-methyladenosine can be readily detected from as little as two picomoles of sample.

The authors thank Mr. Robert Herrell for his expert welding of the vacuum flange to accomodate the cesium ion gun, and for his precision work in fabricating the source block, lens holder, and sample probe. We also thank Mr. Harry Rees for his assistance with all aspects of instrumental electronics. We are grateful to the Cancer Association of Greater New Orleans for financial support of this project.

REFERENCES

1 M. Barber, R.S. Bordoli, R.D. Sedgwick and A.N. Tyler, J. Chem. Soc. Chem. Commun., (1981) 325.
2 H.D. Beckey, Principles of Field Ionization and Field Desorption Mass Spectrometry, Pergamon, Oxford, 1977.
3 F. Hillenkamp, E. Unsold, R. Kaufmann and R. Nitsche, Nature, 256 (1975) 119.
4 D.F. Torgerson, R.P. Skowronski and R.D. Macfarlane, Biochem. Biophys. Res. Commun., 60 (1974) 616.
5 A. Benninghoven, D. Jaspers and W. Sichtermann, Appl. Phys., 11 (1976) 35.
6 M. Barber and B.N. Green, Rapid Commun. Mass Spectrom., 1 (1987) 80.
7 C. Fenselau, Anal. Chem., 54 (1982) 105A.
8 M. Barber, R.S. Bordoli, G.J. Elliott, R.D. Sedgwick and A.N. Tyler, Anal. Chem., 54 (1982) 645A.
9 S. Pachuta and R.G. Cooks, Chem. Rev., 87 (1987) 647.
10 C. Fenselau and R.J. Cotter, Chem. Rev., 87 (1987) 501.
11 W. Aberth, K.M. Straub and A.L. Burlingame, Anal. Chem., 54 (1982) 2029.
12 A.M. Falick, G.H. Wang and F.C. Walls, Anal. Chem., 58 (1986) 1308.
13 W. Aberth and A.L. Burlingame, Anal. Chem., 60 (1988) 1426.
14 R.B. Cole, C. Guenat, J.R. Hass and R.W. Linton, Anal. Chem., 59 (1987) 1930.
15 W. Aberth, personal communication, 1990.
16 J.F. Mahoney, J. Perel, P.C. Goodley, C.N. Kenyon and K. Faull, Int. J. Mass Spectrom. Ion Phys., 48 (1983) 419.
17 R.B. Cole, S. LeMeillour and J.-C. Tabet. Anal. Chem. 64 (1992) 365.
18 B. Paszkowski, Electron Optics, Elsevier, New York, 1968, p. 279.
19 R.T. Short, C.C. Grimm and P.J. Todd, J. Am. Soc. Mass Spectrom., 2 (1991) 226.
20 M. Barber, R.S. Bordoli, G.V. Garner, D.B. Gordon, R.D. Sedgwick, L.W. Tetler and A.N. Tyler, Biochem. J., 197 (1981) 401.
21 I. Katakuse and D.M. Desiderio, Int. J. Mass Spectrom. Ion Proc., 54 (1983) 1.
22 P. Roepstorff and J. Fohlman, Biomed. Mass Spectrom., 11 (1984) 601.

Analytica Chimica Acta, 267 (1992) 131–136
Elsevier Science Publishers B.V., Amsterdam

Electrothermal atomic absorption spectrometric determination of silver in biological materials with a molybdenum tube atomizer

Kiyohisa Ohta, Satoshi Kaneco, Syn-ichi Itoh and Takayuki Mizuno

Department of Chemistry for Materials, Faculty of Engineering, Mie University, Tsu, Mie 514 (Japan)

(Received 3rd March 1992; revised manuscript received 21st April 1992

Abstract

Electrothermal atomic absorption spectrometry (ETAAS) of silver with a molybdenum tube atomizer was investigated. Hydrogen was added to the argon purge gas to protect the metal atomizer from oxidation by trace oxygen in the atomizer chamber. The optimum gas flow-rates were argon 480 ml min^{-1} and hydrogen 20 ml min^{-1}. The characteristic mass (the mass of the analyte giving a peak absorbance of 0.0044) of silver using this atomizer was 5.4 fg, which is better than that obtained with a graphite atomizer. The interferences caused by large amounts of interferents were evaluated. Ammonium thiocyanate as a chemical modifier eliminated the interferences. The amount of silver determined in biological materials was in good agreement with the certified value.

Keywords: Atomic absorption spectrometry; Biological samples; Molybdenum tube atomizer; Silver

Silver is a non-essential metal of low toxicity, but it is well known that toxic effects may result from the local corrosive or irritative action of large doses of silver compounds [1,2]. The determination of silver in biological samples is therefore of interest, and analysis by electrothermal atomic absorption spectrometry with a graphite furnace has been reported [2–7]. There is, however, the problem of interferences by matrix species [2–15] and AAS determination has been combined with a prior separation by liquid–liquid extraction [4,8,9], chemical modification with the use of phosphate, ascorbic acid, Ir, Pd and Cu [2,11–14] or a standard addition method [5,15]. Of these methods, the chemical modification method is the most simple and convenient.

In recent years, metal tubes have been developed as atomizers in electrothermal atomic absorption spectrometry (ETAAS) [16–18] and have been found to be superior to graphite atomizers. There is, however, little information on the determination of silver by ETAAS using a molybdenum tube atomizer.

This paper reports the determination of silver in biological samples by ETAAS with a molybdenum tube atomizer, and describes interference studies with the atomizer and a method for the elimination of the interferences.

Correspondence to: K. Ohta, Department of Chemistry for Materials, Faculty of Engineering, Mie University, Tsu, Mie 514 (Japan).

EXPERIMENTAL

Apparatus

Atomic absorption was measured at 328.1 nm (silver hollow-cathode lamp; Hamamatsu Photonics) using a monochromator (Nippon Jarrell-Ash 0.5-m Ebert-type), an amplifier, a storage oscilloscope (Iwatsu MS-5021) and a microcomputer

(Sord M223). The molybdenum tube atomizer (25 mm × 1.8 mm i.d., wall thickness 0.05 mm) was made from high-purity (99.5%) molybdenum foil (Rembar). A 0.3-mm diameter hole was drilled at the mid-point of the tube to inject the sample solution. The electric power for heating the atomizer was supplied with a step-down transformer and a transformer (Yamabishi volt-slider, S-130-30, capacity 3 kVA). Two pinhole apertures were placed in front of and at the rear of the atomizer, in order to collimate the light beam and eliminate the radiation from the atomizer surface. Background absorption was checked with a deuterium lamp (Original Hanau D200F). The absorption signal from the amplifier and the output signal from the photodiode for the measurement of the atomizer temperature were simultaneously fed into the microcomputer. Calibration of the temperature of the atomizer was done against the photodiode voltage with an optical pyrometer (Chino Works) and a microcomputer program [17].

Reagents

All chemicals used were of analytical-reagent grade.

A stock standard solution of silver (1 mg ml^{-1}) was prepared as the nitrate in 0.1 M nitric acid after dissolving the high-purity metal in 14 M nitric acid. Stock standard solutions of the matrix elements for the interference study were prepared as nitrates or chlorides in 0.1–6 M nitric or hydrochloric acid. Working standard solutions with concentrations appropriate to the atomic absorption measurements were prepared by dilution of the stock standard solutions with the water immediately before use.

Procedures

For the interference study, a 1-μl portion of sample solution containing silver (0.3 ng ml^{-1}) and interferent (3–30 μg ml^{-1}) was pipetted into the molybdenum tube atomizer. The sample was dried at 90°C for 10 s and 500°C for 10 s and heated to atomize at 2070°C for 3 s. The atomizing temperature corresponded to a heating rate of 2.3°C ms^{-1}.

An accurately weighed biological sample (about 0.5 g) was treated with 3 ml of nitric acid (14 M) and 1 ml of hydrogen peroxide (30%) in a Uni-seal decomposition vessel and heated for 3 h in an electric oven at 120°C. After the decomposition, the solution was evaporated in a Teflon beaker by heating in a polyethylene glycol bath (110°C) and then the wetted residue was dissolved in 5 ml of 1 M nitric acid on the bath. Finally, the solution was transferred into a 50-ml volumetric flask and diluted to volume with ammonium thiocyanate solution (5 mg ml^{-1}). If required for AA measurement, the solution was further diluted with the thiocyanate solution. ETAAS measurements were performed in the same manner as described for the interference study.

RESULTS AND DISCUSSION

Effect of heating rate

For the sensitive ETAAS determination of silver using the molybdenum tube atomizer, it is important to investigate the effect of the atomization rate on the silver AA profile. Therefore, the AA signals were measured at various heating rates of the atomizer (3.2, 2.7, 2.3, 1.9 and 1.5°C ms^{-1}). The absorption profile of silver was characterized by a sharper and narrower peak with increase in heating rate, as shown in Fig. 1. The appearance temperature of the silver signal (880°C), which is defined as the temperature of

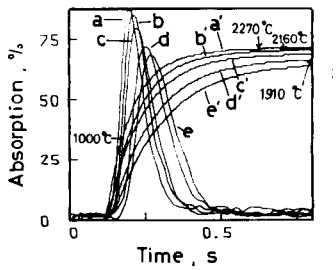

Fig. 1. Effect of heating rate of the molybdenum atomizer on atomic absorption of silver. a and a', 3.2°C ms^{-1}; b and b', 2.7°C ms^{-1}; c and c', 2.3°C ms^{-1}; d and d', 1.9°C ms^{-1}; e and e', 1.5°C ms^{-1}; a–e, atomization profiles; a'–e', increasing temperature. Silver, 1.0 pg; purge gas, 480 ml min^{-1} argon–20 ml min^{-1} hydrogen.

atomizer giving a peak absorbance of 0.0044, was independent of the heating rate. However, the temperature at the maximum of the AA signal (peak temperature) was 1190°C at 3.2°C ms^{-1}, 1170°C at 2.7°C ms^{-1}, 1150°C at 2.3°C ms^{-1}, 1125°C at 1.9°C ms^{-1} and 1110°C at 1.5°C ms^{-1}, and therefore the peak temperature of the signal was found to be dependent on the heating rate. These phenomena are the same as those observed for the absorption of cadmium, phosphorus, lead, etc. [17–19]. The highest AA signal of silver was obtained at a heating rate of 3.2°C ms^{-1}. Consequently, 2.3°C ms^{-1} was selected as the optimum heating rate, in view of the background absorption and the lifetime of the metal atomizer.

Effect of hydrogen

A small amount of hydrogen needed to be added to the argon purge gas for the protection of the metal atomizer from oxidization by small amounts of residual oxygen in the argon cylinder. Further, from previous studies [16–19], a small addition of hydrogen has been found to be very effective for the atomization of some elements in ETAAS with a metal tube atomizer. Therefore, absorption signals for silver (1 pg) were evaluated in argon–hydrogen purge gas at a heating rate of 2.3°C ms^{-1}. The total flow-rate of the gas mixed in various ratios was held constant at 500 ml min^{-1}. The addition of hydrogen to the argon purge gas provided narrower and lower peaks than those obtained with pure argon, as shown in Fig. 2. It seems likely that the influence of hydrogen on the silver absorption signal is due to the high specific heat of hydrogen. The phenomena were the same as those observed with tellurium, lead, selenium, etc. [17]. The optimum absorption signal for silver was obtained with argon at 480 ml min^{-1} and hydrogen at 20 ml min^{-1} because of the reproducibility of the signal and the lifetime of the atomizer. The appearance and peak temperatures of the silver absorption signal were 880 and 1160°C, respectively, in the argon–hydrogen atmosphere. These temperatures are not explicable from the boiling point (2212°C) of silver metal [20]. Silver nitrate decomposes completely into the metal at 444°C [20,21]. The vapour pressure of liquid silver at 970°C is 3.11×10^{-6} atm, corresponding to 4.3×10^{-9} g in the atomizer tube [21]. At this temperature, the absorbance of silver calculated from the AA signal was 0.183, which gave an absorbance of 0.0043 per 100 pg of silver. This value is far from the characteristic mass of silver given later. Accordingly, the metal may sublime at a temperature lower than the melting point.

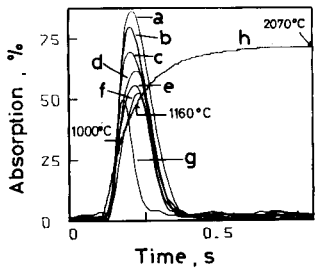

Fig. 2. Effect of hydrogen on atomic absorption of silver. a, 500 ml min^{-1} Ar, b, 480 ml min^{-1} Ar–20 ml min^{-1} H_2; c, 400 ml min^{-1} Ar–100 ml min^{-2} H_2; d, 300 ml min^{-1} Ar–200 ml min^{-1} H_2; e, 200 ml min^{-1} Ar–300 ml min^{-1} H_2; f, 100 ml min^{-1} Ar–400 ml min^{-1} H_2; g, 500 ml min^{-1} H_2, h, increasing temperature. Silver, 1.0 pg; heating rate, 2.3°C ms^{-1}.

Effect of pyrolysis temperature

It has been found that high-temperature pyrolysis provides a sensitive analysis by ETAAS for some elements [19]. In order to achieve a sensitive absorption of silver, it is important to select the appropriate pyrolysis temperature for the analysis. Figure 3 shows the effect of pyrolysis temperature (120–800°C) on the absorbance of

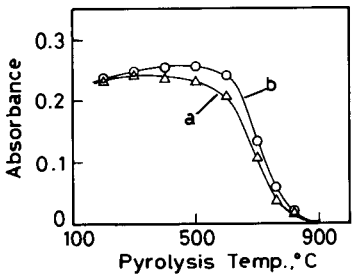

Fig. 3. Effect of pyrolysis temperature on atomic absorption signal of silver with and without ammonium thiocyanate. a, 0.3 pg of silver alone, b, silver in the presence of 5 μg of NH_4SCN.

silver. The highest absorbance was obtained at a pyrolysis temperature of 300°C, and in the presence of ammonium thiocyanate at 500°C. At temperatures above 600°C, the absorbance decreased significantly. Silver nitrate is stable in air up to 350°C, but at 444°C decomposes into silver metal [20,21]. At pyrolysis temperatures > 300°C, the compound may decompose into the metal with loss of the compound vapour. Ammonium thiocyanate reacts with many elements to form thiocyanate compounds and by heating the compounds mainly decompose the metal sulphide, carbon disulphide, dicyanogen and nitrogen [22]. On adding ammonium thiocyanate to a silver solution, a white precipitate (AgSCN) is obtained [21]. The precipitate is converted into silver sulphide on mild heating and then the sulphide is reduced to the metal by hydrogen above 200°C [21,23]. In this study, however, the hydrogen concentration is very low. Therefore, at 500°C the major part of the silver to which ammonium thiocyanate is added seems to be the sulphide. The appearance temperature of the silver in the presence of the thiocyanate was 960°C in the molybdenum tube atomizer. The melting point of silver sulphide is 825°C [20] and at around 500°C the sulphide is more stable than the oxide. Hence the pyrolysis temperature for silver in the presence ammonium thiocyanate seems to be higher than that for silver nitrate alone.

Detection limit, characteristic mass and reproducibility

The characteristic mass of silver, which is defined as the mass of the analyte giving a peak absorbance of 0.0044, with the molybdenum tube atomizer was 5.4 fg. In the presence of ammonium thiocyanate, the value was 5.0 fg. The detection limit, i.e., the weight of analyte which gives an atomic absorption signal equal to three times the standard deviation of the background (obtained from the measurement of a solution blank), was calculated from the height of the silver absorption signal. The detection limit of silver with the use of the molybdenum tube atomizer was 3.7 fg (corresponding to 0.37 pg ml^{-1}, 10 μl injected). These values are 10–1000 times better than the detection limit (6 pg ml^{-1} [24]) and characteristic mass (2.1 pg [11]) obtained with graphite atomizers.

The reproducibility with the use of the molybdenum tube atomizer was investigated. The relative standard deviations for 0.3 pg of silver and for silver in the presence of ammonium thiocyanate (5 μg) were 3.3% and 2.9%, respectively, for ten measurements.

Interference study

The problem of interferences from matrix elements on the determination of silver in biological materials by GFAAS has been reported [2–7]. In

TABLE 1

Interferences on the atomic absorption signal of silver and effect of ammonium thiocyanate [a]

Interferent		Without NH_4SCN		With NH_4SCN	
Element	Amount (ng)	Peak-height absorbance	Peak-area (integrated) absorbance · time	Peak-height absorbance	Peak-area (integrated) absorbance · time
Ag	0.3 pg	0.243 ± 0.008	6.69 ± 0.11	0.261 ± 0.007	7.36 ± 0.22
Al	30	0.229 ± 0.008	6.60 ± 0.24	0.251 ± 0.009	7.18 ± 0.25
Ca	30	0.228 ± 0.009	6.76 ± 0.39	0.251 ± 0.013	7.07 ± 0.31
Cu	30	0.169 ± 0.016	5.31 ± 0.42	0.253 ± 0.012	7.56 ± 0.14
Fe	30	0.229 ± 0.014	6.18 ± 0.41	0.250 ± 0.007	7.06 ± 0.14
K	30	0.245 ± 0.015	6.79 ± 0.45	0.269 ± 0.004	7.70 ± 0.13
Mg	30	0.213 ± 0.008	5.84 ± 0.30	0.249 ± 0.006	7.19 ± 0.23
Na	30	0.245 ± 0.012	6.92 ± 0.39	0.257 ± 0.003	7.57 ± 0.15
Pb	30	0.212 ± 0.019	5.85 ± 0.48	0.236 ± 0.016	6.77 ± 0.58
	3	0.226 ± 0.004	6.10 ± 0.13	0.254 ± 0.012	7.11 ± 0.27
Zn	30	0.234 ± 0.007	6.34 ± 0.33	0.251 ± 0.008	7.37 ± 0.18

[a] Number of measurements ⩾ 5.

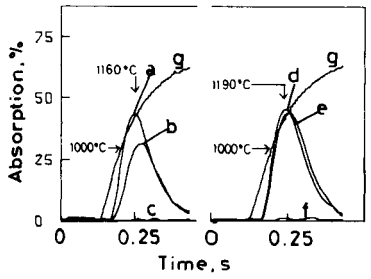

Fig. 4. Interferences of copper on the silver signal. a, 0.3 pg of Ag alone; b, 0.3 pg of Ag + 30 ng of Cu; c, 30 ng of Cu alone; d, 0.3 pg of Ag + 5 μg of NH_4SCN; e, 0.3 pg of Ag + 30 ng of Cu + 5 μg of NH_4SCN; f, 30 ng of Cu + 5 μg of NH_4SCN; g, increasing temperature.

this study with the molybdenum tube atomizer, the effects of Al, Ca, Cu, Fe, K, Mg, Na, Pb and Zn on the silver absorption signal were investigated. The results are summarized in Table 1. In a peak-height measurement, the silver (0.3 pg) signal were influenced by these elements (30 ng) except for K, Na and Zn. In a peak-area measurement, Cu, Fe, Mg, Pb and Zn affected the silver absorption. Copper in the silver solution depressed the silver absorbance greatly in both measurement methods.

In order to eliminate the interferences, liquid–liquid extraction [4,8,9], chemical modification [2,11–14] and standard addition methods [5,15] have been proposed for the accurate determination of silver. The second is simple and effective, and phosphate, ascorbic acid, Ir, Pd and Cu as chemical modifiers for the determination of silver by ETAAS have been reported [2,11–14]. However, Manning and Slavin [13] pointed out that phosphate as a chemical modifier could not be recommended for silver determination when Zeeman effect background correction was used, because of the spectral interference by Zeeman splitting of the PO band. It has been found that the addition of ammonium thiocyanate served for the sensitive determination of some elements by ETAAS with a metal tube atomizer [25]. Therefore, the effect of ammonium thiocyanate on the absorbance of silver (0.3 pg) in the presence of those elements (3–30 ng) was examined. A typical interference and the modification are shown in Fig. 4. The results are summarized in Table 1. With the addition of ammonium thiocyanate the silver signal was recovered. Peak-height and peak-area measurements gave almost the same results. However, the peak-height method is faster than the peak-area method, and is therefore recommended for the determination of silver in biological materials. Ammonium thiocyanate reacts with many elements to form thiocyanate compounds, which mainly decompose into the metal sulphides by heating [22,23]. From the information in the literature, however, these phenomena (chemical modification) in the molybdenum tube atomizer could not be explained.

It was concluded that the effect of interfering elements could be eliminated by adding ammonium thiocyanate.

Determination of silver

Following the digestion of a biological sample, the solution was analysed for silver in the presence of ammonium thiocyanate under the optimum conditions. The calibration graph constructed from standard solutions of silver was linear up to 5 pg. Table 2 gives the results obtained for some biological materials (NIST) compared with the certified values. The relative standard deviations were better than 11.8% for three replicate analyses. The average value found for the standards lies within the limits of the certified values. Recovery tests were also performed. After weighing Orchard Leaves (NIST SRM 1571) and adding the acid mixture, 0.5–1 ml

TABLE 2

Determination of silver in biological materials

Sample	Concentration of silver			
	Added (ng g^{-1})	Found (ng g^{-1}) [b]	Recovery (%)	Certified value (ng g^{-1})
Bovine liver SRM 1577a [a]		37 ± 1		40 ± 10
Non-fat milk SRM 1549 [a]		0.30 ± 0.04		< 0.3 [c]
Orchard leaves SRM 1571 [a]	–	Not detected	–	–
	0.200	0.194 ± 0.015	97.0	
	0.300	0.297 ± 0.016	99.0	

[a] NIST standards. [b] Number of analyses = 3. [c] Uncertified concentration.

of silver solution (0.2 ng Ag ml^{-1}) was added. The subsequent procedure was applied as described above. The recovery obtained can be considered to be satisfactory for the determination of silver in biological materials.

As described above, for the determination of silver the advantages of the molybdenum tube atomizer with an argon–hydrogen atmosphere are high sensitivity and long lifetime (more than 5000 firings). In addition, ammonium thiocyanate as a chemical modifier eliminated the interferences caused by various elements (10^4–10^5-fold). The performance characteristics of the molybdenum tube atomizer with the chemical modifier will serve for the accurate determination of silver in complex samples.

This work was supported financially by the Ministry of Education, Science and Culture of Japan.

REFERENCES

1 H. Vik, K.J. Andersen, K. Julshamn and K. Todnem, Lancet, (1985) 872.
2 K.J. Andersen, A. Wikshaaland, A. Utheim, K. Julshamn and H. Vik, Clin. Biochem., 19 (1986) 166.
3 H.V. Warren, S.J. Horsky and J.J. Barakso, CIM Bull., 77 (1984) 95.
4 G. Kacimi, P.L. Nguyen, P. Fabiani and R. Truhaut, C.R. Acad. Sci., Ser. 2, 302 (1986) 421.
5 J.C. Amiard, A. Pineau, H.L. Boiteau and C. Amiard-Triquet, Water Res., 21 (1987) 693.
6 C.M. Lau, A.M. Ure and T.S. West, Bull. Chem. Soc. Jpn., 61 (1988) 79.
7 K.S. Subramanian, At. Spectrosc., 9 (1988) 169.
8 B. Ebarvia, E. Macalalad, N. Rogue and I. Rubeska, J. Anal. At. Spectrom., 3 (1988) 199.
9 I.M. Gibalo, S.G. Dmitrienko, A.N. Shkil and N.R. Togaeva, Zh. Anal. Khim., 43 (1988) 819.
10 Y.M. Yukhin, T.A. Udalova, V.G. Tsimbalist and S.S. Shatskaya, Zh. Anal. Khim., 43 (1988) 1020.
11 F. Luo and S. Wu, Fenxi Huaxue, 15 (1987) 739.
12 S. Huang, Yankuang Ceshi, 6 (1987) 23.
13 D.C. Manning and W. Slavin, Spectrochim. Acta, Part B, 42 (1987) 755.
14 H. Niskavaara and E. Kontas, Anal. Chim. Acta, 231 (1990) 273.
15 F. Liu, Guangpuxue Yu Guangpu Fenxi, 8 (1988) 71.
16 K. Ohta and M. Suzuki, Talanta, 22 (1975) 465.
17 M. Suzuki and K. Ohta, Prog. Anal. Atom Spectrosc., 6 (1983) 49.
18 K. Ohta, S. Itoh and T. Mizuno, Talanta, 38 (1991) 325.
19 K. Ohta, T. Sugiyama and T. Mizuno, Analyst, 115 (1990) 279.
20 D.R. Lide (Ed.), Handbook of Chemistry and Physics, CRC Press, Boca Raton, FL, 72nd edn., 1991; pp. 4-95–96.
21 N.R. Thompson, in J.C. Bailar Jr., H.J. Emeleus, R. Nyholm and A.F. Trotman-Diekeson (Eds.), Comprehensive Inorganic Chemistry, Vol. 3, Silver, Pergamon, Oxford, 1973 pp. 96, 97, 104, 105.
22 S. Takagi, Teisei Bunseki Kagaku, Vol. 2 Nanko-do kk., Tokyo, 1964, p. 338.
23 K. Ohta and T. Mizuno, Spectrochim. Acta, Part B, 44 (1989) 95.
24 A.I. Sumchuk, Ukr. Khim. Zh., 55 (1989) 491.
25 K. Ohta, S.Y. Su and T. Mizuno, Anal. Lett., 20 (1987) 1399.

Analytica Chimica Acta, 267 (1992) 137–139
Elsevier Science Publishers B.V., Amsterdam

Fluorescent products of the reaction for the determination of catecholamines with 1,2-diphenylethylenediamine

Hitoshi Nohta, Myong-Koo Lee and Yosuke Ohkura

Faculty of Pharmaceutical Sciences, Kyushu University 62, Maidashi, Higashi-ku, Fukuoka 812 (Japan)

(Received 12th February 1992; revised manuscript received 15th April 1992)

Abstract

The fluorescent product formed in the reaction between epinephrine and 1,2-diphenylethylenediamine was determined to be 2-phenyl(4,5-dihydro-4-hydroxy-1-methylpyrrolo) [2,3-*f*]benzoxazole. The difference in the mechanisms of the reactions of 1,2-diphenylethylenediamine and ethylenediamine with epinephrine is discussed. The fluorescent products from the other catecholamines were also characterized as the corresponding 2-phenyl(4,5-dihydropyrrolo) [2,3-*f*]benzoxazole derivatives on the basis of their mass spectral data.

Keywords: Fluorimetry; Mass spectrometry; Catecholamines; Dopamine; Epinephrine; Norepinephrine

Catecholamines (dopamine, norepinephrine and epinephrine) react with 1,2-diphenylethylenediamine (DPE) in the presence of potassium hexacyanoferrate(III) in a slightly acidic medium to give the corresponding fluorescent products [1], which can be separated by reversed-phase liquid chromatography (LC) [2]. This paper describes the structural analysis and spectral properties of the isolated fluorescent product from epinephrine. The reaction mechanism is compared with that of the reaction of ethylenediamine with epinephrine. The structures of the products from the other catecholamines are also discussed based on their fast atom bombardment mass spectral (FAB MS) data.

Correspondence to: Y. Ohkura, Faculty of Pharmaceutical Sciences, Kyushu University 62, Maidashi, Higashi-ku, Fukuoka 812 (Japan).

EXPERIMENTAL

Chemicals and apparatus

DPE and 1,2-bis(4-chlorophenyl)ethylenediamine were synthesized as described previously [1,3]. All other chemicals were of analytical-reagent grade.

Uncorrected fluorescence spectra and intensities were measured with a Hitachi MPF-4 spectrofluorometer in 10×10 mm quartz cells; spectral band widths of 5 nm were used in both the excitation and emission monochromators. FAB mass spectra were measured with a JEOL JMS-DX300 mass spectrometer interfaced to a JEOL JNM-3500 data system. ^{1}H NMR spectra were obtained with a JEOL JNMPS-110 spectrometer at 100 MHz using approximately 5% (w/v) solutions in pyridine-d_5 containing tetramethylsilane which served as an internal standard. Splitting patterns were designated as follows: s, singlet; d,

doublet; t, triplet; m, multiplet. Melting points are uncorrected.

Isolation of the fluorescent product from epinephrine and its elemental analysis and spectral data

To an aqueous 50% (v/v) methanolic solution of L-epinephrine (6 mmol in 200 ml), DPE and potassium hexacyanoferrate(III) solutions [both 6 mmol in 300 ml of aqueous 50% (v/v) methanol, pH 6.5–6.9] were added dropwise over a period of 2–3 h with stirring at 20–25°C. After additional stirring (for 12 h at the same temperature), methanol was removed in vacuo. The precipitates that separated on cooling in ice–water were filtered off, washed with water, dried in vacuo and recrystallized from benzene to give pale yellow needles m.p. 164–166°C; yield 0.15 g (11%). Elemental analysis, calculated for $C_{16}H_{14}N_2O_2$, C 72.35, H 5.35, N 10.32; found, C 72.18, H 5.26, N 10.53%. FAB MS, $m/z = 266$ (M^+, base peak), 249 ($M^+ - OH$). ^1H NMR spectral data are given in Fig. 3.

RESULTS AND DISCUSSION

The fluorescence excitation and emission spectra of the purified product dissolved in the reagent blank in the method of determination [1] were identical with those of the reaction mixture of epinephrine (Fig. 1).

The retention time of the product under the conditions of reversed-phase LC reported previously [2] coincided with that for the reaction mixture of epinephrine, and the fluorescence excitation and emission spectra of the eluates for both peaks were identical. The product gave the most intense fluorescence at pH 7–12 in Britton–Robinson buffers (excitation and emission maxima 340 and 490 nm, respectively) (Fig. 2); the pH dependence also conformed well with that of the reaction mixture. These observations suggest that the product is the only fluorescent compound formed in the reaction of epinephrine.

The molecular ion in FAB MS and the elemental analysis data indicate that the molecular formula of the fluorescent product is $C_{16}H_{14}N_2O_2$. These data and the ^1H NMR spectral data (Fig. 3) indicate that the fluorescent product is 2-phenyl(4,5-dihydro-4-hydroxy-1-methylpyrrolo)-[2,3-*f*]benzoxazole.

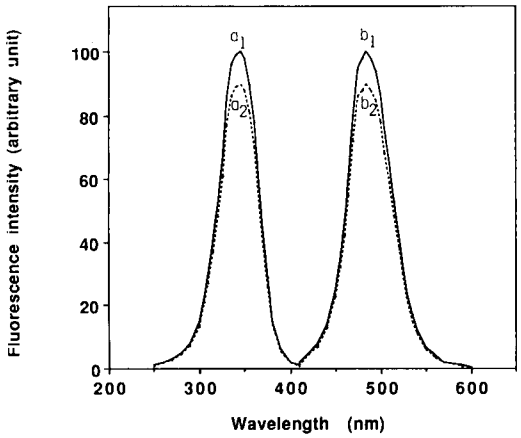

Fig. 1. (a) Excitation and (b) emission spectra of the product from epinephrine (a_1 and b_1) and the derivatization reaction mixture of epinephrine (a_2 and b_2). The product was dissolved in the reagent blank solution in the derivatization reaction (50 pmol ml^{-1}) and the epinephrine concentration in the derivatization mixture was 50 pmol ml^{-1}. Excitation and emission maxima were at 345 and 485 nm, respectively.

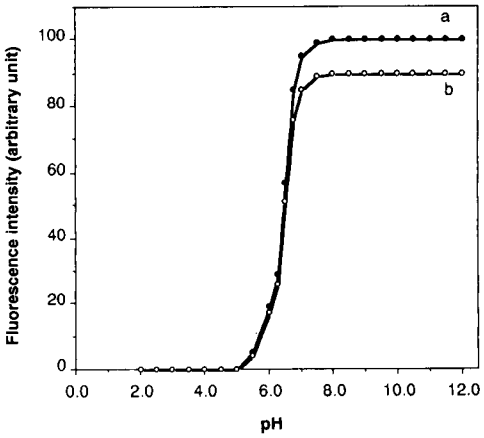

Fig. 2. Effect of pH on the fluorescence intensity of the isolated product and that produced in the derivatization reaction. (a) product dissolved in 40 mM Britton–Robinson buffers of various pH (50 pmol ml^{-1}); (b) to portions (50 μl) of the derivatization reaction mixture of epinephrine were added 4.95 ml of the buffers (epinephrine concentration in the final mixture, 50 pmol ml^{-1}).

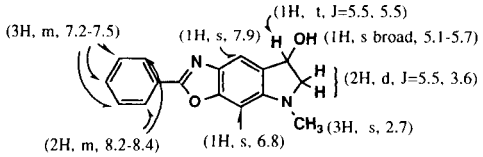

Fig. 3. Fluorescent product from epinephrine with DPE and (in parentheses) its ^{1}H NMR spectral data: number of protons, splitting patterns [and coupling constants (J, Hz)] and chemical shifts (ppm), in that order.

Ethylenediamine affords 2,3-dihydro-3-hydroxy-1-methylpyrrolo[2,3-*g*]quinoxaline by reaction with epinephrine [4]; epinephrine is oxidatively converted into adrenochrome, then ethylenediamine is cyclocondensed with two carbonyl groups in the *o*-quinone moiety. In the DPE reaction, one amino group of DPE reacts first with adrenochrome, then an oxazole ring is formed, accompanying the elimination of benzylamine moiety (Fig. 4). The liberated benzylamine could not be identified because of its oxidative

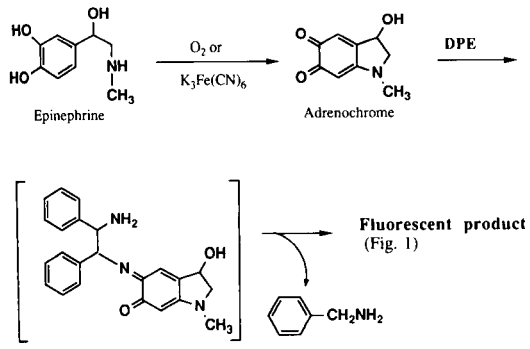

Fig. 4. Possible pathway of the fluorescence reaction between epinephrine and DPE.

degradation in the presence of potassium hexacyanoferrate(III).

The other catecholamines (dopamine and norepinephrine) and isoproterenol (*N*-isopropylnorepinephrine) also afforded the corresponding 2-phenyl-(4,5-dihydropyrrolo)[2,3-*f*]benzoxazole derivatives, the FAB mass spectra of which had their molecular ion peaks (m/z 236, 252 and 295, respectively) as base peaks. The reaction between 1,2-bis(4-chlorophenyl)ethylenediamine and epinephrine also gave the corresponding fluorescent product, 2-(4-chlorophenyl)-(4,5-dihydro-4-hydroxy-1-methylpyrrolo)[2,3-*f*]benzoxazole that showed a molecular ion peak of $m/z = 300$ in the FAB mass spectrum.

From these observations, the fluorescence reactions of catecholamines or other 3,4-dihydroxyphenylethylamine derivatives with 1,2-diarylethylenediamines [3] should afford the corresponding 2-aryl(4,5-dihydropyrrolo)[2,3-*f*]benzoxazole derivatives.

REFERENCES

1 H. Nohta, A. Mitsui and Y. Ohkura, Anal. Chim. Acta, 165 (1984) 171.
2 A. Mitsui, H. Nohta and Y. Ohkura, J. Chromatogr., 344 (1985) 344.
3 Y. Umegae, H. Nohta and Y. Ohkura, Anal. Chim. Acta, 208 (1988) 59.
4 J. Harley-Mason and A.H. Laird, Tetrahedron, 7 (1959) 70.

Analytica Chimica Acta, 267 (1992) 141–146
Elsevier Science Publishers B.V., Amsterdam

Ion chromatography of inorganic cations using microcolumns coated with micellar bile salt

Wenzhi Hu

Department of Applied Chemistry, School of Engineering, Nagoya University, Chikusa-ku, Nagoya 464-01 (Japan)

Toyohide Takeuchi

Faculty of Engineering, Gifu University, 1–1 Yanagido, Gifu 501-11 (Japan)

Hiroki Haraguchi

Department of Applied Chemistry, School of Engineering, Nagoya University, Chikusa-ku, Nagoya 464-01 (Japan)

(Received 28th January 1992; revised manuscript received 13th April 1992)

Abstract

Octadecylsilica coated with a micellar taurine-conjugated bile salt was investigated for the ion chromatography of inorganic cations. Monovalent and divalent cations could be separated by the proposed system, in which cerium(III) chloride was employed as the mobile phase component and the cations were determined by indirect UV-absorption measurement. The system was applied to the determination of inorganic cations in wine, isotonic beverage and water samples.

Keywords: Ion chromatography; Beverages; Inorganic cations; Micellar bile salt coated column; Waters; Wine

Bile salts are important biological surfactants synthesized in the liver, which play an important role in many physiological and biological systems. The main biological function of the bile salt micelles is to solubilize dietary lipids and thus to accelerate greatly their absorption [1]. Other functions of bile acids involve their complexation properties with cations, which enhance the intestinal absorption of calcium or iron(II) ions [1]. The structures of micellar bile salts are different from those of other traditional micelles formed from linear surfactants. Bile salt micelles are chiral, helically shaped aggregates [2–6], and have been successfully employed as chiral mobile phase additives for enantiomeric separations in liquid chromatography (LC) [7–11] and electrokinetic capillary chromatography [12–14]. Previous work [7,8] suggested that micellar bile salts adsorb on the stationary phase in reversed-phase LC. This is also confirmed by the fact that bile salt micelles are reversed micelles [6–9]. The outside of the bile salt micelles is hydrophobic, which leads to their strong adsorption on the hydrophobic stationary phase. The chiral separation achieved is due to the bile salt micelles sorbed on the stationary phase under certain specific conditions [7,8]. In contrast, the interior of the bile salt micelles is filled with sodium counter ions surrounded by water molecules [2–6]. Hence it is expected that the inside of the bile salt micelles provides cation-exchange sites.

In this work, the separation ability of micellar bile salts coated on the stationary phase for the

Correspondence to: H. Haraguchi, Department of Applied Chemistry, School of Engineering, Nagoya University, Chikusa-ku, Nagoya 464-01 (Japan).

ion chromatography of inorganic cations was examined.

EXPERIMENTAL

Apparatus

A microcolumn LC system was assembled in the laboratory from an MF-2 microfeeder (Azumadenki Kogyo, Tokyo) equipped with a 0.5-ml gas-tight syringe (MS-GAN 050; Ito, Fuji) as a pump, a microvalve injector with an injection volume of 0.02 μl (ML-522; JASCO, Tokyo), a 15 cm × 0.35 mm i.d. separation column packed with Develosil ODS-5 (5 μm) (Nomura Chemical, Seto), a Uvidec-100V UV detector (JASCO) with a modified flow cell and a Chromatopac C-R4AX data processor (Shimadzu, Kyoto). The microcolumn was prepared from fused-silica tubing by a slurry packing method as previously reported [15]. The flow-rate of the mobile phase was 2.8 μl min^{-1}. The separation was carried out at room temperature (ca. 25°C). An inductively-coupled plasma atomic emission spectrometer (Model 075 Plasma Atomcomp MK II; Thermo Jarrell Ash, Franklin, MA) was employed for the determination of inorganic cations for comparison with the results obtained by the present method.

Reagents

Reagents were of analytical-reagent grade from Wako (Osaka), unless stated otherwise, and were used as received. Purified water was prepared in the laboratory by using a Milli-Q system (Nihon Millipore Kogyo, Tokyo). Bile salt surfactants, sodium taurocholate (NaTC) and sodium taurodeoxycholate (NaTDC), were obtained from Sigma (St. Louis, MO). Inorganic cations used as analytes were sodium, potassium, cesium, magnesium, calcium, and barium, and were obtained as chloride salts. Cerium(III) chloride hexahydrate dissolved in pure water was used as the light-absorbing mobile phase.

Preparation of cation-exchange column

A 100 mM concentration of NaTC or NaTDC dissolved in pure water was passed through the octadecylsilica (ODS) microcolumn for 30 min at a flow-rate of 2.8 μl min^{-1}, followed by washing with pure water for 20 min at the same flow-rate. A 2 mM concentration of cerium(III) chloride solution was then passed through the micellar bile salt-coated microcolumn until the baseline became stable.

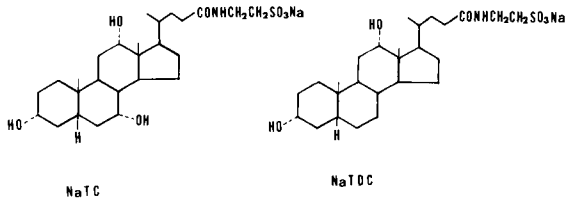

Fig. 1. Structures of NaTC and NaTDC.

RESULTS AND DISCUSSION

NaTC and NaTDC were chosen because they possess a strong cation-exhange group, viz., sulphonate (Fig. 1). The critical micellar concentrations (CMC) of these bile salts in pure water are 4–10 and 2.4–6 mM, respectively [16,17]. An important property of the bile salt surfactants is their ability to form micelles, i.e., aggregates of monomers by means of ion–ion and ion–dipole interactions together with hydrogen bonding [2–6]. These bile salts form reversed micelles, and they adsorb on the reversed-phase stationary phase by hydrophobic interaction [7,8]. This was confirmed by the fact that enantiomers of a binaphthyl compound could be separated by using the mobile phase containing no bile salt on the ODS column, through which micellar bile salt solution had been passed beforehand [8]. This result supports the assumption that the micelles adsorbed on the stationary phase retain their specific configuration. Monomers of bile salts also show some slight partitioning to the ODS when water is used as the mobile phase. In principle, monomers adsorbed on the ODS can also act as cation exchangers. Therefore, if a solution such that the bile salt concentration is lower than its CMC is used, the prepared stationary phase retains monomers only. In this event, however, the prepared column would have a lower cation-ex-

change capacity. Under the present preparation conditions, it is presumed that bile salt monomers co-elute from the ODS column when breakthrough of the micelles takes place during the preparation, and thus the analytes are mostly retarded at the cation-exchange sites in the micelle rather than at those of the monomers adsorbed. In this study, NaTC or NaTDC micelles coated on the ODS surface were assessed as ion exchangers with the aid of an indirect detection method.

Indirect UV-absorption and fluorimetric detection methods have been utilized in ion chromatography. So far, copper(II) [18–20] and cerium(III) [18,21] have been used as the light-absorbing mobile phase ion for the indirect photometric or fluorimetric detection of cations. In this work, cerium(III) was used because the detection limit achieved with cerium(III) was at least 100 times better than that with the copper(II) mobile phase [18]. Cerium(III) is a UV-absorbing and fluorescent cation. Indirect UV-absorption detection was chosen in this work because a larger value of "dynamic reserve" (defined as the ratio of background to its noise level) was obtained by UV-absorption detection compared with fluorimetric detection.

In indirect UV-absorption detection, a light-absorbing ion is incorporated in the mobile phase, which will be replaced with photometrically inactive sample ions in the column effluents giving rise to negative peaks. When cerium(III) ions are passed through the column coated with micellar bile salts, the sodium ions in the micellar interior are replaced with cerium(III) ions. A breakthrough curve observed for the substitution is shown in Fig. 2; 2 mM cerium(III) chloride solution was initially introduced into the flow cell to mark the absorbance of the original solution and then the 2 mM cerium(III) solution was passed through the micellar NaTDC-coated column. The amount of cerium(III) ions substituted on the column was 0.38 μmol, which was calculated from the concentration of cerium(III), the flow-rate of the mobile phase and the breakthrough time. The amount of NaTDC coated on the ODS surface can be also obtained in the same way, viz., 1.14 μmol. These values indicate that the sodium cations in the micellar bile salt coated on the ODS were completely replaced with cerium(III) ions.

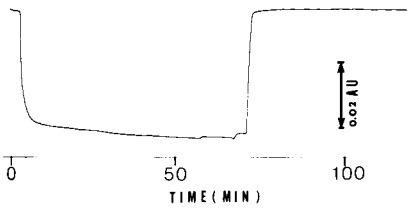

Fig. 2. Breakthrough curve for substitution with cerium(III) ion. Column, 150×0.35 mm i.d. packed with Develosil ODS-5 coated with NaTDC micelles; mobile phase, 2.0 mM cerium(III) chloride solution; flow-rate, 2.8 μl min^{-1}; temperature, ca. 25°C; wavelength of UV detection, 253 nm.

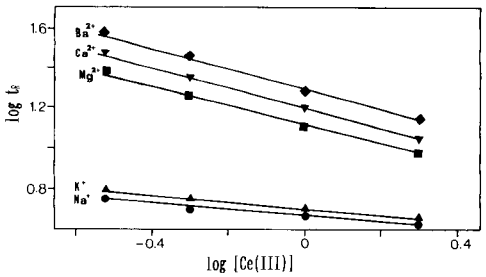

Fig. 3. Relationships between the logarithm of retention times (t_R) of analyte ions and the logarithm of cerium(III) concentration. Column, 150×0.35 mm i.d. packed with Develosil ODS-5 coated with NaTDC micelles; mobile phase, cerium(III) chloride solution; flow-rate, 2.8 μl min^{-1}.

The effect of the concentration of the mobile phase ions on the retention behaviour was examined. Figure 3 shows the logarithm of the retention times of the analytes as a function of the logarithm of the concentration of cerium(III) in the eluent. In ion-exchange chromatography, linear relationships between the logarithm of the adjusted retention times and the logarithm of the eluent concentration have been observed [22]. Figure 3 shows almost linear relationships indicating that the present system works like common ion-exchange chromatographic systems.

Figure 4 demonstrates the indirect UV-absorption detection of inorganic cations using 0.5 mM cerium(III) as the eluent, in which 4 mM each of monovalent cations and 2 mM each of divalent cations were separated on (A) the micellar

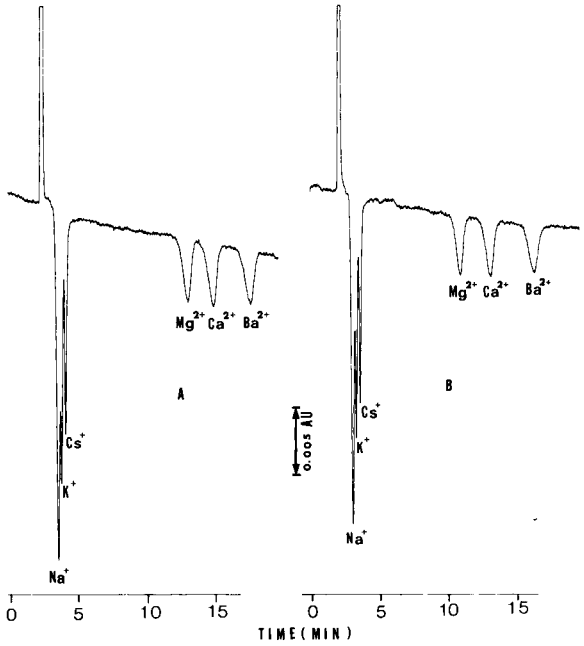

Fig. 4. Indirect detection of inorganic monovalent and divalent cations on (A) NaTDC and (B) NaTC-coated columns. Columns, Develosil ODS-5 coated with (A) NaTDC or (B) NaTC; mobile phase, 0.5 mM cerium(III) chloride solution; analyte ions, 4 mM each sodium, potassium and cesium, 2 mM each magnesium, calcium and barium; other operating conditions as in Fig. 3.

NaTDC or (B) the NaTC ion-exchange stationary phase. An advantage of the present system is that monovalent and divalent cations can be simultaneously separated in a reasonable period of time, owing to the strong eluting property of cerium(III) ion [18,21]. Although the divalent cations are baseline separated, monovalent ions such as sodium and potassium are not perfectly separated by using a 0.5 mM cerium(III) eluent as demonstrated in Fig. 4.

In order to improve the separation of these monovalent cations, the cerium(III) concentration in the mobile phase can be adjusted. If monovalent cations are of interest, the concentration of cerium(III) in the mobile phase should be decreased. Figure 5 demonstrates the baseline separation of sodium, potassium and cesium ions using a 0.1 mM cerium(III) eluent. On the other hand, if the the divalent cations are of interest,

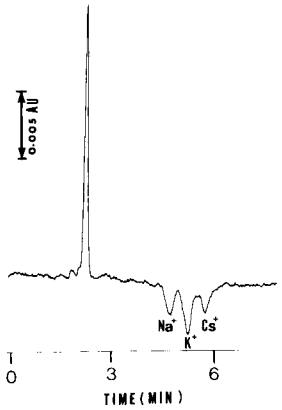

Fig. 5. Baseline separation of monovalent cations. Operating conditions as in Fig. 3, except the mobile phase, 0.1 mM cerium(III) chloride aqueous solution. Analyte ions: 1 mM each sodium and cesium and 2 mM potassium.

the cerium(III) concentration should be increased to achieve the separation in a shorter period of time. Figure 6 demonstrates the separation of divalent cations using a 2.0 mM cerium(III) mobile phase; magnesium, calcium and barium ions elute within 10 min. Linear relationships between the peak areas and the concentrations of the divalent cations were obtained. The peak areas of the divalent cations were double those of the monovalent cations at the same concentration.

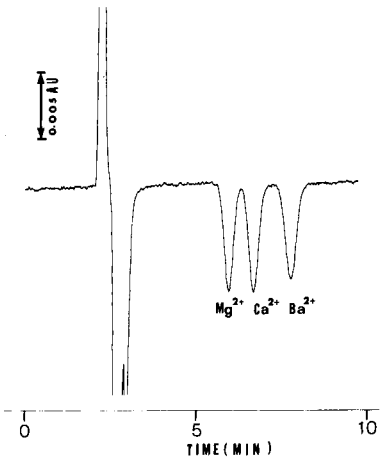

Fig. 6. Separation of divalent cations. Operating conditions as in Fig. 3, except the mobile phase, 2 mM cerium(III) chloride solution. Analyte ions: 2 mM each magnesium, calcium and barium.

The present separation system was applied to the determination of divalent cations contained in white wine, as shown in Fig. 7. In addition to negative peaks based on magnesium and calcium ions, several positive peaks appeared in the chromatogram. The concentrations of magnesium and calcium were determined as 3.3 and 1.3 mM, respectively.

Possible interference from trivalent cations was examined. Iron(III) eluted between magnesium and calcium ions, and these three cations could be separated. Aluminium ion did not elute under the conditions in Fig. 7.

Applications of the present system to the determination of inorganic divalent cations contained in other samples, such as red wine, isotonic beverage, well water and tap water, were also examined under the same conditions as in Fig. 7. The results are summarized in Table 1. It was found that the results obtained with the present method agree well with those obtained by inductively coupled plasma atomic emission spectrometry. The results for monovalent cations are not shown because even if an eluent with a lower cerium(III) concentration, e.g., 0.1 mM, was employed, the resolution was not sufficient for their accurate determination. The detection limits for the divalent cations at a signal-to-noise ratio of 3 were ca. 6 pmol or 0.3 mM per injection.

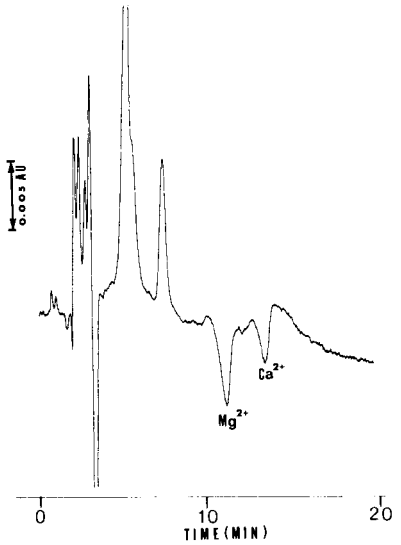

Fig. 7. Detection of components in white wine. Operating conditions as in Fig. 4.

TABLE 1

Determination of divalent cations in real samples using the operating conditions as in Fig. 7

Sample	Concentration (mM)			
	Present method		ICP-AES [a]	
	Mg^{2+}	Ca^{2+}	Mg^{2+}	Ca^{2+}
White wine	3.3	1.3	3.31	1.31
Red wine	3.0	1.0	3.01	0.98
Isotonic beverage	ND [b]	1.2	0.01	1.18
Well water	0.2	0.6	0.18	0.55
Tap water	ND [b]	0.1	ND [b]	0.11

[a] Inductively coupled plasma atomic emission spectrometry.
[b] Not detected.

The detection limit of the present system is not always satisfactory, because cerium(III) ion is not a strongly UV-absorbing species. The detection limits can be improved by using a cation with a higher molar absorptivity.

The authors thank Hideyuki Sawatari for his help in the determination of the inorganic cations by inductively-coupled plasma atomic emission spectrometry.

REFERENCES

1 A.F. Hofmann and K.J. Mysels, Colloids Surf., 30 (1988) 154.
2 G. Conte, R.D. Blasi, A. Parretta and N.V. Pavel, J. Phys. Chem., 88 (1984) 5720.
3 G. Esposito, E. Giglio, N.V. Pavel and A. Zanobi, J. Phys. Chem., 91 (1987) 356.
4 G. Esposito, A. Zanobi, E. Giglio, N.V. Pavel and I.D. Campbell, J. Phys. Chem., 91 (1987) 83.
5 E. Giglio, S. Loreti and N.V. Pavel, J. Phys. Chem., 92 (1988) 2858.
6 A.R. Campanelli, S.C.D. Sanctis, E. Chiessi, M. D'Alagni and E. Giglio, J. Phys. Chem., 93 (1989) 1536.
7 W. Hu, T. Takeuchi and H. Haraguchi, Chromatographia, 33 (1992) 58.
8 W. Hu, T. Takeuchi and H. Haraguchi, Chromatographia, 33 (1992) 63.
9 M.F. Borgerding, R.L. Williams, Jr., W.L. Hinze and F.H. Quina, J. Liq. Chromatogr., 12 (1989) 1367.
10 W.L. Hinze, R.W. Williams, Jr., Z-S. Fu, Y. Suzuki and F.H. Quina, Colloids Surf., 48 (1990) 79.

11 R.W. Williams, Jr., Z-S. Fu and W.L. Hinze, J. Chromatogr. Sci., 28 (1990) 292.
12 H. Nishi, T. Fukuyama, M. Matsuo and S. Terabe, J. Microcol. Sep., 1 (1989) 234.
13 H. Nishi, T. Fukuyama, M. Matsuo and S. Terabe, J. Chromatogr., 515 (1990) 233.
14 R.O. Cole and M.J. Sepaniak, J. High Resolut. Chromatogr., 13 (1990) 579.
15 T. Takeuchi and D. Ishii, J. Chromatogr., 213 (1981) 25.
16 A. Roda, A.F. Hofmann and K.J. Mysels, J. Biol. Chem., 258 (1983) 6362.
17 H. Kawamura, Y. Murata, T. Yamaguchi, H. Igimi, M. Tanaka, G. Sugihara and J.P. Kratohvil, J. Phys. Chem., 93 (1989) 3321.
18 J.H. Sherman and N.D. Danielson, Anal. Chem., 59 (1987) 490.
19 H. Small and T.E. Miller, Jr., Anal. Chem., 54 (1982) 462.
20 J.R. Larson and C.D. Pfeiffer, Anal. Chem., 55 (1983) 393.
21 J.H. Sherman and N.D. Danielson, Anal. Chem., 59 (1987) 1483.
22 J.H. Knox and G.R. Laird, J. Chromatogr., 122 (1976) 17.

Analytica Chimica Acta, 267 (1992) 147–156
Elsevier Science Publishers B.V., Amsterdam

Séparation des sucres et polyalcools par chromatographie en phase liquide sur gel de silice avec un détecteur évaporatif à diffusion de lumière

B. Herbreteau, M. Lafosse, L. Morin-Allory et M. Dreux

Laboratoire de Chimie Bioorganique et Analytique, Université d'Orléans, URA CNRS 499, 45067 Orléans Cedex 2 (France)

(Received 20th January 1992)

Abstract

(*Separation of sugars and polyols by liquid chromatography using bare silica gels and evaporative light scattering detection*) Bare silica gel in combination with a dichloromethane–methanol mobile phase and a low water content, appears to be capable of offering large selectivities for sugars. A comparison is made with amino bonded phases and acetonitrile–water eluents, since the elution order in both systems is quite similar. Nevertheless, complementary selectivities are obtainable using underivatized silica gels which have the advantages of providing good stability and to avoid Schiff base formation with reducing sugars and amino bonded silica. It is also shown that the problem resulting from the variation in hydration of bare silica can be controlled. Results on isocratic sugar separations are described together with the advantages of evaporative light scattering detection which is sensitive and compatible with gradient elution.

Résumé

Les gels de silice employés avec une phase mobile de type dichlorométhane–méthanol et un faible pourcentage d'eau se révèlent capables d'offrir des sélectivités importantes vis à vis des sucres. Ces systèmes sont comparés avec les systèmes classiques utilisant des phases greffées amino en milieu acétonitrile–eau puisque l'ordre d'élution est relativement semblable. Cependant, des sélectivités complémentaires sont obtenues sur ces systèmes qui présentent l'avantage d'une bonne stabilité et qui évitent la formation de bases de Schiff observées avec les sucres réducteurs et les phases greffées amino. Il apparait également que les problèmes liés aux variations d'hydratation de la silice peuvent être maîtrisés. Les premiers résultats concernant la séparation isocratique des sucres sont décrits, de même que les avantages présentés par l'emploi d'une détection à diffusion de lumière en phase gazeuse, technique sensible et compatible avec les gradients d'élution.

Keywords: Evaporative light scattering detection; Liquid chromatography; Polyols; Silica gels; Sugars

Appelés glucides, oses, saccharides, hydrates de carbone, les sucres sont d'une importance capitale dans un grand nombre de domaines. Il est nécessaire de disposer de moyens d'investigations suffisamment performants pour les identifier et les quantifier car la difficulté de leur analyse provient alors dans le grand nombre d'isomères et la grande ressemblance des formules chimiques. De plus, ces molécules ne présentent pas de groupements chromophores facilement exploitables dans l'UV ou le visible, ce qui rend leur mise en évidence très délicate dans les milieux complexes. La chromatographie li-

Correspondence to: M. Dreux, Laboratoire de Chimie Bioorganique et Analytique, Université d'Orléans, URA CNRS 499, 45067 Orléans Cedex 2 (France).

Elsevier Science Publishers B.V.

quide haute performance apparait comme répondant le mieux à ces exigences, mais elle garde malgré tout des points faibles puique, même si les premières séparations datent des années 30 [1], constamment des améliorations sont proposées tant dans le domaine séparatif que dans le domaine de la détection comme en témoignent les nombreuses mises au point [2–6].

De par leurs groupements silanols, les gels de silice permettent la rétention et la séparation des sucres. Rocca et Rouchouse [7] ont séparé un mélange simple de mono- et disaccharides sur Lichrosorb Si60, 5 μm en 15 min environ avec une phase mobile formiate d'éthyle–methanol–eau. La variation du pourcentage de méthanol influence fortement la rétention tandis que celle de l'eau n'a qu'une faible influence. Linden et Lawhead [8] ont amélioré la séparation en utilisant un mélange acétonitrile–eau (84:16) par rapport à eau–acétate d'éthyle–isopropanol (25:50:35) sur une colonne couplée Corasil. McGinnis et Fang [9] ont également obtenu des séparations en milieu acétonitrile–eau sur Partisil 10. Certains sucres donnent lieu à deux pics provenant de la séparation des anomères. Pour cela et en raison de la faible résolution obtenue avec ces éluants, la chromatographie des sucres sur silice a été remplacée par d'autres systèmes depuis les années 80. Actuellement, les systèmes les plus répandus utilisent les phases de silice greffée amino et les résine échangeuses de cations avec respectivement comme phase mobile un mélange acétonitrile–eau et l'eau pure. Cependant, nous nous proposons de montrer que les sélectivités peuvent être grandement améliorées sur silice par l'utilisation d'une phase mobile organique comportant un faible pourcentage d'eau.

La silice présente l'avantage d'une grande résistance mécanique par rapport aux résines, son prix de revient est moindre et elle ne demande pas de régénération fréquente. Cependant, la liaison siloxane s'hydrolyse en milieu aqueux: à température ambiante et à l'équilibre, environ 100 mg l^{-1} de silice amorphe sont solubilisés dans l'eau pure [10]. Mais des dosages effectués en sortie de colonne avec un éluant entièrement aqueux [11] nous donne une valeur beaucoup plus faible (Si < 1 mg l^{-1}). Par contre, pour des phases de silice greffée amino en milieu acétonitrile–eau, les valeurs observées sont beaucoup plus importantes [11], ce qui explique leur manque de stabilité, largement évoquée dans la littérature [12–15]. Les phases de silice greffée amino présentent un autre inconvénient important qui est provoqué par la formation de base de Schiff entre les groupements amino de la phase stationnaire et les sucres réducteurs, ce qui perturbe leur détermination quantitative et même parfois qualitative [3,16–18].

Les hydroxyles à la surface de la silice peuvent s'organiser de différentes façons [10]. La présence d'eau influence directement l'activité de surface lorsque la rétention se fait par un mécanisme d'adsorption. Dans ce cas, la rétention est très dépendante du degré d'hydratation de la silice; une faible quantité d'eau et (ou) de solvant polaire est indispensable pour obtenir des résultats reproductibles. Mais à partir d'un certain pourcentage d'eau, qui dépend de la nature de l'éluant, la surface de la silice est entièrement désactivée. On peut alors considérer que la rétention n'est plus influencée de manière aussi importante par la teneur en eau: ceci est d'autant plus vrai en présence d'un alcool qui désactive également la silice. Nous présenterons dans cet article les résultats obtenus avec un éluant ternaire: dichlorométhane ou chloroforme et méthanol avec un faible pourcentage d'eau. L'influence de cette dernière composante sera étudiée. Des éluants binaires, dichlorométhane–méthanol, ont fait l'objet également d'études chromatographiques des sucres sur des silices greffées de différentes natures, [19]. L'utilisation de ce type d'éluant nous a été suggérée, notamment, par les résultats obtenus avec ces mêmes types de phases greffées en chromatographie en phase supercritique [20] où l'éluant est un mélange CO_2–méthanol dont la polarité est proche en première approximation de celle des éluants liquides cités.

Le couplage du système séparatif avec un détecteur évaporatif à diffusion de lumière (DEDL) [11,21] offre une bonne sensibilité pour les analyses de sucres et autorise l'emploi de gradient d'élution, ce qui n'est pas le cas avec une détection réfractométrique et pratiquement impossible en UV avec de tels éluants.

PARTIE EXPÉRIMENTALE

L'appareillage comprend une pompe à gradient Bruker, une vanne d'injection Rhéodyne 7125 munie d'une boucle d'injection de 20 μl, un détecteur évaporatif à diffusion de lumière Modèle Sedex 45 (Sedere) et un intégrateur Shimadzu CR3A.

Le dichlorométhane Hiper Solv (BDH), le méthanol qualité RS (Carlo-Erba), le chloroforme (Aldrich), l'acétonitrile LiChrosolv (Merck) et l'eau distillée (Coopération Pharmaceutique Française, Melun) constituent les éléments de la phase mobile. Le solvant d'injection est le méthanol.

Les caractéristiques des colonnes sont les suivantes: LiChrospher Si60, 5 μm (125 × 4 ou 250 × 4 mm) (Merck); Ultrasphère Si, 5 μm (250 × 4,6 mm) (Beckman); Zorbax Sil (250 × 4,6 mm) (Dupont); Carbohydrate NH_2 (300 × 3,9 mm) (Waters Assoc.).

Pour les calculs des facteurs de capacité, les volumes morts sont déterminés à partir des pics du dodécane et du périlène, élués a même temps, avec un éluant dichlorométhane–méthanol–eau (80 : 19,8 : 0,2).

RÉSULTATS ET DISCUSSION

Sélectivité

En milieu acétonitrile–eau, les sélectivités et les résolutions obtenues pour les monosaccharides sont très faibles (Fig. 1). Le Tableau 1 rapporte les facteurs de capacité de monosaccharides et polyalcools obtenus avec trois gels de silice différents et des éluants organiques très faiblement aqueux (0,2% en volume) et révèle le bénéfice obtenu avec de tels éluants.

L'ordre d'élution sur les différentes colonnes de silice reste similaire à celui obtenu sur colonne NH_2 en milieu acétonitrile–eau sauf pour les

TABLEAU 1

Facteurs de capacité de monosaccharides et polyalcools sur silice en milieu CH_2Cl_2–MeOH–H_2O ou $CHCl_3$–MeOH–H_2O et sur une silice greffée NH_2 en milieu ACN–H_2O

	Lichrospher Si60 (125 × 4 mm) CH_2Cl_2–MeOH–H_2O (80 : 19,8 : 0,2)	Ultrasphère Si (250 × 4,6 mm) CH_2Cl_2–MeOH–H_2O (80 : 19,8 : 0,2)	Zorbax Sil (250 × 4,6 mm)		Carbohydrate NH_2 (300 × 3,9 mm) ACN–H_2O (80 : 20)
			CH_2Cl_2–MeOH–H_2O (80 : 19,8 : 0,2)	$CHCl_3$–MeOH–H_2O (80 : 19,8 : 0,2)	
Déoxy-oses					
L-Rhamnose	4,5	1,22	1,8	1,3	1,3
Cétopentoses					
D-Ribose	3,9	1,2	1,6	1,2	1,1
D-Xylose	5,4/5,7 [a]	1,3	2,2	1,6	1,5
L-Arabinose	6,0/6,5 [a]	1,5	2,2	1,7	1,8
Cétohexoses					
D-Fructose	7,9	2,4	2,8	2,1	2,3
L-Sorbose	8,9	2,2	3,05	2,0	2,3
Aldohexoses					
D-Mannose	9,1	2,0	2,9	2,0	2,8
D-Galactose	11,5/13,2 [a]	2,3	3,5/3,9 [a]	2,4/2,8 [a]	3,5
D-Glucose	11,0	2,0	4,0	2,5	3,3
Polyalcools					
m-Erythritol	6,5	1,7	2,5	1,6	1,2
Xylitol	10,2	3,0	4,8	2,6	2,0
Mannitol	16,2	3,4	5,7	3,5	3,1

[a] Doublets dûs à la séparation des anomères du sucre.

polyalcools beaucoup moins retenus sur cette dernière. Le xylitol et le xylose ou le mannitol et le mannose sont ainsi beaucoup mieux séparés sur colonne de silice.

Considérons maintenant la comparaison entre les différents systèmes proposés employant la silice comme support. Si sur la colonne Zorbax Sil, le dichlorométhane est remplacé dans l'éluant par du chloroforme (Fig. 2), l'ordre d'élution est changé notamment pour le méso-Erythritol, mais on remarque surtout que la rétention diminue globalement. Les interactions possibles avec ces deux solvants sont différentes; le chloroforme est caractérisé par un pouvoir donneur de protons (δ_d) supérieur à celui du dichlorométhane selon les paramètres de solubilité de Hildebrand et Scott [22]. Cette différence permet d'expliquer en partie le comportement différent des deux solvants et les rétentions plus faibles avec le chloroforme.

Si on compare maintenant les trois phases de silice avec le même éluant [CH_2Cl_2–MeOH–H_2O (80:19,8:0,2], on peut noter (Tableau 1) une élution tardive du fructose et du sorbose, les deux cétohexoses, par rapport aux autres monosaccharides sur la colonne Ultrasphère Si et une faible rétention du galactose par rapport aux autres

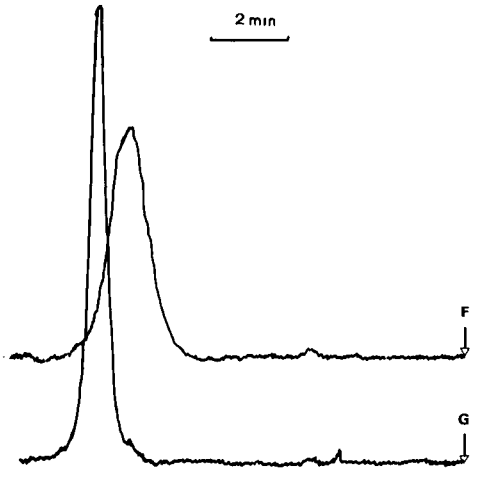

Fig. 1. Chromatogrammes du glucose (G) et du fructose (F) sur silice en milieu ACN–eau. Concentration des solutés: 100 mg l^{-1}. Colonne: Zorbax Sil (250×4,6 mm). Eluant: ACN–eau (95:5), 1 ml min^{-1}. Détection: DEDL PM 5, 40°C, 2,2 bars. Volume d'injection 20 μl.

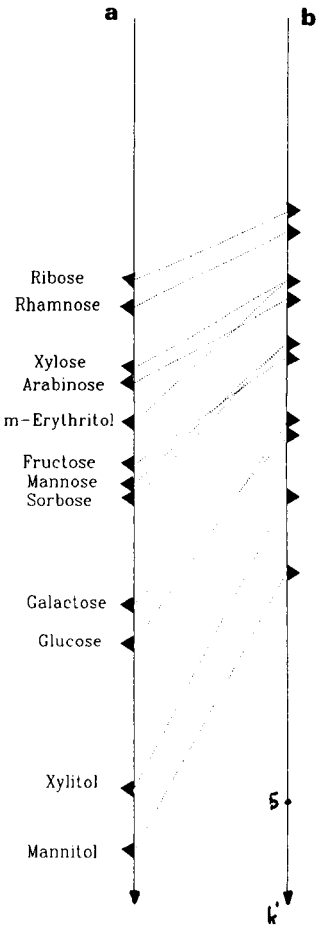

Fig. 2. Comparaison des facteurs de capacité obtenus sur Zorbax Sil avec un éluant. (a) CH_2Cl_2–MeOH–H_2O (80:19,8:0,2) et (b) $CHCl_3$–MeOH–H_2O (80:19,8:0,2).

aldohexoses sur la colonne Zorbax Sil. Mais on observe surtout, pour l'ensemble des 12 produits, une rétention plus grande sur la colonne LiChrospher Si que sur la colonne Zorbax Sil, la colonne Ultrasphère Si présentant la plus faible rétention. La rétention globale, estimée en prenant la moyenne (k'_{12}) des facteurs de capacité des 12 sucres et polyalcools du Tableau 1, augmente en même temps que la surface spécifique de la phase stationnaire (Tableau 2). Pour conclure de façon rigoureuse, il serait judicieux de comparer des phases de même origine, cependant on peut raisonnablement penser que la rétention est liée entre autres à cette caractéristique de la silice.

TABLEAU 2

Comparaison de la rétention moyenne (k'_{12}) des 12 monosaccharides et polyalcools avec la surface spécifique (S)

Phase stationnaire	k'_{12}	S ($m^2\ g^{-1}$)
LiChrospher Si60	8,6	650
Zorbax Sil	3,1	350
Ultrasphère Si	2,0	200

Le Tableau 3 présente les facteurs de capacité obtenus avec des di-, trisaccharides et polyalcools. Il apparait nettement que la rétention est très supérieure sur la colonne LiChrospher par rapport aux autres phases de silice pour une phase mobile identique ou de plus forte force éluante. Les sélectivités, par contre, ne sont pas extrèmement différentes à l'exception du sorbitol qui occupe une position très particulière dans chacun des trois cas. Une meilleure séparation du maltose et du cellobiose peut être remarquée notamment sur LiChrospher Si par rapport à une colonne aminopropyle en éluant acétonitrile–eau, sur laquelle ces deux disaccharides ne sont pas séparés.

La Fig. 3 illustre les séparations obtenues de monosaccharides (Fig. 3a) et de di-, trisaccharides (Fig. 3b) sur de tels systèmes.

Influence de l'eau

La teneur en eau dans les éluants organiques est critique lorsque les phases de silice sont employées, et suivant la valeur de celle-ci on peut s'orienter vers un mécanisme prépondérant d'adsorption ou de partage. Les traces d'eau s'adsorbent à la surface de la silice en couche monomoléculaire qui peut recouvrir plus ou moins la silice, puis en couche multimoléculaire si la concentration en eau augmente. Pour différentes silices de diamètres de pores variables, il a été noté [10,23] que 1500 $\mu l\ l^{-1}$ d'eau dans le dichlorométhane permet de remplir la majorité des pores et que l'on a alors apparition d'un phénomène de partage. Un alcool, en l'occurrence le méthanol, désactive également la surface de la silice.

Comme les facteurs de capacité du glucose et du fructose augmentent de façon linéaire en fonction du pourcentage d'eau rajouté dans l'étuant (Fig. 4), le mécanisme de rétention majoritaire n'est pas un mécanisme d'adsorption. Les forts pourcentages en méthanol (19,8% minimum) dans les éluants utilisés et les quantités totales d'eau, souvent supérieures à 1500 $\mu l\ l^{-1}$ sont des éléments supplémentaires qui nous font donc supposer que c'est un mécanisme de partage qui prédomine. Les limites des teneurs en eau de la Fig. 4 sont imposées d'une part par la présence de traces d'eau dans les solvants annoncées par les fabricants ($< 200\ \mu l\ l^{-1}$ pour le dichlorométhane et $< 800\ \mu l\ l^{-1}$ pour le méthanol) et d'autre part par la non miscibilité des solvants qui empêche l'utilisation d'un pourcentage d'eau supérieur à 1%.

TABLEAU 3

Facteurs de capacité de di-, trisaccharides et polyalcools sur silices (Le débit de la phase mobile est de 1,5 ml min^{-1})

	Zorbax Sil (250 × 4,6 mm) CH_2Cl_2–MeOH–H_2O (72:27,8:0,2)	LiChrospher Si60 (125 × 4 mm) CH_2Cl_2–MeOH–H_2O (72:27,8:0,2)	Ultrasphère Si (250 × 4,6 mm) CH_2Cl_2–MeOH–H_2O (75:24,8:0,2)
Saccharose	1,8	7,3	1,9
Sorbitol	1,9	6,1	3,3
Maltose	2,0	8,5	2,6
Cellobiose	2,1	9,5	2,5
m-Inositol	2,2	10,1	2,5
Lactose	2,8	12,5	3,2
Tréhalose	2,9	14,4	3,6
Mélibiose	3,0	13,9	3,6
Raffinose	3,7	21,3	4,4

On peut également observer sur la Fig. 5 que les temps de rétention de tous les sucres étudiés augmentent quand on rajoute un faible pourcentage d'eau dans l'éluant mais aussi quelques légères variations de sélectivité. Afin d'obtenir des rétentions reproductibles, les solvants pouvant contenir des traces d'eau en proportions variables, nous avons rajouté systématiquement 0,2% (2000 μl l^{-1}) d'eau dans l'éluant.

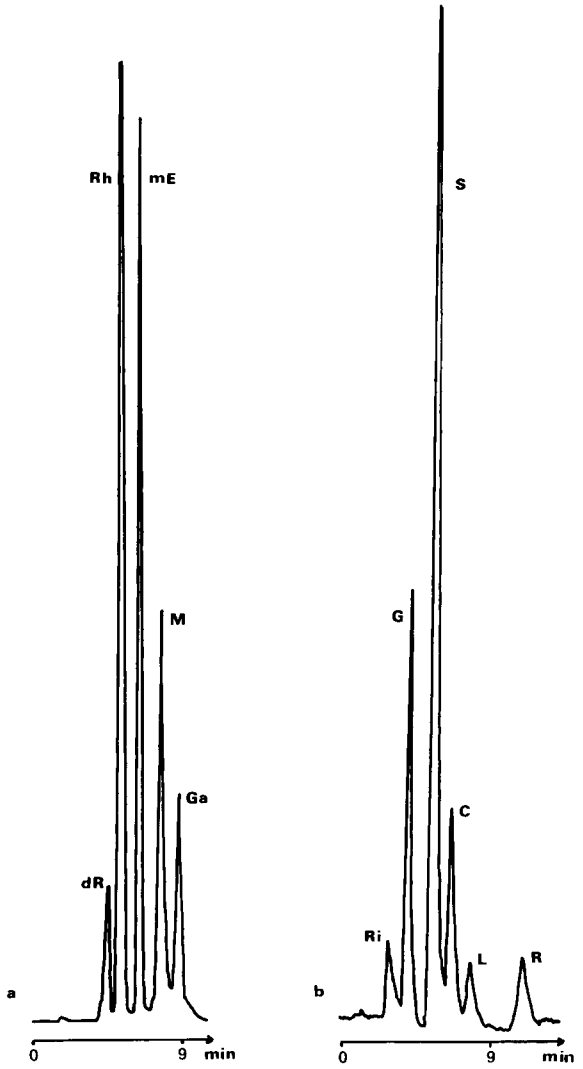

Fig. 3. Séparation isocratique sur silice de (a) monosaccharides: colonne, Zorbax Sil (250×4,6 mm); eluant, CH_2Cl_2–MeOH–H_2O (80:20:0,2), 1,5 ml min^{-1}. (b) mono-, di-, trisaccharides: colonne, Ultrasphère Si (250×4,6 mm); eluant, CH_2Cl_2–MeOH–H_2O (77:22,8:0,2), 2 ml min^{-1}. Détection: DEDL PM 8, 40°C, 2,2 bars. Solutés: 2-déoxyribose (dR), rhamnose (Rh), *m*-erythritol (mE), mannose (M), galactose (Ga), ribose (Ri), glucose (G), saccharose (S), cellobiose (C), lactose (L), raffinose (R). Concentration des solutés: 100 mg l^{-1}.

Ajout d'un catalyseur de mutarotation

Sur ces systèmes, il arrive que les anomères des sucres soit séparés et donnent lieu à un doublet ou à un pic élargi sur le chromatogramme. C'est le cas notamment du galactose. Avec les éluants utilisés, une augmentation de la température de la colonne pour éviter la résolution des anomères n'est pas possible. Par contre, l'ajout d'une amine tertiaire à l'éluant, la triéthylamine à une concentration de 0,1% qui agit comme catalyseur de mutarotation est efficace. En effet, dans ce cas, le passage rapide d'une forme anomèrique à l'autre moyenne les interactions, ce qui conduit à l'élimination du doublet du galactose.

Il faut noter que l'ajout de triéthylamine dans de tels éluants n'entraine pas une augmentation de la lumière diffusée ou du bruit de fond. Cela signifie qu'aucune particle non évaporable ne traverse le faisceau incident dans le détecteur et cette absence de lumière diffusée permet de conclure à une bonne stabilité de la phase stationnaire [11] même en milieu basique avec un éluant contenant très peu d'eau. Ceci a d'ailleurs déjà été signalé [23] lors d'études sur la durée de vie des colonnes.

Temps d'équilibrage et reproductibilité des temps de rétention

Les temps d'équilibrage des systèmes utilisant les silices sont parfois très longs à cause de l'organisation lente des molécules d'eau en interaction avec la surface de la silice. Avec les éluants que nous avons utilisés, CH_2Cl_2–MeOH–H_2O (80:19,8:0,2), l'équilibre du système est atteint en 10 min si on conditionne préalablement la colonne avec du dichlorométhane pur. Le conditionnement de la colonne par le méthanol pur avant l'éluant aboutit à un temps d'équilibrage beaucoup plus long (1 heure environ). La reproductibilité de la rétention est donnée dans le Tableau 4. Entre les séries de mesures 1 et 2, la

TABLEAU 4

Reproductibilité des temps de rétention (min) du Glucose sur Zorbax Sil (250×4,6 cm) avec un éluant CH_2Cl_2–MeOH–H_2O (72:27,8:0,2) à 1,5 ml min^{-1} (entre les séries 1 et 2, la colonne est rincée avec du méthanol, de l'eau, du méthanol et du dichlorométhane)

	Série 1	Série 2
t_R	3,98	3,95
	3,92	4,00
	3,89	4,11
	4,02	4,08
	3,96	4,00
	3,99	3,99
	3,89	4,04
Moyenne	3,95	4,02
Écart-type	0,05	0,05
C.V. (%)	1,2	1,2

colonne est rincée successivement par du méthanol, de l'eau, du méthanol et du dichlorométhane, puis équilibrée avec l'éluant.

Une bonne corrélation entre les deux séries est obtenue. Par contre, nous avons noté qu'un rinçage avec de l'éthanol à la place du méthanol entre les deux séries de mesures aboutit à une diminution notable des temps de rétention qui peuvent être rétablis par le protocole de rincage décrit ci-dessus. Le protocole de conditionnement, préalablement décrit, conduit à des équilibrages rapides avec les éluants employés et à des facteurs de capacités reproductibles. Cette souplesse du système chromatographique peut être notamment mise à profit lors de l'utilisation de gradients d'élution.

Gradient d'élution et détection

Avec les phases stationnaires constituées de résine Ca^{2+}, le système reste isocratique et ne permet pas de variation de la force éluante. Les gradients d'élution sont très difficiles avec les colonnes NH_2, car elles produisent en milieu acétonitrile–eau une dérive de la ligne de base au niveau du DEDL [11], voire impossible si un détecteur réfractométrique ou UV est utilisé. Les possibilités de séparation de différents monosaccharides, disaccharides et trisaccharides sont donc très restreintes sur ces systèmes couramment utilisés pour l'analyse des sucres. La possibilité de gradient d'élution avec le DEDL a permis jusqu'à présent seulement ce type de séparations sur colonne de silice greffée Diol en milieu acétonitrile–eau, mais la sélectivité pour les monosaccharides reste faible [11].

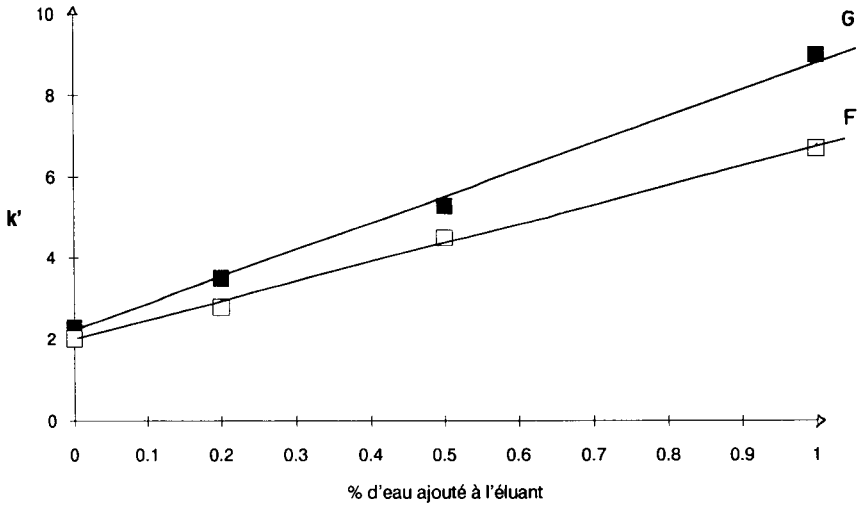

Fig. 4. Variation des facteurs de capacité du glucose (G) et du fructose (F) en fonction du pourcentage d'eau rajouté à l'éluant. Colonne: Zorbax Sil (250 × 4,6 mm). Eluant: CH_2Cl_2–MeOH–H_2O (80:20:0) à (80:19:1). Débit: 1,5 ml min^{-1}.

Sur colonne de silice, avec un éluant composé de dichlorométhane–méthanol et d'un faible pourcentage d'eau constant (0,2%), des gradients d'élution reproductibles peuvent être réalisés et la séparation de mono-, di- et trisaccharides est possible (Fig. 6). Il en est de même pour la séparation de différents polyalcools, qui n'est pas

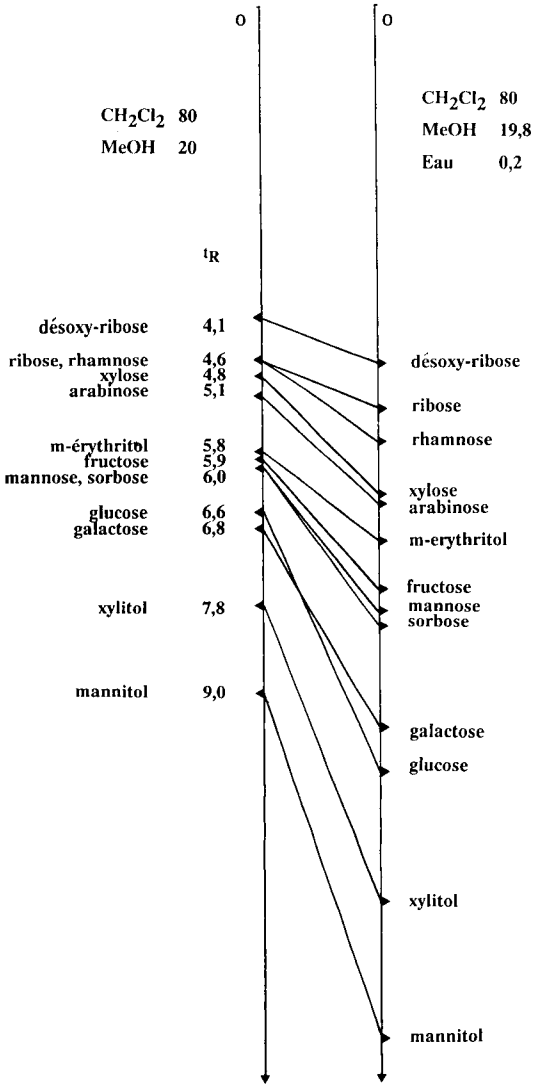

Fig. 5. Variation des temps de rétention des sucres avec ou sans ajout d'un faible pourcentage d'eau. Colonne: Zorbax Sil (250×4,6 mm). Débit: 1,5 ml min^{-1}. Le système de droite correspond aux temps de rétention données dans le Tableau 1.

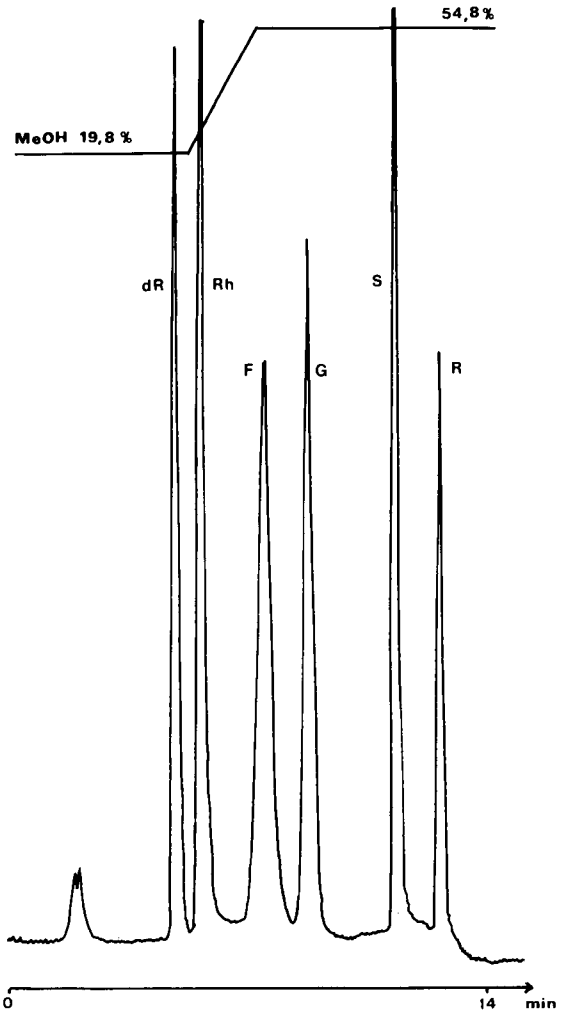

Fig. 6. Séparation de mono-, di- et trisaccharide en gradient d'élution sur Zorbax Sil (250×4,6 mm). Gradient CH_2Cl_2–MeOH–H_2O (80:19,8:0,2) maintenus pendant 5 min puis amenés à 45:54,8:0,2 en 2 min. Débit: 1,5 ml min^{-1}. Détecteur: Sedex 45, PM 5, 40°C, 2,2 bars. dR = désoxyribose, Rh = rhamnose, F = fructose, G = glucose, S = saccharose, R = raffinose. Concentrations des solutés: 100 mg l^{-1}.

aisées sur les systèmes classiques. La Fig. 7 présente une séparation de cinq polyalcools en moins de 12 min. Le temps d'équilibrage entre chaque injection est inférieur à 10 min pour le système chromatographique et l'appareilage utilisés.

La détection par diffusion de lumière permet d'obtenir dans ces conditions une limite de détec-

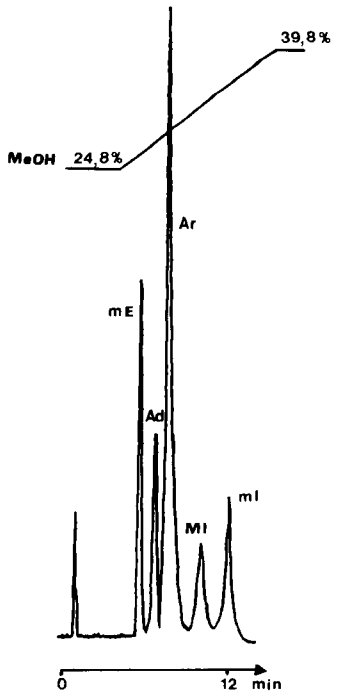

Fig. 7. Séparation de différents polyalcools en gradient d'élution sur LiChrospher Si 60 (250×4 mm). Gradient: CH_2Cl_2–MeOH–H_2O (75:24,8:0,2) maintenus pendant 4 min puis amenés à 60:39,8:0,2 en 11 min. Débit: 2 ml min^{-1}. Détecteur Sedex 45, PM 5, 40°C, 2,2 bars. mE = *m*-erythritol, Ad = adonitol, Ar = arabitol, MI = mannitol, mI = *m*-inositol. Concentrations des solutés: 100 mg l^{-1}.

tion de l'ordre de 20 ng de sucre injectés. Des études complémentaires sur la réponse du DEDL avec de tels éluants sont actuellement en cours, ceci par rapport à l'analyse quantitative des sucres mais aussi d'autres familles de composés [19,25].

Conclusion

Il n'existe pas de système de chromatographie en phase liquide capable de séparer tous les mélanges de sucres connus, mais l'opérateur doit choisir le système le mieux adapté aux problèmes posés. Les phases stationnaires à base de silice avec une phase mobile du type dichlorométhane–méthanol avec un faible pourcentage d'eau peuvent venir en complément de la panoplie des systèmes déjà disponibles. Ils apportent de nouvelles sélectivités sans présenter les inconvénients de certains systèmes puisqu'ils sont stables et ne conduisent pas à la formation de base de Schiff avec les sucres réducteurs. La rétention sur ces systèmes se fait vraisemblablement par un mécanisme majoritaire de partage. De plus, le couplage avec la détection à diffusion de lumière offre une bonne sensibilité et rend possible les gradients d'élution. Ceci en fait un système prometteur pour l'analyse de mélanges complexes comportant différents mono-, di- et trisaccharides.

Ce travail n'est pas une étude exhaustive de tels systèmes mais simplement la synthèse des premiers résultats. En parallèle à ceci, d'autres études sur des phases de silice greffée en chromatographie en phase liquide, avec des éluants dichlorométhane–méthanol [19], et en chromatographie en phase suprcritique, avec des éluants CO_2–méthanol [20], ont permis d'accumuler un grand nombre de données sur la rétention des sucres. Ces études chromatographiques ont données lieu à des analyses chimiométriques [26]. Les résultats obtenus sont encourageants et, par leurs développements en cours, ils permettront de prolonger ces études de façon rationnelle.

BIBLIOGRAPHIE

1 W.S. Reich, C.R. Hebd. Seances Acad. Sci., 208 (1939) 589.
2 A. Meunier, M. Caude et R. Rosset, Analusis, 14 (1986) 363.
3 M. Verzele, G. Simoens et F. Van Damme, Chromatographia, 23 (1987) 292.
4 P.E. Shaw, Handbook of Sugar Separation in Food by HPLC, CRC Press, Boca Raton, FL, 1988.
5 K.B. Hicks, Adv. Carbohydr. Chem. Biochem., 46 (1988) 17.
6 S.C. Churms, J. Chromatogr., 500 (1990) 555.
7 J.L. Rocca et A. Rouchouse, J. Chromatogr., 117 (1976) 216.
8 J.C. Linden et C.L. Lawhead, J. Chromatogr., 105 (1975) 125.
9 G.D. McGinnis et P. Fang, J. Chromatogr., 153 (1978) 107.
10 K.K. Unger, Porous Silica, Elsevier, Amsterdam, 1979.
11 M. Lafosse, B. Herbreteau, M. Dreux et L. Morin-Allory, J. Chromatogr., 472 (1989) 209.
12 D. Karlesky, D.C. Shelly et I. Warner, Anal. Chem., 53 (1981) 2146.
13 R.E.A. Escott et A.F. Taylor, J. High Resolut. Chromatogr. Chromatogr. Commun., 8 (1985) 290.

14 D.M. Wannacott et E.V. Patton, J. Chromatogr., 389 (1987) 103.
15 G.K. Grimble et A.M. Adam, Chromatogr. Anal., Feb. (1989) 5.
16 G.P. Ellis et J. Honeyman, Adv. Carbohydr. Chem., 10 (1955) 95.
17 S.R. Abott, J. Chromatogr. Sci., 18 (1980) 540.
18 B. Porsh, J. Chromatogr., 253 (1982) 49.
19 B. Herbreteau, M. Lafosse, L. Morin-Allory et M. Dreux, Chromatographia, 33 (1992) 325.
20 B. Herbreteau, M. Lafosse, L. Morin-Allory et M. Dreux, J. Chromatogr., 505 (1990) 299.
21 M. Lafosse, M. Dreux et L. Morin-Allory, Analusis, 15 (1987) XLV.
22 J.H. Hildebrand et R.L. Scott, Regular Solutions, Prentice Hall, Englewood Cliffs, NY, 1962.
23 Z. Elrassi, C. Gonnet et J.L. Rocca, J. Chromatogr., 125 (1976) 179.
24 B. Law et P.F. Chan, J. Chromatogr., 467 (1989) 267.
25 S. Brossard, M. Lafosse et M. Dreux, J. Chromatogr., 591 (1992) 149.
26 L. Morin-Allory et B. Herbreteau, J. Chromatogr., 590 (1992) 203.

Analytica Chimica Acta, 267 (1992) 157–164
Elsevier Science Publishers B.V., Amsterdam

Determination of elemental sulphur, sulphide and their mixtures in electrolyte solutions by a.c. voltammetry

Nikola Batina, Irena Ciglenečki and Božena Ćosović

Centre for Marine Research Zagreb, Ruđer Bošković Institute, Zagreb (Croatia)

(Received 1st November 1991; revised manuscript received 7th April 1992)

Abstract

The electrochemical behaviour of elemental sulphur, sulphide and their mixtures on a mercury electrode in 0.5 mol dm^{-3} NaCl–NaOH supporting electrolyte at pH 10 with and without the addition of 10% (v/v) methanol and 1×10^{-5} mol dm^{-3} toluene was studied. Investigations were carried out over a wide concentration range (from 1×10^{-8} to 1×10^{-3} mol dm^{-3}) of sulphur species in solution by a.c. voltammetry. Differences in the electrochemical behaviour during the formation of HgS at the electrode surface were observed between the two investigated species under different experimental conditions such as accumulation at different potential and voltammetric scan directions. Based on these differences, a method for the determination of sulphide, elemental sulphur and their mixtures in the aqueous solution is proposed. The solubility of elemental sulphur in aqueous medium at room temperature was determined as 1.7×10^{-6} mol dm^{-3}. The usefulness of the proposed method for the direct determination of sulphide and elemental sulphur in natural waters is discussed.

Keywords: Voltammetry; Sulphide; Sulphur; Waters

Modern polarographic techniques have been shown to be very suitable for the determination of sulphur species in a wide variety of different samples such as natural lake waters that have become anoxic owing to biological activity [1–3], foods (mostly fruits and vegetables) [4] and different industrial petroleum products (e.g., jet fuel) [5]. Electroanalytical methods such as differential-pulse polarography, cathodic sweep voltammetry and normal-pulse polarography, in combination with different spectroscopic and chromatographic techniques, have been used to provide not only information about concentration, but also about the identity, origin, distribution and behaviour of sulphur species in natural water systems [6,7]. So far, most studies have been focused on the electroanalytical determination of sulphide, with very few on the determination of elemental sulphur.

In principle, these determinations are based on a two-electron reversible electrochemical process, involving the oxidation of mercury to mercury(II) ions with immediate formation of insoluble mercury(II) sulphide at the electrode surface [8,9]. In contrast to the current methods for the direct determination of sulphide in aqueous solution [1,10–13], the determination of elemental sulphur usually involves chemical pretreatment, such as extraction with an organic solvent or working in organic solutions such as ethanol–water (1 + 1, v/v) [6,14], toluene–methanol (1 + 1, v/v) [5] or methanol–pyridine [15].

Such an indirect determination is necessary because of the lack of solubility of elemental sulphur in aqueous solutions and the interference from sulphide inherent to the electroanalytical methods used. There have been several other

Correspondence to: B. Ćosović, Centre for Marine Research Zagreb, Ruđer Bošković, Institute, Zagreb (Croatia).

suggestions for overcoming these problems encountered when measuring elemental sulphur, such as removing sulphide by acidifying the sample to pH 5 [6] and subsequently applying an appropriate electrochemical treatment which, by oxidation or reduction of elemental sulphur, forms new, easily detectable species [16–19].

The sensitivity of such methods is reported to be around 10^{-6} mol dm^{-3} for either sulphide or elemental sulphur. It should be emphasized that direct measurement, without addition of reagents, is the only method that leaves the equilibrium state of the solution undisturbed. In this way a true representation of those species which exist under natural conditions may be obtained (e.g., colloidal, particulate and soluble sulphur species in fresh waters, waste waters and marine waters).

The aim of the present work was to develop an electrochemical method for the direct determination of sulphur species in natural waters. As a first step, in this paper the electrochemical behaviour of elemental sulphur and sulphide in aqueous electrolyte solutions is presented. A direct method of determination of sulphur species was developed using phase-sensitive a.c. voltammetry.

The choice of the method was partly influenced by the fact that phase-sensitive a.c. voltammetry is widely used in the authors' laboratory in studies of surface-active substances in various natural waters and effluents. The presence of sulphur species in aqueous samples from anoxic environments was clearly indicated by an additional peak on the capacity current–potential curves obtained by a.c. voltammetry which increased with accumulation time.

In this work a hanging mercury drop electrode, with a prolonged accumulation period of the investigated substance at the selected potential, was used, which improved the sensitivity of the determination of sulphur species at least tenfold compared with earlier electroanalytical methods.

EXPERIMENTAL

A PAR Model 303A static mercury drop electrode (EG & G Princeton Applied Research, Princeton, NJ), used as the working electrode (electrode surface are $A = 2.57 \times 10^{-2}$ cm^{-2}) was connected to a BAS-100A electrochemical analyser (Bioanalytical Systems, West Lafayette, IN). The reference electrode was an Ag/AgCl (1 M KCl) electrode and a platinum wire served as the auxiliary electrode. Instrumental parameters were operating mode, phase-sensitive a.c. voltammetry for faradaic current (in-phase) measurements at a frequency of 80 Hz; modulation peak-to-peak amplitude of a.c. signal, 10 mV; and potential scan rate, 1 mV s^{-1}. The measurements were made at room temperature (293 K). The potential scan was applied after accumulation of electroactive substance on the electrode surface by diffusion and stirring processes at the starting potential for 0, 30, 60, 120 and 300 s.

The solutions, in a 50-cm^3 glass cell, were first deaerated with purified nitrogen for 15 min prior to measurement. In addition, nitrogen was continuously passed over the surface of the solution during the measurements.

All chemicals were of analytical-reagent grade and the water used was doubly distilled and further purified in a Milli-Q filter apparatus (Millipore).

As volatile H_2S is the predominant form of sulphide in aqueous solution below pH 7, all measurements were made at pH 10 in sodium hydroxide solution.

Solutions were prepared by dissolving Na_2S in two different supporting electrolyte solutions: 0.5 mol dm^{-3} NaCl, adjusted to pH 10 with 1 mol dm^{-3} NaOH; and 0.5 mol dm^{-3} NaCl pH 10, NaOH with addition of 10% (v/v) of methanol and 1×10^{-5} mol dm^{-3} of toluene.

A stock solution of elemental sulphur was prepared by dissolving elemental sulphur in toluene. Solutions of lower concentrations were prepared by diluting the stock solution with supporting electrolyte solution. All solutions were freshly prepared prior to each run. Solutions of investigated mixtures in the supporting electrolyte in the presence of methanol and toluene were prepared from aliquots of stock solutions of the selected components. The experiment was maintained in such a manner that sulphide and elemental sulphur (as individual components in the

mixture) were either of the same concentration or made similar contributions to the total peak current measured.

The mixtures were investigated in two different ways; directly, without any chemical pretreatment, and with elimination of sulphide by acidification of the sample.

An aqueous solution of elemental sulphur was prepared by shaking ca. 0.02 g of sulphur in 1 l of water. The fine, visible suspension was filtered through a Whatman glass-fibre filter (GF/F, pore size 0.7 μm).

RESULTS AND DISCUSSION

As mentioned in the Introduction, the determination of sulphide in aqueous media is based on the formation of insoluble mercury(II) sulphide during the accumulation period at potentials more positive than ca. −0.58 V vs. Ag/AgCl:

$$Hg + S^{2-} \rightarrow HgS + 2e^-$$

At more negative potentials the reverse reaction occurs with the Hg^{2+} in HgS being reduced back to mercury. When the freshly prepared mercury drop electrode is exposed to the first negative potentials (−0.7 or −0.8 V in these experiments) sulphide ions are adsorbed on the mercury electrode and then, during the positive-going scan, the oxidation of elemental mercury occurs with the formation of HgS. The advantages and disadvantages of using different polarographic techniques for the determination of sulphide, based on these reactions, have been well documented [1,8,9,20].

In this work, sulphide, in a wide concentration range from 1×10^{-8} to 9×10^{-4} mol dm^{-3} was studied on the basis of the changes in the height and shape of a.c. voltammograms obtained by in-phase faradaic current measurements. As expected, the voltammetric peaks had well defined shapes and were found in the potential range between −0.58 and −0.65 V vs. Ag/AgCl, the exact potential being dependent on the sulphide concentration in solution and the time of accumulation prior to scanning in either direction (more positive than −0.8 V or more negative than −0.5 V).

Typical a.c. voltammograms of sulphide in 0.5 mol dm^{-3} NaCl–NaOH at pH 10, obtained with a negative-going scan after 60-s accumulation at a potential $E = -0.5$ V vs. Ag/AgCl, are shown in Fig. 1a and b and for different accumulation periods in Fig. 1c. Typical a.c. voltammograms obtained with a positive-going scan are presented in Fig. 1d.

At sulphide concentrations below 1×10^{-5} mol dm^{-3} with a negative- and below 1×10^{-4} mol dm^{-3} with a positive-going scan, a single peak was observed (Fig. 1a, c and d). Higher concentrations of sulphide in solution or longer accumulation times caused an increase in the peak current and a shift towards more negative potentials. The peak height, expressed as the current value measured at the peak potential (Fig. 2a and b), increased linearly with increasing sulphide concentration in solution.

The difference between the peaks obtained using negative- and positive-going scan directions is ca. 50% in favour of the negative direction. It is also important to note that there is virtually no effect of the accumulation under stirring conditions on the peak height obtained with a positive-going scan (Fig. 2b). This agrees well with the explanation that during the positive-going scan anodic dissolution of mercury occurs, which is proportional to the adsorbed sulphide on the mercury electrode.

In contrast, at concentrations above 1×10^{-5} mol dm^{-3} (Fig. 2a) the peak height was no longer proportional to sulphide concentration, probably because of the film-forming electrode reaction [4,8,21]. Additional waves, peak broadening and a significant potential shift towards more negative values offer further evidence for the formation of a polylayer of mercury(II) sulphide at the electrode surface (Fig. 1b) [8,22–24]. However, as can be seen in Fig. 2a, at very high concentrations, the peak current was inversely proportional to the time allowed for accumulation at the electrode.

An identical behaviour of sulphide to that described above was obtained in the presence of small amounts of methanol and toluene in the

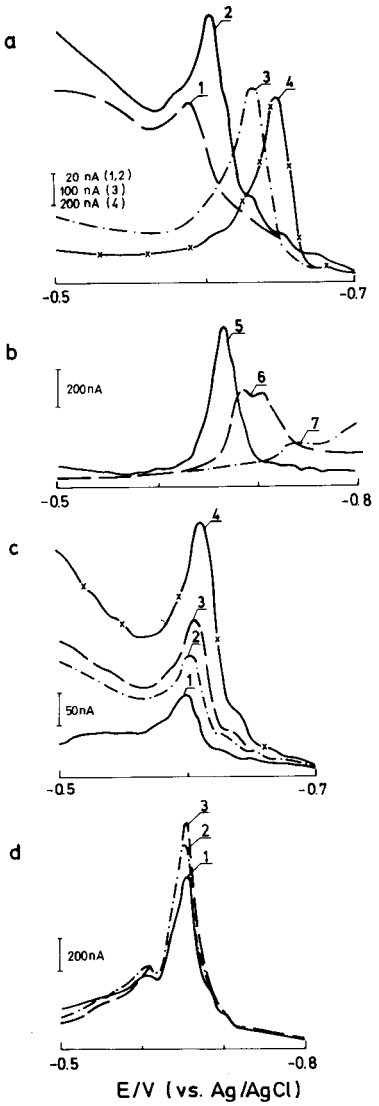

Fig. 1. Typical a.c. voltammograms of sulphide in 0.5 mol dm^{-3} NaCl–NaOH (pH 10). (a and b) Negative-going scans after 60 s accumulation at a potential $E = -0.5$ V vs. Ag/AgCl. Concentrations of sulphide: (1) 5×10^{-7}; (2) 1×10^{-6}; (3) 5×10^{-6}; (4) 1×10^{-5}; (5) 5×10^{-5}; (6) 1×10^{-4}; (7) 9×10^{-4} mol dm^{-3}. (c) Negative-going scans of 1×10^{-6} mol dm^{-3} sulphide after (1) 0, (2) 60, (3) 120 and (4) 300 s accumulation at a potential $E = -0.5$ V vs. Ag/AgCl. (d) Positive-going scans of 1×10^{-4} mol dm^{-3} sulphide after (1) 0, (2) 60 and (3) 120 s accumulation at a potential $E = -0.8$ V vs. Ag/AgCl. Experimental conditions: scan rate, 1 mV s^{-1}; frequency, 80 Hz; a.c. amplitude, 10 mV.

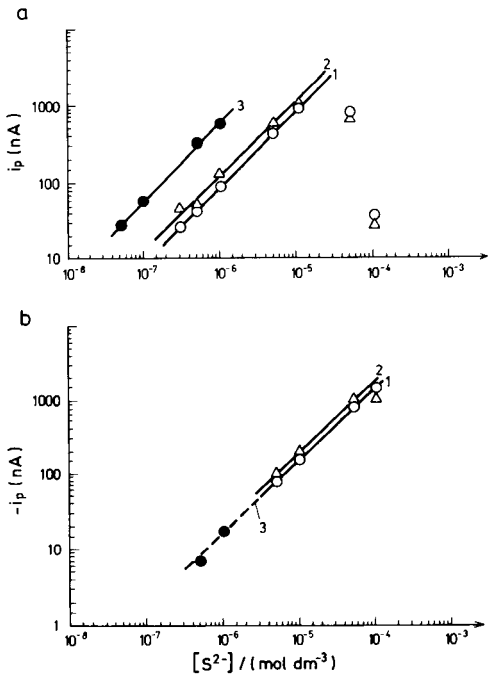

Fig. 2. Calibration graphs of peak current (i_p) versus concentration of sulphide in 0.5 mol dm^{-3} NaCl–NaOH (pH 10). (a) Obtained from negative-going a.c. voltammetric scans after accumulation at a potential $E = -0.5$ V vs. Ag/AgCl. (b) Obtained from positive-going a.c. voltammetric scans after accumulation at a potential $E = -0.8$ V vs. Ag/AgCl. Experimental conditions: scan rate, 1 mV s^{-1}; frequency, 80 Hz; a.c. amplitude, 10 mV; accumulation time, by diffusion (1) 60 and (2) 120 s and by stirring (3) 60 s.

electrolyte solution. The only difference is that the measured values of the peak current in the presence of organic solvents are ca. 50% lower than for pure aqueous medium. This is probably due to the adsorptive effect of added methanol and toluene. It should be mentioned that the addition of such a small amount of toluene and methanol to the pure electrolyte solution was not sufficient to cause any changes in the measured electrochemical response, either capacity or faradaic current.

According to expectation, the additional improvement in the determination of sulphur species (lower detection limit) was obtained as a result of faster transport of material to the electrode surface, i.e. under stirring conditions. Measurements under stirring conditions shifted the detection

limit towards lower concentrations (compare curves 1 and 3 in Fig. 2a) over approximately one order of magnitude.

Elemental sulphur is known to be almost insoluble in water. Nevertheless, a saturated aqueous solution of elemental sulphur showed in typical voltammetric peak for mercury(II) sulphide layer formation on the electrode surface. The solubility of sulphur at room temperature was determined by the electrochemical method using the calibration graph for sulphide in water as 1.7×10^{-6} mol dm^{-3}. In the presence of 10^{-5} mol dm^{-3} of toluene and 10% (v/v) of methanol the solubility of sulphur is significantly increased and these solutions were used for further investigation.

The overall behaviour of dissolved elemental sulphur was very similar to that reported for sulphide under the same experimental conditions. The a.c. voltammetric peaks of elemental sulphur appeared around −0.6 V vs. Ag/AgCl and showed a dependence of concentration on accumulation time (Fig. 3a). The measured a.c. (in-phase) faradaic current increased with increasing concentration in solution or at the electrode surface by the process of accumulation of electroactive species. Linearity between peak height and concentration, in the range 5×10^{-7}–1×10^{-5} mol dm^{-3} of elemental sulphur was observed and used later for calibration and quantification. Above 1×10^{-5} mol dm^{-3} of sulphur, the response was no longer proportional to the concentration of sulphur in solution (Fig. 3b).

The main difference between the behaviour of sulphide (discussed above) and elemental sulphur was observed during the positive-going scans after accumulation at negative potentials (−0.7 or −0.8 V vs. Ag/AgCl). For elemental sulphur, even at the highest concentrations used in our experiment, the weak and broad a.c. voltammetric wave was observed only after a long accumulation time under conditions of diffusion-controlled mass transport (Figs. 3c and d). It is believed that the behaviour of sulphur at the mercury electrode can be explained by the following mechanism:

$$S^0 + Hg \rightarrow HgS(ads.)$$

$$HgS(ads.) + 2e^- \rightarrow Hg^0 + S^{2-}(ads.)$$

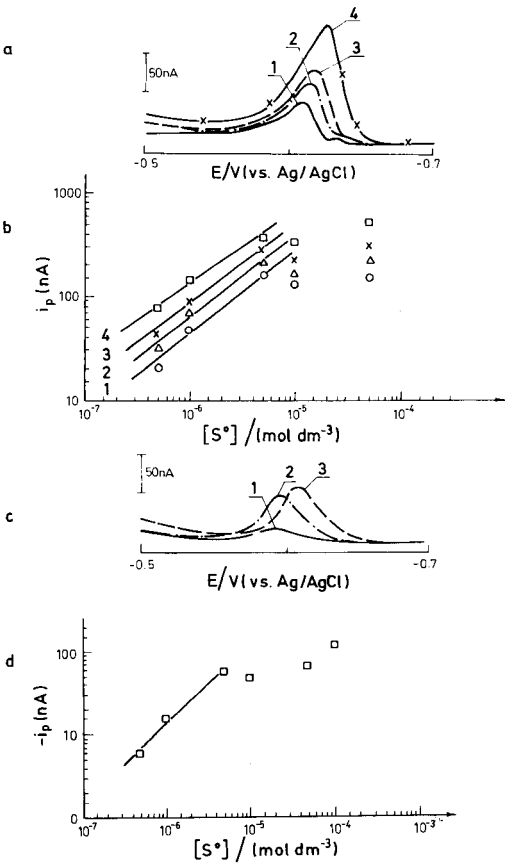

Fig. 3. (a) A.c. voltammograms of 1×10^{-6} mol dm^{-3} elemental sulphur in 0.5 mol dm^{-3} NaCl–NaOH–10% (v/v) methanol–1×10^{-5} mol dm^{-3} toluene (pH 10). Negative-going scans after (1) 0, (2) 60, (3) 120 and (4) 300 s accumulation at a potential $E = -0.5$ V vs. Ag/AgCl. Experimental conditions: scan rate, 1 mV s^{-1}; frequency, 80 Hz; a.c. amplitude, 10 mV. (b) Calibration graphs of peak current (i_p) versus concentration of elemental sulphur. Conditions as in (a). (c) A.c. voltammograms of elemental sulphur in 0.5 mol dm^{-3} NaCl–NaOH–10% (v/v) methanol–1×10^{-5} mol dm^{-3} toluene (pH 10). Concentrations of elemental sulphur: (1) 1×10^{-6}; (2) 5×10^{-6}; (3) 5×10^{-5} mol dm^{-3}. Positive-going scans after 300 s accumulation at a potential $E = -0.7$ V vs. Ag/AgCl. Experimental conditions: scan rate, 10 mV s^{-1}, frequency, 80 Hz; a.c. amplitude, 10 mV. (d) Calibration graph of peak current ($-i_p$) versus concentration of elemental sulphur. Conditions as in (c).

as has been partially suggested by others [25,26]. First, oxidation of elemental mercury occurs owing to the great affinity of elemental sulphur for chemical adsorption at the electrode surface at

potentials more positive than −0.6 V vs. Ag/AgCl. At more negative potentials, the insoluble mercury(II) sulphide formed has a tendency to decompose by reduction to elemental Hg and S^{2-} ions. The result is that during the accumulation period at a potential of −0.7 V or more negative, the concentration of S^{2-} just slightly increases in the vicinity of the electrode surface. It is obvious that these S^{2-} ions will be a limiting factor, and they control the reaction of HgS formation when the electrode is exposed to potentials more positive than −0.6 V, i.e., in the positive-going scan. If there are no additional sulphide ions present in solution, the measurable peak height in the positive-going scan can be observed for elemental sulphur only after longer accumulation time periods at −0.7 V (e.g., 300 s accumulation by diffusion, see Fig. 3d). This explanation is supported by the data obtained by investigating different mixtures of sulphide and elemental sulphur in the aqueous electrolyte in the presence of methanol and toluene.

Results are presented in Table 1. As with the individual components, quantitative interpretation of the investigated mixtures was performed on the basis of the measurements of the current during the positive- and negative-going voltammetric scans. Independently of the scan direction, after using the appropriate calibration graph, fairly good agreement between added and found values of the total concentration of sulphur species in solution was obtained for most of the samples. It should be noted that the concentration of the components in sample 6 was too high, actually above the upper limit of detection (multi-layers at the electrode surface).

When elemental sulphur was the dominant component of the investigated mixture (with regard to concentration, samples 1 and 2), the anodic current was very low, as expected. In contrast, a higher content of S^{2-} in the mixture led to an increase in the anodic current value (samples 4 and 5).

On the basis of these results, Fig. 4 was constructed by plotting the cathodic/anodic peak current ratio versus the percentage of sulphide in the mixture. A linear relationship was obtained, which can be used as a calibration line for the direct and rapid determination of the composition of the mixture. The total content of sulphide

TABLE 1

Determination of sulphur species in a mixture of elemental sulphur and sulphide in 0.5 mol dm^{-3} NaCl–NaOH–10% (v/v) methanol–1×10^{-5} mol dm^{-3} toluene (pH 10) by a.c. voltammetry

No.	Sample composition		i_p (nA) [a]	$-i_p$ (nA) [b]	$i_p/-i_p$	Content of sulphur found	
	mol dm^{-3}	% (w/w)				mol dm^{-3}	% (w/w) S^{2-} [d]
1	5×10^{-7} S^0	90	68	5	13.6	7.5×10^{-7}	10
	5×10^{-8} S^{2-}	10					
2	5×10^{-7} S^0	80	63	–	–	7.0×10^{-7}	0
	1×10^{-7} S^{2-}	20					
3	5×10^{-7} S^0	50	197	26	7.5	1.8×10^{-6}	50
	5×10^{-7} S^{2-}	50					
4	5×10^{-7} S^0	10	381	170	2.2	6.0×10^{-6}	90
	5×10^{-6} S^{2-}	90					
5	1×10^{-6} S^0	50	115	14	8.1	1.5×10^{-6}	47
	1×10^{-6} S^{2-}	50					
6	1×10^{-5} S^0	50	389	169	2.3	$> 7.0 \times 10^{-6}$	(Saturation)
	1×10^{-5} S^{2-}	50					

[a] Peak current of the negative-going scan after 120 s accumulation at $E = -0.5$ V vs. Ag/AgCl. [b] Peak current of the positive-going scan after 120 s accumulation at $E = -0.8$ V vs. Ag/AgCl. [c] According to the calibration graph for sulphide in 0.5 mol dm^{-3} NaCl–NaOH–10% (v/v) methanol–1×10^{-5} mol dm^{-3} toluene (pH 10) (Fig. 2a, curve 2). [d] According to the graph of the cathodic/anodic peak current ratio versus percentage of sulphide in the mixture (Fig. 4).

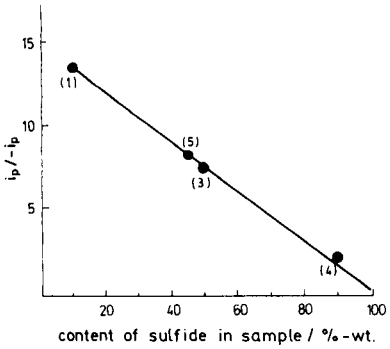

Fig. 4. A.c. voltammetric peak-current ratio ($i_p - i_p$) versus content of sulphide (%, w/w) in the sample (mixture of elemental sulphur and sulphide). Points: 1, 3, 4 and 5 were obtained from Table 1.

and sulphur in the mixture was determined from the calibration graph for the negative-going scan (of either sulphide or sulphur).

The method is useful in the concentration range between 10^{-7} and 10^{-5} mol dm^{-3} of sulphur species in solution. These investigations were performed with freshly prepared mixtures of sulphur and sulphide at relatively low concentrations of both components. It is assumed that the formation of polysulphides was probably avoided under such conditions. Nevertheless, there were still a few samples (Table 1, samples 3 and 5) that showed considerable discrepancies between the added and found values of total sulphur, which could be ascribed to the effect of chemical transformation of the mixture. This provides additional motivation for the study of the electrochemical behaviour of polysulphides and other sulphur species, which could be of interest with regard to natural waters.

Mixtures of sulphur and sulphide in the aqueous electrolyte in the presence of methanol and toluene were also investigated by a procedure that included the removal of hydrogen sulphide in acidic solution. The determination was based on measurement of the peak current of sulphur species (sulphur + sulphide) before and (sulphur) after acidifying the samples.

In Figure 5 shows a.c. voltammograms of the investigated species and their mixture obtained under the conditions described above. As no signal was observed in acidic solution, the solution was adjusted to pH 10 after removal of H_2S. According to the present hypothesis, on acidification of the solution sulphide was removed and only dissolved sulphur remained in the solution. The difference between the current values for the mixture and the remaining sulphur in the sample

TABLE 2

Determination of sulphur species in a mixture of elemental sulphur and sulphide in 0.5 mol dm^{-3} NaCl–NaOH–10% (v/v) methanol–10^{-5} mol dm^{-3} toluene (pH 10) by using the procedure of acidic treatment of the sample

Sample No.	Composition (mol dm^{-3})	Content of sulphur found (mol dm^{-3}) [a]		
		Mixture	Elemental sulphur	Sulphide
1	5×10^{-8} S^0 5×10^{-8} S^{2-}	9×10^{-8}	4.0×10^{-8}	5.0×10^{-8}
2	1×10^{-7} S^0 1×10^{-7} S^{2-}	2×10^{-7}	7.3×10^{-8}	1.3×10^{-7}
3	1×10^{-6} S^0 1×10^{-6} S^{2-}	2×10^{-6}	9.0×10^{-7}	1.1×10^{-6}

[a] According to the calibration graph for elemental sulphur in 0.5 mol dm^{-3} NaCl–NaOH–10% (v/v) methanol–1×10^{-5} mol dm^{-3} toluene (pH 10), obtained from negative-going a.c. voltammetric scans after accumulation by stirring at a potential $E = -0.5$ V vs. Ag/AgCl for 30, 60 and 120 s.

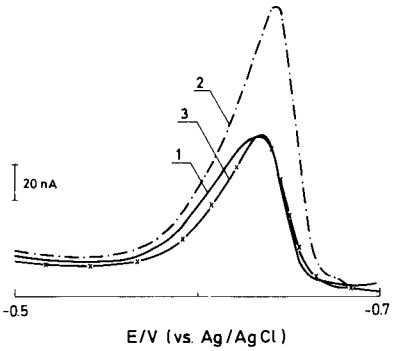

Fig. 5. A.c. voltammograms of sulphur species in 0.5 mol dm^{-3} NaCl–NaOH–10% (v/v) methanol–1×10^{-5} mol dm^{-3} toluene (pH 10). Sample composition: (1) 1×10^{-6} mol dm^{-3} elemental sulphur; (2) mixture of 1×10^{-6} mol dm^{-3} elemental sulphur and 1×10^{-6} mol dm^{-3} sulphide; (3) the same as (2) after removal of sulphide by acidification. Negative-going scans after 30 s accumulation by stirring at a potential $E = -0.5$ V vs. Ag/AgCl. Experimental conditions: scan rate, 1 mV s^{-1}; frequency, 80 Hz; a.c. amplitude, 10 mV.

is equal to the concentration of sulphide, as shown in Fig. 5. This method makes possible the determination of sulphide and elemental sulphur even in the lower concentration range (a negative voltammetric scan has a higher detection limit) and with slightly higher accuracy than the method based on the a.c. voltammetric cathodic-to-anodic peak ratio, as can be seen from the results in Table 2.

These initial results suggest that the method may be suitable not only for the determination of sulphur species in aqueous electrolytes, but also for the study of the interaction between sulphur species and materials present in natural and waste waters.

The interactions of sulphur species with organic matter are under investigation in two directions: the effect of organic matter on the solubility and binding properties of sulphur on the one hand, and investigation of possible effects and interferences of organic matter in the determination of sulphur species on the other.

The financial support of the Ministry of Science of the Republic of Croatia and the National Institute for Standards and Technology (Gaithersburg, MD) (Grant NIST JF 849) is gratefully acknowledged.

REFERENCES

1 W. Davison and C.D. Gabbut, J. Electroanal. Chem., 99 (1979) 311.
2 W. Davison, Limnol. Oceanogr., 22 (1977) 746.
3 W. Davison, Limnol. Oceanogr., 23 (1978) 1194.
4 H.H. van den Broek, C.E. Goewie and J. Struijs, Anal. Chim. Acta, 207 (1988) 305.
5 B.R. Olofsson, Anal. Chim. Acta, 177 (1985) 167.
6 J. Buffle, O. Zali, J. Zumstein and R.R. de Vitre, Environ. Sci. Technol., 64 (1987) 41.
7 R.R. de Vitre, J. Buffle, D. Perret and R. Baudat, Geochim. Cosmochim. Acta, 52 (1988) 1601.
8 D.R. Canterford, J. Electroanal. Chem., 52 (1974) 144.
9 J.A. Turner, R.H. Abel and R.A. Osteryoung, Anal. Chem., 47 (1975) 1343.
10 W. Davison, C.P. Woof and D.R. Turner, Nature (London), 295 (1982) 582.
11 L.K. Leung and D.E. Bartak, Anal. Chim. Acta, 131 (1981) 167.
12 G.W. Luther, A.E. Giblin and R. Varsolona, Limnol. Oceanogr., 30 (1985) 727.
13 J.J. Renard, G. Kubes and H.I. Bokler, Anal. Chem., 47 (1975) 1347.
14 K. Wenzel, Z. Lebensm.-Unters.-Forsch., 170 (1980) 5.
15 M.E. Hall, Anal. Chem., 22 (1950) 1137.
16 S.S. Roy and B.P. Balodi, Fresenius' Z. Anal. Chem., 32 (1981) 308.
17 M.Q. Al-Abachi, F.H. Al-Dabbagh and S.T. Sulaiman, Talanta, 27 (1980) 1077.
18 J. Polak, R. Hozman and J. Volke, Chem. Listy, 79 (1985) 882.
19 L.M. Alexio, S. Rath, O.E.S. Godinho and A.U. Ivaska, Analyst, 113 (1988) 1427.
20 D.R. Canterford and A.S. Buchanan, J. Electroanal. Chem., 44 (1973) 291.
21 L.M. Peter, J.D. Reid and B.R. Scharifker, J. Electroanal. Chem., 119 (1981) 73.
22 C. Benucci and B.R. Scharifker, J. Electroanal. Chem., 190 (1985) 199.
23 M. Youssefi and R.L. Birke, Anal. Chem., 49 (1977) 1380.
24 R.D. Armstrong, D.R. Porter and H.R. Thirsk, J. Electroanal. Chem., 14 (1967) 17.
25 W. Davison, J. Buffle and R. de Vitre, Pure Appl. Chem., 60 (1988) 1535.
26 O. Zali, PhD, Thesis, University of Geneva, Geneva, 1983.

Analytica Chimica Acta, 267 (1992) 165–169
Elsevier Science Publishers B.V., Amsterdam

Stripping potentiometry for organolead compounds: application to the determination of total lead in gasoline

Daniel Jagner, Lars Renman and Yudong Wang

Department of Analytical and Marine Chemistry, University of Göteborg and Chalmers University of Technology, S-412 96 Göteborg (Sweden)

(Received 25th March 1992)

Abstract

A 10-μl gasoline sample is added to 590 μl of a modifying matrix composed of 1.5 g l^{-1} mercury(II), 0.50 M nitric acid and 1% (v/v) Triton X-100 in 90% ethanol. Tetraethyl- and/or tetramethyllead (TEL and TML, respectively) are reduced and simultaneously amalgamated on a glassy carbon electrode employing a pulsed electrolysis sequence, and the amalgamated lead is re-oxidized by means of a constant current. One analysis, which is performed automatically under computer control with a commercial potentiometric stripping analyser, takes approximately 5 min including the time for sample preparation and result evaluation. The system is calibrated by means of a single-point calibration using a standard prepared in isooctane and containing 15 mg l^{-1} of lead, half from TEL and half from TML. The relative difference in sensitivity between TEL and TML is 8%, in accordance with theory. The method is best suited for unleaded gasoline with total lead concentrations in the range 0.1–30 mg l^{-1} of total lead. The results obtained agree well with those obtained by atomic absorption spectrometry. The estimated precision is 4–8% (R.S.D.) and the detection limit 0.07 mg l^{-1} of total lead.

Keywords: Potentiometry; Stripping voltammetry; Gasoline; Lead; Organolead compounds; Tetraethyllead; Tetramethyllead

Tetramethyllead (TML) and tetraethyllead (TEL) have for a long time been added to gasoline as antiknock agents. These additives are, however, not compatible with exhaust gas catalysts in modern cars. As most refineries produce both leaded and unleaded gasoline in the same production line, a certain amount of organic lead is unavoidable in unleaded gasoline. The maximum concentration of lead allowed in unleaded gasoline varies from one country to another, a typical limit being 10 mg l^{-1} of total lead.

Obviously there is a demand for simple and rapid methods for the determination of total lead in gasoline. Current methods seem to exploit mostly atomic absorption spectrometry (AAS) for this purpose [1]. Although details of the procedure used no doubt differ from one laboratory to another, the main features of the standard method are based on treatment of the gasoline sample with iodine or bromine at elevated temperature prior to analysis by flame AAS [2,3]. However, this procedure is elaborate and time consuming. Recently a method based on inductively coupled plasma mass spectrometry (ICP-MS) has been reported [4].

Surprisingly few attempts have been made to exploit electroanalytical methods for the determination of lead in gasoline, the most successful probably being those of Guinón and Grima [5] using emulsion formation polarography, and the application reported by Environmental Sciences [6]. In these procedures treatment with iodine monochloride was necessary, however.

Correspondence to: D. Jagner, Department of Analytical and Marine Chemistry, University of Göteborg and Chalmers University of Technology, S-412 96 Göteborg (Sweden).

This paper reports a procedure, based on a newly introduced commercial instrument for stripping potentiometry, in which the organic lead is reduced directly to amalgamated lead. The only necessary sample pretreatment is to dilute the gasoline sample in a matrix containing ethanol, nitric acid, mercury ions and detergent. Calibration is performed using known concentrations of TML and TEL and the total time of analysis is less than 5 min, including the time for sample preparation, result evaluation and display.

EXPERIMENTAL

Instrumentation and software

A combined potentiometric and constant-current stripping analyser (Tracelab, Potentiometric Stripping Unit PSU20, Radiometer, Copenhagen) connected to an IBM-compatible personal computer equipped with a QuietJet (Hewlett-Packard, Palo Alto, CA) printer was used for all experiments. The real-time measurement rate of this instrument is 30 kHz and it is capable of generating oxidative or reductive currents from 0 to 50 μA with a resolution of 0.1 μA. The total weight of the analyser is 7 kg and the size is $0.22 \times 0.16 \times 0.47$ m.

The analyser was operated under the control of the TAP2 Trace Talk Method Builder and Commander software package (Radiometer). Using this program, complete analytical procedures including random potential control, multiple scanning, stripping peak localization and integration, concentration evaluation by means of calibration plots, standard addition or internal standard can be constructed. Digital and graphical display can also be included in the analytical procedure. The analytical procedure was stored in the computer memory and when running the analysis the only operations needed were to perform the relevant standard and sample preparations and to activate the program.

Electrodes and electrochemical cell

A three-electrode system consisting of a 3 mm diameter glassy carbon electrode, a platinum wire counter electrode and a saturated calomel reference electrode (SCE) (F 3500, P 736 and K 436, respectively; Radiometer), arranged as shown in Fig. 1 in order to minimize the sample volume needed, were used for all measurements. The sample holder was a polyethylene tube of 12.5 mm i.d. which hung unsupported under the three-electrode assembly by means of friction and elasticity.

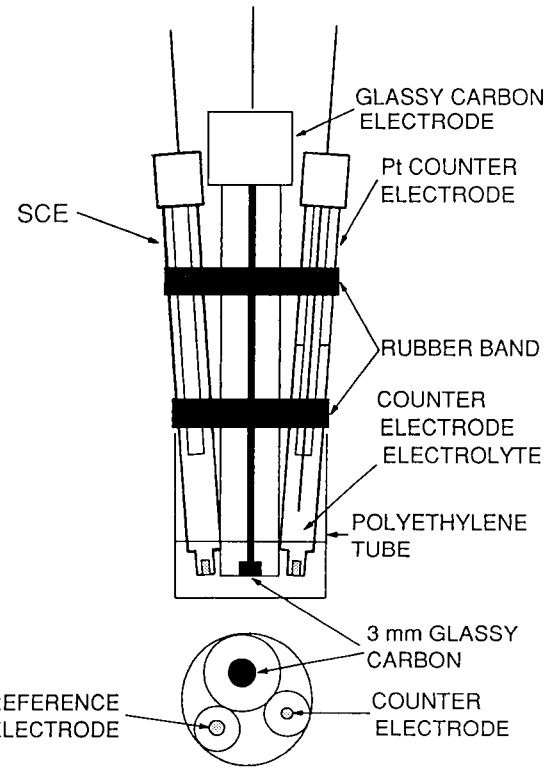

Fig. 1. Electrode assembly used. The counter electrode compartment contains 0.50 M nitric acid and is separated from the sample by means of a ceramic plug.

All electrochemical measurements were made under quiescent conditions and all potentials referred to below are versus the SCE.

Reagents

All metal ion standards and the ethanol and isooctane used were of analytical-reagent grade and the mineral acids were of Suprapur grade (Merck, Darmstadt). TML and TEL of at least 99% purity were obtained from the local British Petroleum refinery.

Sample modification matrix

The sample modification matrix contained 1.5 g l^{-1} of mercury(II), 0.5 M nitric acid and 1% (v/v) Triton X-100 in 90% ethanol.

Standards and intercalibration samples

A mixture of 7.5 mg l^{-1} of lead from TML and 7.5 mg l^{-1} of lead from TEL in isooctane was used as a single-point calibration standard for the determination of lead in gasoline. Prior to analysis the instrument was calibrated with this standard using the origin as the second point on the calibration graph.

The three intercalibration standards (total volume 1 ml) were obtained from the local British Petroleum refinery. These standards had been used in an intercalibration involving seven different laboratories, all of them using AAS for the determination of the total lead content.

Sample preparation

A 10-μl volume of a sample, or of the TML/TEL standard, was added by means of a glass microsyringe to 590 μl of the modification matrix in the polyethylene sample tube and the mixture was homogenized by shaking. Evaporation was avoided by capping the tube except during analysis.

Electroanalytical procedure

Prior to analysis of a TML/TEL standard or a sample, the electrode was cleaned with a tissue soaked in 95% ethanol whereby the mercury film from the previous analysis was also removed. Calibration was performed by running the TML/TEL standard and re-calibration was performed approximately every 20th sample.

The electrochemical procedure consists of three major steps. In the first step, a new mercury film was plated on to the glassy carbon electrode surface. The second step involved the enrichment of lead amalgam by means of pulsed potentiostatic pre-electrolysis and the third was the multi-scanning stripping step. Formation of a fresh mercury film was achieved by electrolysis at −0.50 V for 20 s followed by open-circuit mode for 1 s, this cycle being repeated four times with the difference that the electrolysis potential was decreased by 0.10 V in each cycle. Deposition of lead amalgam was performed by five pulsed electrolysis cycles, each cycle consisting of a potential of −1.20 V for 9 s and −1.50 V for 1 s. The potential was then increased to −0.90 V and finally stripping was initiated by means of a constant oxidizing current equal to 30 μA until a potential of −0.30 V was reached. The potential was then immediately decreased to −1.2 V, whereby the newly formed lead(II) ions at the electrode surface in completely quiescent solution were re-reduced to lead amalgam. After 10 s at this potential and 1 s at −1.50 V, a new constant-current stripping curve was recorded. Four such stripping curves were accumulated in the PSU 20 and then transferred to the personal computer for subsequent result evaluation and presentation.

RESULTS AND DISCUSSION

Diffusion-controlled reduction of TML and TEL

TML and TEL are added to gasoline in proportions known only to the manufacturer. Consequently, an ideal method for the determination of total lead should give the same response for the two compounds. In stripping potentiometry, the response for TML differs from that of TEL for two reasons, one of them being the difference in diffusion rate due to different molecular size. Assuming that the neutral compounds TML and TEL behave as gaseous substances in the sample matrix, the relative difference in the diffusion rate could be estimated to be ca. 8.5%, the smaller molecule TML, of course, giving the highest sensitivity. The other reason for the difference in response between TML and TEL is the possible difference in the overpotential needed for the reduction of the two substances. In stripping potentiometry, as in all electroanalytical stripping techniques, it is highly desirable that the rate of analyte reduction is diffusion controlled, i.e., that all of the analyte species diffusing to the working electrode surface are reduced and amalgamated. If this is not the case, both the reproducibility and sensitivity will be poor.

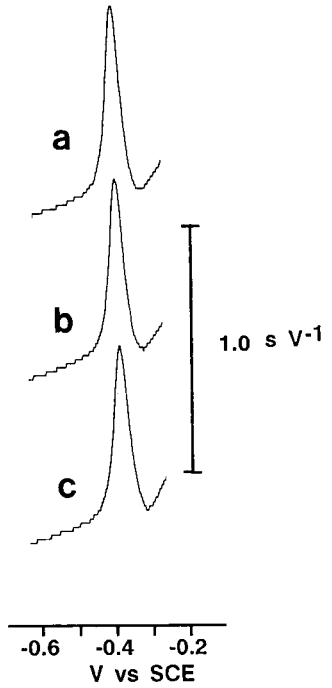

Fig. 2. Stripping curves obtained in the analysis of samples containing 10 mg l^{-1} of lead in the form (a) TML, (b) TEL and (c) inorganic lead(II). The samples were diluted 60-fold prior to analysis.

In order to investigate the overpotentials needed for diffusion-controlled reduction of TML and TEL, two standards, each containing 10 mg l^{-1} of lead, were prepared from the two compounds in isooctane. The two solutions were analysed according to the electroanalytical procedure described above with the difference that the potentiostatic deposition potentials varied between −0.40 and −1.20 V in steps of −0.05 V. The same experiment was also performed with a sample prepared from inorganic lead(II) ions with the same total concentration of lead. For inorganic lead a constant stripping signal was obtained at deposition potentials below −0.80 V, the corresponding values for TML and TEL being −0.90 and −0.95 V, respectively. Hence by exploiting electrolysis potentials below these values, diffusion-controlled conditions will prevail for both TML and TEL.

Figure 2 shows the stripping curve obtained in the analysis of the samples containing 10 mg l^{-1} lead from TEL, TML and inorganic lead(II) using the electroanalytical procedure described above.

The sensitivity difference due to the different molecular weights of TML and TEL was investigated by using the electroanalytical procedure described above on samples, prepared in isooctane, containing 0.50, 1.0, 3.0, 7.0, 10.0 and 15.0 mg l^{-1} of lead obtained from TML, TEL and inorganic lead(II), respectively. On plotting the potentiometric stripping signals (in ms) vs. total lead concentrations (in mg l^{-1}) and applying linear regression, the slopes were found to be 3.53, 3.22 and 3.37 ms l mg^{-1} for TML, TEL and Pb(II), respectively, the regression coefficients being 0.99908, 0.99916 and 0.99923, respectively. The intercept on the concentration axis was less than 0.15 mg l^{-1} for the three linear plots.

The relative difference in sensitivity between TML and TEL of 9.1% found experimentally is very close to the theoretical value of 8.5% calculated assuming ideal molecular diffusion. Consequently, the systematic analytical error when using a standard containing equal concentrations of TML and TEL in the analysis of samples containing unknown relationships between TML and TEL contents will not exceed 4.3%. In fact, standards prepared from inorganic lead(II) in aqueous solutions could equally well be used.

Accuracy and detection limit

The accuracy of the proposed method was investigated by analysing samples containing known concentrations of TML and TEL. The analyser was calibrated by means of a single-point calibration through the origin using a sample containing a total lead concentration of 15 mg l^{-1}, half from TML and half from TEL. As can be seen from the results in Table 1, the agreement between the known and the experimentally obtained values is better than 0.5 mg l^{-1} (or 10% above a concentration of 5 mg l^{-1} of total lead).

Analysis of a sample containing 1 mg l^{-1} of lead from TML yielded a stripping signal equal to 4.5 ms and analysis of solution to which no TML or TEL had been added (isooctane blank) yielded a stripping signal equal to 0.03 ms. From this, it can be concluded that the lead content in the sample modification matrix was negligible. As

TABLE 1

Results obtained in the analysis of synthetic mixtures of TML and TEL by the proposed method [a]

TML (mg Pb l^{-1})	TEL (mg Pb l^{-1})	Total Pb taken (mg l^{-1})	Total Pb found (mg l^{-1})
0.0	0.0	0.0	0.1
0.5	0.5	1.0	1.3
1.0	1.0	2.0	2.2
0.0	4.0	4.0	3.6
1.0	4.0	5.0	4.8
3.0	3.0	6.0	6.4
3.0	4.0	7.0	7.1
7.0	0.5	7.5	7.9
3.0	7.0	10.0	10.2
10.0	4.0	14.0	13.9
15.0	7.0	22.0	21.4
15.0	15.0	30.0	28.4

[a] Single-point calibration using a sample containing 15 mg l^{-1} of lead, half from TML and half from TEL

mentioned above, the real-time sampling rate of the instrument was 30 kHz, i.e., the smallest signal measurable was 0.033 ms. Empirically, it has been found that the minimum detectable signal is approximately ten times this value, i.e., 0.33 ms. From this it can be concluded that the signal obtained at a concentration of 1 mg l^{-1} corresponds to approximately 14 times the detection limit, i.e., the detection limit is 0.07 mg l^{-1}.

Analysis of standard samples and precision

The three intercalibration samples were analysed six times in random order by the proposed method and the results were compared with those obtained from an intercalibration study. Prior to analysis the analyser was calibrated with the 15 mg l^{-1} TML/TEL calibration solution and the same calibration was used for all samples. As can be seen from Table 2, the values obtained by the proposed method are all in the higher part of the concentration range obtained by AAS. This might indicate a bias in the method but it is more likely that it is due to the fact that the standard samples had been opened many times prior to the registration of the results shown in Table 2, the slightly higher values thus being due to evaporation of hydrocarbons in the samples.

TABLE 2

Comparison between the results obtained by the proposed method and those obtained in an intercalibration between seven laboratories using AAS

Sample No.	Intercalibration results range ($n = 7$) (mg l^{-1})	Mean value (this work) ($n = 6$) (mg l^{-1})	Relative standard deviation (%)
1	12–16	15.2	2.2
2	8–9.7	10.3	2.1
3	2.5–5.2	4.6	3.8

From Table 2, it can be concluded that the relative precision of the method is in the range 2–4% if the same calibration is used for all measurements. Assuming the same relative standard deviation in the measurement of the calibration sample as in the measurement of the samples, the relative standard deviation of the method could be estimated to be 4–8%.

Conclusions

Compared with the standard AAS method, the proposed electroanalytical method provides a considerably simpler procedure with respect to sample pretreatment and time of analysis. In addition, the cost and size of the instrumentation are considerably less and no flames or plasmas are involved, the latter aspect probably being an advantage in a refinery environment.

This work was supported by the Swedish Natural Research Council. The authors thank Dr. Bo Edroth for providing the reference samples.

REFERENCES

1 IP Standards for Petroleum and Its Products. Part I, Vol. 1, Institute of Petroleum, London, 1985.
2 E. Cardelli, M. Cifani, M. Mecozzi and G. Sechi, Talanta, 33 (1986) 279.
3 C.G. Taylor and J.M. Trevaskis, Anal. Chim. Acta, 179 (1986) 491.
4 Varian Instrument Applications, 20 (1991) 7.
5 J.L. Guinón and R. Grima, Analyst, 113 (1988) 613.
6 Environmental Sciences, Bedford, MA, application note, 1977.

Analytica Chimica Acta, 267 (1992) 171–177
Elsevier Science Publishers B.V., Amsterdam

Computerized pipettes with programmable dispension for batch injection analysis

Joseph Wang, Liang Chen, Lucio Angnes [1] and Baomin Tian

Department of Chemistry, New Mexico State University, Las Cruces, NM 88003 (USA)

(Received 20th January 1992; revised manuscript received 14th April 1992)

Abstract

New computer controlled pipettes are used to establish several dispension patterns and thus to enhance considerably the power of batch injection analysis (BIA). The unique delivery functions offered by these programmable pipettes permit advanced BIA operations with greater versatility and solution handling capability. Particularly attractive are the abilities to induce the dispersion (via prolonged or reversed sample dispensions), to inject simultaneously two (air-segmented) sample/standard solutions, to inject accurately extremely small samples (down to 0.5 μl) at different rates, or to perform acid–base titrations. Repetitive oscillations of the dispension greatly improve the contact of reactants, as illustrated for enzymatic reactions. High precision accrues from the highly reproducible (operated-independent) piston movement. Repetitive injections of 1 μl solutions are performed with a sample throughput of 300 per hour, with a relative standard deviation of 1.5%. The effect of these novel dispension patterns on the BIA response are evaluated using potentiometric and amperometric detection schemes. Prospects of using these pipettes in other automated analytical systems are discussed.

Keywords: Batch injection analysis; Pipettes

The recent development of batch injection analysis (BIA) represents an advance in the area of automated analysis [1–4]. BIA resembles flow injection analysis (FIA) in that an injected sample zone is transported in a reproducible fashion toward a detector. For this purpose, the flow manifold is eliminated with samples being injected directly onto a nearby detector, immersed in a large-volume blank solution. Passage of the sample zone over the detector surface results in sharp peak readouts, similar to those of FIA. Such dynamic measurements performed in batch operation result in many of the attractive features (speed, sample size, sensitivity, reproducibility, simplicity) of FIA systems. However, because of the limited dispersion associated with the short injector–detector distance, BIA (as now practiced) is less versatile than FIA in terms of the solution handling capabilities. Hence, it currently relies on the use of specific or reactive sensors, including amperometric [1], potentiometric [4], thermal [2], and optical [3] devices.

This paper describes the utility of new computer-controlled electronic pipettes for addressing the limited versatility of batch injection systems. Earlier BIA work has relied on standard manual micropipettes (e.g. Eppendorf), with a single normal dispension mode. In contrast, newly introduced motorized/computerized pipettes (series EDP Plus™ from Rainin, Woburn, MA) possess different and unique functions [5], and are thus very attractive for the BIA operation. In particular, the ability to program the sample dis-

Correspondence to: J. Wang, Department of Chemistry, New Mexico State University, Las Cruces, NM88003 (USA).
[1] Permanent address: Instituto de Quimica de USP São Paulo (Brazil).

pension to perform various solution handling and delivery schemes (e.g. titration, mixing, volume sequencing, dilution, etc.) is exploited in the following sections for manipulating and prolonging the degree of dispersion to meet specific BIA needs. In addition to sophisticated dispension programming, induced dispersion and novel BIA applications, such operated-independent pipettes permit highly reproducible injections of a wide range of sample volumes (down to 0.5 μl). These and other capabilities and possibilities are illustrated and assessed in the following sections. Even though the new pipettes are illustrated within the framework of BIA, the novel options offered by their programmable dispension should benefit numerous other analytical schemes based on solution delivery.

EXPERIMENTAL

Apparatus

The BIA amperometric and potentiometric cells were similar to those described earlier [1,4]. The cylindrical cells were filled with 300 and 500 ml blank solutions, respectively. Inverted glassy carbon disk (Model MF2012, BAS, W. Lafayette, IN) and pH glass (Model 989B, Markson) electrodes, introduced through the cell bottom, were used as detectors in most experiments. A platinum disk electrode (Model MF 2013, BAS), connected to a Tygon-tube jacket [2] was used in the dispension-reversal enzyme experiment. A hole, located exactly opposite the center of the detector, was used to accommodate the motorized pipette (Model EDP Plus-100 μl, Rainin, Woburn, MA). The pipette tip was usually kept at a fixed distance (0.5–1 mm) from the center of the detector. When needed, stirring was accomplished by rotating a 2.5-mm diameter glass rod, inserted through a hole in the cell cover (at ca. 3 cm from the pipette) and connected to a low voltage DC motor (Model 273-223, Radio Shack). The stirring rate ($\sim$ 1000 rpm) was controlled through a variable high-precision resistor connected in series to a transformer. Amperometric and potentiometric experiments were performed with an EG & G PAR (Princeton, NJ) Model 264 A voltammetric analyzer and a home-built amplifier, respectively, connected to an Omniscribe strip-chart recorder.

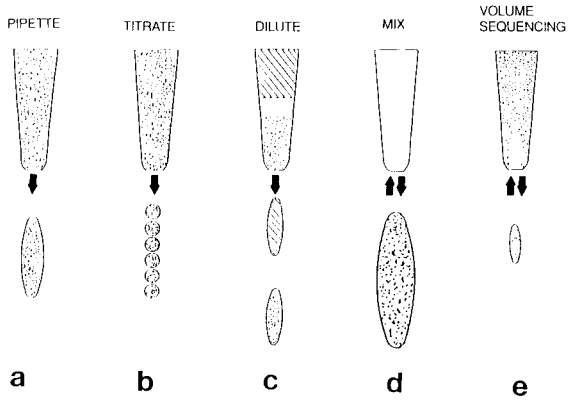

Fig. 1. Dispension patterns offered by motorized electronic pipettes: the "Pipette" (a), "Titrate" (b), "Dilute" (c), "Mix" (d), and "Volume sequencing" (e) modes of operation.

Reagents

All solutions were prepared from doubly-distilled water. Catechol (Sigma, St. Louis, MO), ferrocyanide, hydrochloric acid (Baker, Phillipsburg, PA), potassium chloride, mono and dihydrogen phosphate (Fisher, Pittsburgh, PA), glucose and glucose oxidase (EC 1.1.3.4) (Sigma) were used without further purification.

Procedure

The amperometric and potentiometric BIA experiments were similar to those reported earlier [1,4], with the exception that the computerized pipette replaced the Eppendorf pipette. The computerized pipette was operated under different dispension patterns (Fig. 1), as recommended by its manufacturer [5], and detailed in the following sections. In addition to highly-accurate normal ("pipette") mode (Fig. 1a), various distinct patterns were tested, including the "Titrate", "Dilute", "Mix" and "Volume sequencing" modes (Fig. 1, b, c, d, and e, respectively).

RESULTS AND DISCUSSION

Through the use of a miniature onboard computer, to program the piston movement, motor-

ized electronic pipettes offer a variety of dispension patterns. Several of these unique delivery functions greatly manipulate the dispersion of the sample zone and thus lead to various interesting BIA modes of operation. Such possibilities are illustrated below from a series of different experiments, carried out with amperometric and potentiometric detection schemes.

Normal operation

If the sole purpose of the BIA experiment is to rapidly transport samples to the detector, then normal dispensions (via the "Pipette" or "Multiple Dispense" modes) should be employed. Even in this simplest case of normal sample dispension, motorized electronic pipettes greatly improve the BIA operation through an extremely accurate and precise dispension of small volumes (down to 0.5 μl). Fig. 2 displays typical BIA peaks for 8 repetitive injections of 1 μl catechol (A) and 10 μl pH 4 (B) solutions, as obtained with amperometric and potentiometric detectors, respectively. Very sharp and reproducible peak readouts are observed, reflecting the fast and reproducible transport and replenishment of the sample zone over the surface. The peak widths are very short

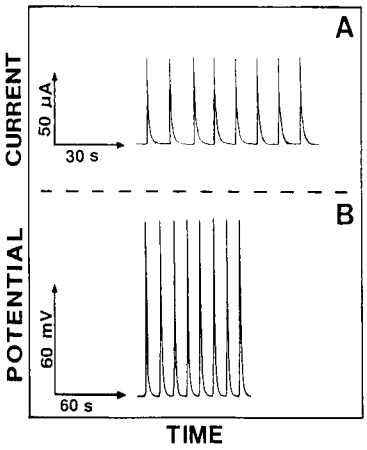

Fig. 2. Batch injection amperometric (A) and potentiometric (B) peaks for solutions of 1 mM catechol and of pH 4.0. Sample volume, 1 (A) and 10 (B) μl. Dispension rate, 78 μl s^{-1}. Detectors, glassy carbon held at +0.65 V (A) and pH glass (B) electrodes. Cell solutions, 0.05 M phosphate buffer of pH 7.4 (A) and 7.0 (B), with no stirring. Injector–detector distance, 0.5 mm; "Multiple Dispense" mode.

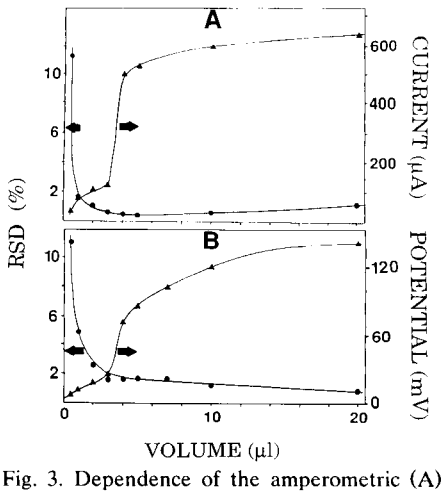

Fig. 3. Dependence of the amperometric (A) and potentiometric (B) peak height and R.S.D. on the sample volume. R.S.D. was calculated for 10 repetitive injections. Conditions as in Fig. 2.

(4–6 s), leading to extremely high sampling frequencies (of 300–360 samples h^{-1}). The eight peaks shown in Fig. 2 are part of a series of 20 repetitive injections for which relative standard deviations (R.S.D.s) of 1.5 (A) and 1.7 (B)% were calculated. The high precision observed with small sample volumes is attributed to the reproducible piston strokes associated with the operated-independent dispension. Beside obvious advantages when sample availability or disposal are concerned, the use of extremely small sample volumes greatly increases the dilution factor in the BIA cell solution (to nearly one millionfold!) and hence the tolerance of the system against memory effects. Note that in addition to huge dilution, BIA systems retain their tolerance against analyte buildup through the unique hydrodynamic pattern of flat ("wall-jet" like) sensor surfaces [1].

Figure 3 shows the dependence of the BIA peak height and RSD upon the sample volume over the 0.5–20 μl range. For both detection modes the response increases slowly with the volume at first (0.5–3 μl range), then more rapidly (3–5 μl range), and finally slowly again (5–20 μl range). The R.S.D., in contrast, decreases rapidly upon increasing the volume, stabilizing around 1.0 and 1.7% for volumes larger than 3 μl (for amperometric and potentiometric detections, re-

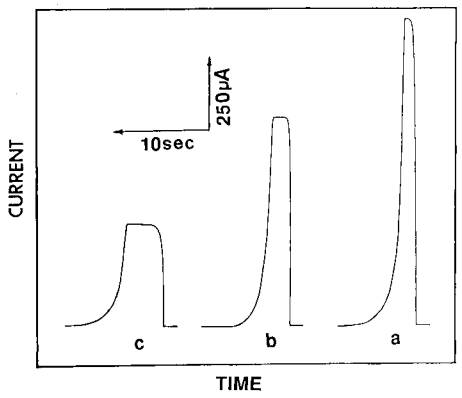

Fig. 4. Batch injection amperometric peaks for a 100 μl catechol (1 mM) solution, obtained at different dispension rates: 78 (a), 46 (b) and 23 (c) μl s^{-1}. Other conditions as in Fig. 2A.

spectively). Note also that the use of extremely small volumes is more favorable with the amperometric detection (e.g. R.S.D. of 1.6% vs. 5.0% for 1 μl injections).

One attractive option of the normal dispension mode is the use of different dispension rates. Such control of the dispension represents a useful approach for extending the dispersion in batch injection systems. Figure 4, for example, displays BIA amperometric peaks for 1 mM catechol, obtained with rates of 78 (a), 46 (b) and 23 (c) μl s^{-1}. The peak width at 0.6 C_{max} increases from 1.4 to 4.6 s upon decreasing dispension rate. The dispension rate has also some effect upon the reproducibility of the BIA data (Fig. 5a); R.S.D.s of 1.2, 0.7 and 0.6% are observed at 23, 46 and 78 μl s^{-1}, respectively. The improved precision at

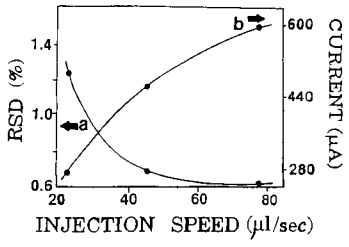

Fig. 5. Dependence of the R.S.D. (a) and peak height (b) upon the injection speed. Amperometric response to a 5 μl catechol (1 mM) solution. R.S.D. was calculated for 30 repetitive injections. Conditions, as in Fig. 2A.

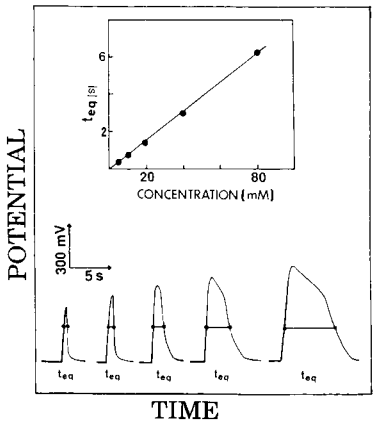

Fig. 6. Acid–base BIA titration. Injections of 10 μl solutions containing increasing levels of KOH (from left to right): 5×10^{-3} M, 1.0×10^{-2} M, 2.0×10^{-2} M, 4×10^{-2} M and 8×10^{-2} M to the unstirred 0.01 M HCl cell solution. Detector, pH glass electrode placed 1 mm from the injector. Also shown (inset), the resulting plot of t_{eq} vs. KOH concentration.

slower dispension rates is attributed to the finite response time of the electronics involved. As expected, the amperometric response increases rapidly upon increasing the dispension rate (Fig. 5b). By controlling the dispersion rate, the sample zone is reproducibly "flowing" towards the surface (i.e. FIA without a "pushing" carrier stream). The adjustable speed capability should be useful also for accommodating samples of different viscosities or densities [5]. As will be shown in the following sections, more advanced operation modes of motorized electronic pipettes further stretch the sample zone (and dramatically increase the dispersion) as desired for performing lengthy operations.

Even the normal dispension mode is sufficient for promoting fast reactions. For example, acid–base BIA titrations can be performed in a manner analogous to FIA titrations. Figure 6 displays a potentiometric titration of HCl with KOH. Localized pH changes, resulting from the injection of 10 μl of KOH solutions of increasing concentration, are monitored with a pH electrode. The time interval which elapses between two points (on the ascending and descending portions of each curve), t_{eq}, serves as a measure of the concentration of the injected sample. The resulting

plot of t_{eq} vs. [KOH] (also shown) is linear (correlation coefficient, 0.998). The exact reason for such dependence (compared to the logarithmic one of FIA titration) is not clear at the present time.

Novel options based on programmable dispension

The main feature of computer-controlled pipettes is their ability to manipulate the dispension to meet specific solution delivery needs. Such dispension programming greatly increases the information content from one injection. Advanced BIA experiments, based on these novel options, are illustrated below.

For example, the "Titrate" mode of operation has been designed for performing titrations through repetitive dispensions of very small fractions of the sample. As applied for BIA operation, such a mode allows stretching of the sample zone over a long time, as desired for promoting reactions. Figure 7 presents typical recorder tracings for amperometric (A) and potentiometric (B) BIA experiments performed with the normal

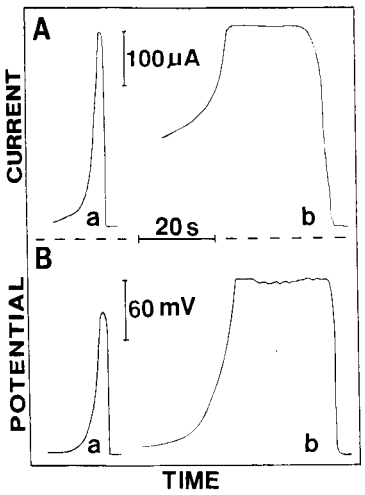

Fig. 7. Amperometric (A) and potentiometric (B) BIA peaks, using the normal (a) and "Titrate" (b) modes of operation. Solutions (100 μl) of 5 mM ferrocyanide (A) and pH 4.0 (B). Cell solutions, 0.05 M KCl (pH 4) (A) and 0.05 M phosphate buffer (pH 7) (B), with no stirring. Applied potential (B), +0.55 V. Dispension rate, 46 μl s^{-1}. Other conditions, as in Fig. 2.

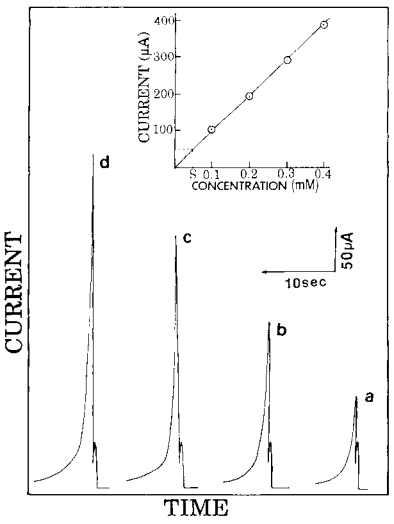

Fig. 8. Amperometric BIA response using the "Dilute" mode of operation. Simultaneous injection of two solutions (separated by air gap in the tip): 50 μM catechol solution (25 μl) coupled to catechol solutions (25 μl) of increasing concentration: 100 (a), 200 (b), 300 (c), and 400 (d) μM. Other conditions, as in Fig. 2A.

pipette (a) and "Titrate" (b) modes of operation. The latter greatly increases the dwell time of the sample zone, with peak widths (at 0.6 C_{max}) ca. 12–14-fold larger than those achieved in the normal operation. (The dispension of small droplets – illustrated in Fig. 1b – is performed at a rate of 4 μl s^{-1}, i.e. over 25 s for the 100 μl samples of Fig. 7.) Note that the sensitivity is not compromised by the sample stretching, as compared to the smaller peaks associated with increased dispersion in FIA systems. This is attributed to the prolonged dispension of *fresh* (undiluted) samples. The large increase in the dwell time is accomplished without changing the injector–detector distance or the overall volume.

In the next experiment, the viability of the "Dilute" mode was assessed (Fig. 8). The "Dilute" function of the motorized pipettes is based on picking up two (or more) solutions separately (with an air gap between them), but dispensing them together, by the simultaneous injection of the two (air-segmented) samples. One useful use of this "Dilute" mode is a simultaneous sample/standard injection to facilitate the quantitation.

For example, Fig. 8 presents the BIA amperometric response for 25 μl samples of 50 μM catechol in connection with 25 μl catechol standard solutions of increasing concentration (100–400 μM, Fig. 8, a–d). Defined double peaks are observed for each injection (in less than 10 s). While the first peak – corresponding to the 50 μM zone – remains constant (R.S.D. = 1.2%), the second one increases linearly with the catechol concentration (slope, 938 $\mu A/mM^{-1}$; correlation coefficient, 0.999). The resulting calibration data thus offer convenient quantitation of the sample concentration (see inset). By accommodating a large number of separated zones in one tip (through a more sophisticated program), it may be possible to construct the entire calibration curve in one injection.

Another attractive dispensing programming mode is the "Volume Sequencing" (Fig. 1e). This unique function involves oscillation of the dispension by picking up the sample volume and then dispensing and picking up sequentially and repetitively smaller aliquots (through an up-and-down piston motion). Figure 9 presents typical BIA recording tracings for the "Volume Sequencing" mode, using a single 100 μl sample and 20 μl modulations. Such operation results in multiple amperometric (A) and potentiometric (B) peaks for the single sample over a prolonged period of several minutes. The peaks rapidly decrease at first and then more slowly (reflecting the continuously changing concentration profile within the tip, i.e., sample dilution by the blank BIA cell solution). Highly reproducible tracings were obtained for repetitive "Volume Sequencing" operations (not shown). By incorporating a suitable reagent in the cell solution, the "Volume Sequencing" mode should be ideal for promoting chemical reactions.

The "Mix" mode represents another oscillating approach to improve the contact of reactants. It is based on a similar dispension pattern as the "Volume Sequencing" function, but it repetitively moves the entire injected zone forward and backward (Fig. 1d). Such a dispension reversal operation – and the resulting BIA output – are analogous to flow reversal injection analysis [6]. For example, Fig. 10 illustrates the dispension

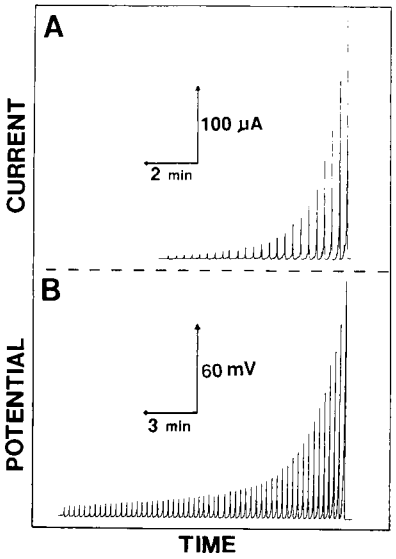

Fig. 9. Amperometric (A) and potentiometric (B) BIA response using the "Volume Sequencing" mode of operation. Sample; 100 μl of ferrocyanide (5 mM) (A) and of pH 4 (B). Aliquots dispensed and picked, 20 μl. Cell solutions, 0.05 M KCl (pH 4) (A) and 0.05 M phosphate buffer (pH 7) (B), with stirring. Applied potential (A), +0.55 V. Other conditions, as in Fig. 2.

reversal amperometric response for a 100 μl glucose oxidase solution in the presence of glucose in the BIA cell (B), along with the response for

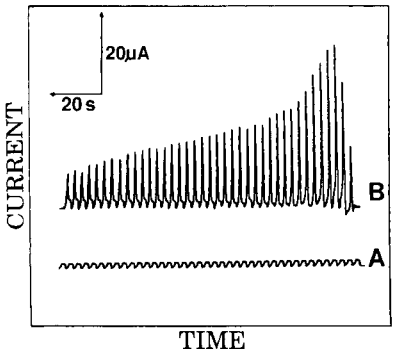

Fig. 10. Amperometric BIA response using the "Mix" mode of operation. Dispension reversal of a 100 μl glucose oxidase (50 U)/phosphate buffer solution to the cell solution, containing 33 mM glucose (in 0.05 M phosphate buffer) (B). The corresponding response for injections of the blank (phosphate buffer) solution is shown in A. Detector, platinum disk (held at +0.80 V) with a Tygon tube jacket of 1 cm long and 7 mm diameter. Injector–detector distance, 8 mm.

dispensions of the blank solution (A). The efficient mixing of the sample zone and cell solution components (characterizing the "Mix" operation) greatly facilitates the efficiency of the enzymatic conversion reaction. The current oscillations of the liberated hydrogen peroxide reflect the repetitive passage of the sample plug over the detector. Accordingly, the sample is active over a prolonged period (of more than 2 min). Such multiple peak recording with decreased current upon increasing the number of reversals, is similar to that of flow reversal experiments [6]. As expected, no response is observed in the absence of the enzyme. Obviously, the use of expensive reagents in the cell solution represents a problem.

CONCLUSIONS

We have demonstrated that the novel dispension patterns, offered by computer-controlled pipettes, open up unique possibilities for automated analysis, in general, and for BIA, in particular. By programming the sample dispension, it is possible to manipulate the dispersion to meet specific BIA needs. The induced dispersion achieved through the greatly prolonged or reversed sample dispensions, may thus bring together reactants (from the sample and cell solutions) in a highly reproducible fashion, as desired for handling a wide variety of chemical assays and other procedures (e.g. preconcentration, as in stripping voltammetry). Other steps (e.g., dilution, extraction) may be accomplished through a more sophisticated dispension programming. Hence, greater versatility and solution handling capabilities are added to BIA systems (thus addressing early limitations associated with their short injector detector distances). In addition, the highly reproducible (operated-independent) piston movement allows greater accuracy and precision, and convenient injections of extremely small samples. Full realization of these advantages will require automation of the pipette introduction to the BIA cell. Additional future advantages may be achieved using new multichannel pipettes (with parallel tips), coupled to sensor arrays for multianalyte BIA detection (analogous to multichannel flow analyzers). Other BIA detection schemes (e.g. optical) should also benefit from these dispension programming capabilities. While the advantages of motorized/electronic pipettes have been illustrated within the context of BIA, a wide variety of other analytical systems should benefit from their sophisticated dispension modes (e.g. the use of the "Mix" mode for perform flow reversal injection experiments). Hence, programmable pipettes hold prospects for many interesting analytical applications.

L.A. acknowledges a fellowship from Fundacão de Amparo a Pesquisa do Estado de São Paulo (Brazil).

REFERENCES

1 J. Wang and Z. Taha, Anal. Chem., 63 (1991) 1053.
2 J. Wang and Z. Taha, Anal. Lett., 24 (1991) 1389.
3 J. Wang, G.D. Rayson, and Z. Taha, Appl. Spectrosc., 46 (1992) 107.
4 J . Wang and Z. Taha, Anal. Chim. Acta, 252 (1991) 215.
5 EDP Plus Motorized Microliter Pipette – User Guide, Rainin Instrument Co., Woburn, MA, 1989.
6 A. Rios, M.D. Luque de Castro, and M. Valcárcel, Anal. Chem., 60 (1988) 1540.

ANALYTICA CHIMICA ACTA, VOL. 267 (1992)

AUTHOR INDEX

Analytical Abstracts Now on CD-ROM!

Available in Macintosh™ and IBM Compatible Formats

The premier source of current awareness information in analytical chemistry is now available on a single SilverPlatter CD-ROM.

Analytical Abstracts on CD-ROM features:

- Approximately 140,000 items from 1980 onwards
- Easy to use SilverPlatter software
- Quarterly updates with more than 3,000 items
- Unlimited searching – no additional costs

Special Discount for Hardcopy Subscribers

Contact us today for further information and a FREE demo disk.

Judith Barnsby, Royal Society of Chemistry,
Thomas Graham House, Science Park, Milton Road,
Cambridge CB4 4WF, United Kingdom
Tel: +44 (0) 223 420066 Fax: +44 (0) 223 423623
Telex: 818293 ROYAL

ROYAL SOCIETY OF CHEMISTRY
Information Services

PUBLICATION SCHEDULE FOR 1993

	S'92	O'92	N'92	D'92	J	F
Analytica Chimica Acta	267/1 267/2	268/1 268/2	269/1 269/2	270/1 270/2	271/1 271/2	272/1 272/2
Vibrational Spectroscopy		4/1				4/2

INFORMATION FOR AUTHORS

Manuscripts. The language of the journal is English. English linguistic improvement is provided as part of the normal editorial processing. Authors should submit three copies of the manuscript in clear double-spaced typing on one side of the paper only. *Vibrational Spectroscopy* also accepts papers in English only.

Abstract. All papers and reviews begin with an Abstract (50–250 words) which should comprise a factual account of the contents of the paper, with emphasis on new information.

Figures. Figures should be prepared in black waterproof drawing ink on drawing or tracing paper of the same size as that on which the manuscript is typed. One original (or sharp glossy print) and two photostat (or other) copies are required. Attention should be given to line thickness, lettering (which should be kept to a minimum) and spacing on axes of graphs, to ensure suitability for reduction in size on printing. Axes of a graph should be clearly labelled, along the axes, outside the graph itself. All figures should be numbered with Arabic numerals, and require descriptive legends which should be typed on a separate sheet of paper. Simple straight-line graphs are not acceptable, because they can readily be described in the text by means of an equation or a sentence. Claims of linearity should be supported by regression data that include slope, intercept, standard deviations of the slope and intercept, standard error and the number of data points; correlation coefficients are optional.

Photographs should be glossy prints and be as rich in contrast as possible; colour photographs cannot be accepted. Line diagrams are generally preferred to photographs of equipment.

Computer outputs for reproduction as figures must be good quality on blank paper, and should preferably be submitted as glossy prints.

Nomenclature, abbreviations and symbols. In general, the recommendations of the International Union of Pure and Applied Chemistry (IUPAC) should be followed, and attention should be given to the recommendations of the Analytical Chemistry Division in the journal *Pure and Applied Chemistry* (see also *IUPAC Compendium of Analytical Nomenclature, Definitive Rules*, 1987).

References. The references should be collected at the end of the paper, numbered in the order of their appearance in the text (*not* alphabetically) and typed on a separate sheet.

Reprints. Fifty reprints will be supplied free of charge. Additional reprints (minimum 100) can be ordered. An order form containing price quotations will be sent to the authors together with the proofs of their article.

Papers dealing with vibrational spectroscopy should be sent to: Dr J.G. Grasselli, 150 Greentree Road, Chagrin Falls, OH 44022, U.S.A. Telefax: (+1-216) 2473360 (Americas, Canada, Australia and New Zealand) or Dr J.H. van der Maas, Department of Analytical Molecule Spectrometry, Faculty of Chemistry, University of Utrecht, P.O. Box 80083, 3508 TB Utrecht, The Netherlands. Telefax: (+31-30) 518219 (all other countries).

0003-2670/92/$05.00

This issue is printed on acid-free paper.

PRINTED IN THE NETHERLANDS

Capillary Electrophoresis

Principles, Practice and Applications

by **S.F.Y. Li**, *National University of Singapore, Singapore*

Journal of Chromatography Library Volume 52

Capillary Electrophoresis (CE) has had a very significant impact on the field of analytical chemistry in recent years as the technique is capable of very high resolution separations, requiring only small amounts of samples and reagents. Furthermore, it can be readily adapted to automatic sample handling and real time data processing. Many new methodologies based on CE have been reported. Rapid, reproducible separations of extremely small amounts of chemicals and biochemicals, including peptides, proteins, nucleotides, DNA, enantiomers, carbohydrates, vitamins, inorganic ions, pharmaceuticals and environmental pollutants have been demonstrated. A wide range of applications have been developed in greatly diverse fields, such as chemical, biotechnological, environmental and pharmaceutical analysis.

This book covers all aspects of CE, from the principles and technical aspects to the most important applications. It is intended to meet the growing need for a thorough and balanced treatment of CE. The book will serve as a comprehensive reference work and can also be used as a textbook for advanced undergraduate and graduate courses. Both the experienced analyst and the newcomer will find the text useful.

Contents:

1992 xxvi + 586 pages
Price: US$ 225.50 / Dfl. 395.00
ISBN 0-444-89433-0

TO ORDER

Contact your regular supplier or:

ELSEVIER SCIENCE PUBLISHERS
P.O. Box 211
1000 AE Amsterdam
The Netherlands

Customers in the USA & Canada:

ELSEVIER SCIENCE PUBLISHERS
Attn. Judy Weislogel
P.O. Box 945
Madison Square Station
New York, NY 10160-0757, USA

No postage will be added to prepaid book orders. US $ book prices are valid only in the USA and Canada. In all other countries the Dutch guilder (Dfl.) price is definitive. Customers in The Netherlands please add 6% BTW. In New York State please add applicable sales tax. All prices are subject to change without prior notice.

ELSEVIER
SCIENCE PUBLISHERS